Phase-field modeling for ferroelectrics in a multi-scale approach

Zur Erlangung des akademischen Grades
Doktor der Ingenieurwissenschaften

der Fakultät für Maschinenbau des
Karlsruher Instituts für Technologie (KIT)
genehmigte

Dissertation

von

Dipl.-Ing. Benjamin Völker

geboren am 20.05.1982
in Bad Kissingen

Abstract

Today's development and improvement of ferroelectric materials is mainly based on experimental approaches. In order to significantly reduce development time and costs in the future, there is a demand for a virtual material development. The primary objective of this thesis is applying phase-field modeling in a knowledge based multi-scale simulation approach for the ferroelectric polycrystalline ceramics lead titanate (PTO) and lead zirconate titanate (PZT). Within this approach, phase-field modeling bridges the gap between predictive atomistic methods on one side and micromechanical modeling methods on the other side. Therefore, two interfaces in this multi-scale simulation chain have been developed and established in this work.

In order to link the atomic level to the meso-scale, results from first-principles calculations and atomistic shell-model simulations are employed as input parameters for the phase-field model. The core of a phase-field model is its thermodynamical free energy function, containing all crystallographic and domain wall information of the ferroelectric material. Based on a sensitivity analysis of the coefficients of the free energy function, a novel adjustment method has been developed for these coefficients that solely requires input parameters from atomistic calculations and thereby is completely knowledge based. Furthermore, the free energy function of the phase-field model has been improved by introducing a new elastic energy term: It allows for a separate adjustment of the cubic and tetragonal elastic properties for PTO and PZT, as well as an independent fitting of the spontaneous strains and the piezoelectric coefficients.

Typical ferroelectric domain configurations have been identified and investigated under electromechanical loading. The obtained domain effective small-signal and large-signal parameters serve as input for micromechanical modeling methods, thereby bridging the gap between the meso- and the micro-scale in the simulation chain. Therefore, the adjusted phase-field model has been implemented into a finite-element formulation. By investigating the monodomain state, the $90°$ domain stack as well as multidomain configurations, and taking defect mechanisms such as electrically charged point defects and grain boundaries into account, reversible domain wall motion and bending have been identified as governing processes on the meso-scale influencing the small-signal behavior. Furthermore, a clear correlation between the complexity of a domain structure and the resulting coercive field strength for initiating irreversible switching processes has been illustrated by the performed large-signal analysis.

Zusammenfassung

Herkömmliche Ansätze zur Weiterentwicklung und Verbesserung ferroelektrischer Materialien beruhen hauptsächlich auf experimentellen Vorgehensweisen. Um zukünftig den Zeit- und Kostenaufwand für die Optimierung von Werkstoffen deutlich senken zu können, bedarf es einer Methodik zur virtuellen Werkstoffentwicklung. Das vorrangige Ziel dieser Arbeit bestand darin, die Methodik der Phasenfeldmodellierung in einem wissensbasierten Multiskalensimulationsansatz für die ferroelektrischen polykristallinen Werkstoffe Blei-Titanat (PTO) und Blei-Zirkonat-Titanat (PZT) zu etablieren. Hierzu wurden zwei Schnittstellen in der Multiskalensimulationskette entwickelt.

Ergebnisse aus prädiktiven quantenmechanischen ab-initio Rechnungen und atomistischen Simulationen wurden als Eingangswerte für das Phasenfeldmodell verwendet, um die atomare Ebene mit der Mesoskala zu verbinden. Die thermodynamisch motivierte Freie Energiefunktion, die sämtliche kristallographischen und Grenzflächeninformationen des Ferroelektrikums enthält, stellt das Herzstück eines Phasenfeldmodells dar. Auf der Grundlage einer Sensitivitätsstudie der Freien Energiefunktion wurde eine neuartige Anpassungsmethode für deren Koeffizienten entwickelt, die ausschließlich Eingangswerte aus atomistischen Berechnungen benötigt und somit komplett wissensbasiert ist. Des Weiteren wurde die bestehende Energiefunktion um einen neuen Energieterm höherer Ordnung zur Beschreibung der elastischen Energie erweitert. Dieser ermöglicht nun für PTO und PZT eine getrennte Anpassung der elastischen Eigenschaften in der kubischen und in der tetragonalen Phase sowie eine unabhängige Anpassung der spontanen Verzerrungen und der piezoelektrischen Koeffizienten.

Typische ferroelektrische Domänenkonfigurationen wurden identifiziert und unter elektromechanischer Belastung untersucht. Die so ermittelten domänen-effektiven Kleinsignal- und Großsignalparameter stellen Eingangwerte für mikromechanische Modellierungsmethodiken, womit in der Multiskalensimulationskette die Lücke zwischen der Mesoskala und der Mikroskala geschlossen werden kann. Um ferroelektrische Domänenkonfigurationen auf der Mesoskala untersuchen zu können, wurde das zuvor an Ergebnisse atomistischer Berechnungen angepasste Phasenfeldmodell in die Finite-Element-Formulierung implementiert. Anschließend wurden verschiedene Domänenzustände untersucht: die Monodomäne, der ideale 90°-Domänenstapel sowie verschiedene Multidomänenkonfigurationen. Darüber hinaus wurden Defektmechanismen, beispielsweise elektrisch geladene Punktdefekte und Korngrenzen, in den Modellen berücksichtigt. Auf der Ebene der Mesoskala wurden reversible Domänenwandbewegungen sowie das Durchbiegen von Domänenwänden als maßgebliche extrinsische Einflussfaktoren auf die Kleinsignalwerte identifiziert. Im Rahmen einer Großsignalanalyse wurde die Koerzitivfeldstärke (bei der irreversibles Domänenschalten einsetzt) in Abhängigkeit von der Komplexität von Domänenstrukturen betrachtet. Dabei wurde ein eindeutiger Zusammenhang zwischen steigender Komplexität der Domänenstruktur und einem Abnehmen der resultierenden Koerzitivfeldstärke festgestellt.

Preface

Piezoelectricity, which is the generation of electric polarity in a material by application of stress, was discovered by J. Curie and P. Curie in 1880 when systematically studying the effect of inducing electric charge under pressure in crystals, such as tourmaline, quartz and other minerals [54]. About 40 years later, in 1921, Valasek recognized a reorientable electric moment in Rochelle salt [73]. Since experiments on the dielectric properties showed many aspects similar to the nature of ferromagnetism in iron, the group of materials exhibiting permanent internal dipol moments became known as ferroelectrics. In retrospect, the late discovery of ferroelectricity when compared to ferromagnetism might be explained by the fact that the spontaneous polarization within a ferroelectric material is shielded by electric charges on the surface, thereby impeding its detection. During World War II, ferroelectric materials were used in first applications: Capacitors made of barium titanate gained in importance due to its high dielectric constant [32]. This man-made ferroelectric ceramic exhibits piezoelectric properties that significantly exceed those found in natural materials. A first phenomenological theory of barium titanate was introduced by Devonshire in 1949. In the following years the technical exploitation of ferroelectric ceramics began, certainly boosted by the development of lead zirconate titanate (PZT) in the mid-1950s, which became today's most widely commercially used ferroelectric ceramic. Striking reasons for employing ferroelectrics for piezoelectric applications are their unique properties, such as a high dielectric permittivity, high pyroelectric coefficients and the high piezoelectric effect found in these materials, leading to an efficient electromechanical conversion of energy and signal. Furthermore, ferroelectrics can be poled: After processing of the ferroelectric ceramic, the remnant polarization can be oriented in the desired direction by application of an external electric field. The result is a macroscopic unipolar imprint in the material [82].

Nowadays, various commercial applications are available, and ferroelectric materials are used as sensors and actuators, for instance in ultrasonic medical imaging, in fuel injectors of high-performance common rail diesel engines, in precise positioning systems, in active vibration damping systems as well as in energy harvesting applications. Moreover, in the last years ferroelectric materials became increasingly interesting for a broad range of applications down to micro- or even nanosystems, and ferroelectric thin films are employed in Micro-Electro-Mechanical Systems (MEMS) as well as for information storage in nonvolatile memory applications [17, 66, 68].

When further improving and developing ferroelectric materials, companies in today's auto-

motive and electrical industry are confronted with enormous challenges: high cost pressure, decreasing product cycles, increasing system complexity of the products and a high demand on the material's performance at the same time. Therefore, the common empiric approach in developing new materials based primarily on experiments is no longer sufficient. Instead, methods and tools of virtual material development are to be applied in order to significantly reduce development time and costs in the future.

For increasing the performance of ferroelectric materials and allowing for a cost-efficient design of performant materials for specific purposes, it is of great importance to understand the fundamental physics of this multicomponent material system and to be able to predict the behavior of the material. The complex properties of ferroelectric polycrystalline ceramics originate over a wide range of length and time scales: While the ceramic consists of differently oriented grains on the micro-scale, each of these grains exhibits a substructure of ferroelectric domains on the meso-scale. On the nano-scale, each domain in turn consists of atoms arranged in distorted perovskite unit cells. Therefore, the understanding of the microstructure is not possible by using a single theory or method. Moreover, the complexity of the PZT microstructure does not allow an understanding of all mechanisms on a purely experimental basis.

Hence, a knowledge based multi-scale modeling approach is needed. Within the scope of the project COMFEM[1], such a multi-scale simulation chain is developed for polycrystalline ferroelectric ceramics. Following the basic concept of multi-scale material modeling approaches, material properties are calculated on one simulation level while using input parameters and methods of other levels. When applied to ferroelectrics, the multi-scale approach has to cover all physically involved scales from the atomistic level over the meso-scale up to the micro-scale, utilizing methods of computational physics.

Here, the thermodynamically motivated phase-field method can provide the critical link between calculations and simulations on the atomistic level on one side and micromechanical modeling methods on the other side. Based on the fundamental principles of thermodynamics, phase-field modeling is capable of describing microstructure evolution on the meso-scale. In this continuum theory, thermodynamic energies are formulated with respect to well-defined order parameters. Landau theory, which describes a system near a phase transition, employs the spontaneous polarization as the order parameter for the paraelectric-ferroelectric phase transition. The ferroelectric polarization is zero in the high-symmetry cubic phase and changes to a finite value once the symmetry is lowered [10]. Temporal and spatial evolution of the polarization order parameter take place in order to reduce the total free energy. This is predicted by the time-dependent Ginzburg-Landau equation [9, 60]. The thermodynamical free energy functions containing all crystallographic information of the material can be approximated by series expansions in terms of the order parameter. It is common to obtain the coefficients of the

energy functions from experiments in a phenomenological approach, as shown e.g. in the work of Devonshire [18, 20] who first applied Landau's theory of phase transitions to ferroelectrics. In the scope of this work, the necessary interfaces for employing the phase-field methodology in a knowledge based multi-scale approach for polycrystalline ferroelectric ceramics will be developed and established. Therefore, results from first-principles calculations and atomistic shell-model simulations on the nano-scale will be used for adjusting the thermodynamical free energy functions of the phase-field model. This represents a novel completely knowledge based modeling approach for the class of ferroelectrics, since all existing phase-field models found in literature for this class of material are at least partially adjusted to empirical input parameters. Similar multi-scale approaches combining first-principles and phase-field methodology have only been demonstrated for other classes of materials, e.g. for the problem of θ'-Al$_2$Cu precipitates in Al [12, 72] or for modeling the dendritic solidification in highly undercooled melts [6]. Furthermore, the formulation of the thermodynamical free energy function of the phase-field model will be extended by an elastic energy part that has not appeared in literature before, allowing for a more precise and realistic adjustment of the elastic properties. In order to establish the interface between phase-field modeling and micromechanical modeling methods, typical ferroelectric domain configurations on the meso-scale will be investigated using the adjusted phase-field model. By gradually increasing the complexity of the considered domain configurations and taking defect mechanisms such as charged point defects and grain boundaries into account, governing processes on the meso-scale will be identified that influence the small-signal and large-signal behavior of ferroelectric domain configurations. The obtained results then provide domain effective input parameters for micromechanical modeling methods, thereby bridging the gap between atomistic methods and micromechanical methods in the multi-scale simulation chain.

The outline of this thesis is as follows: An overview of the theoretical background of ferroelectrics and piezoelectrics is given in Chapter 1, regarding their thermodynamics, their phenomenological description as well as phase-field modeling approaches. In Chapter 2, the interface for linking the atomic level to the meso-scale is defined and developed. The introduction of a novel elastic energy term of the phase-field model's free energy as well as consequential further developments of this interface are shown in Chapter 3. In order to prepare the second interface in the multi-scale approach, Chapter 4 shows the finite-element implementation of the phase-field theory into COMSOL Multiphysics. Various typical ferroelectric domain configurations of increasing complexity are investigated under electromechanical loading in Chapter 5, yielding an understanding of mechanisms and processes taking place in ferroelectric domain patterns on the meso-scale. Thereby, domain-effective small-signal and large-signal parameters are obtained that can serve as input for micromechanical modeling methods. Concluding this work, the essential results are summarized in Chapter 6.

List of abbreviations

Symbol	Meaning
Latin symbols	
a_i	Landau energy coefficients
A	surface
b_i	electromechanical coupling energy coefficients
c_i	elastic energy coefficients
c_{ij}	elastic stiffness tensor (Voigt Notation)
$c_{\text{cub},ij}$	cubic elastic stiffness tensor (Voigt Notation)
$c_{\text{tetr},ij}$	tetragonal elastic stiffness tensor (Voigt Notation)
c_{ijkl}	elastic stiffness tensor
C_{ij}	elastic energy coefficients
d_{ij}	piezoelectric coefficients (Voigt Notation)
d_{ijk}	piezoelectric coefficients
D_i	dielectric displacement
$e_{\parallel}$	spont. strain parallel to P_0
$e_{\perp}$	spont. strain perpendicular to P_0
e_{ijk}	piezoelectric coefficients
E_i	electric field
E_{C}	coercive electric field strength
E_{C90}	coercive electric field for 90° switching
E_{C180}	coercive electric field 180° switching
f_i	elastic energy coefficients
g_i	electromechanical coupling coefficients
G	Gibbs free energy
G_1	elastic Gibbs free energy
G_{ij}	gradient energy coefficients
h_i	elastic energy coefficients
h_{ijk}	piezoelectric coefficients
H	Helmholtz free energy
n_i	surface normal
P_i	electric polarization

P_0	spontaneous polarization
P_i^+, P_i^-	ferroelectric domain types
q	electric charge density
q_{ij}	electrostrictive coefficients
Q_{ij}	electromechanical coupling energy coefficients
Q	heat
r_i	position
s_{ijkl}	elastic compliance tensor
S	entropy
$\tilde{S}_{ij}$	global strain in periodic boundary conditions
t	time
t_i	surface traction
T	temperature
T_0	transition temperature
T_C	Curie temperature
u_i	mechanical displacement
U	internal energy
V	volume
W	work
x_i	cartesian coordinate

Greek symbols

α_i, α_{ij}, α_{ijk}	Landau energy coefficients
β_{ij}	inverse mobility tensor
γ_i	external body micro-force
γ_{90}	90° domain wall energy
γ_{180}	180° domain wall energy
ε_{ij}	mechanical strain tensor
$\mathfrak{h}$	electric enthalpy
κ_0	vacuum permittivity
κ_{ij}	dielectric permittivity
ν	domain fraction
ξ_{ij}	micro-stress tensor
ξ_{90}	90° domain wall thickness
ξ_{180}	180° domain wall thickness
π_i	internal body micro-force
ρ	mass density

σ_{ij}	stress tensor
ϕ	electric potential
χ_{ij}	reciprocal dielectric permittivity
Ψ	total Helmholtz free energy density
ψ_{coup}	electrostrictive coupling energy density
ψ_{elec}	electric energy density
ψ_{elast}	elastic energy density
ψ_{ES}	elastic strain energy density
ψ_{grad}	gradient energy density
ψ_{Landau}	Landau energy density
ω	surface charge density

Contents

1. Theory

1.1. Basic description of ferroelectrics

Ferroelectric and piezoelectric materials belong to the broader class of dielectrics, which are defined as electrically isolating materials that can be polarized by an external electric field. Unlike conductors, where free electric charges drift through the material when an electric field is applied, the electrons in dielectrics are bound to the charged ions, so that practically no electric current flows. Instead, the differently charged ions in the material shift from their average thermal equilibrium position: Positive charges are displaced in the direction of the electric field, whereas negative charges are displaced in the opposite direction. This separation of charges results in an electric polarization, which lowers the electric field inside the dielectric. The overall charge neutrality of matter is expressed by

$$\vec{D} = \kappa_0 \vec{E} + \vec{P}, \tag{1.1}$$

consisting of a vacuum contribution $\kappa_0 \vec{E}$ and the electric polarization $\vec{P}$ (defined as the value of electric dipole moment per unit volume) in the material. Here, $\vec{D}$ is the dielectric displacement, $\vec{E}$ the externally applied electric field and κ_0 the vacuum permittivity. This relation is generally valid regardless of the nature of polarization, which could e.g. be pyroelectric, piezoelectric or dielectric [44].

Piezoelectrics are classified as materials that can be polarized not only by an electric field, but also by application of mechanical stress. Whether a specific material shows polar properties depends on the symmetry of its crystallographic structure. Out of the 32 crystallographic point groups describing all crystalline systems, 12 groups are not in possession of piezoelectric or polar properties because of their centrosymmetric structure (exception: group 432, which is cubic), while 20 point groups exhibit an electric polarization when subject to mechanical stress and are termed piezoelectric. Similarly, by application of an electric field a linear strain response is induced in these crystals. Of the 20 piezoelectric groups, 10 show a uniquely polar axis, i.e. they exhibit a spontaneous polarization parallel to the polar axis in the absence of an electric field and are termed pyroelectric or polar. In analogy to ferromagnetism, materials are called ferroelectric if it is possible to switch this spontaneous polarization between crystallographically equivalent configurations by appyling an external electric field. Thus, a ferroelectric material not only has to possess a spontaneous polarization, but it also has to be
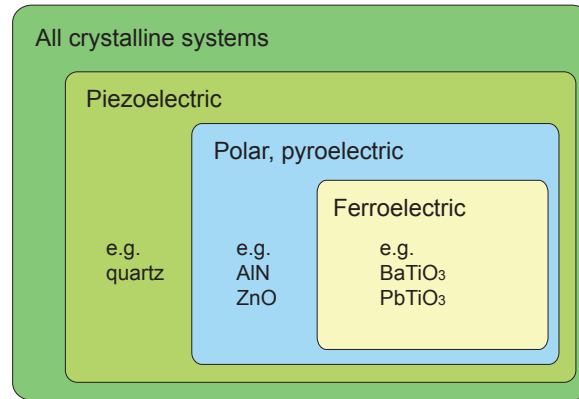
Figure 1.1.: Crystallographic groups classified by their electrical properties (after [7])

possible to reorient this spontaneous polarization by applying an external electric field. Figure 1.1 shows this classification of crystallographic groups by their electrical properties. In this work, ferroelectric materials of the oxygen octahedral ABO_3 crystal class are considered. Ceramics based on this perovskite microstructure are of special importance, because they are already widely used in applications like capacitors, PTC (positive temperature coefficient) resistors, sensors or actuators. Therefore, broad experience of mass production and reliability is available [82]. Barium titanate and lead zirconate titanate (PZT) are the most prominent representatives of the ferroelectric perovskite-type polycrystalline ceramics due to their profound scientific examination and commercial availability. PZT is the abbreviation for the solid solutions of the $Pb(Zr_xTi_{1-x})O_3$ (0<x<1) binary system. Considering the microstructure of PZT, Pb^{2+} cations are located at the corners of the perovskite unit cell on the A sites, and O^{2-} anions at the face center positions. On the B sites at the center of the unit cell, octahedrally coordinated Zr^{4+} or Ti^{4+} cations are located, depending on the composition of the $PbZrO_3$-$PbTiO_3$ system (Fig. 1.3). Determined by temperature and composition, PZT adopts distorted versions of the perovskite structure. From the phase diagram (Fig. 1.2) can be seen that above the Curie temperature T_C the unit cell is cubic. In this paraelectric phase, the central Zr^{4+} (or Ti^{4+}) cation constitutes an inversion center of the unit cell so that a spontaneous polarization is not possible. On cooling below the Curie temperature, the crystal structure changes to a phase of lower symmetry, which can be tetragonal, rhombohedral or orthorhombic. Table 1.1 gives an overview of the symmetry properties and possible polarization directions of these perovskite phases [61]. Considering the case of a tetragonal crystal phase, it becomes energetically more favorable for the Zr^{4+} (or Ti^{4+}) cation to shift from its central position in one of the six possible directions along the [100]-axis [24]. Therefore, the positively charged lead and zirconium (or titanium) cations are displaced with respect to the negatively charged oxygen anions, resulting in the formation of a polar axis with a spontaneous polarization and a tetragonal deformation of the perovskite unit cell (Fig. 1.3). Compared to the cubic state, the tetragonal unit cell elongates
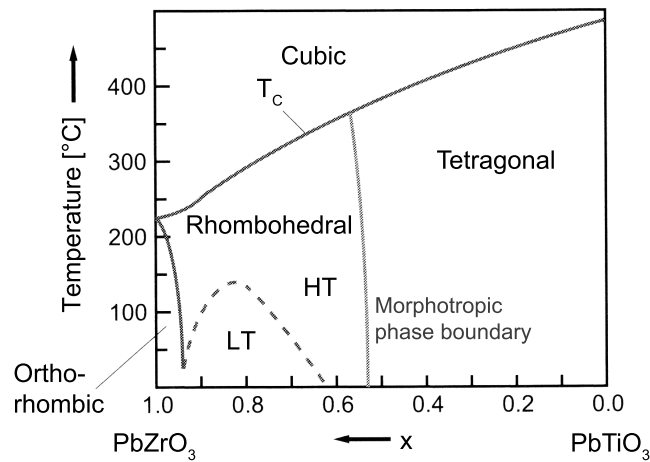
Figure 1.2.: Phase diagram of the $Pb(Zr_xTi_{1-x})O_3$ solid solutions system. Depending on temperature and composition, the unit cell of PZT can show cubic, tetragonal, rhombohedral or orthorhombic symmetry (after [45]).
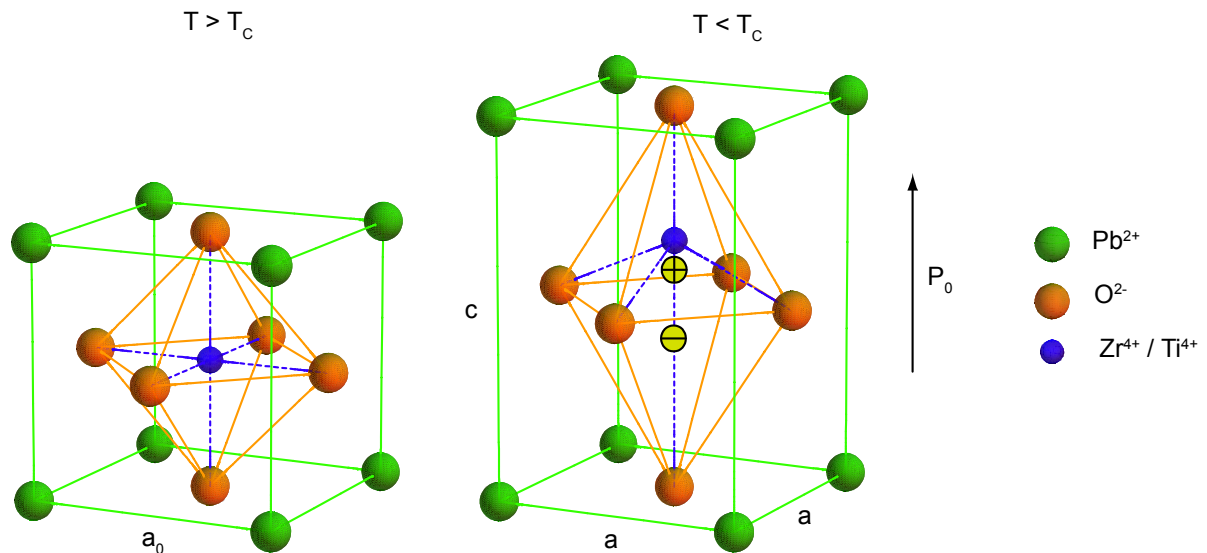
Figure 1.3.: Perovskite structure of PZT. Left: Above the Curie temperature T_C the unit cell is cubic. Right: Below T_C, the central ion is shifted along the polar [100] axis causing a tetragonally distorted unit cell. Since the centers of positive and negative charge no longer coincide, the unit cell shows a spontaneous polarization.

Table 1.1.: Possible crystalline phases of perovskite ferroelectrics

crystal symmetry	point group	polar axis	number of equivalent directions
cubic	$m3m$	-	-
tetragonal	$4mm$	[100]	6
rhombohedral	$3m$	[111]	8
orthorhombic	$mm2$	[110]	12

along the c-axis and contracts along the perpendicular a-axes. The relative deformation is called spontaneous strain and is found to be up to a few per cent. Starting with PbTiO$_3$ (PTO) in the PZT solid solutions system (cf. Fig. 1.2), a successive substitution of Zr^{4+} for Ti^{4+} reduces the tetragonal distortion and finally causes the appearence of a rhombohedral ferroelectric phase, which divides into a low- and a high-temperature phase. The orthorhombic phase near PbZrO$_3$ (PZO) shows an antiferroelectric distortion in which the polarization is cancelled on a unit cell level [7, 45]. Of special technological interest is the vicinity of the so-called morphotropic phase boundary (MPB): Due to the co-existing tetragonal and rhombohedral phases, the material has a large number of possible polarization directions (six from the tetragonal phase, eight from the rhombohedral phase) and therefore shows strong maxima of the dielectric and piezoelectric properties nearly independent of temperature at this composition [7].

When the material undergoes the phase transition from the non-polar paraelectric to the ferroelectric state, the perovskite unit cell is distorted, and a spontaneous polarization P_0 arises. The non-compensated polarization charges lead to the formation of a surface charge, which produces an electric field oppositely oriented to P_0 called depolarization field. Additionally, mechanical stresses occur in the material after the phase transition originating from the spontaneous strain of the unit cell and the induced interaction of differently oriented and strained grains in the poly-crystal ceramic. The resulting electric depolarization field energy and the elastic energy can be reduced by the formation of differently oriented ferroelectric domains (schematically shown in Fig. 1.4). These regions with a uniform orientation of polarization are separated by transition
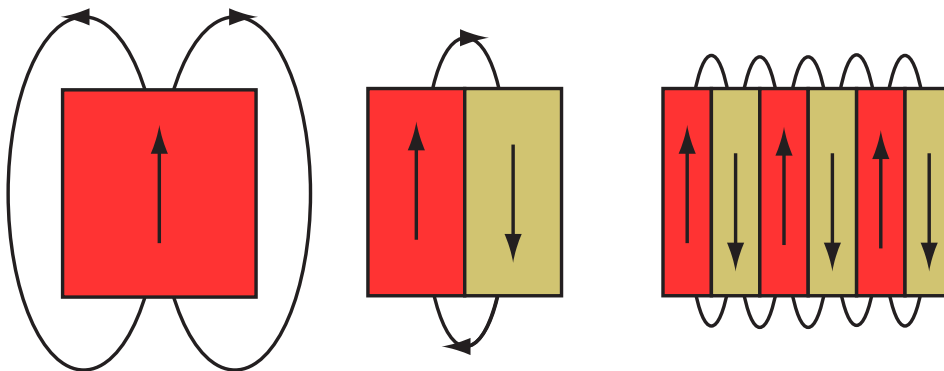

Figure 1.4.: Formation of oppositely oriented ferroelectric domains reduces the depolarization field energy (after [7]).

zones – so-called domain walls, in which the polarization changes over a short distance but gradually between the orientations in the two adjacent domains. Because of the six equivalent polar axes, only two types of domain walls exist in a tetragonal ferroelectric. Domains of oppositely oriented polarization are separated by 180° domain walls, whereas 90° domain walls separate domains which are perpendicular to each other. While both types of domain walls can reduce the depolarization field, only the 90° domain wall can lower the elastic energy evoked by the spontaneous strain [17]. In the rhombohedral ferroelectric phase with eight equivalent polar axes, three types of domain walls exist: 71° and 109° domain walls that are strain-producing, as well as the non-strain-producing 180° domain wall [32].

The outstanding dielectric and piezoelectric properties of ferroelectrics originate from their ability to switch spontaneous polarization and strain. This happens by shifts of domain walls, allowing the currently preferred ferroelectric domains to grow at the expense of energetically less favorable domains. Macroscopic switching of domains can be achieved by applying an external electric field that exceeds the so-called coercive field strength E_C, causing irreversible switching processes in the material and a hysteresis behavior. After reversing the electric field, the domain walls remain in their new equilibrium position, and the material therefore shows an altered domain structure and macroscopic net polarization. In addition to these polarization reversal processes, domain walls can move reversibly under weak or moderate sub-switching external fields, either by vibration or bending around an equilibrium position or by small jumps into a new equilibrium state. This reversible domain wall motion has a significant influence on the dielectric, mechanical and piezoelectric properties of the ferroelectric and is called extrinsic (nonlattice) contribution [17].

In order to summarize the basic properties of ferroelectrics, the structure of a perovskite polycrystalline ferroelectric ceramic is shown schematically in Fig. 1.5. On the nano-scale, the atoms are arranged in distorted perovskite unit cells, forming a single crystal which exhibits a spontaneous polarization and strain. The resulting depolarization field energy and elastic energy cause the formation of ferroelectric domains on the meso-scale: Each grain of the ceramic can be considered a single crystal and is split into a system of domains. Finally, on the micro-scale, the polycrystalline ceramic consists of a structure of mutually interacting grains. Fig. 1.5 also shows exemplary microscope images of the respective scales: The nano-scale can be depicted by transmission electron microscopy (TEM) or X-ray diffraction (XRD). To measure the ferroelectric domain structure on the meso-scale, methods of piezoresponse force microscopy (PFM) or atomic force microscopy (AFM) can be applied, whereas the grain structure on the micro-scale can be displayed using scanning electron microscopy (SEM) or optical microscopy methods.

Real ferroelectrics always contain electrical and elastic imperfections that interfere with domain walls and the polarization within domains. By grain boundaries, dopants as well as point de-
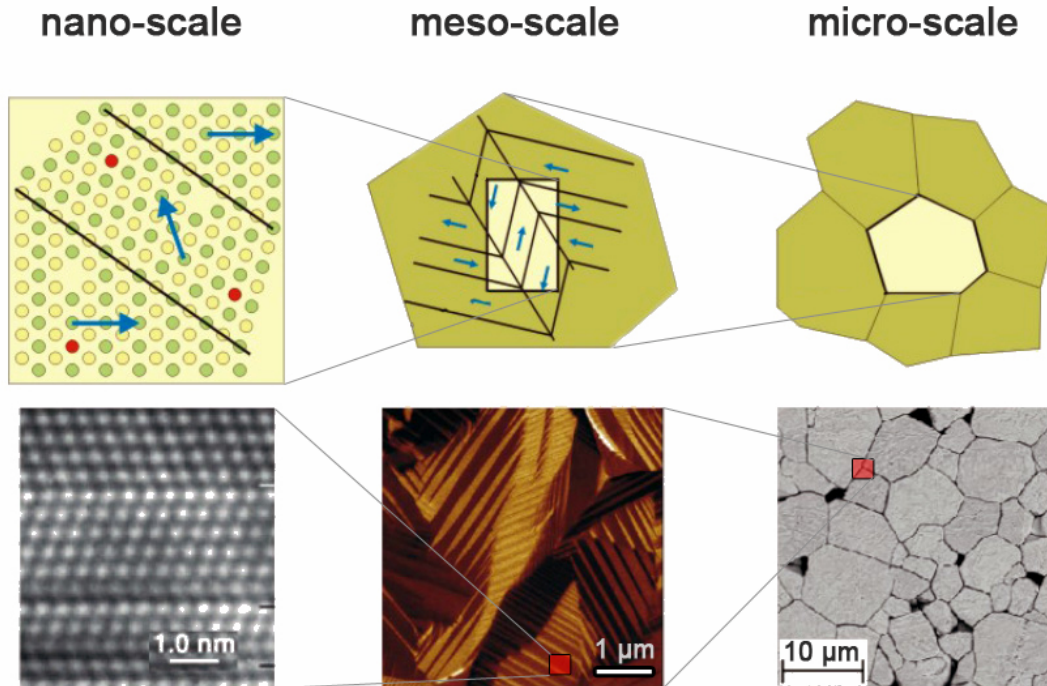
Figure 1.5.: Schematical structure of a polycrystalline ferroelectric ceramic: On the micro-scale, the ceramic consists of differently oriented grains. Each of these grains exhibits a substructure of ferroelectric domains on the meso-scale. On the nano-scale, each domain consists of atoms arranged in distorted perovskite unit cells. For all length scales, the corresponding experimentally measured microstructure is shown by exemplary images using different microscopical techniques: TEM (nano-scale), PFM (meso-scale) and SEM (micro-scale).

fects and defect complexes, the domain walls can be pinned or clamped. This constrains both reversible domain wall motion and irreversible switching, leading to dielectric, mechanical and piezoelectric losses in the material. Since the grains and the lattice orientations within the grains are randomly distributed, the piezoelectric and ferroelectric contribution of all domains cancel each other out on the macroscopic scale. To imprint a unipolar direction in the material, the ferroelectric ceramic is poled after processing by applying a strong external electric field above the coercive field E_C. Domains in the material are reorientated, resulting in a remnant polarization and strain in the desired direction. Due to the polycrystalline character of the material, the remnant properties are always lower than the spontaneous properties of a single crystal [17].

In order to increase the performance of ferroelectrics and allow for a cost-efficient design of performant materials for specific purposes, it is of great importance to understand the fundamental physics of this complex multicomponent material system on all involved scales and predict the behavior of the material. The complexity of the microstructure does not allow an understanding of all mechanisms on a purely experimental basis. This is especially the case for PZT, which has not been processed in the form of a single crystal up to today. Therefore, ferroelectrics are extensively studied using methods of computational physics. Since processes within ferroelectric

ceramics take place over a wide range of length and time scales, it is not possible to describe all effects by a single theory or method. Instead, there is a need for a multi-scale approach covering all scales involved: On the atomistic nano-scale, first-principles density function theory (DFT) calculations and classical atomistic calculations can be employed to predict the single crystal properties, whereas micromechanical modeling methods are used for calculating the electrical and mechanical properties of the polycrystal on the micro-scale. In between, phase-field modeling is capable of closing the gap between atomistic methods and micromechanical constitutive modeling by describing the microstructure evolution of the ferroelectric domain system on the meso-scale.

The emphasis of this work is to develop and establish the interfaces in the described multi-scale simulation chain for ferroelectric materials. Results from atomistic calculations will be used to adjust a phase-field model. Based on this model, phase-field simulations of ferroelectric domain systems will be performed, providing input parameters that can be used for micromechanical modeling methods. Within the phase-field methodology, the ferroelectric will be described by a phenomenological theory, where the material is treated as a continuum and the underlying atomistic structure is not regarded. Therefore, fields are postulated to describe the thermal, elastic and dielectric properties of the macroscopic ensemble, and the laws of thermodynamic and classical mechanics are used to relate these fields [54]. Hence, the thermodynamics of piezoelectric materials are discussed in the next chapter, providing a fundament for the subsequently following phenomenological description of ferroelectrics.

1.2. Thermodynamics of piezoelectric materials

Linear relations

The properties of a piezoelectric material are governed by the coupling of its mechanical, electrical and thermal parameters. Mechanical strain in a piezoelectric material can be induced by an external mechanical stress, an electric field and a temperature change, according to Hooke's law of elasticity, the converse piezoelectric effect and thermal expansion, respectively. Likewise, in a polar material electric charge can be induced by application of mechanical stress, electric field or a temperature change, described by the dielectric susceptibility, the direct piezoelectric effect and the pyroelectric effect [17, 43]. These mechanisms are illustrated in the Heckmann Diagram (Fig. 1.6). To relate the thermal, elastic and electrical parameters, a thermodynamic approach can be used. Following the work of Lines and Glass [54], it can be assumed that the thermal, elastic and dielectric properties of a piezoelectric or ferroelectric material are described by a set of the six parameters temperature T, entropy S, stress σ, strain ε, electric field $\vec{E}$ and dielectric
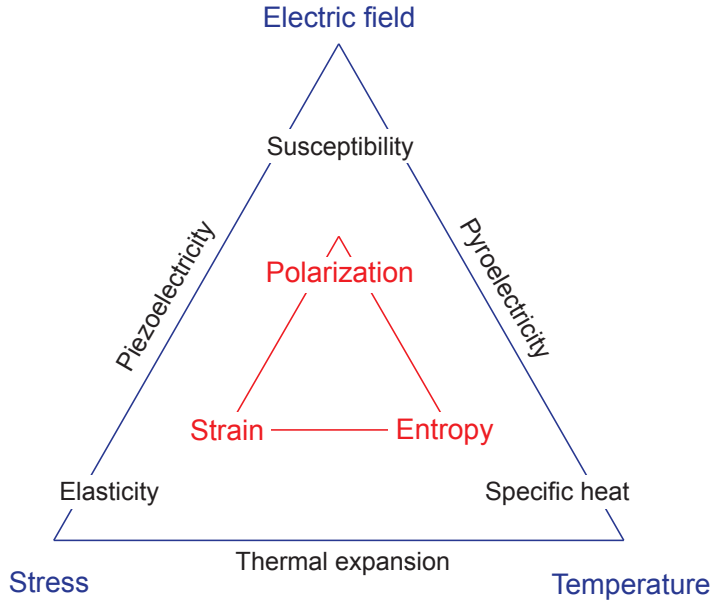
Figure 1.6.: Heckmann Diagram relating mechanical, thermal and electrical variables (after [61]). The outer triangle (blue) contains the intensive variables, which do not depend on the size of the described system, whereas the inner triangle (red) contains the extensive variables, which are directly proportional to the system size.

displacement $\vec{D}$. The strain

$$\varepsilon_{ij} = \frac{1}{2}\left(\frac{\partial u_i}{\partial r_j} + \frac{\partial u_j}{\partial r_i}\right) \tag{1.2}$$

in a solid is a measure of how the displacement $\vec{u}$ varies with position $\vec{r}$. This symmetrical 3×3 matrix has in general six independent components. In linear-elastic materials, the strain is generally related to the tensile stress by Hooke's law of elasticity

$$\sigma_{ij} = c_{ijkl} \cdot \varepsilon_{kl}, \tag{1.3}$$

where c_{ijkl} is the elastic stiffness tensor. Since there are three independent components of the electric field, the dielectric displacement as well as six independent stress and strain components, a total of 20 thermodynamic co-ordinates describes the system. From the first law of thermodynamics, the change in the internal energy U is given by

$$dU = dQ + dW, \tag{1.4}$$

where dQ is an infinitesimal amount of heat recieved by the piezoelectric and dW is an applied work by electric or mechanical forces. Under the assumption of a quasi-static transformation and reversibility, the second law of thermodynamics can be written as $dQ = T dS$. Thus, for a

uniform increment of strain and electric displacement, the internal energy (1.4) can be transformed into

$$dU = T dS + \sigma_{ij} d\varepsilon_{ij} + E_i dD_i. \tag{1.5}$$

In its simplest form, the internal energy U is described by the independent or natural variables S, ε_{ij} and D_i. Hence, the state variables T, σ_{ij} and E_i of the thermodynamic system can be calculated as

$$T = \left(\frac{\partial U}{\partial S} \right)_{\varepsilon_{ij}, D_i}, \qquad \sigma_{ij} = \left(\frac{\partial U}{\partial \varepsilon_{ij}} \right)_{S, D_i}, \qquad E_i = \left(\frac{\partial U}{\partial D_i} \right)_{S, \varepsilon_{ij}}, \tag{1.6}$$

where the subscripts indicate variables that are kept constant. Consequently, all thermodynamic properties of the system can be determined by partial differentiation of the internal energy U. The three equations (1.6) are referred to as the calorimetric, elastic and dielectric equation of state. To choose a different set of independent variables, additional thermodynamic potentials have to be determined. Two of the eight possible combinations of the conjugate pairs (T, S), $(\sigma_{ij}, \varepsilon_{ij})$ and (E_i, D_i) are the Helmholtz free energy H and the Gibbs free energy G, defined as

$$H = U - TS \tag{1.7}$$

$$G = U - TS - \sigma_{ij}\varepsilon_{ij} - E_i D_i, \tag{1.8}$$

and its associated differential forms, describing infinitesimal changes:

$$dH = -SdT + \sigma_{ij} d\varepsilon_{ij} + E_i dD_i \tag{1.9}$$

$$dG = -SdT - \varepsilon_{ij} d\sigma_{ij} - D_i dE_i. \tag{1.10}$$

Under equilibrium conditions, these thermodynamic potentials are stationary functions with respect to virtual displacements of the unconstrained or state variables. In a *non-equilibrium* configuration, where a particular set of independent variables is held constant, irreversible processes will take place and the system will strive towards its thermodynamical equilibrium by minimizing the free energy. If there is more than one locally stable state in the system for the same set of constraints, the state of lowest free energy is called *absolutely stable*, while all others are called *metastable*.

When choosing temperature, strain and dielectric displacement as natural variables, the Helmholtz free energy H is used to describe the system. The corresponding equations of state are obtained from (1.9) as

$$-S = \left(\frac{\partial H}{\partial T} \right)_{\varepsilon_{ij}, D_i}, \qquad \sigma_{ij} = \left(\frac{\partial H}{\partial \varepsilon_{ij}} \right)_{T, D_i}, \qquad E_i = \left(\frac{\partial H}{\partial D_i} \right)_{T, \varepsilon_{ij}}. \tag{1.11}$$

In an analogous manner, for choosing temperature, stress and electric field as independent variables, the equations of state of the Gibbs free energy G from (1.10) are

$$-S = \left(\frac{\partial G}{\partial T}\right)_{\sigma_{ij}, E_i}, \qquad -\varepsilon_{ij} = \left(\frac{\partial G}{\partial \sigma_{ij}}\right)_{T, E_i}, \qquad -D_i = \left(\frac{\partial G}{\partial E_i}\right)_{T, \sigma_{ij}}. \qquad (1.12)$$

For the Gibbs free energy G, the linear differentials of the equations of state are

$$
\begin{aligned}
\mathrm{d}S &= \left(\frac{\partial S}{\partial T}\right)_{\sigma_{ij}, E_i} \mathrm{d}T + \left(\frac{\partial S}{\partial \sigma_{ij}}\right)_{T, E_i} \mathrm{d}\sigma_{ij} + \left(\frac{\partial S}{\partial E_i}\right)_{T, \sigma_{ij}} \mathrm{d}E_i \qquad (1.13) \\
\mathrm{d}\varepsilon_{ij} &= \left(\frac{\partial \varepsilon_{ij}}{\partial T}\right)_{\sigma_{ij}, E_i} \mathrm{d}T + \left(\frac{\partial \varepsilon_{ij}}{\partial \sigma_{ij}}\right)_{T, E_i} \mathrm{d}\sigma_{ij} + \left(\frac{\partial \varepsilon_{ij}}{\partial E_i}\right)_{T, \sigma_{ij}} \mathrm{d}E_i \\
\mathrm{d}D_i &= \left(\frac{\partial D_i}{\partial T}\right)_{\sigma_{ij}, E_i} \mathrm{d}T + \left(\frac{\partial D_i}{\partial \sigma_{ij}}\right)_{T, E_i} \mathrm{d}\sigma_{ij} + \left(\frac{\partial D_i}{\partial E_i}\right)_{T, \sigma_{ij}} \mathrm{d}E_i,
\end{aligned}
$$

and their coefficients are called compliances. They are functions of the unpertubated independent variables and quantitatively describe the coupling between fields in the ferroelectric material. The compliances of most common use are those relating stress to strain (elastic compliance), dielectric displacement to electric field (dielectric constant or permittivity), stress or strain to dielectric displacement or electric field (piezoelectric compliance), dielectric displacement to temperature (pyroelectric compliance) and strain to temperature (thermal expansion). Assuming isothermal conditions ($\mathrm{d}T = 0$) and taking equations (1.12, 1.13) leads to the *constitutive piezoelectric equations*

$$
\begin{aligned}
\mathrm{d}\varepsilon_{ij} &= s_{ijkl}^{E_i} \mathrm{d}\sigma_{kl} + d_{ijk}^{\dagger} \mathrm{d}E_k \qquad (1.14) \\
\mathrm{d}D_i &= d_{ijk} \mathrm{d}\sigma_{jk} + \kappa_{ij}^{\sigma_{ij}} \mathrm{d}E_j. \qquad (1.15)
\end{aligned}
$$

Proceeding the same way with equation (1.12) results in another set of linear piezoelectric equations, now based on the Helmholtz free energy with strain and dielectric displacement as natural variables:

$$
\begin{aligned}
\mathrm{d}\sigma_{ij} &= c_{ijkl}^{D_i} \mathrm{d}\varepsilon_{kl} - h_{ijk}^{\dagger} \mathrm{d}D_k \qquad (1.16) \\
\mathrm{d}E_i &= -h_{ijk} \mathrm{d}\varepsilon_{jk} + \chi_{ij}^{\varepsilon_{ij}} \mathrm{d}D_j. \qquad (1.17)
\end{aligned}
$$

Here, the elastic compliance s_{ijkl} and the elastic stiffness c_{ijkl} are fourth-rank tensors, while the dielectric permittivity κ_{ij} and its reciprocal χ_{ij} (also referred to as dielectric susceptibility) are of second rank. The third-rank tensors describing the piezoelectric effect are denoted d_{ijk} and h_{ijk}, whereas $d_{ijk}^{\dagger}$ and $h_{ijk}^{\dagger}$ are the piezoelectric tensors of the converse piezoelectric effect. These compliances can be derived directly from a thermodynamical potential by partial differentiation: The isothermal elastic compliance at constant electric field $s_{ijkl}^{E_i, T}$ and the elastic stiffness at

constant dielectric displacement $c_{ijkl}^{D_i,T}$ are given as

$$s_{ijkl}^{E_i,T} = \left(\frac{\partial \varepsilon_{ij}}{\partial \sigma_{ij}}\right)_{E_i,T} = -\left(\frac{\partial^2 G}{\partial \sigma_{ij}^2}\right)_{E_i,T}, \qquad c_{ijkl}^{D_i,T} = \left(\frac{\partial \sigma_{ij}}{\partial \varepsilon_{kl}}\right)_{D_i,T} = \left(\frac{\partial^2 H}{\partial \varepsilon_{ij}\partial \varepsilon_{kl}}\right)_{D_i,T} \tag{1.18}$$

whereas the isothermal permittivity $\kappa_{ij}^{\sigma_{ij},T}$ and its reciprocal $\chi_{ij}^{\varepsilon_{ij},T}$ are

$$\kappa_{ij}^{\sigma_{ij},T} = \left(\frac{\partial D_i}{\partial E_i}\right)_{\sigma_{ij},T} = -\left(\frac{\partial^2 G}{\partial E_i^2}\right)_{\sigma_{ij},T}, \qquad \chi_{ij}^{\varepsilon_{ij},T} = \left(\frac{\partial E_i}{\partial D_i}\right)_{\varepsilon_{ij},T} = -\left(\frac{\partial^2 H}{\partial D_i^2}\right)_{\sigma_{ij},T} \tag{1.19}$$

and the isothermal linear piezoelectric compliances d_{ijk} and h_{ijk} are

$$d_{ijk} = \left(\frac{\partial D_i}{\partial \sigma_{jk}}\right)_{T,E_i} = -\left(\frac{\partial^2 G}{\partial \sigma_{jk}\partial E_i}\right)_T = \left(\frac{\partial \varepsilon_{jk}}{\partial E_i}\right)_{T,\sigma_{ij}} = d_{kij}^\dagger \tag{1.20}$$

$$h_{ijk}^\dagger = -\left(\frac{\partial \sigma_{ij}}{\partial D_i}\right)_{T,\varepsilon_{ij}} = -\left(\frac{\partial^2 H}{\partial \varepsilon_{ij}\partial D_k}\right)_T = -\left(\frac{\partial E_k}{\partial \varepsilon_{ij}}\right)_{T,D_i} = h_{kij}. \tag{1.21}$$

The last two equations demonstrate the thermodynamic equivalence of the direct and the converse piezoelectric effect. For the case of small dielectric displacements and strains, as in ferroelectrics close to the Curie temperature, the thermodynamic potential is commonly defined as a linear or low-order Taylor series expansion in D_i and ε_{ij} around the equilibrium prototype state $D_i = \varepsilon_{ij} = 0$. For example, the Helmholtz free energy H with the independent variables D_i and ε_{ij} up to quadratic terms can be expressed as

$$H = H_0 + \left(\frac{\partial H}{\partial \varepsilon_{ij}}\right)\varepsilon_{ij} + \left(\frac{\partial H}{\partial D_i}\right)D_i + \left(\frac{\partial^2 H}{\partial \varepsilon_{ij}\partial \varepsilon_{kl}}\right)\varepsilon_{ij}\varepsilon_{kl} \tag{1.22}$$

$$+ \left(\frac{\partial^2 H}{\partial D_i\partial D_j}\right)D_iD_j + \left(\frac{\partial^2 H}{\partial D_i\partial \varepsilon_{jk}}\right)D_i\varepsilon_{jk}. \tag{1.23}$$

Note that for the components of the compliance tensors several conditions are imposed by the symmetry of the material. Some of the elements have to be zero, while others are required to be interrelated. In this work, ferroelectrics with a paraelectric cubic and a polarized phase of tetragonal symmetry are considered. Using Voigt's notation (cf. section 5.2.2), the compliances exhibit the structure shown in appendix A.1.

Non-linear relations

To this point, only linear material behavior has been taken into account, valid for small applied fields and deformations. However, some characteristic properties of dielectrics and ferroelectrics have been experimentally observed that can not be described using a linear material

model. One phenomenon that can not be explained by the linear approach is electrostriction: An electric field applied to a material of arbitrary symmetry generally shifts the ions from their equilibrium position, leading to a deformation of the unit cell. This effect, called electrostriction, is even observed in totally isotropic materials and therefore has to be of different nature than the inverse piezoelectric effect. Considering a material with a centrosymmetric, non-polar unit cell, the centers of positive and negative charges are situated at the same position in the absence of an external electric field. If an electric field is applied, the centers of charges are separated and the unit cell is elongated. Upon reversal of the electric field, the elongation of the unit cell will be exactly the same, while the polarization is now inverted. Since this electrically induced deformation is independent of the sign of the applied electric field, the effect is assumed to be quadratic. Electrostriction is a higher order effect and dominated by the linear piezoelectric effect in materials possessing a polar unit cell. For strong non-linear materials, such as ferroelectrics, the linear approach is also not sufficient since it does not yield the observed hysteresis behavior of the polarization.

Therefore, an extension of the differential equation of state to higher orders is necessary. A common assumption is that the strains in the material are small, so only strain terms of the order $\varepsilon_{ij}\varepsilon_{kl}$ and $\varepsilon_{ij}D_kD_l$ are taken into account (all other lower order strain terms are symetrically incompatible). Thus, the non-linear Helmholtz free energy takes the form

$$
\begin{aligned}
H(D_i, \varepsilon_{ij}) &= \frac{1}{2}\overline{\alpha}_{ij}D_iD_j + \frac{1}{2}c_{ijkl}\varepsilon_{ij}\varepsilon_{kl} + \frac{1}{2}q_{ijkl}D_iD_j\varepsilon_{kl} + \\
&+ \frac{1}{4}\overline{\overline{\alpha}}_{ijkl}D_iD_jD_kD_l + \frac{1}{6}\overline{\overline{\overline{\alpha}}}_{ijklmn}D_iD_jD_kD_lD_mD_n,
\end{aligned}
\tag{1.24}
$$

where the coefficients $\overline{\alpha}$, $\overline{\overline{\alpha}}$ and $\overline{\overline{\overline{\alpha}}}$ are the Devonshire coefficients for constant stress that depend on the material composition and the temperature. Under the assumption that the free energy function describes both the polar and the non-polar phase, there are several restrictions to these coefficients. For crystals with a cubic non-polar prototype phase, all odd-ranked tensors in the thermodynamic potential vanish. Further, there are only one independent component of $\overline{\alpha}$ (termed α_1), two components of $\overline{\overline{\alpha}}$ (α_{11}, α_{12}) and three components of $\overline{\overline{\overline{\alpha}}}$ ($\alpha_{111}, \alpha_{112}, \alpha_{123}$). The resulting elastic non-linear equation of state

$$
\sigma_{ij} = c_{ijkl}\varepsilon_{kl} + \frac{1}{2}q_{ijkl}D_kD_l
\tag{1.25}
$$

shows that the strains are of the same order of smallness as D_i^2, justifying the expansion (1.24) since the terms retained are consistently of lower order than those neglected. Likewise, the non-linear Gibbs free energy can be obtained. The now following phenomenological description of ferroelectrics will be based on this free energy function and the shown thermodynamical considerations.

1.3. Phenomenological description of ferroelectrics

In a phenomenological approach, empirical observations are related to one another using a minimum set of input parameters [11]. Although the approach has to be consistent with fundamental physical theories, it does not have to be derived directly from them. The set of input parameters can be obtained either from experiments or from calculations, e.g. on the atomistic level. Maybe the most prominent example of a phenomenological approach is the Ginzburg-Landau theory of superconductivity [29]. Based on macroscopic observations and thermodynamic considerations, the theory predicts essential properties of superconductivity without regarding the underlying microscopic mechanisms, which were unknown by the time the theory was proposed.

The phenomenological approach is also well suited to characterize the behavior of ferroelectric materials on the mesoscale. Landau's general theory of second-order phase transitions is needed as a fundament of the approach. This theory descibes the behavior of physical entities – so-called order parameters – in the vicinity of a phase transition. It relies solely on symmetry considerations and on the assumption that the free energy of the system is an analytical function. Landau's theory was first applied to ferroelectris by Devonshire in order to phenomenologically describe this class of materials. The Landau-Devonshire theory is well suited to characterize uniformly poled bulk systems near the ferroelectric phase transition. For systems containing a spatially non-uniform polarization, e.g. domains of differently orientated polarization that occur naturally in ferroelectrics caused by the minimization of electrostatic energy, the theory has to be extended to take polarization-polarization interaction into account. This is considered in the Landau-Ginzburg theory by an extension of the free energy density that allows not only the description of ferroelectric bulk systems with a spatial polarization gradient, but also, by applying boundary conditions, that of ferroelectric thin films.

1.3.1. General Landau theory of phase transitions

In his 1937 work, Landau shows a phenomenological approach to describe second-order phase transitions in a general way [51]. As mentioned above, his theory is based solely on symmetry considerations and the presumption of an analytical free energy function that describes the equilibrium behavior of the system near the regarded phase transition. It is especially well suited for systems with long-range[1] interactions and a high coordination number, like superconductors and ferroelectrics.

Landau's theory (LT) is based on the observation that a system cannot change smoothly between two phases of different symmetry. Since the two phases must have the same symmetry at a

---

[1]On the contrary to e.g. magnetic systems, where couplings are predominantly short range: While in conventional ferromagnetic systems the dipolar interactions play a role in determining the domain structure, the analogous dipolar couplings in ferroelectrics are important on essentially all length scales [11].

shared transition line, one phase has to be of higher symmetry than the other. This fact is used to introduce a so-called order parameter – a physical quantity serving as a measure of the degree of order in the system and characterizing the phase transition. Once the symmetry is broken during a phase transition from a high-symmetry phase to a phase of lower symmetry, one or more additional parameters are needed to completely describe the system. This is achieved by the introduced order parameter, which is zero in the high-symmetry phase and changes (continuously for a second-order phase transition) to a finite value in the low-symmetry phase. The order parameter can be scalar, complex or vectorial, depending on the phase transition to be characterized and the physics involved. In the phenomenological Ginzburg-Landau theory of superconductivity for example, a complex order parameter indicates how deep the system is in the superconducting phase.

The free energy function containing all information about the system can be expressed in terms of a Taylor series expansion of the order parameter in the vicinity of the phase transition. Here, only symmetry compatible terms of the order parameter are retained. Under the assumption that the system will always strive towards its state of lowest free energy, the thermal equilibrium value of the order parameter can be obtained by minimizing the free energy function. For LT to be valid, it is essential for fluctuations of the order parameter to be small compared to the order parameter itself [11].

1.3.2. Thermodynamics of ferroelectric phase transitions

Before applying LT to ferroelectrics, it is important to get a proper insight into the thermodynamics of ferroelectric phase transitions. The behavior of the substance near the transition is characterized by its free energy which can be expressed by different sets of independent variables. For the description of ferroelectric phase transitions it is most convenient to choose the *elastic Gibbs free energy*

$$G_1 = U - TS - \sigma_{ij}\varepsilon_{ij}, \tag{1.26}$$

which is expressed as a function of temperature, stress and dielectric displacement, as can be seen from its associated differential form:

$$\mathrm{d}G_1 = -S\mathrm{d}T - \varepsilon_{ij}\mathrm{d}\sigma_{ij} + E_i\mathrm{d}D_i, \tag{1.27}$$

This polynomial thermodynamic potential is expanded in terms of the deviation from the prototype state with the fewest possible number of terms that can still completely describe the system. We consider the simplest conceivable theoretical situation of a stress-free system with a centrosymmetric non-polar phase and a polarization directed only along one of the crystallographic axes in the uniformly polarized phase. The approach can be extended to the three-dimensional

case in a straight forward manner without loss of generality. Choosing the origin of the unpolarized elastic Gibbs free energy density G_1 to be zero, it can be written as

$$G_1(D) = \frac{1}{2}aD^2 + \frac{1}{4}bD^4 + \frac{1}{6}cD^6 \tag{1.28}$$

where a, b, and c are material coefficients that generally depend on the temperature. However, first- and second order transitions can be described with only coefficient a depending on the temperature. Of the two temperature-independent coefficients, c always has to be positive in order to fulfill the stability criterion

$$\lim_{D \to \pm\infty} G_1(D) = +\infty, \tag{1.29}$$

and the sign of b defines the order of the phase transition. The non-linear terms in the free energy function allow possible divergencies in the dielectric response, like the experimentally found anomaly of the dielectric constant showing a strong maximum near the Curie point [70] or hysteresis behavior. The dielectric equation of state can be computed by differentiation of (1.28), directly relating the electric field E parallel to the polarization direction and the dielectric displacement D:

$$\frac{\partial G_1}{\partial D} = E = aD + bD^3 + cD^5. \tag{1.30}$$

Further, from the definition (1.19) of the reciprocal dielectric permittivity χ follows

$$\frac{\partial E}{\partial D} = \chi = a + 3bD^2 + 5cD^4. \tag{1.31}$$

Phase transitions are classified by the Ehrenfest scheme: In this basic thermodynamic classification, the thermodynamic potential as well as its derivatives at the phase transition are considered. If first derivations of the thermodynamic potential exhibit jump singularities, the phase transition is denoted *first order*, whereas continuous first derivatives and discontinuous second derivatives indicate a *second order* phase transition [5, 27]. For temperature-driven phase transitions in ferroelectrics in the absence of external stresses and electric fields, the behavior of the dielectric displacement D at the transitions temperature characterizes the phase transition: For a first order phase transition, D exhibits a jump singularity at the phase transition temperature, whereas D is continuous for a second order phase transition. Since both types of phase transitions are relevant for ferroelectrics, their properties are discussed below.

Second order ferroelectric phase transition

For a second order phase transition with continuous a continuous dielectric displacement D, parameter b in the elastic Gibbs free energy function (1.28) has to be positive. Without loss of generality, c is set to zero, since the stability criterion (1.29) is fulfilled when the coefficient of the highest-order term is positive. The sign of the temperature dependent coefficient a defines the phase: For $a > 0$, the elastic Gibbs free energy G_1 has only one minimum at $D = 0$ (non-polar paraelectric phase), whereas it has two symmetrical minima for $a < 0$ corresponding to the spontaneous polarization $D = \pm P_0$. The phase transition takes place at the Curie-temperature $T = T_C$ for $a = 0$. From (1.31) follows that the reciprocal dielectric permittivity $\chi = a$ in the paraelectric non-polar phase ($D = 0$). Thus, a possible linear approach for a is

$$a = \chi^{T>T_C} = \beta(T - T_C), \tag{1.32}$$

where β is a positive constant. Also known as the Curie-Weiss form, this behavior is confirmed by experiments [45] and mean-field statistical models [54]. The elastic Gibbs free energy G_1 is plotted in Figure 1.7a for various temperatures.

a)

b)
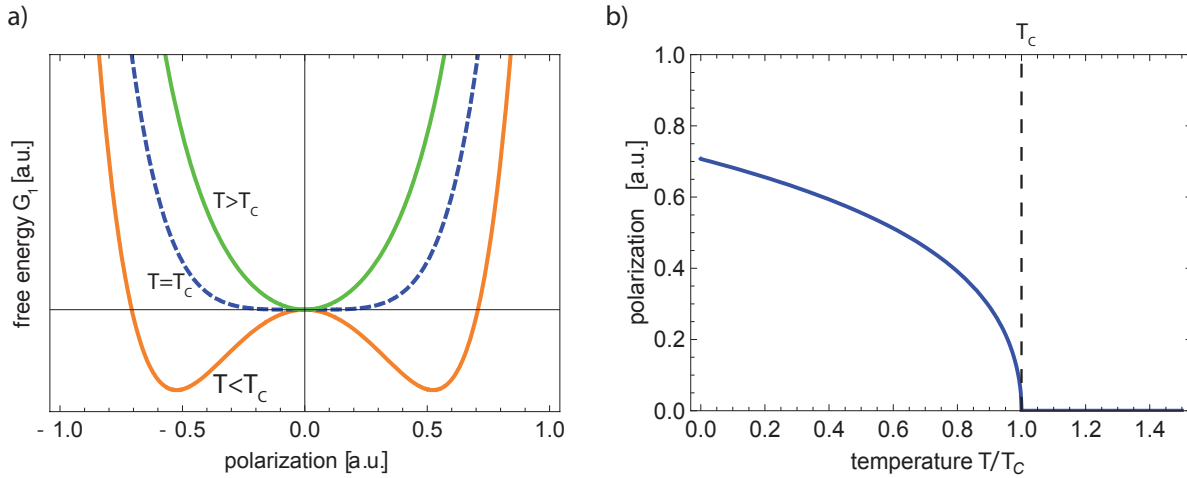
Figure 1.7.: a) Qualitative temperature dependence of the elastic Gibbs free energy G_1 plotted versus the polarization. Above the Curie point T_C, the minimum at $D = 0$ corresponds to the paraelectric phase, whereas below T_C the energy has two equivalent minima at the spontaneous polarized states. (b) Spontaneous polarization versus temperature, dropping continuously to zero at the Curie temperature.

By finding the absolute minimum of the free energy, the spontaneous polarization

$$P_0 = \sqrt{\frac{\beta(T_C - T)}{b}}, \tag{1.33}$$

is computed from equation (1.30) for $E = 0$. Finally, the reciprocal permittivity of the ferro-

electric phase $\chi^{T<T_C}$ is found by substituting equations (1.32) and (1.33) in (1.31), yielding

$$\chi^{T<T_C} = \beta(T - T_C) + 3bD^2 = -2\beta(T - T_C). \tag{1.34}$$

Figure 1.8.: Temperature dependence of the dielectric permittivity κ and its reciprocal χ for a second order phase transition. At the transition temperature (T_C), the reciprocal permittivity becomes zero, causing the divergence of the dielectric permittivity.

Qualitative sketches in Figures 1.7b and 1.8 show the temperature dependence of the spontaneous polarization $P_0(T)$, the dielectric permittivity $\kappa(T)$ and its reciprocal $\chi(T)$. The continuity of the energy function's first derivatives (e.g. P_0) – classifying a second-order phase transition – can be seen, as wel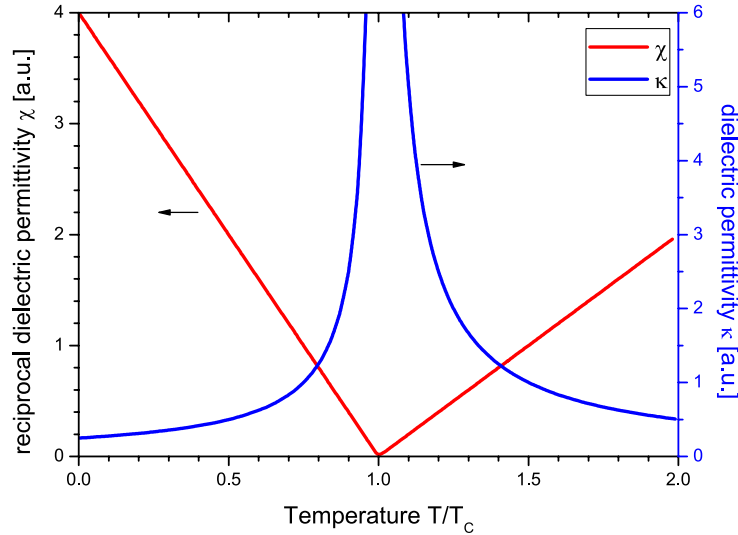l as the divergence of the dielectric permittivity near the Curie point caused by the reciprocal permittivity becoming zero. Note that the slope of the reciprocal permittivity in the polarized phase is negative and twice as big as in the paraelectric phase above T_C.

First order ferroelectric phase transition

A first order ferroelectric phase transition is characterized by a discontinuous jump of the dielectric displacement D. When choosing the coefficients $b < 0$ and $c > 0$, the elastic Gibbs free energy G_1 has energetically equal minima for $D = 0$ and $D = \pm P_0$ at a certain temperature T_0. At this temperature T_0, denoted as transition temperature, the phase transition from the non-polar paraelectric phase to the polarized phase takes place. Contrary to the case of a second order phase transition, where the transition temperature T_0 coincides with the Curie temperature T_C (for which according to the Curie-Weiss law (1.32) the dielectric permittivity becomes zero), the transition temperature T_0 exceeds the Curie temperature T_C for the case of a first order phase transition.

Figure 1.9 a qualitatively shows the elastic Gibbs free energy G_1 for various temperatures: For $T < T_0$, i.e. in the paraelectric phase, the free energy may now have subsidiary local minima for non-zero dielectric displacements D. As the temperature is decreased, these minima drop and become energetically more favorable at the transition temperature $T = T_0$. Thus, the transition takes place when the elastic Gibbs free energy G_1 and its first derivative with respect to D both vanish for a finite value of D. For temperatures below T_0, the free energy has two symmetrical minima located at $D = \pm P_0$, corresponding to the ferroelectric phase. In the absence of an electric field, combining (1.28) and (1.30) leads to the transition temperature and spontaneous polarization

$$T_0 = T_C + \frac{3}{16}\frac{b^2}{\beta c} \tag{1.35}$$

$$P_0(T) = \frac{1}{2}\sqrt{\frac{-3b + \sqrt{9b^2 + 48c\beta(-T + T_C)}}{c}} \quad ,T < T_0. \tag{1.36}$$
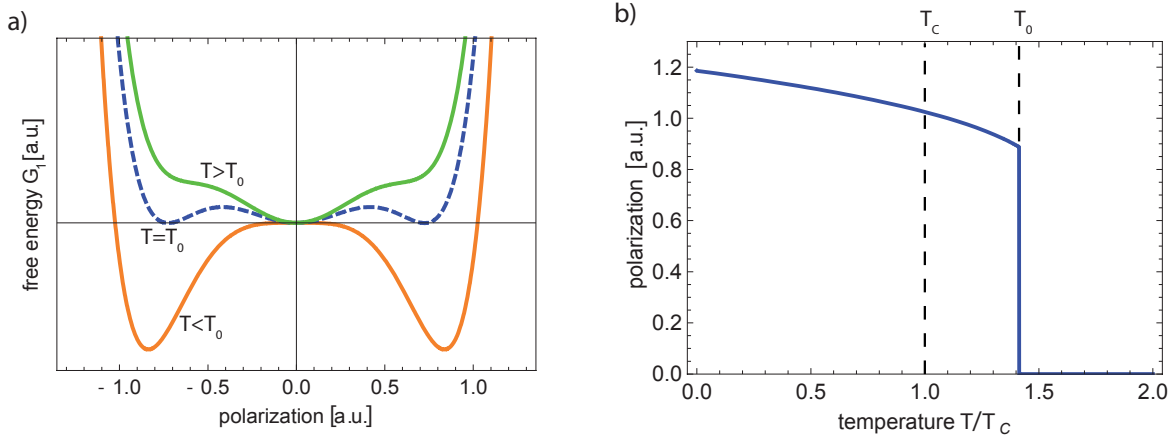
Figure 1.9.: a) Qualitative temperature dependence of the elastic Gibbs free energy plotted versus the polarization. Contrary to the case of a second order phase transition, the free energy now can have subsidiary (local) minima above the transition temperature T_0. (b) Temperature dependence of the spontaneous polarization. The first order phase transition takes place at the transition temperature T_0 higher than the Curie temperature T_C. Note that the big difference between T_0 and T_C in this schematical illustration was chosen in order to enhance the visibility of the properties of a first order phase transition. For instance for $BaTiO_3$, the difference $T_0 - T_C$ is experimentally found to be in the range of 10K [18].

In like manner as for the second order phase transition, the temperature dependent reciprocal dielectric permittivity χ at $D = \pm P_0(T)$ is computed with eqn. (1.31):

$$\chi = \beta(T - T_C) + 3bP_0(T)^2 + 5cP_0(T)^4 \tag{1.37}$$

The temperature dependence of both the spontaneous polarization and the dielectric permittivity for a first order phase transition are sketched in Figures 1.9b and 1.10, respectively. Contrary to a second order phase transition, the polarization shows a discontinuity at the transition temperature, while the dielectric permittivity κ no longer diverges because its reciprocal χ is now non-zero at T_0. Extrapolating the reciprocal permittivity of the high-temperature to temperatures below T_0 yields the Curie temperature T_C, which is by definition the intersection of the dielectric permittivity with the zero-line (cf. eqn. 1.32). Here, the difference to a second order phase transition becomes obvious, for which the transition temperature T_0 and the Curie temperature T_C coincide, i.e. the phase transition takes place at the Curie temperature.
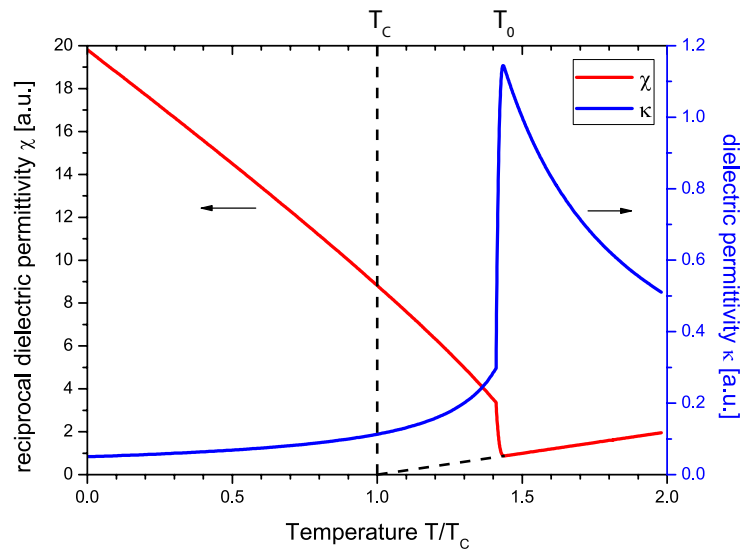
Figure 1.10.: Temperature dependence of the dielectric permittivity κ and its reciprocal χ for a first order phase transition.

1.3.3. Landau-Devonshire theory of ferroelectrics

Since long-range dipole-dipole interactions are dominating in ferroelectrics, LT of phase transitions is well-suited to describe this class of materials in the vicinity of the ferroelectric phase transition. Devonshire was the first to apply LT to ferroelectrics by taking the dielectric polarization vector as the order parameter to characterize the paraelectric-ferroelectric phase transition. Starting in the high-symmetric prototype phase and cooling the system down, the phase transition takes place at the transition temperature T_0, and the order parameter changes from zero in the high-symmetric unpolarized paraelectric phase to a finite value in the polarized ferroelectric phase of lower symmetry. Whether this change of polarization is continuous or discontinuous depends on the nature of the phase transition, which can be of first or second order. In its simplest form, the order parameter is completely uniform in the whole system, with no spatial or temporal fluctuations. This is considered by the Landau-Devonshire theory (LDT), which is

appropriate to describe uniformly poled bulk systems [18, 19, 20].

Landau's and Devonshire's key assumption is that a system in the vicinity of a phase transition can be expressed by a thermodynamical potential (e.g. the Helmholtz free energy) in terms of the order parameter. The substance is considered a strained cubic crystal. This approximation is legitimate, since all changes from the cubic symmetry prototype phase are small. With the electric polarization as the order parameter and admitting both first and second order phase transitions, the non-linear Helmholtz free energy is expanded in terms of the polarization and can be written as

$$
\begin{aligned}
H_{\mathrm{LD}}(P_i) = {} & \alpha_1(P_1^2 + P_2^2 + P_3^2) + \alpha_{11}(P_1^4 + P_2^4 + P_3^4) + \alpha_{12}(P_1^2 P_2^2 + P_2^2 P_3^2 + P_1^2 P_3^2) + \\
& + \alpha_{111}(P_1^6 + P_2^6 + P_3^6) + \alpha_{112}(P_1^4(P_2^2 + P_3^2) + P_2^4(P_1^2 + P_3^2) + P_3^4(P_1^2 + P_2^2)) + \\
& + \alpha_{123}(P_1^2 P_2^2 P_3^2),
\end{aligned}
\tag{1.38}
$$

describing a stress-free, uniformly poled bulk system. This energy function depends solely on the polarization and is referred to as Landau energy. All dielectric information about the ferroelectric material is encoded in the so-called Landau coefficients ($\alpha_1 - \alpha_{123}$). Within the phenomenological approach of Devonshire, these coefficients are fitted to experimental results in the vicinity of the phase transition.

Following Devonshire's 1949 work [18], the fitting-procedure to a first order phase transition for the Landau coefficients is shown here. In this early work, the coefficients α_{112} and α_{123} are not present yet. Though all coefficients generally are allowed to be dependent on temperature, the previous considerations of first and second order phase transitions have shown that only α_1 depending on temperature is sufficient while all other coefficients are considered temperature-independent. To fulfill the Curie-Weiss law in the paraelectric cubic phase, the coefficient α_1 has to pass through a zero value at the Curie temperature and be a linear function of temperature, as found experimentally. Since α_1 is the reciprocal dielectric permittivity for zero polarization (see Eqn. 1.31), $\chi_{\mathrm{exp}}^{T_0}$ can be obtained from experiment directly above the transition temperature, where the polarization is zero for zero field, leading to:

$$
\alpha_1(T) = \chi_{\mathrm{exp}}^{T_0} \frac{T - T_{\mathrm{C}}}{T_0 - T_{\mathrm{C}}}.
\tag{1.39}
$$

This guarantees H_{LD} to have only one minimum at $P = 0$ above the transition temperature, whereas below the transition temperature the minimum values of H_{LD} correspond to a finite polarization. Further requirements for H_{LD} at T_0 are

$$
\frac{\partial H_{\mathrm{LD}}(P_0(T_0))}{\partial P} = 0 \quad \text{and} \quad H_{\mathrm{LD}}(P_0(T_0)) = 0,
\tag{1.40}
$$

so that the Landau energy has minima at the spontaneous polarization state P_0 and these minima

are energetically equivalent to the non-polar minimum at $P = 0$. Solving these equations with respect to α_{11} and α_{111} yields the temperature-independent Landau coefficients

$$\alpha_{11} = -\frac{4\chi_{\text{exp}}^{T_0}}{P_0^2(T_0)}, \qquad \alpha_{111} = \frac{3\chi_{\text{exp}}^{T_0}}{P_0^4(T_0)}. \tag{1.41}$$

Hence, for fitting the Landau coefficients, the characteristical parameters of a phase transition have to be known from experiment: the transition temperature T_0, the Curie-Weiss-temperature T_C as well as the dielectric permittivity $\chi_{\text{exp}}^{T_0}$ at the transition temperature and the spontaneous polarization $P_0(T)$ at any temperature in the tetragonal region. The remaining Landau coefficient α_{12} has to be fitted to other phase transitions within the Devonshire approach.

Up to this point, only the polarization in the material has been taken into account as degree of freedom. In order to also consider the electromechanical coupling between strain and polarization as well as linear elastic behavior, strain- or stress-dependent terms have to be added to the free energy function (1.38). These additional terms have to contain the physics of Hooke's law and electrostriction. Within Devonshire's cubic symmetry approximation, the leading order terms for the strain-polarization and strain-strain coupling take the form

$$\begin{aligned}
H_{\text{coup}}(P_i, \varepsilon_{ij}) &= \frac{1}{2}C_{11}(\varepsilon_{11}^2 + \varepsilon_{22}^2 + \varepsilon_{33}^2) + C_{12}(\varepsilon_{11}\varepsilon_{22} + \varepsilon_{11}\varepsilon_{33} + \varepsilon_{22}\varepsilon_{33}) + \\
&+ \ 2C_{44}(\varepsilon_{12}^2 + \varepsilon_{13}^2 + \varepsilon_{23}^2) + \\
&+ \ q_{11}(\varepsilon_{11}P_1^2 + \varepsilon_{22}P_2^2 + \varepsilon_{33}P_3^2) + q_{44}(\varepsilon_{12}P_1^2P_2^2 + \varepsilon_{13}P_1^2P_3^2 + \varepsilon_{23}P_2^2P_3^2) + \\
&+ \ q_{12}(\varepsilon_{11}(P_2^2 + P_3^2) + \varepsilon_{22}(P_1^2 + P_3^2) + \varepsilon_{33}(P_1^2 + P_2^2)).
\end{aligned} \tag{1.42}$$

The equations of state (eqn. 1.11) yield the six components of the elastic stress. By taking for example the stress component

$$\sigma_{33} = \frac{\partial(H_{\text{LD}} + H_{\text{coup}})}{\partial \varepsilon_{33}} = C_{11}\varepsilon_{33} + C_{12}(\varepsilon_{11} + \varepsilon_{22}) + q_{11}P_3^2 + q_{12}(P_1^2 + P_2^2), \tag{1.43}$$

two limits can be discussed that show the properties of the added terms. First, for zero polarization, equation (1.43) yields Hooke's law of elasticity, so that the coefficients C_{ij} in the energy function are directly identified as components of the elastic stiffness tensor c_{ijkl}. Second, when no external stresses are applied ($\sigma_{ij} = 0$), the tetragonal strains occur proportionally to the square of the spontaneous polarization. The coefficients q_{ij} are therefore called electrostrictive constants for constant stress. In the Devonshire approach, they are calculated taking the spontaneous strains, the spontaneous polarization and the elastic stiffness from experiment [18].

This phenomenological approach by Devonshire is the commonly accepted way of obtaining the Helmholtz energy coefficients for BaTiO$_3$ solely based on experimental observations. In a modified way, the Devonshire approach was applied to the PZT system by Amin et. al. [3]. In

order to describe the simple proper phases in PZT, it was necessary to add the higher order terms α_{112} and α_{123} in H_{LD}. The coefficients of the extended Gibbs energy function were determined in a series of steps for different parts of the phase diagram, using indirect methods. Especially the polarization interaction terms were fitted to the morphotropic phase boundary and then extrapolated across the phase diagram to PZO and PTO. For a more complete phenomenological theory of PTO, Haun et. al. [38] developed an approach similar to those of Devonshire and Amin, based on unit cell parameters from high-temperature x-ray diffraction measurements. Due to a lack of single-crystal data, all coefficients of the Gibbs free energy were again determined using indirect methods. Later, this approach was applied to the PZT-system, and a free energy function was developed that takes all phases in PZT properly into account, including also the tilting of the oxygen octahedra in the low-temperature rhombohedral phase by introducing the tilt angle as an additional order parameter [34, 35, 36, 37, 39, 40]. Note that all described approaches to determine the energy function's coefficients are based on experimental results only.

1.3.4. Landau-Ginzburg-Devonshire theory

The Landau-Devonshire theory is well suited to describe a poled bulk ferroelectric with a spatially homogeneous polarization near its phase transition. However, in real ferroelectrics the polarization will not be spatially uniform, caused e.g. by the presence of ferroelectric domains or grain boundaries. Hence, the existing theory has to be extented with respect to fluctuations of the polarization. This is the subject of the Landau-Ginzburg theory: Small spatial variations of the order parameter are incorporated into the Landau-Devonshire theory with assumptions originally used by Ornstein-Zernike [11].

Spatial variations of the polarization within the material lead to an additional contribution in the free energy. In order to take this polarization-polarization interaction into account as well, additional terms have to be introduced that depend only on the gradient of the polarization. Based on symmetry considerations, the isotropic polarization gradient energy term takes the quadratic form

$$H_{grad}(P_{i,j}) = \frac{1}{2}G_0(P_{1,1}^2 + P_{2,2}^2 + P_{3,3}^2), \tag{1.44}$$

where the coefficient G_0 is a constant. H_{grad} represents the additional free energy cost for non-parallel polarization at neighboring positions and penalizes a non-uniform polarization, leading for instance to localized domain walls. In conclusion, the total free energy density describing the ferroelectric,

$$H_{total}(P_i, \varepsilon_{ij}, P_{i,j}) = H_{LD}(P_i) + H_{coup}(P_i, \varepsilon_{ij}) + H_{grad}(P_{i,j}), \tag{1.45}$$

now includes the Landau terms, strain-strain coupling, strain-polarization coupling as well as polarization-polarization coupling. For a system with a spatial polarization distribution $\vec{P}(\vec{r})$ and strain distribution $\varepsilon(\vec{r})$, the total energy $\mathscr{H}_{\text{total}}$ can be calculated as

$$\mathscr{H}_{\text{total}} = \int \left(H_{\text{LD}}(\vec{P}(\vec{r})) + H_{\text{coup}}(\vec{P}(\vec{r}), \varepsilon(\vec{r})) + H_{\text{grad}}(\triangledown \vec{P}(\vec{r})) \right) d^3\vec{r} \tag{1.46}$$

by integrating the total free energy density over the volume. Under the assumption that the system will be in a state of minimal energy in equilibrium, the total energy as a functional of the polarization field has to be minimized with respect to the order parameter. Following the work of Cao et. al. [9] and Nambu et. al. [60], the temporal and spatial evolution of the non-conserved polarization order parameter can be obtained by solving the time-dependent Ginzburg-Landau (TDGL) equation

$$\frac{\partial P_i(\vec{r},t)}{\partial t} = -L \frac{\delta \mathscr{H}_{\text{total}}}{\delta P_i(\vec{r},t)} \tag{1.47}$$

where L is the kinetic coefficient related to the domain wall mobility and $\delta \mathscr{H}_{\text{total}}/\delta P_i(\vec{r},t)$ represents the thermodynamic driving force. One way of solving this dynamic equation that describes the pattern formation of ferroelectric domains is based on the assumption that the relaxation of the polarization field is much slower than that of the elastic field, which instantaneously relaxes for a given polarization configuration [60]. In this adiabatic approximation, the elastic field can be eliminated from the total free energy functional (1.46). Another approach is solving the TDGL equation numerically in the Fourier space, using the semi-implicit Fourier-spectral method [13, 42, 79]. Concluding the Landau-Ginzburg theory, any evolution of the ferroelectric domain structure is always driven by a minimization of the total energy of the system.

1.4. Phase-field modeling for ferroelectrics

The emphasis of the previous chapters was to discuss the definition of ferroelectrics and the physical behavior of single crystals. Only the Landau-Ginzburg theory admitted inhomogenities in the spatial distribution of the polarization and dynamic processes. However, the macroscopic properties of ferroelectrics are mainly governed by the behavior of ferroelectric domains on the mesoscale. It is therefore very important to gain insight into the mechanisms of microstructure formation and evolution [58]. This chapter will focus on general techniques to predict the evolution of the domain structure in ferroelectrics. Here, the phase-field method is of special interest, since it provides a versatile technique to simulate heterogeneous systems consisting of different phases (e.g. ferroelectric domains) on the mesoscale.

1.4.1. Phase-field modeling

Generally speaking, phase-field modeling is a mathematical method for solving interfacial problems. It has emerged as a powerful computational approach to describe the often complex and non-linear morphological and microstructure evolution of materials taking place on the mesoscale to reduce the total free energy. The following discussion of the phase-field method is based on the works of Chen [12], Moelans et. al. [58] and Gonzáles-Cinca et. al. [30] that give a detailed overview of the phase-field method for microstructure evolution including various applications.

Most materials are not homogeneous on the meso-scale. Instead, the microstructure consists of spatially distributed coexisting phases that differ in structure, orientation or chemical composition. Examples are grains of different crystal orientation, domains of different electrical or magnetic orientation or domains of different structural variants.

If one is interested in the dynamic evolution of these phases (and hence the microstructure), not only the distribution of the governing fields in the material has to be considered, but also how these fields cause the evolution of the phases. Therefore, the problem falls into the broader class of free-boundary problems: The location of interfaces, i.e. the regions separating the different phases, always has to be determined as part of the solution.

The traditional way to model microstructure evolution is the so-called sharp-interface method: Here, interfaces are treated as mathematically sharp, and their local velocity is determined by driving forces for interface motion, interface mobility or as part of the boundary conditions. Thus, the position of the interfaces has to be tracked explicitly by means of mathematical equations. This interface-tracking approach can be sucessfully applied to one- or two-dimensional systems, but becomes impractical for complicated three-dimensional configurations. Also, the approach is restricted to connected interfaces.

In contrast to the sharp-interface formulation, the phase-field method is based on a diffuse-interface description developed by van der Waals [74] and independently by Cahn & Hilliard [8]. Mathematically, the moving boundary problem of the sharp-interface approach is converted into a set of partial differential equations. In a phase-field model, an additional parameter is introduced which takes distinct constant values in each phase and is continuous in space. At the interface region between two adjacent phases, this parameter changes steadily, forming a transition layer of finite thickness. The evolution of this parameter (and hence the microstructure) is described by the Cahn-Hilliard nonlinear diffusion equation and the Allan-Cahn equation.

Basically, two general types of phase-field models exist. The aim of the first type is simply to avoid tracking of the interface. Therefore, field-variables (so-called phase-fields) are introduced to distinguish the coexisting phases of different structure. These phase-fields are phenomenological variables and indicate which phase is present at a particular position in the system.

Essentially solidification can be described by this kind of phase-field model. The input parameters for the model are chosen to match the conventional parameters of a sharp-interface model through asymptotic analyses. Another application for this kind of model are solid-state phase transformations, like the austenite to ferrite phase transformation in steel.

The second type of phase-field model is based on an introduced well-defined physical order parameter, such as long-range order parameters for order-disorder transformations or displacive transformations. The concept of the order parameter originates from Landau's theory of phase transformations involving symmetry reduction and has been discussed before in section 1.3.1. Here, all thermodynamic and kinetic coefficients are related to microscopic parameters. This kind of model has been applied sucessfully to material processes like grain growth and coarsening, crack propagation or ferroelectric domain evolution and will be used in the present work.

In both kinds of phase-field models, a thermodynamical free energy F is formulated in terms of the phase-field or the order parameter. Conserved fields that have to satisfy local conservation conditions (e.g. molar concentrations) and non-conserved fields (e.g. crystal orientations) are distinguished. The evolution of the microstructure is predicted by the Cahn-Hilliard and Allan-Cahn equations

$$\frac{\partial c_i(\vec{r},t))}{\partial t} = \nabla M_{ij} \nabla \frac{\delta F}{\delta c_j(\vec{r},t))} \tag{1.48}$$

$$\frac{\partial \eta_p(\vec{r},t))}{\partial t} = -L_{pq} \frac{\delta F}{\delta \eta_q(\vec{r},t))}, \tag{1.49}$$

respectively. Here, M_{ij} and L_{pq} are atom or interface mobilities, c_i are conserved fields and η_i are non-conserved fields. It can be seen that the previously discussed time-dependent Ginzburg-Landau equation (1.47) corresponds to the generalized Allan-Cahn equation for a phase-field model with the non-conserved polarization as order parameter.

1.4.2. Continuum thermodynamics approach for domain evolution

The phase-field equations discussed above are based on a set of simple, physically justifiable assumptions. Although the traditional derivation of the Cahn-Hilliard and Allan-Cahn equations [8] is physically sound, it obscures the modern continuum physics distinction between fundamental balance laws, which are general and hold for a broad class of materials (e.g. laws for mass, force, etc.), and constitutive equations, which are only valid for a specific material. In order to separate the balance laws from the constitutive equations, Fried and Gurtin [25, 26, 31] developed a general continuum mechanics approach based on the introduction of a new balance law for microforces associated with the order parameter. Su and Landis [71] adopted this approach and applied it to the evolution of ferroelectric domains. Within this continuum thermodynamics framework, constitutive relations for the introduced microforces are developed and

applied within the second law of thermodynamics, yielding a generalized form of the Ginzburg-Landau equation. In the following, this approach will be discussed in detail, closely following the works (and terminology) of Gurtin [31] as well as Su and Landis [71].

First of all, the fundamental balance laws and kinematic relations governing the electromechanical fields will be described for the theory of linear piezoelectricity. Under the assumption of small deformations and rotations, the balances of linear and angular momentum in any arbitrary volume V and its bounding surface S are

$$\sigma_{ji,j} + b_i = \rho \ddot{u}_i \qquad \text{in} \qquad V, \tag{1.50}$$

$$\sigma_{ij} = \sigma_{ji} \qquad \text{in} \qquad V, \tag{1.51}$$

$$\sigma_{ji} n_j = t_i \qquad \text{on} \qquad S, \tag{1.52}$$

where σ_{ij} represents Cartesian components of the Cauchy stress, b_i components of a body force (per unit volume), ρ the density of mass, t_i components of traction applied to the surface and n_i components of a unit vector perpendicular to the surface. For linear kinematics, the strain components ε_{ij} are related to the mechanical displacements u_i as shown in equation (1.2). Furthermore, assuming quasi-static electromagnetic fields that vary slowly with respect to the speed of light in the material, Maxwell's equations [44] take the form

$$D_{i,i} - q = 0 \qquad \text{in} \qquad V, \tag{1.53}$$

$$D_i n_i = -\omega \qquad \text{on} \qquad S, \tag{1.54}$$

$$E_i = -\phi_{,i} \qquad \text{in} \qquad V, \tag{1.55}$$

with the volume charge density q, the surface charge density ω and the electric potential ϕ. The relation between polarization P_i, electric field E_i and dielectric displacement D_i is given in equation (1.1). Note that the Maxwell equations not only describe the material, but also include regions of free space occupied by the material.

For the phase-field method, the free energy of the considered system has to be expanded so that it depends also on the order parameter and its gradient. The introduction of the order parameter as a new independent variable motivates postulating a new system of so-called "micro-forces". These postulated micro-forces are work conjugate to the order parameter, which is now a configurational quantitiy. Hence, the working of the micro-force system accompanies changes of the order parameter. The microforce system is characterized by a micro-stress tensor ξ_{ji} as well as the body forces π_i and γ_i representing internal and external micro-forces distributed over the volume V. To get a better insight in how these fields can expend power, it is convenient to consider the body of the material as a lattice with atoms being able to move microscopically within this lattice. As a subregion, this body contains an arbitrary control volume R with surface ∂R

and the outward unit vector n_i normal to ∂R. Then, the system of micro-forces is presumed consistent with the micro-force balance law

$$\int_{\partial R} \xi_{ji} n_j \, dS + \int_R \pi_i \, dV + \int_R \gamma_i \, dV \;=\; 0, \tag{1.56}$$

and this integral balance of the set of configurational forces leads to the micro-force balance law in differential form,

$$\xi_{ji,j} + \pi_i + \gamma_i \;=\; 0 \qquad \text{in} \quad V. \tag{1.57}$$

Thus, $(\xi_{ji} n_j)\dot{P}_i$ represents the power density expended across the surface ∂R by neighboring configurations exterior to R. Furthermore, $\pi_i \dot{P}_i$ is the power density expended on the atoms by the lattice, e.g. by ordering of atoms in unit cells of the lattice. This internally expended power density also accounts for dissipation in the material. Finally, $\gamma_i \dot{P}_i$ describes the power density expended on the atoms of the body by external sources. Apart from the strain and the dielectric displacement, the expanded Helmholtz free energy $\psi = \psi(\varepsilon_{ij}, D_i, P_i, P_{i,j}, \dot{P}_i)$ for the phase-field model depends also on the polarization (order parameter), its gradient and its time derivative, to remain as general as possible. For the shown approach, only isothermal processes will be taken into account. Nevertheless, the framework allows for the extension to spatially homogeneous temperature dependence by adjusting the material properties to a given temperature. In contrast, the permission of a spatially inhomogeneous behavior would require to introduce also temperature and entropy as additional field variables. Under the assumption of isothermal processes, the second law of thermodynamics asserts that the rate of energy increase cannot exceed the expended power. This law can be delineated as the Clausius-Duhem inequality

$$\int_V \dot{\psi} \, dV + \frac{d}{dt} \int_V \frac{1}{2} \rho \dot{u}_i \dot{u}_i \, dV \le \int_V (b_i \dot{u}_i + \phi \dot{q} + \gamma_i \dot{P}_i) \, dV + \int_S (t_i \dot{u}_i + \omega \dot{q} + \xi_{ji} n_j \dot{P}_i) \, dS, \tag{1.58}$$

where the left-hand side represents the rate term and the right-hand side the expended power from external sources on the body. The rate term consists of two parts: the change of energy stored in the material as well as the change of the system's kinetic energy. No contribution to the external power term is assumed to come from the internal micro-force π_i. By substituting the fundamental balance laws (1.50) - (1.55) and the micro-force balance law (1.57) into equation (1.58) and applying Gauss' theorem, the Clausius-Duhem inequality can be transformed into

$$\int_V \left(\frac{\partial \psi}{\partial \varepsilon_{ij}} \dot{\varepsilon}_{ij} + \frac{\partial \psi}{\partial D_i} \dot{D}_i + \frac{\partial \psi}{\partial P_i} \dot{P}_i + \frac{\partial \psi}{\partial P_{i,j}} \dot{P}_{i,j} + \frac{\partial \psi}{\partial \dot{P}_i} \ddot{P}_i \right) \, dV \le$$
$$\int_V \left(\sigma_{ji} \dot{\varepsilon}_{ij} + E_i \dot{D}_i + \xi_{ji} \dot{P}_{i,j} - \pi_i \dot{P}_i \right) \, dV. \tag{1.59}$$

In general, the Cauchy stress σ_{ij}, electric field E_i, micro-force stress ξ_{ji} and internal micro-force

π_i are allowed to depend on $\varepsilon_{ij}, D_i, P_i, P_{i,j}$ and $\dot{P}_i$, since the free energy ψ also depends on all these quantities. Because the internal micro-force π_i can depend on $\dot{P}_i$, all other thermodynamic forces must also be allowed to depend on $\dot{P}_i$, as shown by Coleman and Noll [15]. However, a dependence on $\dot{P}_i$ is incompatible with the second law of thermodynamics: By controlling the external sources, it must be possible for $\dot{\varepsilon}_{ij}, \dot{D}_i, \dot{P}_i, \dot{P}_{i,j}$ and $\ddot{P}_i$ to adopt arbitrary levels for a given thermodynamic state. This request can only be fulfilled if $(\partial\psi/\partial\dot{P}_i)$ vanishes in the Clausius-Duhem inequation (1.59), and ultimately only the internal micro-force π_i is allowed to depend on $\dot{P}_i$. Furthermore, the Helmholtz free energy takes the form $\psi(\varepsilon_{ij}, D_i, P_i, P_{i,j})$, and the dissipation inequation yields the equations of state

$$\sigma_{ji} = \frac{\partial\psi}{\partial\varepsilon_{ij}}, \qquad E_i = \frac{\partial\psi}{\partial D_i}, \qquad \xi_{ji} = \frac{\partial\psi}{\partial P_{i,j}}. \tag{1.60}$$

Comparing the remaining parts of the Clausius-Duhem inequality and defining $\eta_i \equiv (\partial\psi/\partial\dot{P}_i)$ leads to

$$\begin{aligned} \int_V \eta_i \dot{P}_i \, \mathrm{d}V &\leq \int_V -\pi_i \dot{P}_i \, \mathrm{d}V \\ \Rightarrow \eta_i \dot{P}_i &\leq -\pi_i \dot{P}_i \\ \Rightarrow \pi_i &= \eta_i - \beta_{ij}\dot{P}_j \,, \end{aligned} \tag{1.61}$$

where $\beta_{ij}(\varepsilon_{ij}, D_i, P_i, P_{i,j}, \dot{P}_i)$, called the inverse mobility tensor, has to be non-negative definite. For systems with a high-temperature phase of cubic symmetry, this tensor is constant and takes the form $\beta_{ij} = \beta\delta_{ij}$ with $\beta \geq 0$. Substituting equation (1.61) into the micro-force balance law (1.57) yields

$$\xi_{ji,j} - \eta_i - \beta_{ij}\dot{P}_j + \gamma_i = 0, \tag{1.62}$$

and finally, after resubstituting the equations of state (1.60), a generalized form of the Ginzburg-Landau equation

$$\left(\frac{\partial\psi}{\partial P_{i,j}}\right)_j - \frac{\partial\psi}{\partial P_i} + \gamma_i = \beta_{ij}\dot{P}_j \tag{1.63}$$

characterizing the spatial and temporal evolution of the polarization order parameter in a ferroelectric material. Hence, the postulated system of micro-forces as well as the micro-force balance law can be justified by the fact that their existence implies the well-established form of the phase-field equations.

Since its publication in 2007, this continuum thermodynamics framework by Su and Landis [71] has been applied to simulate a broad range of systems containing ferroelectric domain

structures, e.g. nanodots [59, 77], nanotubes [78, 88] and thin films [49], as well as the effect of cracks [81], defects [71] and dislocations [48] on domain walls. It will also be employed in this work for investigating periodic bulk domain structures under electromechanical loading.

1.4.3. Free energy for phase-field modeling

The heart of a phase-field model is its free energy density, an analytical thermodynamic potential containing all information on the described ferroelectric system: dielectric, piezoelectric and elastic properties, spontaneous parameters (polarization and strain) as well as energy and thickness of the occurring domain walls. In sections 1.3.3 and 1.3.4, an approach for a Helmholtz free energy has been shown in the context of the Landau-Ginzburg-Devonshire theory. This approach will now be extended in a more general way. The structure and physical meaning of all parts of the energy function are to be discussed in detail. Especially for the electromechanical coupling energy, a differently motivated derivation than before will be shown. The structure of the eventually developed energy density will then be used throughout this work.

Under consideration of the continuum thermodynamics framework discussed in the previous section, the Helmholtz free energy depends on the independent variables P_i, $P_{i,j}$, ε_{ij} and D_i. It consists of five basic parts: the Landau energy ψ_{Landau}, the gradient energy ψ_{grad}, the electrostrictive coupling energy ψ_{coup}, the elastic energy ψ_{elast} and the electric energy ψ_{elec}:

$$\Psi(P_i, P_{i,j}, \varepsilon_{ij}, D_i) = \psi_{\text{Landau}}(P_i) + \psi_{\text{grad}}(P_{i,j}) + \psi_{\text{coup}}(P_i, \varepsilon_{ij}) + \psi_{\text{elast}}(\varepsilon_{ij}) + \psi_{\text{elec}}(P_i, D_i) \quad (1.64)$$

Landau energy

The Landau potential ψ_{Landau} depends on the polarization order parameter only. By taking a sixth order Taylor series at $P_i = 0$ and retaining all symmetrical compatible terms, it can be expressed as

$$\begin{aligned}
\psi_{\text{Landau}}(P_i) = {} & \alpha_1(P_1^2 + P_2^2 + P_3^2) + \alpha_{11}(P_1^4 + P_2^4 + P_3^4) \\
& + \alpha_{12}(P_1^2 P_2^2 + P_1^2 P_3^2 + P_2^2 P_3^2) + \alpha_{111}(P_1^6 + P_2^6 + P_3^6) \\
& + \alpha_{112}(P_1^4(P_2^2 + P_3^2) + P_2^4(P_1^2 + P_3^2) + P_3^4(P_1^2 + P_2^2)) + \alpha_{123}(P_1^2 P_2^2 P_3^2).
\end{aligned} \quad (1.65)$$

It describes a non-convex energy landscape with a certain number of energetically equivalent global minima. These global minima define the spontaneous polarization states, and their symmetry specifies the phase of the material. For a tetragonal polarized ferroelectric like PTO, there are six equivalent global minima located along the $\langle 100 \rangle$ crystal axes, as illustrated in figure 1.11. By adjusting the set of Landau coefficients α_{ijk}, rhombohedral or orthorhombic symmetry is also possible, with an orientation of the global minima as shown in table 1.1. The

Landau energy represents bulk material behavior in the absence of mechancial stress, electrome-chanical coupling and domain walls.
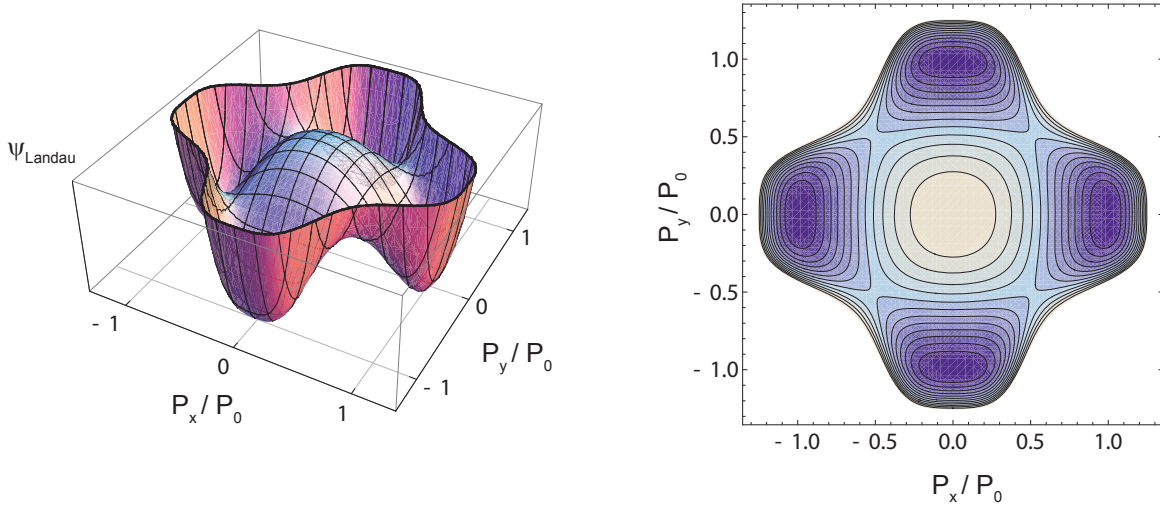

Figure 1.11.: Three-dimensional representation (left) and contour plot (right) of a two-dimensional Landau free energy density ψ_{Landau} for a tetragonal polarized ferroelectric material. Four equivalent minima located along the $\langle 100 \rangle$ axes define the possible states of the spontaneous polarization in the x-y-plane.

Gradient energy

Depending only on the gradient of the polarization, the second part of the free energy is the anisotropic gradient energy

$$
\begin{aligned}
\psi_{\text{grad}}(P_{i,j}) = {} & \frac{1}{2}G_{11}(P_{1,1}^2 + P_{2,2}^2 + P_{3,3}^2) + G_{12}(P_{1,1}P_{2,2} + P_{1,1}P_{3,3} + P_{2,2}P_{3,3}) \\
& + \frac{1}{2}G_{44}((P_{1,2} + P_{2,1})^2 + (P_{1,3} + P_{3,1})^2 + (P_{2,3} + P_{3,2})^2).
\end{aligned}
\tag{1.66}
$$

Here, all terms for cubic symmetry are considered, so that there are three independent gradient coefficients G_{11}, G_{12} and G_{44}. The gradient energy part only contributes when the polarization changes spatially, e.g. in domain walls. Hence, it penalizes large gradients of the polarization order parameter and enforces the formation of domain walls as localized regions with spatially changing polarization.

Elastic energy and electromechanical coupling energy

The elastic energy ψ_{elast} and the electromechanical coupling energy ψ_{coup} form the third and fourth part of the free energy and are here discussed together. Following [52], the total strain ε_{ij}

consists of two portions (figure 1.12): the elastic strain $\varepsilon_{ij}^{\text{elas}}$, induced e.g. by external mechanical loading, and the stress-free electrostrictive strain $\varepsilon_{ij}^{\text{strict}}$, caused by the polarization field:

$$\varepsilon_{ij} = \varepsilon_{ij}^{\text{elas}} + \varepsilon_{ij}^{\text{strict}} \tag{1.67}$$

Assuming a quadratic coupling between strain and polarization, the electrostrictive strains $\varepsilon_{ij}^{\text{strict}}$ can be expressed as

$$
\begin{aligned}
\varepsilon_{11}^{\text{strict}} &= Q_{11}P_1^2 + Q_{12}(P_2^2 + P_3^2) \\
\varepsilon_{22}^{\text{strict}} &= Q_{11}P_2^2 + Q_{12}(P_1^2 + P_3^2) \\
\varepsilon_{33}^{\text{strict}} &= Q_{11}P_3^2 + Q_{12}(P_1^2 + P_2^2) \\
\varepsilon_{12}^{\text{strict}} &= \varepsilon_{21}^{\text{strict}} = Q_{44}P_1P_2 \\
\varepsilon_{13}^{\text{strict}} &= \varepsilon_{31}^{\text{strict}} = Q_{44}P_1P_3 \\
\varepsilon_{23}^{\text{strict}} &= \varepsilon_{32}^{\text{strict}} = Q_{44}P_2P_3
\end{aligned} \tag{1.68}
$$

where Q_{ij} are the electrostrictive constants [20]. The elastic strain energy density can be written as

$$\psi_{\text{ES}} = \frac{1}{2}c_{ijkl}\varepsilon_{ij}^{\text{elas}}\varepsilon_{kl}^{\text{elas}} = \frac{1}{2}c_{ijkl}\left(\varepsilon_{ij} - \varepsilon_{ij}^{\text{strict}}\right)\left(\varepsilon_{kl} - \varepsilon_{kl}^{\text{strict}}\right) \tag{1.69}$$

where c_{ijkl} is the elastic stiffness tensor. Inserting decomposition (1.67), the elastic strain energy density ψ_{ES} can be divided into the pure elastic energy density ψ_{elast}, which depends on the strains only, and the electrostrictive coupling energy density ψ_{coup}:

$$\psi_{\text{ES}}(P_i, \varepsilon_{ij}) = \psi_{\text{elast}}(\varepsilon_{ij}) + \psi_{\text{coup}}(P_i, \varepsilon_{ij}) \tag{1.70}$$

For a cubic material, the elastic stiffness tensor in Voigt's notation has the three independent components C_{11}, C_{12} and C_{44}. Substituting equations (1.67) and (1.68) into (1.69) and applying (1.70) subsequently yields the elastic energy density

$$\psi_{\text{elast}}(\varepsilon_{ij}) = \frac{1}{2}C_{11}(\varepsilon_{11}^2 + \varepsilon_{22}^2 + \varepsilon_{33}^2) + C_{12}(\varepsilon_{11}\varepsilon_{22} + \varepsilon_{11}\varepsilon_{33} + \varepsilon_{22}\varepsilon_{33}) + 2C_{44}(\varepsilon_{12}^2 + \varepsilon_{13}^2 + \varepsilon_{23}^2) \tag{1.71}$$

as well as the coupling energy density

$$
\begin{aligned}
\psi_{\text{coup}}(P_i, \varepsilon_{ij}) &= q_{11}(\varepsilon_{11}P_1^2 + \varepsilon_{22}P_2^2 + \varepsilon_{33}P_3^2) + \\
&+ q_{12}(\varepsilon_{11}(P_2^2 + P_3^2) + \varepsilon_{22}(P_1^2 + P_3^2) + \varepsilon_{33}(P_1^2 + P_2^2)) \\
&+ q_{44}(P_1P_2\varepsilon_{12} + P_1P_3\varepsilon_{13} + P_2P_3\varepsilon_{23}) + \\
&+ \beta_1(P_1^4 + P_2^4 + P_3^4) + \beta_2(P_1^2P_2^2 + P_1^2P_3^2 + P_2^2P_3^2)
\end{aligned} \tag{1.72}
$$

with

$$
\begin{aligned}
q_{11} &= -C_{11}Q_{11} - 2C_{12}Q_{12} \\
q_{12} &= -C_{12}(Q_{11}+Q_{12}) - C_{11}Q_{12} \\
q_{44} &= -4C_{44}Q_{44} \\
\beta_1 &= \frac{C_{11}Q_{11}^2}{2} + 2C_{12}Q_{11}Q_{12} + C_{11}Q_{12}^2 + C_{12}Q_{12}^2 \\
\beta_2 &= C_{11}Q_{12}(2Q_{11}+Q_{12}) + C_{12}(Q_{11}^2+2Q_{11}Q_{12}+3Q_{12}^2) + 2C_{44}Q_{44}^2.
\end{aligned}
$$

cubic: tetragonal: tetragonal + applied stress:

$\epsilon_{ij} = 0$ $\epsilon_{ij} = \epsilon_{ij}^{\text{strict}}$ $\epsilon_{ij} = \epsilon_{ij}^{\text{strict}} + \epsilon_{ij}^{\text{elas}}$
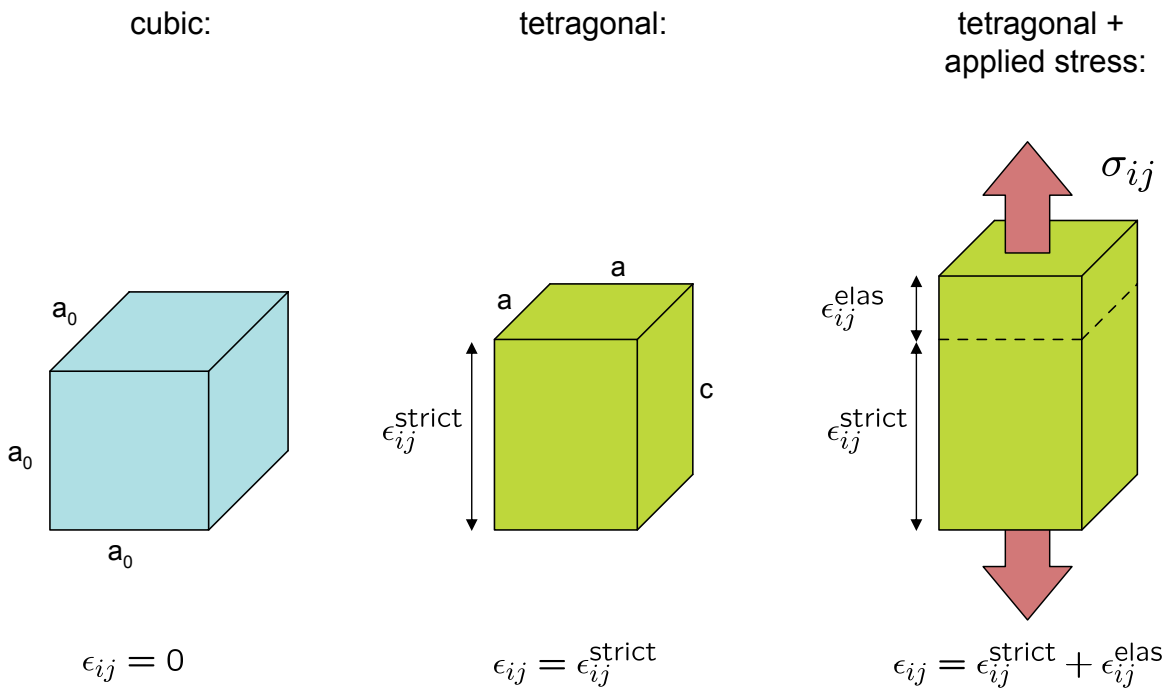
Figure 1.12.: Schematic illustration of the strains in equation (1.67): No spontaneous strains occur in the cubic phase (left) above T_{C}. Due to the spontaneous polarization below T_{C} (middle), the coupling between strain and polarization evokes electrostrictive strains $\varepsilon_{ij}^{\text{strict}}$, called spontaneous strains. Applying external mechanical stress σ_{ij} (right) leads to additional elastic strains $\varepsilon_{ij}^{\text{elas}}$.

Concluding the elastic and electromechanical coupling terms of the free energy, two cases have to be discussed. In the cubic phase, i.e. in the absence of a spontaneous polarization, the electrostrictive strains $\varepsilon_{ij}^{\text{strict}}$ and, as a consequence, the spontaneous strains vanish. Therefore, the elastic strain energy ψ_{ES}, the elastic energy $\psi_{\text{elast}}(\varepsilon_{ij})$ and the electrostrictive coupling energy $\psi_{\text{coup}}(P_i, \varepsilon_{ij})$ are zero when no mechanical field is applied. In the tetragonal polarized phase, $\psi_{\text{elast}}(\varepsilon_{ij})$ and $\psi_{\text{coup}}(P_i, \varepsilon_{ij})$ are non-zero, since the material now exhibits a spontaneous polarization and strain. From equation (1.69) can be seen that the elastic strain energy density ψ_{ES}

only contributes when an elastic strain $\varepsilon_{ij}^{\text{elas}}$ is induced externally, e.g. by an applied mechanical stress. Hence, in a homogeneously polarized material under equilibrium condition, i.e. without any external mechanical or electrical loading, the elastic energy density ψ_{elast} and the coupling energy density ψ_{coup} are of the same size but different signs and cancel each other out. So, the coupling energy ψ_{coup} – caused by the electrostrictive interaction between spontaneous polarization and strain – and the counteracting elastic energy are in equilibrium. In this case, the electrostrictive strains $\varepsilon_{ij}^{\text{strict}}$ are the spontaneous strains and can be found from equations (1.68) for $P = P_0$.

The β_1- and β_2-terms of the coupling energy $\psi_{\text{coup}}(P_i, \varepsilon_{ij})$ take the effect of mechanical loading on the spontaneous polarization into account. Since β_1 and β_2 are of the same polynomial order as the Landau energy coefficients α_{11} and α_{12}, they directly influence the Landau energy and therefore the spontaneous polarization. Thus, in some works the β_1/β_2 and α_{11}/α_{12} coefficients are combined and called relaxed Landau coefficients [9, 60, 41]. The Landau energy then already contains the electromechancial coupling between the spontaneous polarization and the spontaneous strains.

Electric field energy

The last remaining part of the free energy to be discussed is

$$\psi_{\text{elec}}(P_i, D_i) = \frac{1}{2\kappa_0}((D_1 - P_1)^2 + (D_2 - P_2)^2 + (D_3 - P_3)^2), \qquad (1.73)$$

representing the electric field energy which is stored in the free space that is occupied by the material. Here, κ_0 is the vacuum permittivity. This part considers the relationship $D_i = \kappa_0 E_i + P_i$ between the material polarization, the electric field and the dielectric displacement.

2. Interface between atomistic and phase-field methods

Within a knowledge based multi-scale simulation chain for ferroelectric materials, phase-field modeling is capable of bridging the gap between atomistic methods and micromechanical methods. This chapter deals with the definition and development of an interface between atomistic and phase-field methods as illustrated in figure 2.1:
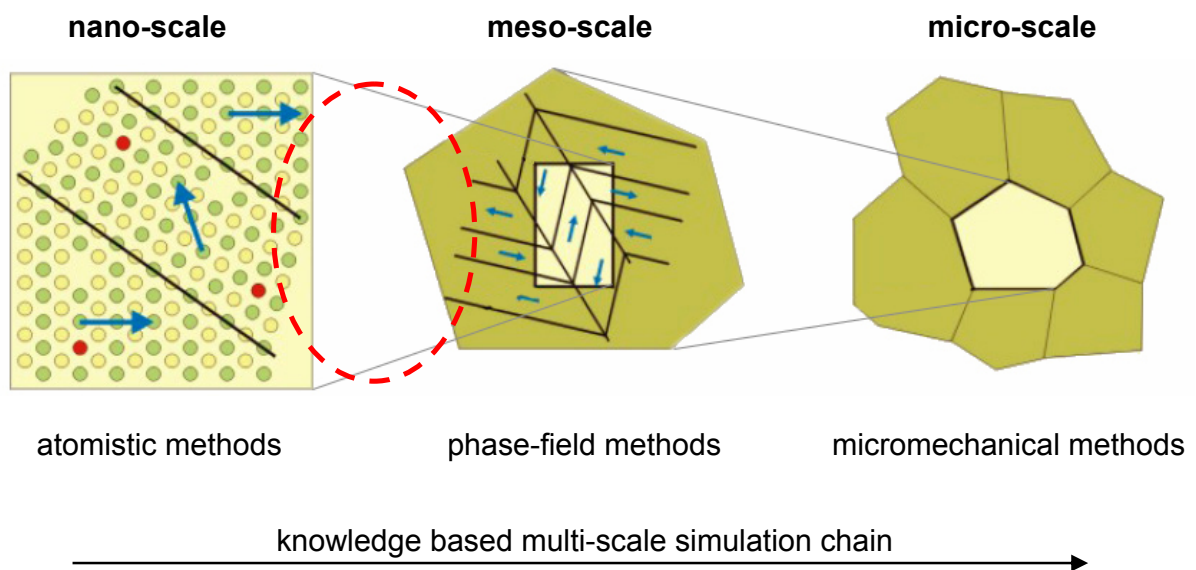

Figure 2.1.: An interface has to be developed in order to close the gap between atomistic and phase-field methods within the knowledge based multi-scale simulation chain for ferroelectrics.

As discussed in section 1.4.3, the core of a phase-field model is its free energy, and the coefficients of this thermodynamical potential contain all information about the material on the phase-field level. The interface to be developed is based on the idea that results from atomistic calculations are transferred into the phase-field model, where they are used as input parameters. Therefore, the coefficients of the free energy have to be adjusted to single crystal data from atomistic calculations.

Before describing the development of the interface, it will be clarified which parameters are available from first-principles calculations and atomistic simulations, and a short overview of these methods will be given. After that, a sensitivity study of the free energy is performed, providing the basis for the development of a strategy to adjust the coefficients of the free energy solely based on atomistic results. Finally, the limits of the shown interface between the nano-scale and the meso-scale will be discussed.

2.1. Atomistic calculations

In order to provide input parameters for the phase-field model, first-principles calculations and atomistic simulations have been performed in the scope of the BMBF project COMFEM by P. Marton and C. Elsässer (Fraunhofer IWM Freiburg). In the following sections, a short overview is given concerning the considered materials, the computational methods used by Marton and Elsässer and their obtained results. Further information on this topic can be found in [76].

Considered material

Two different compositions of the $Pb(Zr_xTi_{1-x})O_3$ (0<x<1) binary system are considered in this work, and therefore input parameters from atomistic calculations are needed for these two materials: PTO, where all B sites of the perovskite ABO_3 unit cell are occupied by Ti ions, and PZT with equal fractions of Zr and Ti ions on the B sites ($Pb(Zr_{0.5}Ti_{0.5})O_3$). For atomistic calculations, the specific arrangement of the Zr and Ti ions has an impact on the properties of the material, as shown by Sághi-Szabó et. al. and Kitamura et. al. [65, 47]. Since there is no evidence for a B cation ordering [23], Marton and Elsässer adopted an alternative approach and treated the Zr and Ti ions as one single atom with statistically averaged properties of both constituents within a virtual crystal approximation (VCA). Furthermore, tetragonality of PZT is assumed in agreement with the PZT phase-diagram (see figure 1.2), in which $Pb(Zr_{0.5}Ti_{0.5})O_3$ is on the tetragonal side of the morphotropic phase boundary [45]. All atomistic calculations and simulations yielding input parameters for the phase-field model take place at zero temperature.

First-principles calculations

The first-principles density functional theory (DFT) is a computational electronic-structure based approach in materials science, which is capable of providing predictive results without the need of any experimental input. First-principles calculations were employed to explain the phenomenon of ferroelectricity in perovskites [14]. Since then, the density functional theory has been used to determine structural properties, spontaneous ferroelectric polarization, elastic and piezoelectric tensors, phonon frequencies, etc. [87, 65, 4, 47, 28]. Some of these intrinsic properties in complicated materials are extremely difficult to investigate experimentally in PZT, which has so far not been produced in the form of a monocrystal. With increasing computational power it has become possible to use first-principles calculations for the study of different types of defects and spatial inhomogenities in ferroelectrics, such as point defects and ferroelectric domain walls [22, 57]. Nevertheless, because of the high demand on computational resources, DFT calculations are still limited to relatively small model atomic arrangements relevant for a particular studied phenomenon. Issues concerning domain wall mobility under an electric field

or mechanical stress, formation of domain patterns, or interaction of different types of domain walls between themselves or with grain boundaries are certainly beyond the scope of the DFT calculations.

Marton and Elsässer applied first-principles total energy calculations based on the density functional theory (DFT) with the local-density approximation (LDA) to determine the intrinsic and extrinsic parameters for PTO and PZT: lattice parameters, spontaneous ferroelectric polarization and deformation, elasticity and piezoelectricity tensors as well as domain wall properties. Details of the DFT calculations setup can be found in [76]. In the course of the study it was found that the ground state of PZT within the virtual crystal approximation is not exactly tetragonal, but slightly monoclinic (in agreement with experimenal observations [23, 62, 63]). Therefore, some properties of PZT required for the development of the phase-field model could not be obtained directly from first-principles calculations. These are, e.g., some components of the tetragonal material tensor showing the symmetry of the monoclinic phase, or properties of the 90° domain wall where the tetragonal symmetry is broken. In order to overcome this difficulty, Marton and Elsässer used the first-principles data to develop a classical empirical shell-model, discussed in the following.

Classical atomistic simulations

The simplification of interatomic interactions allows atomistic simulations of larger structures compared to DFT calculations. Sepliarsky et. al. [67] and Kitamura et. al. [47] recently carried out atomistic simulations for ferroelectrics using empirical potentials. These empirical shell-model potentials for PTO were fitted to first-principles data and were shown to be capable of reproducing important intrinsic properties of PTO as well as properties of domain walls in the tetragonal phase [69]. Such classical atomistic models allow to deal with domain walls and defects in ferroelectrics, while preserving important features of the atomic structure and energy. In order to get the remaining input parameters necessary for the phase-field model that could not be obtained from DFT calculations, Marton and Elsässer applied classical atomistic simulations based on a shell-model potential (SMP). Details of the SMP simulations setup can also be found in [76]. For PTO, the shell-model potential by Shimada et al. [69] was fitted to first-principles target data and is therefore suitable for the combined DFT atomistic approach. Moreover, this parametrization proved to yield properties of domain walls, such as thickness and planar energy, close to the DFT predictions. For PZT, Marton and Elsässer used a modification of the shell-model potential for PTO [69], which mainly consisted of an adjustment of the lattice parameters. The shell-model potential was fitted to the PZT-VCA first-principles data, and therefore the Zr and Ti atoms were treated as a single species as well.

These classical atomistic SMP simulations yielded 90° and 180° domain wall properties for PTO and PZT. Contrary to DFT calculations, the SMP simulations of PZT showed a strictly

tetragonal equilibrium ground state.

Ferroelectric properties from atomistic calculations

In Table 2.1, the atomistic calculations for PTO and PZT performed by Marton and Elsässer are summarized. All computed ferroelectric properties are shown, and it is indicated whether they were obtained from DFT calculations or SMP simulations. The elastic stiffness tensor and

Table 2.1.: Compilation of the ferroelectric properties calculated by Marton and Elsässer using first-principles DFT calculations and atomistic SMP simulations. Results from atomistic calculations are tagged by a hat (throughout this work).

ferroelectric property	phase	symbol	PTO (DFT)	PTO (SMP)	PZT (DFT)	PZT (SMP)
elastic stiffness	cub.	$\hat{c}_{\text{cub},ijkl}$	x	-	x	-
elastic stiffness	tetr.	$\hat{c}_{\text{tetr},ijkl}$	x	-	x	-
lattice parameters	cub.	$\hat{a}_{\text{cub}}$	x	-	x	-
lattice parameters	tetr.	$\hat{a}_{\text{tetr}}, \hat{c}_{\text{tetr}}$	x	-	x	-
piezoelectricity tensor	tetr.	$\hat{d}_{ijk}$	x	-	x	-
spontaneous polarization	tetr.	$\hat{P}_0$	x	-	x	-
dielectric permittivity	tetr.	$\hat{\kappa}_{ij}$	-	x	-	x
180°/90° domain wall width (DWW)	tetr.	$\hat{\xi}_{90/180}$	x	x	-	x
180°/90° domain wall width (DWE)	tetr.	$\hat{\gamma}_{90/180}$	x	x	-	x

the lattice parameters of the perovskite unit cell were calculated for both the paraelectric cubic phase and the tetragonally polarized phase, whereas all other parameters were only derived for the tetragonal phase. From the tetragonal lattice constants $\hat{a}_{\text{tetr}}$, $\hat{c}_{\text{tetr}}$ and the cubic lattice constant $\hat{a}_{\text{cub}}$, the spontaneous strains

$$\hat{e}_\perp = \frac{\hat{a}_{\text{tetr}} - \hat{a}_{\text{cub}}}{\hat{a}_{\text{cub}}}, \qquad \hat{e}_\parallel = \frac{\hat{c}_{\text{tetr}} - \hat{a}_{\text{cub}}}{\hat{a}_{\text{cub}}} \tag{2.1}$$

can be computed, where $\hat{e}_\parallel$ and $\hat{e}_\perp$ are the spontaneous strains parallel and perpendicular to the spontaneous polarization, respectively. Note that throughout this work results from atomistic calculations are labelled by a hat symbol.

Before the results from DFT and SMP calculations can be transferred into the phase-field model, a thorough study of the free energy function is necessary. Therefore, a sensitivity analysis will be performed in the following in order to identify the parameters of the phase-field model.

2.2. Sensitivity analysis

The free energy function (1.64) depends on 15 parameters (α_{ijk}, Q_{ij}, C_{ij}, G_{ij}) that have to be adjusted to physical properties obtained by first-principles DFT calculations and empirical

SMP simulations. These physical properties are the so-called small signal parameters of the ferroelectric near the equilibrium state, which are piezoelectric, dielectric and elastic behavior as well as information about the spontaneous polarization and the spontaneous strain. The small signal parameters of the ferroelectric are encoded in the energy function. As a preparation for the parameter identification, a sensitivity analysis has been performed in which all parameters of the energy function are systematically varied in order to determine the effect on the physical properties.

First of all, the small signal parameters have to be determined from the energy function. Obtaining the state variables as partial derivatives with respect to the natural variables yields the following system of equations:

$$\sigma_{ij} = \frac{\partial}{\partial \varepsilon_{ij}} \Psi(P_i, P_{i,j}, \varepsilon_{ij}, D_i) \qquad E_i = \frac{\partial}{\partial D_i} \Psi(P_i, P_{i,j}, \varepsilon_{ij}, D_i) \qquad \eta_i = \frac{\partial}{\partial P_i} \Psi(P_i, P_{i,j}, \varepsilon_{ij}, D_i) \tag{2.2}$$

Here, σ_{ij} are the mechanical stresses, E_i is the electric field and η_i are the micro-forces as discussed in section 1.4.2. The global minimum of the energy function defines the state in which the system is in equilibrium. Assuming a single crystal with uniform polarization in x_3-direction, the gradient of the polarization $P_{i,j}$ vanishes. Furthermore, with no electric and mechanical loading applied ($E_i = 0$, $\sigma_{ji} = 0$, $\eta_i = 0$), solving the system of equations (2.2) yields the spontaneous polarization $P_3 = P_0$ as well as the spontaneous strains $\varepsilon_{33} = e_\parallel$ parallel and $\varepsilon_{11} = \varepsilon_{22} = e_\perp$ perpendicular to the direction of polarization, respectively.

The elastic stiffness c_{ijkl} can also be computed analytically by considering a single crystal homogeneously polarized in x_3-direction in the vicinity of its equilibrium state according to

$$c_{ijkl} = \frac{\partial}{\partial \varepsilon_{kl}} \sigma_{ij} = \frac{\partial}{\partial \varepsilon_{kl}} \left(\frac{\partial}{\partial \varepsilon_{ij}} \Psi(P_3 = P_0, \varepsilon_{11} = \varepsilon_{22} = e_\perp, \varepsilon_{33} = e_\parallel, D_3 = P_0) \right), \tag{2.3}$$

with all other natural variables P_i, $P_{i,j}$, ε_{ij} and D_i taken to be zero. In order to determine the dielectric and piezoelectric small signal parameters directly, small perturbations in the form of a small mechanical or electrical load about the equilibrium state are applied to the energy function of a single domain to carry out a numerical differentiation. Solving the system of equations (2.2) for a small perturbation and fitting to the slope near the origin, the piezoelectric coefficients d_{ijk} and the dielectric permittivities κ_{ij} can be calculated, respectively:

$$d_{ijk} = \left. \frac{\partial D_i}{\partial \sigma_{jk}} \right|_{\sigma=0} \qquad \kappa_{ij} = \left. \frac{\partial D_i}{\partial E_j} \right|_{E=0} \tag{2.4}$$

Another characteristic feature encoded in the energy function are the properties of the domain walls. For a tetragonal polarized material, 180° and 90° domain walls exist. The energy barriers between the minima of the energy function define the properties of 90° and 180° domain walls.
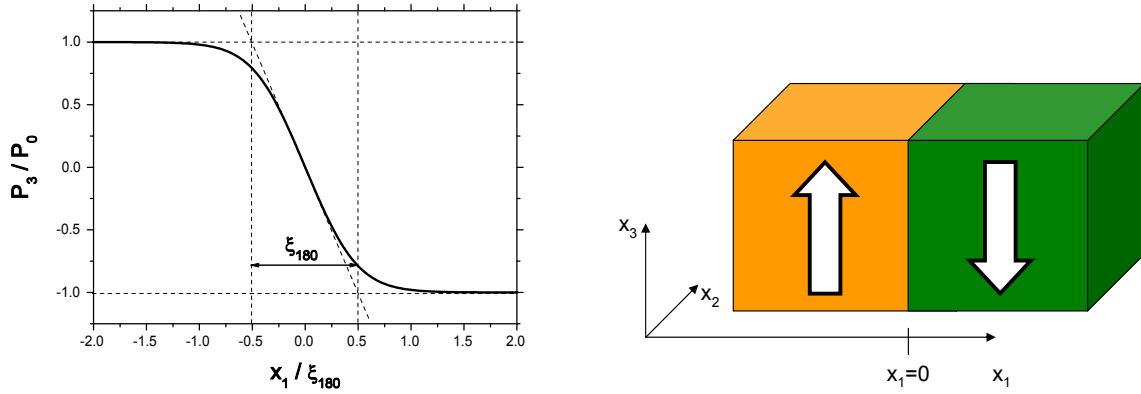
Figure 2.2.: Profile of the polarization in a 180° domain wall. The thickness ξ_{180} is marked as defined in eqn.(2.5)

As shown in Figure 2.2 for the case of a 180° domain wall, the thickness of a domain wall $\xi_{90/180}$ is defined by the intersection of the linear slope in the middle of the domain wall and the spontaneous polarization,

$$\xi_{90/180} = \left. \frac{2P_0}{\frac{\partial}{\partial x_1} P(x_1)} \right|_{x_1=0}, \tag{2.5}$$

where $P(x_1)$ denotes the profile of the polarization perpendicular to the domain wall and $x_1 = 0$ is the center of the domain wall. The surface energy density $\gamma_{90/180}$ of a domain wall can be obtained from the integral

$$\gamma_{90/180} = \int_{-\infty}^{\infty} \left(\Psi(P_i(x_1), P_{i,j}(x_1), \varepsilon_{ij}(x_1), D_i(x_1)) - \Psi_{\text{bulk}}(\infty) \right) dx_1 \tag{2.6}$$

where $\Psi_{\text{bulk}}(\infty)$ is the equilibrium bulk energy density.

Table 2.2 shows the results of the sensitivity analysis. The columns contain all coefficients of the energy function, whereas the rows represent the physical properties: ferroelectric small signal behavior and spontaneous parameters of a single domain as well as the domain wall properties. Each coefficient of the energy function is separately increased by 10%. If the change of the coefficient causes a variation of the small signal properties, the positive or negative magnitude of this variation is indicated in per cent. For example, by raising the coefficient α_1 by 10%, the spontaneous polarization P_0 is increased by 3.4%, whereas the piezoelectric coefficient d_{33} is decreased by 7.1% at the same time. The sensitivity analysis shows a nonlinear behavior and a strong coupling between each energy function coefficient and numerous system properties. A linear dependence can be observed for the elastic stiffness as well as for the influence of the electrostrictive coefficients Q_{11}, Q_{12} on the spontaneous strains and the piezoelectric coefficients. In the gradient term, only the coefficient G_{44} influences the properties of 180° domain

Table 2.2.: Sensitivity analysis for all coefficients of a 6th order Helmholtz free energy function. The elastic stiffness c_{ij} as well as the piezoelectric coefficients d_{ij} are given in Voigt's notation. Since it has no influence on any of the shown material properties, the Landau coefficient α_{123} was left out. The analysis is based on free energy coefficients of PTO taken from literature [52].

	α_1	α_{11}	α_{111}	α_{12}	α_{112}	Q_{11}	Q_{12}	Q_{44}	C_{11}	C_{12}	C_{44}	G_{11}	G_{12}	G_{44}
P_0	3.4	-2.0	-1.4											
$e_\perp$	6.9	-4.0	-2.8				10.0							
$e_\parallel$	6.9	-4.0	-2.8			10.0								
κ_{11}	12.6			-12.6	-6.2			-0.4			-0.2			
κ_{33}	3.7	-5.8	-6.9											
c_{11}									10.0					
c_{33}									10.0					
c_{12}										10.0				
c_{13}										10.0				
c_{44}											10.0			
c_{66}											10.0			
d_{33}	-7.1	0.3	-2.5			10.0								
d_{31}	-7.1	0.3	-2.5				10.0							
d_{15}	-4.5	10.2	7.0	-12.8	-6.3			10.0						
ξ_{180}	-2.5	0.1	-0.2			-2.2			-3.4	1.1				5.0
γ_{180}	6.6	-2.5	-1.4			-2.6			3.3	-1.1				4.9
ξ_{90}	-3.4	4.3	2.3	-4.9	-1.8	0.9	-0.1	-0.4	-0.2		-0.6	2.3	-2.4	5.7
γ_{90}	9.3	-6.9	-4.3	4.7	1.7	-3.4	0.6	0.4	0.2		0.6	2.2	-2.2	4.8

walls, while the properties of 90° domain walls are dependent on all three gradient coefficients. The dielectric coefficients κ_{11} and κ_{33} are mainly determined by the Landau energy coefficients α_{ijk}. The sensitivity study also shows the limits of the Helmholtz energy function (eqn. 1.64) employed here: Firstly, only cubic adjustment of the elastic stiffness and the piezoelectric coefficients is possible. For example, c_{11} and c_{33} depend on the same coefficient in the energy function only and cannot be tuned separately. Secondly, the number of coefficients in the energy function is not sufficient to adjust both spontaneous strains and piezoelectric coefficients independently. The sensitivity analysis provides a basis for the following fitting process of the Helmholtz energy function coefficients to results of atomistic calculations.

2.3. Adjustment process

In the phase-field model, the coefficients of the free energy function contain all information on the considered material. Usually these coefficients are adjusted to experimental data following Devonshire's phenomenological approach as discussed in section 1.3.3. Necessary input parameters for Devonshire's adjustment method are (among others) the transition temperature T_0, the Curie temperature T_C, and the dielectric permittivity $\chi(T_0)$ at the transition temperature. However, the atomistic calculations, performed at zero temperature, do not yield these parameters. In order to enable a completely knowledge based multi-scale simulation chain for ferroelectrics, a new type of adjustment method for the coefficients of the free energy has been

developed which is solely based on the available input parameters from DFT calculations and SMP simulations compiled in Table 2.1.

This adjustment process, shown in the following, consists of five major steps. Throughout the process, a homogeneous polarization in x_3-direction is assumed, unless stated otherwise.

Step 1: Elastic properties   First of all, the coefficients of the elastic energy term (1.71) are determined. In section 1.3.3, these coefficients have already been identified as components of the elasticity tensor. Additionally, the sensitivity study showed that the elastic constants are completely decoupled from the rest of the energy function, so that the elastic stiffness of the paraelectric phase obtained from DFT calculations can directly be transferred into the phase-field model:

$$C_{ij} = \hat{c}_{\text{cub},ij} \tag{2.7}$$

Step 2: Electromechanical coupling   The electromechanical coupling term (1.72) describes the interaction between polarization and the crystal's distortion in a homogeneously polarized state. The adjustment of the electrostrictive coefficients Q_{ij} follows the work of Devonshire [20]. Under equilibrium, stress-free conditions, the tetragonally polarized material exhibits the spontaneous strains $e_\parallel$ and $e_\perp$ parallel and perpendicular to the direction of polarization, respectively. Using the system of equations (1.68) as well as $\hat{e}_\parallel$, $\hat{e}_\perp$ and $\hat{P}_0$ from first-principles DFT calculations, the electrostrictive constants can be determined as

$$Q_{11} = \frac{\hat{e}_\parallel}{\hat{P}_0^2} \qquad Q_{12} = \frac{\hat{e}_\perp}{\hat{P}_0^2}. \tag{2.8}$$

Step 3: Landau energy   The Landau energy term described in (1.65) contains information about the spontaneous polarization, the dielectric properties, as well as the phase of the material, i.e. whether the polarized material has a tetragonal, rhombohedral or orthorhombic crystal structure. Figure 1.11 shows a plot of an equilibrium two-dimensional Landau energy density. While the positions of the global minima in the plot correspond to the spontaneous polarization states, the curvature of the energy function at its minima defines the dielectric permittivities κ_{11} and κ_{33} [18]:

$$\frac{\partial^2}{\partial P_3^2}\Psi(P_i, P_{i,j}, \varepsilon_{ij}, D_i) = \frac{1}{\kappa_{33}}, \qquad \frac{\partial^2}{\partial P_1^2}\Psi(P_i, P_{i,j}, \varepsilon_{ij}, D_i) = \frac{1}{\kappa_{11}} \tag{2.9}$$

The energy barriers between neighboring minima determine the properties of $90°$ and $180°$ domain walls. The crystallographic phase is determined by the direction in which the global minima are located: For a tetragonally polarized and distorted material, the global minima are along the $\langle 100 \rangle$ crystal directions, whereas they are located in $\langle 110 \rangle$ directions for an orthorom-

bic polarization and in $\langle 111 \rangle$ directions for a rhombohedral polarization. Under equilibrium conditions, i.e. in the absence of mechanical stresses and electric fields, the free energy function (1.64) for a homogeneously polarized state can be expressed as a function $\Psi^{\text{equil}}(P_i)$ depending only on the polarization order parameter. Therefore, the equilibrium strains $\varepsilon_{ij}^{\text{equil}}$ are calculated for the stress- and field-free state and substituted in (1.64):

$$
\begin{aligned}
\frac{\partial \Psi(P_i, 0, \varepsilon_{ij}, P_i)}{\partial \varepsilon_{ij}} &= \sigma_{ij}(P_i, \varepsilon_{ij}) = 0 \\
&\Rightarrow \varepsilon_{ij}^{\text{equil}}(P_i) \\
&\Rightarrow \Psi^{\text{equil}}(P_i) = \Psi(P_i, 0, \varepsilon_{ij}^{\text{equil}}(P_i), P_i)
\end{aligned}
\tag{2.10}
$$

For the adjustment of the Landau energy coefficients, the equilibrium energy function $\Psi^{\text{equil}}(P_i)$ is used. The information on the spontaneous polarization $\hat{P}_0$ and the dielectric permittivities $\hat{\kappa}_{11}$ and $\hat{\kappa}_{33}$ from DFT calculations and SMP simulations yields the three equations

$$
\frac{\partial \Psi^{\text{equil}}(0, 0, \hat{P}_0)}{\partial P_3} = 2\hat{P}_0(\alpha_1 + 2\hat{P}_0^2 \alpha_{11} + 3\hat{P}_0^4 \alpha_{111}) = 0 \tag{2.11}
$$

$$
\frac{\partial^2 \Psi^{\text{equil}}(0, 0, \hat{P}_0)}{\partial P_3^2} = 2(\alpha_1 + 6\hat{P}_0^2 \alpha_{11} + 15\hat{P}_0^4 \alpha_{111}) = \frac{1}{\hat{\kappa}_{33}} \tag{2.12}
$$

$$
\frac{\partial^2 \Psi^{\text{equil}}(0, 0, \hat{P}_0)}{\partial P_1^2} = 2(\alpha_1 + \hat{P}_0^2 \alpha_{12} + \hat{P}_0^4 \alpha_{112} + 2C_{44} Q_{44}^2 \hat{P}_0^2) = \frac{1}{\hat{\kappa}_{11}}, \tag{2.13}
$$

where the first equation defines a minimum of the equilibrium free energy at $P = P_0$, and the second and third equation define the curvature of the free energy at the spontaneous polarization state and hence the (anisotropic) dielectric permittivity. These equations can be solved with respect to α_1, α_{111} and α_{112},

$$
\alpha_1 = -\hat{P}_0^2 \alpha_{11} - \frac{1}{8\hat{\kappa}_{33}} \tag{2.14}
$$

$$
\alpha_{111} = \frac{1 - 8\hat{P}_0^2 \alpha_{11} \hat{\kappa}_{33}}{24\hat{P}_0^4 \hat{\kappa}_{33}} \tag{2.15}
$$

$$
\alpha_{112} = \frac{-16 C_{44} \hat{P}_0^2 Q_{44}^2 + 8\hat{P}_0^2(\alpha_{11} - \alpha_{12}) + \frac{4}{\hat{\kappa}_{11}} + \frac{1}{\hat{\kappa}_{33}}}{8\hat{P}_0^4}, \tag{2.16}
$$

where the coefficients α_1, α_{111} and α_{112} still depend on the remaining Landau energy coefficients α_{11} and α_{12}. Especially the ratio $\Omega = \alpha_{11}/\alpha_{12}$ is crucial for adjusting the phase of the material, because it changes the properties of the free energy in $\langle 110 \rangle$ and $\langle 111 \rangle$ directions while having no influence on the properties in $\langle 100 \rangle$ direction. Also the Landau coefficient α_{123} affects the material's phase, but unlike Ω it only influences the properties of the free energy in $\langle 111 \rangle$ direction. The impact of Ω and α_{123} is illustrated in figure 2.3: The free energy can be
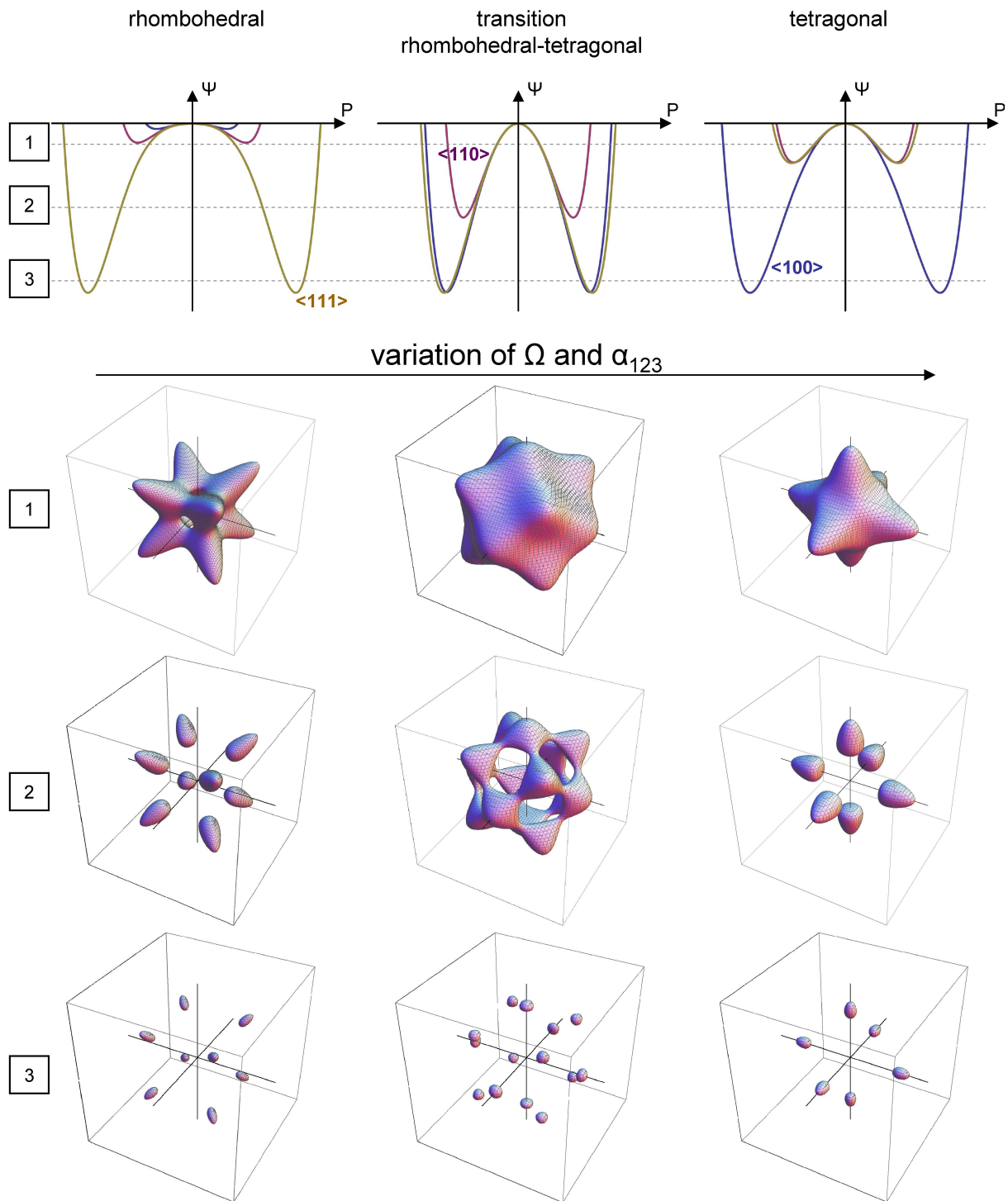
Figure 2.3.: By variation of Ω and α_{123}, the Landau energy can be tuned from a purely rhombohedral state (left) to a purely tetragonal state (right). The upper part shows diagrams of the Landau energy plotted versus the polarization for different crystallographic directions $\langle 100 \rangle$, $\langle 110 \rangle$ and $\langle 111 \rangle$. In each case the crystallographic direction of the global minima defines the phase of the material. For a certain set of Ω and α_{123}, the minima in $\langle 111 \rangle$ and $\langle 100 \rangle$ direction coincide, and the energy function switches from rhombohedral to tetragonal (middle). In the lower part, equipotential plots of the Landau energy for three energy levels (indicated 1, 2 and 3) are illustrated, three-dimensionally showing the form of the Landau energy and the configuration of the global minima.

tuned from a purely tetragonal polarization state to a purely rhombohedral polarization state by variation of parameters Ω and α_{123} only. With equivalent minima in $\langle 100 \rangle$ and $\langle 111 \rangle$ crystal direction, the transition state describes the morphotropic phase boundary in PZT. This phase adjustment makes it possible to describe the complete PZT system within a single formulation of the free energy function.

The remaining Landau coefficients are derived in the following two adjustment steps by fitting the Helmholtz free energy function to the properties of $180°$ and $90°$ domain walls.

Step 4: $180°$ domain wall properties For a single $180°$ domain wall in a perfect, infinite and stress-free crystal, there is a one-dimensional analytical solution as can be found in [9]. Assuming the $180°$ domain wall is located in the x_2-x_3-plane, the polarization $P_3(x_1)$ changes from $P_3(x_1 \to -\infty) = P_0$ to $P_3(x_1 \to \infty) = -P_0$, while $P_1 = P_2 = 0$ (cf. figure 2.2). Considering the symmetry of the infinitely expanded problem, the strains in x_2- and x_3-direction are set to $\varepsilon_{22} = e_\perp$ and $\varepsilon_{33} = e_\parallel$, and only the strain $\varepsilon_{11}(x_1)$ varies in x_1-direction. Furthermore, it is assumed that there are no shear strains in the complete system: $\varepsilon_{ij} = 0$ for $i \neq j$. With all these assumptions, the polarization $P_3(x_1)$ across the domain wall depends on both the parameters α_{11} and G_{44}:

$$P_3(x_1) = \frac{\hat{P}_0 \sinh\left(\frac{x_1}{\eta(\alpha_{11}, G_{44})}\right)}{\sqrt{A(\alpha_{11}) + \sinh^2\left(\frac{x_1}{\eta(\alpha_{11}, G_{44})}\right)}} \tag{2.17}$$

with

$$\alpha_{11}^+ = \alpha_{11} - \frac{q_{12}^2}{2C_{11}}, \tag{2.18}$$

$$A(\alpha_{11}) = \frac{3\alpha_{111}\hat{P}_0^2 + \alpha_{11}^+}{2\alpha_{111}\hat{P}_0^2 + \alpha_{11}^+}, \tag{2.19}$$

$$\eta(\alpha_{11}, G_{44}) = \frac{\sqrt{G_{44}}}{\hat{P}_0\sqrt{6\alpha_{111}\hat{P}_0^2 + 2\alpha_{11}^+}}. \tag{2.20}$$

This is consistent with the previous sensitivity analysis (Table 2.2): Out of the three gradient energy coefficients, only G_{44} shows an influence on the $180°$ DWW and DWE. While a change of G_{44} has a similar impact on both the DWW and the DWE, the Landau energy coefficient α_{11} mainly influences the domain wall energy. In figure 2.4, the impact of G_{44} and α_{11} on the DWW and the DWE is illustrated.

Taking the analytical solution $P_3(x_1)$ of the polarization across a domain wall as well as the $180°$ domain wall thickness $\hat{\xi}_{180}$ and energy $\hat{\gamma}_{180}$ from DFT calculations or empirical SMP
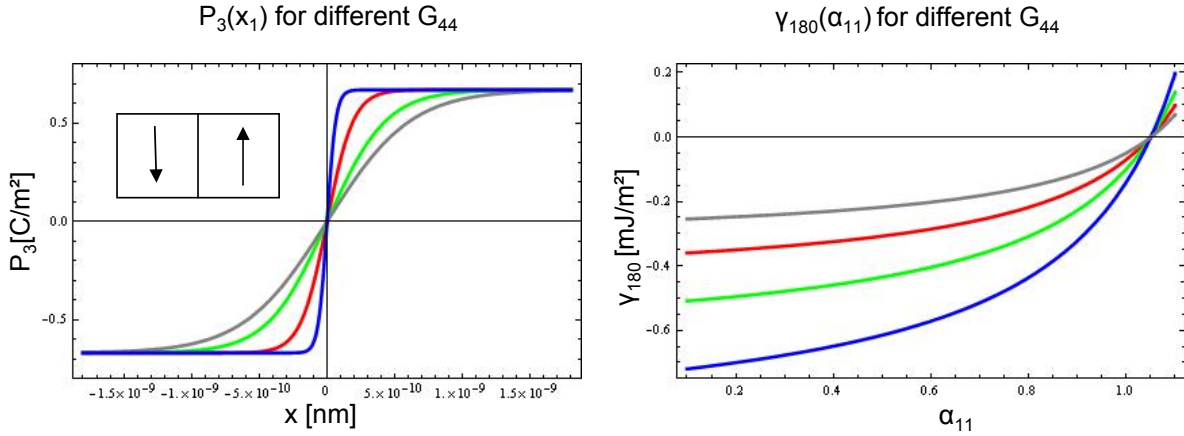
Figure 2.4.: Influence of the coefficients G_{44} and α_{11} on the 180° DWW and DWE. Left: Polarization P_3 in a 180° domain wall for different gradient coefficients G_{44}, showing the impact on the domain wall thickness ξ_{180}. Right: Domain wall energy γ_{180} depending on the Landau coefficient α_{11}, again for different G_{44}. Negative values of γ_{180} indicate that the 180° domain wall becomes energetically favorable and is therefore stable.

simulations and substituting in (2.5) and (2.6) yields the two nonlinear algebraic equations

$$\hat{\xi}_{180} = \left.\frac{2\hat{P}_0}{\frac{\partial}{\partial x_1}P_3(x_1)}\right|_{x_1=0}, \tag{2.21}$$

$$\hat{\gamma}_{180} = \int_{-\infty}^{\infty} \left(\Psi(P_3(x_1), P_{3,1}(x_1), \varepsilon_{11}(x_1)) - \Psi_{\text{bulk}}(\infty)\right) dx_1 \tag{2.22}$$

which can be solved iteratively with respect to the Landau energy coefficient α_{11} and the gradient energy coefficient G_{44}.

Step 5: 90° domain wall properties Beside the 180° domain wall, the second type of twin structure present in a ferroelectric's tetragonal phase is the 90° domain wall. Contrary to the 180° domain wall, there is no general analytical solution for a 90° domain wall. The 90° domain wall is oriented in $[110]$, and only the charge neutral head-to-tail configuration is stable. To compute an equilibrium one-dimensional 90° domain wall, the coordinate system (x_1, x_2, x_3) of the material properties as well as the Helmholtz free energy function is rotated by 45° about x_3. In the new coordinate system (s, r, x_3), the equilibrium polarization far away from the domain wall is

$$\lim_{s \to -\infty} \vec{P} = (\frac{P_0}{\sqrt{2}}, \frac{P_0}{\sqrt{2}}, 0) \qquad \lim_{s \to \infty} \vec{P} = (\frac{P_0}{\sqrt{2}}, -\frac{P_0}{\sqrt{2}}, 0), \tag{2.23}$$
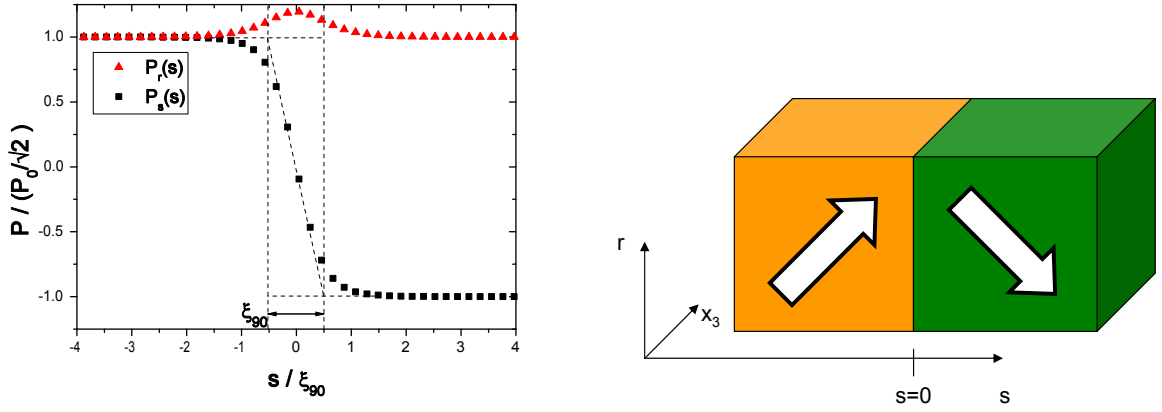
Figure 2.5.: Profile of the polarization in a 90° domain wall. $P_s(s)$ and $P_r(s)$ denote the components of the polarization perpendicular and parallel to the domain wall, respectively. The thickness of the domain wall ξ_{90} is marked as defined in eqn. (2.5).

as can be seen from figure 2.5. Furthermore, a perfect crystal is assumed, and both the applied stress and the electric field far away from the domain wall are zero. In order to obtain the remaining coefficients of the energy function, the phase-field model was implemented in a finite element formulation (this implementation will be discussed in detail in chapter 4). As nodal degrees of freedom, the components of the polarization P_i, the mechanical displacement u_i and the electric potential ϕ are used. The polarization components $P_s(s)$ and $P_r(s)$ in a one-dimensional 90° domain wall were computed as shown in Figure 2.5. Using equations (2.5) and (2.6), the domain wall thickness and energy can be calculated numerically:

$$\hat{\xi}_{90} = \left. \frac{2\frac{\sqrt{\hat{P}_0}}{2}}{\frac{\partial}{\partial s}P_s(s)} \right|_{s=0} , \tag{2.24}$$

$$\hat{\gamma}_{90} = \int_{-\infty}^{\infty} \left(\Psi(P_s(s), P_r(s), P_{s,s}(s), P_{r,s}(s), \varepsilon_{ss}(s), \varepsilon_{rs}(s), \phi(s)) - \Psi_{\text{bulk}}(\infty) \right) ds \tag{2.25}$$

The properties of the 90° domain wall depend on the energy coefficients α_{12}, G_{11} and G_{12}. Since the coefficient α_{12} influences the terms $P_i P_j$ in the Landau energy, it determines the height of the energy barrier between two neighboring minima. As can be seen from the previous sensitivity analysis, the coefficient α_{12} alters the ratio between the DWW and the DWE, while the gradient coefficients G_{11} and G_{12} can be used to shift both the thickness and the energy of a 90° domain wall.

Now, the coefficients α_{12}, G_{11} and G_{12} are systematically varied, and the respective polarization curves $P_s(s)$ and $P_r(s)$ are calculated. Then, for each set of the coefficients α_{12}, G_{11} and G_{12} both the 90° domain wall thickness and energy are obtained. This is iterated until a set is found that matches the atomistic calculations predictions for the 90° DWW and DWE.

The last remaining Landau energy coefficient α_{123} has no influence on the tetragonal (or orthorhombic) material properties at all. It influences the energy barrier by shifting the height of the Landau energy function's saddle point in $\langle 111 \rangle$ direction. This is demonstrated in Figure 2.6: The equilibrium energy function (2.10) is plotted in the $\langle 100 \rangle$ (tetragonal), $\langle 110 \rangle$ (orthorhombic) and $\langle 111 \rangle$ (rhombohedral) crystal directions. A lowest minimum in $\langle 100 \rangle$ direction means that the material exhibits a tetragonally polarized phase. The other minima in the plot indicate the energy barriers between neighboring (global) minima and are actually saddle points in the energy landscape. For $\alpha_{123} = 0$, the height of the energy barriers differs (Figure 2.6a). Variation of α_{123} only shifts the energy barrier in $\langle 111 \rangle$ direction. Thus, for a purely tetragonally polarized material like PTO, the coefficient α_{123} is chosen in a way that the height of the energy barriers in $\langle 110 \rangle$ and $\langle 111 \rangle$ direction coincide (Figure 2.6b).
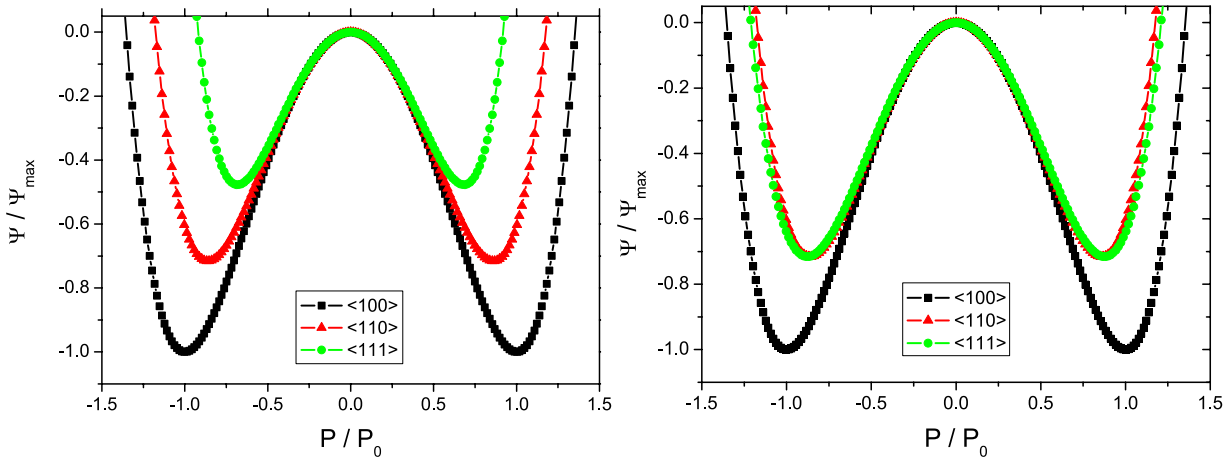

Figure 2.6.: Helmholtz free energy density plotted in $\langle 100 \rangle$, $\langle 110 \rangle$ and $\langle 111 \rangle$ crystal directions for different values of the Landau energy coefficient α_{123}. The lowest minima in $\langle 100 \rangle$ directions determine the tetragonal phase of the material, while the other minima are saddle points in the energy landscape and describe the switching barriers between equivalent tetragonal states. Left: For $\alpha_{123} = 0$, the switching barriers have different heights in $\langle 110 \rangle$ and $\langle 111 \rangle$ directions. Right: α_{123} as chosen in the adjustment process so that the saddle points in $\langle 110 \rangle$ and $\langle 111 \rangle$ direction coincide. The coefficient α_{123} only affects the height of the $\langle 111 \rangle$ minima.

Finally, the coupling energy coefficient Q_{44} is adjusted. Throughout the adjustment process, it has been set to the isotropic symmetry approximation $Q_{44} = 2(Q_{11} - Q_{12})$ [19, 56] as an initial condition. As can be seen from the sensitivity analysis (Table 2.2), Q_{44} increases the piezoelectric coefficient d_{121} directly, so that Q_{44} can easily be set to match the DFT result for d_{121}. Since Q_{44} also has a slight influence on the $90°$ domain wall properties, it may become necessary to repeat step 5 and obtain Q_{44} in an iterative approach. Concluding this section, Figure 2.7 illustrates the complete adjustment process for all coefficients of the free energy in a flow chart.
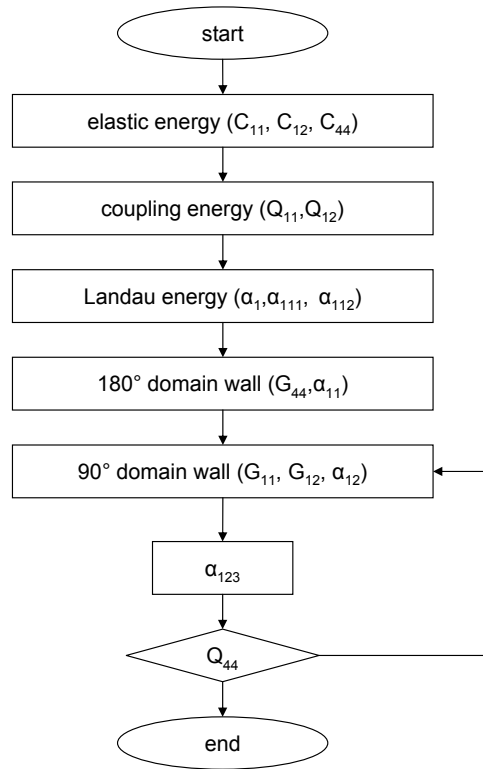
Figure 2.7.: Flow chart of the adjustment process for the coefficients of the free energy.

2.4. Discussion

2.4.1. Adjustment process for PTO and PZT input parameters

As shown in sections 2.1 and 2.1, the input parameters for the phase-field model were determined from first-principles DFT-LDA calculations and classical atomistic SMP simulations. In general, the predictive power of DFT calculations is higher than that of atomistic simulations, which are themselves fitted to DFT calculations. For both PTO and PZT, the set of calculated input parameters is presented in the left columns of Table 2.3. DFT calculations yielded the intrinsic parameters: spontaneous polarization and strain, elastic constants, dielectric permittivities and the piezoelectric constants for PTO and PZT. Note that the spontaneous strains $\hat{e}_{\parallel}$ and $\hat{e}_{\perp}$ are computed from the cubic and tetragonal lattice parameters $\hat{a}_{\mathrm{cub}}$, $\hat{a}_{\mathrm{tetr}}$ and $\hat{c}_{\mathrm{tetr}}$.

For PTO, the domain wall properties (thickness ξ and energy γ) were obtained both from DFT calculations (denoted $\xi_{\mathrm{DFT90/180}}, \gamma_{\mathrm{DFT90/180}}$) and SMP simulations (denoted $\xi_{\mathrm{SMP90/180}}$, $\gamma_{\mathrm{SMP90/180}}$). When calculating the domain wall properties of PZT, it was found that DFT calculations yielded a slightly monoclinic ground state once the tetragonal symmetry was broken when computing a 90° domain wall configuration (for the case of the 180° domain wall in PZT, DFT calculations retained tetragonal symmetry). The 90° domain wall properties were then obtained from atomistic SMP simulations.

Table 2.3.: Atomistic target data compared to the adjusted phase-field model for PTO and PZT. The input parameters (in each case left column) were computed using first-principles DFT calculations and atomistic SMP simulations. Based on these input parameters, a phase-field model was adjusted, the properties of which are shown in the right column, respectively. The spontaneous deformations denoted by a superscript star are calculated from the cubic and tetragonal lattice parameters using eqns. (2.1).

	unit	PTO first-principles data (input)	PTO phase-field model (adjusted)	PZT first-principles data (input)	PZT phase-field model (adjusted)
P_0	[C/m^2]	0.88	0.88	0.58	0.58
$\hat{a}_{cub}$	[Å]	3.8845	-	4.0119	-
$\hat{a}_{tetr}$	[Å]	3.8558	-	4.0047	-
$\hat{c}_{tetr}$	[Å]	4.0480	-	4.0602	-
$e_\parallel$		0.04209*	0.04209	0.012039*	0.012039
$e_\perp$		-0.007388*	-0.007388	-0.0017946*	-0.0017946
κ_{33}		$17\kappa_0$	$17\kappa_0$	$18\kappa_0$	$18\kappa_0$
κ_{11}		$54\kappa_0$	$54\kappa_0$	$76\kappa_0$	$76\kappa_0$
c_{11}	[Pa]	342×10^9	342×10^9	361×10^9	361×10^9
c_{12}	[Pa]	131×10^9	131×10^9	115×10^9	115×10^9
c_{44}	[Pa]	108×10^9	108×10^9	91×10^9	91×10^9
d_{33}	[C/m]	2.46×10^{-11}	1.42×10^{-11}	1.57×10^{-11}	6.58×10^{-12}
d_{31}	[C/m]	-8.04×10^{-12}	-2.52×10^{-12}	-4.32×10^{-12}	-9.87×10^{-13}
d_{15}	[C/m]	1.72×10^{-11}	1.72×10^{-11}	1.53×10^{-12}	1.53×10^{-12}
$\gamma_{DFT,180}$	[mJ/m^2]	112	173	96	96
$\gamma_{DFT,90}$	[mJ/m^2]	24	71	-	-
$\xi_{DFT,180}$	[m]	4.5×10^{-10}	4.5×10^{-10}	6.7×10^{-10}	6.7×10^{-10}
$\xi_{DFT,90}$	[m]	5.4×10^{-10}	5.4×10^{-10}	-	-
$\gamma_{SMP,180}$	[mJ/m^2]	156	156	-	-
$\gamma_{SMP,90}$	[mJ/m^2]	64	64	36	36
$\xi_{SMP,180}$	[m]	3.9×10^{-10}	3.9×10^{-10}	-	-
$\xi_{SMP,90}$	[m]	4.9×10^{-10}	4.9×10^{-10}	6.6×10^{-10}	6.6×10^{-10}

Based on the input parameters from Table 2.3, the adjustment process for the phase-field model as described in section 2.3 was applied for PTO and PZT. Three cases were considered:

1. PTO with domain wall properties from DFT calculations (denoted PTO-DFT)

2. PTO with domain wall properties from SMP simulations (denoted PTO-SMP)

3. PZT with 180° domain wall properties from DFT calculations and 90° domain wall properties from SMP simulations (denoted PZT)

The three corresponding sets of adjusted coefficients of the Helmholtz free energy function are presented in Table 2.4. From the now adjusted phase-field models, the resulting material properties were computed as shown in section 2.2. Table 2.3 shows these properties of the adjusted phase-field models (PTO and PZT) in comparision to the input parameters from first principles DFT calculations and atomistic SMP simulations.

Table 2.4.: Adjusted coefficients of the Helmholtz free energy based on input parameters from atomistic calculations. In the first case (PTO-DFT), domain wall properties for PTO are taken from first principles calculations, while in the second case (PTO-SMP) they are derived from atomistic SMP simulations. In the case of PZT, the 180° domain wall properties are obtained from DFT calculations and the 90° domain wall properties from SMP simulations.

coefficient	PTO-DFT	PTO-SMP	PZT
α_1	$-3.253 \times 10^8 \mathrm{JmC}^{-2}$	$-4.268 \times 10^8 \mathrm{JmC}^{-2}$	$-8.499 \times 10^8 \mathrm{JmC}^{-2}$
α_{11}	$-6.58 \times 10^8 \mathrm{Jm}^5\mathrm{C}^{-4}$	$-5.27 \times 10^8 \mathrm{Jm}^5\mathrm{C}^{-4}$	$1.950 \times 10^8 \mathrm{Jm}^5\mathrm{C}^{-4}$
α_{12}	$-3.29 \times 10^9 \mathrm{Jm}^5\mathrm{C}^{-4}$	$-3.211 \times 10^9 \mathrm{Jm}^5\mathrm{C}^{-4}$	$-9.750 \times 10^8 \mathrm{Jm}^5\mathrm{C}^{-4}$
α_{111}	$7.473 \times 10^8 \mathrm{Jm}^9\mathrm{C}^{-6}$	$6.909 \times 10^8 \mathrm{Jm}^9\mathrm{C}^{-6}$	$2.117 \times 10^9 \mathrm{Jm}^9\mathrm{C}^{-6}$
α_{112}	$6.489 \times 10^9 \mathrm{Jm}^9\mathrm{C}^{-6}$	$6.557 \times 10^9 \mathrm{Jm}^9\mathrm{C}^{-6}$	$1.687 \times 10^{10} \mathrm{Jm}^9\mathrm{C}^{-6}$
α_{123}	$1.55 \times 10^{10} \mathrm{Jm}^9\mathrm{C}^{-6}$	$1.68 \times 10^{10} \mathrm{Jm}^9\mathrm{C}^{-6}$	$4.823 \times 10^9 \mathrm{Jm}^9\mathrm{C}^{-6}$
Q_{11}	$5.435 \times 10^{-2} \mathrm{m}^4\mathrm{C}^{-2}$	$5.435 \times 10^{-2} \mathrm{m}^4\mathrm{C}^{-2}$	$3.579 \times 10^{-2} \mathrm{m}^4\mathrm{C}^{-2}$
Q_{12}	$-9.540 \times 10^{-3} \mathrm{m}^4\mathrm{C}^{-2}$	$-9.540 \times 10^{-3} \mathrm{m}^4\mathrm{C}^{-2}$	$-5.335 \times 10^{-3} \mathrm{m}^4\mathrm{C}^{-2}$
Q_{44}	$1.987 \times 10^{-2} \mathrm{m}^4\mathrm{C}^{-2}$	$1.987 \times 10^{-2} \mathrm{m}^4\mathrm{C}^{-2}$	$1.923 \times 10^{-2} \mathrm{m}^4\mathrm{C}^{-2}$
C_{11}	$342 \times 10^9 \mathrm{Jm}^{-3}$	$342 \times 10^9 \mathrm{Jm}^{-3}$	$361 \times 10^9 \mathrm{Jm}^{-3}$
C_{12}	$131 \times 10^9 \mathrm{Jm}^{-3}$	$131 \times 10^9 \mathrm{Jm}^{-3}$	$115 \times 10^9 \mathrm{Jm}^{-3}$
C_{44}	$108 \times 10^9 \mathrm{Jm}^{-3}$	$108 \times 10^9 \mathrm{Jm}^{-3}$	$91 \times 10^9 \mathrm{Jm}^{-3}$
G_{11}	$5.6 \times 10^{-11} \mathrm{Jm}^3\mathrm{C}^{-2}$	$4.51 \times 10^{-11} \mathrm{Jm}^3\mathrm{C}^{-2}$	$2.9 \times 10^{-11} \mathrm{Jm}^3\mathrm{C}^{-2}$
G_{12}	$5.6 \times 10^{-11} \mathrm{Jm}^3\mathrm{C}^{-2}$	$4.65 \times 10^{-11} \mathrm{Jm}^3\mathrm{C}^{-2}$	$6.95 \times 10^{-11} \mathrm{Jm}^3\mathrm{C}^{-2}$
G_{44}	$3.4 \times 10^{-11} \mathrm{Jm}^3\mathrm{C}^{-2}$	$2.82 \times 10^{-11} \mathrm{Jm}^3\mathrm{C}^{-2}$	$6.95 \times 10^{-11} \mathrm{Jm}^3\mathrm{C}^{-2}$

Furthermore, the adjusted free energy functions $\Psi^{\mathrm{equil}}(P_i)$ for PTO-DFT, PTO-SMP and PZT are illustrated in Figure 2.8 for the stress- and field-free state. The plots in the first row show the free energy for different crystallographic directions. As expected for a tetragonal ground state, the minima of the free energy are located along the $\langle 100 \rangle$ crystal directions in all three cases. In the second and third rows, contour plots depict cuts through the free energy function in the [100] and [110] crystallographic planes, respectively. Here, the [100] contour plots exhibit the four equivalent minima in $\langle 100 \rangle$ directions. In the [110] contour plots, also possible local minima of the free energy in $\langle 111 \rangle$ or $\langle 110 \rangle$ direction can be depicted. While the free energies of PTO-DFT and PTO-SMP have equivalent saddle points in $\langle 111 \rangle$ and $\langle 110 \rangle$ direction, the case of PZT shows slightly developed local minima in $\langle 111 \rangle$ direction that are energetically lower than the saddle points in $\langle 110 \rangle$ direction. This can also be seen from the three-dimensional equipotential plots of the free energy, shown in the fourth row.

2.4.2. Discussion

When comparing the atomic-level input parameters and the corresponding properties of the adjusted phase-field models in Table 2.3, a high level of agreement can be noticed, especially for the spontaneous parameters P_0, $e_\parallel$, $e_\perp$, the dielectric permittivity κ_{ij} as well as for the elastic stiffness c_{ijkl}. Due to their analytical adjustment, the transfer of these quantities into the phase-field model will always be sucessfull, since the adjustment method is designed and optimized for materials exhibiting tetragonal symmetry. Because of the high non-linearity of the adjustment
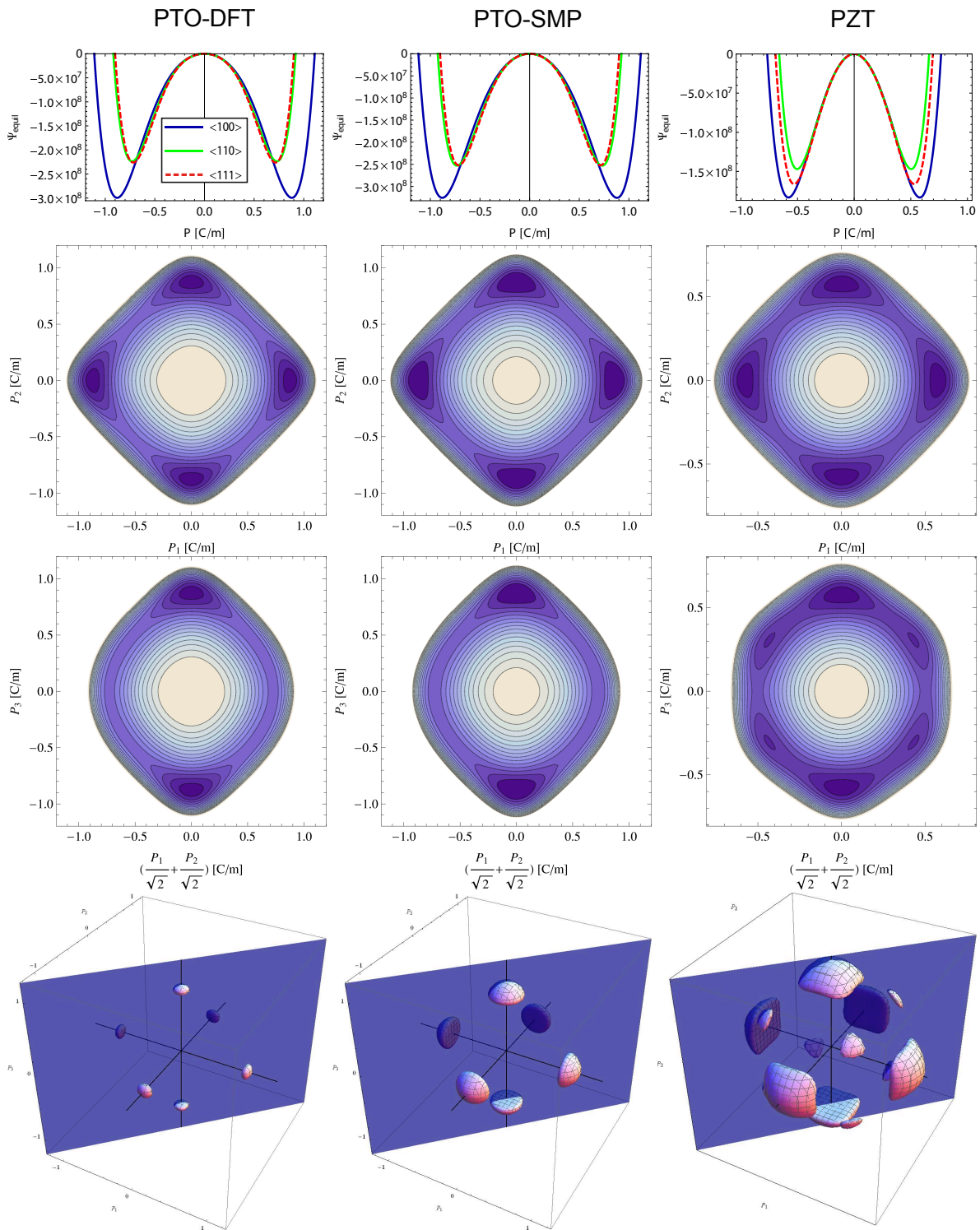
Figure 2.8.: Adjusted free energy functions for the three considered cases PTO-DFT (1st column), PTO-SMP (2nd column) and PZT (3rd column) in the absence of an electric field and mechanical stresses. The first row shows the free energies along different crystallographic directions, the second row contour plots of the free energies in the [100] plane, the third row contour plots in the [110] plane and the fourth row equipotential plots.

problem and additional physical requirements as will be discussed below, other properties have to be within a certain range for an exact adjustment of the phase-field model to the properties calculated at the atomistic level. This is the case for the domain wall thicknesses $\xi_{90/180}$ and energies $\gamma_{90/180}$ and is below illustrated for PTO:
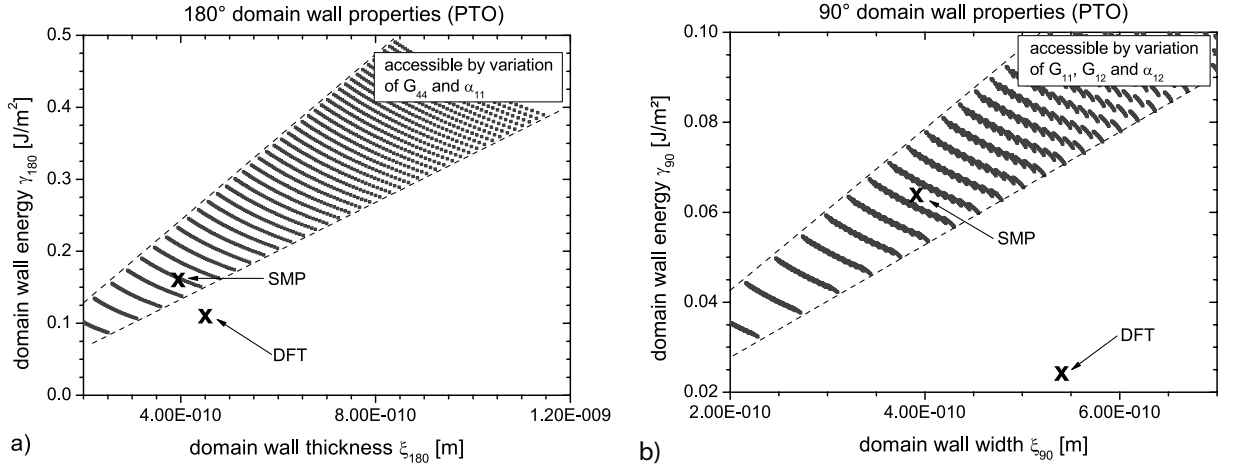
Figure 2.9.: Adjustment of the domain wall properties for PTO. a) 180° domain wall properties: By variation of the coefficients $5 \times 10^{-12} \leq G_{44} \leq 2 \times 10^{-10}$ and $-1 \times 10^9 \leq \alpha_{11} \leq 1 \times 10^9$, the region of ξ_{180}/γ_{180}-ratio between the two dashed lines can be accessed. b) 90° domain wall properties: The reachable range of the ξ_{90}/γ_{90}-ratio is shown for a variation of the coefficients $5 \times 10^{-12} \leq G_{11} \leq 2 \times 10^{-10}$, $5 \times 10^{-12} \leq G_{12} \leq 2 \times 10^{-10}$ and $1.3 \times 10^9 \leq \alpha_{12} \leq 3.3 \times 10^9$. While in both cases the phase-field model can be fitted exactly to results from atomistic SMP simulations (SMP), the predictions from first-principles DFT calculations are beyond the adjustable range.

In Figure 2.9a, the 180° domain wall energy γ_{180} is plotted vs. the domain wall thickness ξ_{180} for various combinations of the only Helmholtz energy coefficients that influence these quantities, G_{44} and α_{11}. All other coefficients are either determined by the prior adjustment to the intrinsic material properties or show no influence on the 180° domain wall properties (cf. Table 2.2). Only the region of ξ_{180}/γ_{180} ratio between the two dashed lines is accessible, since some additional requirements have to be satisfied. It has to be ensured that the Helmholtz free energy function goes to positive infinity for big polarizations in all crystal directions. Furthermore, to guarantee that the Helmholtz energy function only has minima at the spontaneous polarized states of tetragonal symmetry, the Landau energy coefficient α_1 has to be negative. Since the energy coefficient α_{11} that is used to adjust the 180° domain wall properties is directly related to α_1 (see eqn. 2.14), it has to fulfill the condition

$$\alpha_{11} \geq -\frac{1}{8P_0\kappa_{33}}. \tag{2.26}$$

Otherwise, for a positive α_1, an additional minimum appears at $P = 0$ resulting in a metastable phase of cubic symmetry. With these requirements, it can be seen from Figures 2.9 a and b

Table 2.5.: Comparison of elasticity tensor components for the following cases: cubic input-parameters from DFT-calculations, monodomain properties of the adjusted phase-field model and results of DFT-calculations for the tetragonal phase that could not be used in the adjustment process due to cubic symmetry of the elastic part ψ_{elast} of the used Helmholtz free energy density. Although the phase-field model was fitted to input parameters of cubic symmetry, the considered monodomain state clearly shows a tetragonal symmetry.

		unit	c_{11}	c_{12}	c_{13}	c_{33}	c_{44}	c_{66}
	DFT - cubic (input)	[GPa]	342	131	131	342	108	108
PTO	Phase-field (monodomain)	[GPa]	339.8	117.0	116.9	256.0	101.4	108
	DFT - tetragonal	[GPa]	285	119	88	91	65	108
	DFT - cubic (input)	[GPa]	361	115	115	361	91	91
PZT	Phase-field (monodomain)	[GPa]	361.9	114.7	111.2	333.5	88.3	91
	DFT - tetragonal	[GPa]	327	110	107	178	73	92

that for PTO, the domain wall properties of the phase-field model can be adjusted properly to the input parameters from empirical potential simulations. However, for the case of input parameters from DFT calculations, neither the 180° nor the 90° domain wall properties lie within the accessible region and cannot be fitted exactly into the phase-field model. For domain wall input parameters outside the accessible region, eqns. (2.21) cannot be solved, so the 180° domain wall properties have to be adjusted numerically in a similar way as the 90° domain wall properties by solving a one-dimensional 180° domain wall, systematically varying the Helmholtz energy coefficients G_{44} and α_{11} and taking a best possible approximation. Hence, in this work the domain wall thickness was fitted exactly, while the domain wall energy was adjusted as well as possible.

The considered elastic energy function as shown in eqn. (1.69) contains the elastic information of the material and is adjusted here to a state of cubic symmetry. Nevertheless, when taking a phase-field model containing an energy function adjusted to cubic atomistic parameters and modeling a homogeneously polarized monodomain state in the absence of any domain walls, the phase-field model shows tetragonal symmetry. In a two-dimensional phase-field model, an initially stress- and field-free monodomain state polarized along the x_3-direction was loaded mechanically in all directions, and the elastic stiffness tensor of this monodomain state was obtained. The short-circuited electrical boundary condition allows the polarization order parameter to vary when the monodomain is loaded mechanically, causing electromechanical coupling. Table 2.5 shows a comparison of the cubic input elastic stiffness from first-principles DFT calculations and the elastic stiffness obtained from the phase field model. Here, the tetragonal character of the phase-field results can be seen: For instance, the elastic stiffness c_{33} parallel to the polarization is smaller than c_{11} perpendicular to the polarization. This mechanical softening behavior in the direction of polarization is expected and experimentally confirmed for ferroelectrics exhibiting a tetragonally distorted perovskite crystal structure [53, 46].

The described transfer of parameters from the atomistic level to phase-field modeling is subject to certain restrictions. First of all, for the energy function of sixth order in polarization as described in eqn. (1.64), not enough degrees of freedom are provided to fit all available parameters from first-principles calculations into the phase-field model. Especially for the adjustment of all three piezoelectric coefficients the used energy function is insufficient: For fitting the spontaneous strains $e_{\parallel}$, $e_{\perp}$ and the piezoelectric coefficients d_{33}, d_{31}, d_{15}, only the three coupling energy coefficients Q_{11}, Q_{12}, Q_{44} are available. Thus, either the spontaneous strains or the piezoelectric coefficients in the phase-field model can be adjusted correctly, but not all of them simultaneously. In the present work, the spontaneous strains and d_{15} are fitted exactly to DFT results, while the piezoelectric coefficients d_{33} and d_{31} differ from the DFT prediction (cf. Table 2.3).

A possibilty to allow the exact fit to all piezoelectric coefficients is to increase the number of degrees of freedom in the free energy function. As introduced in [71] in a free energy function for BaTiO$_3$, this can be done by adding higher order terms to the energy function's series expansion, also taking a completely tetragonal behavior of all material properties into account.

In the next chapter, this expansion of the free energy to higher order terms will be performed for PTO and PZT, and an improved adjustment process will be shown. Although this improved adjustment process will show a higher fitting accuracy, the numerical effort for solving the Ginzburg-Landau equation using the expanded free energy will rise significantly due to the higher order terms. Therefore, to keep the numerical effort manageable, the free energy discussed in this chapter and its adjusted coefficients will provide the basis for the development of the interface between phase-field modeling and micromechanical methods, following in chapter 4.

3. Further development of the phase-field model's free energy

In the previous chapter, an approach has been discussed for transferring results from atomistic calculations into a phase-field model. The free energy of the phase-field model was successfully fitted to input parameters from DFT calculations and SMP simulations, and it was possible to achieve a high level of agreement between the atomistic target parameters and the adjusted phase-field model. As discussed above, the adjustment method was subject to two main restrictions, caused by a too small number of degrees of freedom in the free energy of the phase-field model: The elastic stiffness could only be fitted to cubic symmetry, and the piezoelectric coefficients could not be adjusted independently of the spontaneous strains.

These restrictions can be eliminated by extending the free energy, strictly speaking the elastic part and the electromechanical part, with higher order terms, as will be shown in this chapter. After motivating and discussing the extensions of the free energy function, a sensitivity study is performed to examine the impact of the added free energy coefficients on the properties of the phase-field model. After that, the adjustment process shown in the previous chapter will be expanded in order to adjust the coefficients of the free energy to results of atomistic calculations. Finally, the adjusted free energy and the benefit of the introduced extensions will be discussed.

3.1. Extension of the free energy

Up to this point, the free energy used in the phase-field model was of the form shown in equation (1.64), with a Landau term up to sixth order in polarization, an elastic term of second order in strain, an electromechanical coupling term of order $\varepsilon_{ij}P_i^2$ and a gradient term of second order in $P_{i,j}$. This basic form of the free energy is well-established and has been applied in a variety of ferroelectricity phase-field models [42, 79, 80]. As discussed above, this basic form does not permit tetragonal elastic behavior and provides too little degrees of freedom, so that the spontaneous strains and the piezoelectric coefficients cannot be adjusted independently. In order to eliminate these restrictions, the basic form of the free energy can be expanded, increasing the disposable number of degrees of freedom: By expanding the elastic part of the free energy, elastic behavior of tetragonal symmetry can be taken into account, whereas an expansion of the electromechancial coupling term enables a decoupling of the spontaneous strains and the piezoelectric coefficients in the free energy. In order to avoid confusion with the coefficients of the basic form of the free energy (eqn. 1.64) used in chapter 2, and because the coefficients will be adjusted in a different way than before, the nomenclature of the coefficients in the Landau

energy, the elastic energy and the electromechanical coupling energy will be changed in this chapter.

For the elastic energy term to allow elastic behavior of tetragonal symmetry, it has to be expanded. In the basic form of the free energy, the elastic energy

$$
\begin{aligned}
\psi_{\text{elast}}(\varepsilon_{ij}) \quad = \quad & \frac{1}{2}C_{11}(\varepsilon_{11}^2 + \varepsilon_{22}^2 + \varepsilon_{33}^2) + \\
+ \quad & C_{12}(\varepsilon_{11}\varepsilon_{22} + \varepsilon_{11}\varepsilon_{33} + \varepsilon_{22}\varepsilon_{33}) + \\
+ \quad & 2C_{44}(\varepsilon_{12}^2 + \varepsilon_{13}^2 + \varepsilon_{23}^2)
\end{aligned}
\tag{3.1}
$$

is of cubic symmetry: The elastic properties in the direction of polarization and perpendicular to the polarization are the same. This also becomes apparent from the sensitivity study in Table (2.2), where for instance a change of the elastic energy coefficient C_{11} has the same impact on the elasticity tensor components c_{11} and c_{33}, inhibiting a separate adjustment. When expanding the free energy in order to allow for tetragonal elastic behavior, the general requirement for the free energy to describe both the high-symmetry paraelectric cubic state and the polarized state of lower symmetry also has to be taken into account: Since atomistic calculations predict different elastic properties for the cubic and the tetragonal phase, the elastic properties of both the paraelectric cubic phase and the polarized tetragonal phase have to be included in the free energy.

One possible way of including the elastic properties of tetragonal symmetry in the free energy while still describing both the cubic and the tetragonal phase in a single analytical function is rendering the elastic energy coefficients C_{ij} in the basic form of the free energy (eqn. 3.1) dependent on the polarization:

$$
C(P) = c_0 + fP^2. \tag{3.2}
$$

This approach is illustrated schematically in Figure 3.1. In the basic form of the free energy, the elastic energy coefficients (and hence the components of the elastic stiffness, as identified in the sensitivity study in section 2.2) are independent of the polarization, as depicted in Figure 3.1a. However, as shown in Figure 3.1b, choosing the approach of equation (3.6) for the elastic coefficients renders the possibility of separately adjusting the elastic stiffness of the paraelectric cubic phase ($P = 0$) and the spontaneously polarized tetragonal phase ($P = P_0$). Regarding the tetragonal symmetry of the polarized state, the extension of the elastic energy takes the following form:

$$
\begin{aligned}
\psi_{\text{elast}}^{\text{extended}}(\varepsilon_{ij}, P_i) \quad = \quad & \frac{c_1}{2}(\varepsilon_{11}^2 + \varepsilon_{22}^2 + \varepsilon_{33}^2) + c_2(\varepsilon_{11}\varepsilon_{22} + \varepsilon_{11}\varepsilon_{33} + \varepsilon_{22}\varepsilon_{33}) + \\
+ \quad & \frac{c_3}{2}(\varepsilon_{12}^2 + \varepsilon_{21}^2 + \varepsilon_{13}^2 + \varepsilon_{31}^2 + \varepsilon_{23}^2 + \varepsilon_{32}^2)
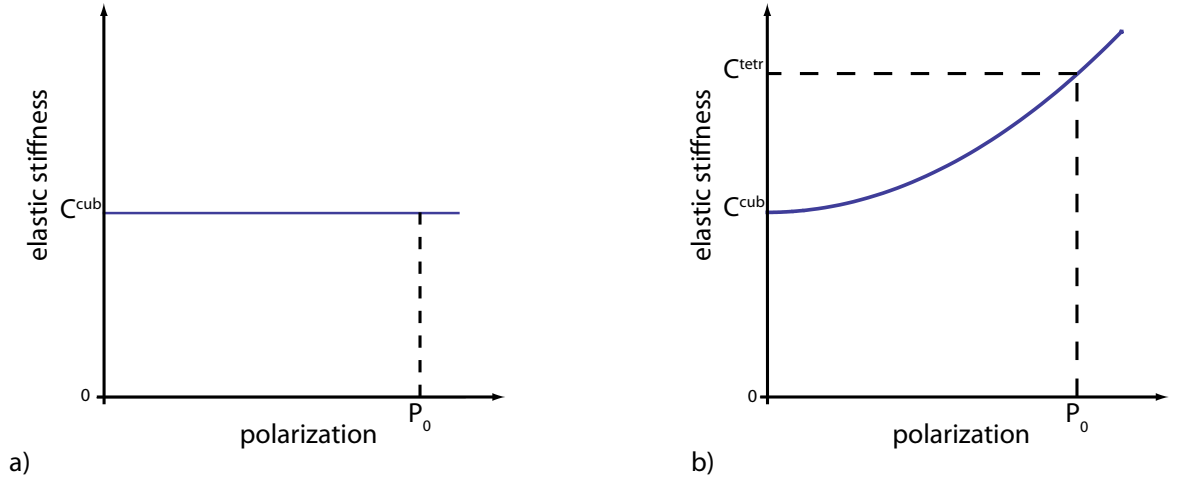\end{aligned}
$$

Figure 3.1.: Schematical illustration of the polarization-dependent elastic stiffness. (a) In the basic form of the free energy (without f-term), the elastic stiffness does not depend on the polarization. (b) Expanding the elastic part of the free energy as shown in eqn. (3.3) results in a polarization-dependence of the elastic stiffness components, enabling a separate adjustment of the elastic behavior in the cubic and the tetragonal phase.

$$
\begin{aligned}
+ & \left(\frac{f_1}{2} \varepsilon_{11}^2 + \frac{f_2}{2} (\varepsilon_{22}^2 + \varepsilon_{33}^2) + f_3 (\varepsilon_{11}\varepsilon_{22} + \varepsilon_{11}\varepsilon_{33}) + f_4 \varepsilon_{22}\varepsilon_{33} + \right. \\
+ & \left. \frac{f_5}{2} (\varepsilon_{12}^2 + \varepsilon_{21}^2 + \varepsilon_{13}^2 + \varepsilon_{31}^2) + \frac{f_6}{2} (\varepsilon_{23}^2 + \varepsilon_{32}^2) \right) P_1^2 + \\
+ & \left(\frac{f_1}{2} \varepsilon_{22}^2 + \frac{f_2}{2} (\varepsilon_{11}^2 + \varepsilon_{33}^2) + f_3 (\varepsilon_{11}\varepsilon_{22} + \varepsilon_{22}\varepsilon_{33}) + f_4 \varepsilon_{11}\varepsilon_{33} + \right. \\
+ & \left. \frac{f_5}{2} (\varepsilon_{12}^2 + \varepsilon_{21}^2 + \varepsilon_{23}^2 + \varepsilon_{32}^2) + \frac{f_6}{2} (\varepsilon_{13}^2 + \varepsilon_{31}^2) \right) P_2^2 + \\
+ & \left(\frac{f_1}{2} \varepsilon_{33}^2 + \frac{f_2}{2} (\varepsilon_{11}^2 + \varepsilon_{22}^2) + f_3 (\varepsilon_{11}\varepsilon_{33} + \varepsilon_{22}\varepsilon_{33}) + f_4 \varepsilon_{11}\varepsilon_{22} + \right. \\
+ & \left. \frac{f_5}{2} (\varepsilon_{13}^2 + \varepsilon_{31}^2 + \varepsilon_{23}^2 + \varepsilon_{32}^2) + \frac{f_6}{2} (\varepsilon_{12}^2 + \varepsilon_{21}^2) \right) P_3^2 .
\end{aligned}
\tag{3.3}
$$

For the case $P_i = 0$, the extended elastic energy $\psi_{\text{elast}}^{\text{extended}}$ takes the form of the basic elastic energy ψ_{elast}, hence representing the elastic properties of the cubic paraelectric phase. Thus, the three coefficients c_i can be adjusted to the elastic properties of the cubic phase, whereas the six additional coefficients f_i can be fitted to the six independent components of the tetragonal elasticity tensor.

In order to increase the number of degrees of freedom in the free energy to allow for an independent adjustment of the piezoelectric coefficients, the electromechanical coupling term (of order $\varepsilon_{ij}P^2$) has to be expanded. Proceeding in the same manner as for the elastic energy, the electromechanical coupling coefficients q_{ij} of the basic form of the free energy (equation (1.64))

are assumed to depend on the polarization:

$$q(P) = b_0 + gP^2. \tag{3.4}$$

Considering the tetragonal symmetry of the polarized phase, this approach yields the following expansion of the electromechanical coupling energy:

$$
\begin{aligned}
\psi_{\text{coup}}^{\text{extended}}(P_i, \varepsilon_{ij}) &= \frac{b_1}{2}(\varepsilon_{11}P_1^2 + \varepsilon_{22}P_2^2 + \varepsilon_{33}P_3^2) + \\
&+ \frac{b_2}{2}((\varepsilon_{22} + \varepsilon_{33})P_1^2 + (\varepsilon_{11} + \varepsilon_{33})P_2^2 + (\varepsilon_{11} + \varepsilon_{22})P_3^2) + \\
&+ b_3((\varepsilon_{12} + \varepsilon_{21})P_1P_2 + (\varepsilon_{13} + \varepsilon_{31})P_1P_3 + (\varepsilon_{23} + \varepsilon_{32})P_2P_3) + \\
&+ \left(\frac{g_1}{4}\varepsilon_{11} + \frac{g_2}{4}(\varepsilon_{22}\varepsilon_{33})\right)P_1^4 + \frac{g_3}{4}(\varepsilon_{12} + \varepsilon_{21})(P_1P_2^3 + P_2P_1^3) + \\
&+ \left(\frac{g_1}{4}\varepsilon_{22} + \frac{g_2}{4}(\varepsilon_{11}\varepsilon_{33})\right)P_2^4 + \frac{g_3}{4}(\varepsilon_{23} + \varepsilon_{32})(P_2P_3^3 + P_3P_2^3) + \\
&+ \left(\frac{g_1}{4}\varepsilon_{33} + \frac{g_2}{4}(\varepsilon_{11}\varepsilon_{22})\right)P_3^4 + \frac{g_3}{4}(\varepsilon_{13} + \varepsilon_{31})(P_1P_3^3 + P_3P_1^3). \tag{3.5}
\end{aligned}
$$

Here, the coefficients b_i take the role of the electromechanical coupling coefficients q_{ij} in the basic form of the free energy, whereas the three new coefficients g_i provide additional degrees of freedom. With a total of six electromechanical coefficients, the two spontaneous strains and three independent components of the piezoelectricity tensor can now be fitted independently – the system is even over-determined.

The described expansion of the elastic energy (f-terms) and the electromechanical coupling energy (g-terms) was first introduced in 2007 by Su and Landis [71] for a free energy function describing BaTiO$_3$. It works fine, provided that the components of the tetragonal elastic stiffness C_{ij}^{tetr} are greater than the respective components of the cubic elastic stiffness C_{ij}^{cub}: For instance, both C_{11}^{tetr} and C_{33}^{tetr} have to be greater than C_{11}^{cub}. If this is not the case and $C^{\text{cub}} > C^{\text{tetr}}$, the polarization-dependent elastic stiffness is a strictly monotonically decreasing function and will be zero for a certain critical polarization P_{crit}. This is illustrated in Figure 3.2a. For the critical polarization P_{crit}, the elastic stiffness vanishes, causing a divergence of the equilibrium strain and therefore a divergence of the free energy, as sketched below:

$$
\begin{aligned}
\Psi(P, \varepsilon) &= q(P)\varepsilon P^2 + C(P)\varepsilon^2 + F(P) \\
\sigma = \frac{\partial \Psi(P, \varepsilon)}{\partial \varepsilon} &= q(P)P^2 + 2C(P)\varepsilon \overset{!}{=} 0 \\
\Rightarrow \varepsilon^{\text{equil}}(P) &= \frac{-q(P)P^2}{2C(P)} \\
\Rightarrow \lim_{P \to P_{\text{crit}}} \varepsilon^{\text{equil}}(P) &= \infty \\
\Rightarrow \lim_{P \to P_{\text{crit}}} \Psi(P, \varepsilon^{\text{equil}}(P)) &= \infty
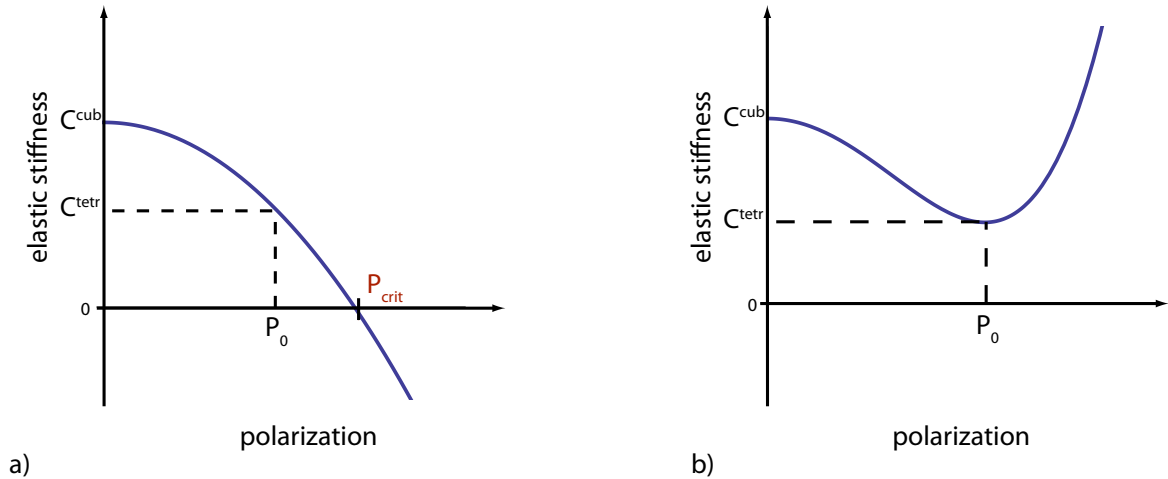\end{aligned}
$$

Figure 3.2.: (a) Considering the free energy expanded by the f-term, the polarization-dependent elastic stiffness is a monotonically decreasing function for $C^{\text{cub}} > C^{\text{tetr}}$ and will become zero for a certain polarization P_{crit}, causing a divergence of the free energy. Therefore, the f-term is not sufficient for the case $C^{\text{cub}} > C^{\text{tetr}}$. (b) By taking a further expansion of the elastic energy (h-term) into account, the polarization-dependent elastic stiffness remains positive for all polarizations while still enabling a separate adjustment of the elastic behavior in the cubic and the tetragonal phase for the case $C^{\text{cub}} > C^{\text{tetr}}$.

Although the system will always be near the spontaneous polarization state and will only vary in a range between $+P_0$ and $-P_0$ (e.g. in a domain wall), this divergence of the free energy causes an instability in the phase-field model and also makes an adjustment of the coefficients impossible. For the developement of their free energy describing BaTiO$_3$, Su and Landis [71] used a set of input elastic parameters that fulfill the condition $C^{\text{cub}} < C^{\text{tetr}}$. Hence, for BaTiO$_3$ the introduced f- and g-terms are sufficient to take tetragonal elastic behavior as well as an independent adjustment of the spontaneous strains and the piezoelectric coefficients into account. However, DFT predictions for PTO and PZT yield the set of elastic parameters presented in Table 3.1. Note that almost all tetragonal components of the elasticity tensor are smaller than the respective cubic components. Thus, for reasons discussed above, the expansion of the free

Table 3.1.: Elastic properties of the cubic and tetragonal phase for PTO and PZT resulting from first-principles DFT calculations performed by Marton and Elsässer [76]. These components of the elastic stiffness tensor are to be used as input parameters for adjusting the respective phase-field models.

		unit	$\hat{C}_{11}$	$\hat{C}_{12}$	$\hat{C}_{13}$	$\hat{C}_{33}$	$\hat{C}_{44}$	$\hat{C}_{66}$
PTO	DFT - cubic	[GPa]	342	131	131	342	108	108
	DFT - tetragonal	[GPa]	285	119	88	91	65	108
PZT	DFT - cubic	[GPa]	361	115	115	361	91	91
	DFT - tetragonal	[GPa]	327	110	107	178	73	92

energy consisting of the f-term and g-term is insufficient for PTO and PZT. Here, a solution for this problem is suggested by introducing a further expansion of the approach of the polarization-dependent elastic stiffness

$$C(P) = c_0 + fP^2 + hP^4, \tag{3.6}$$

consisting of the next higher symmetry compatible order and denoted h-term. Considering the tetragonal symmetry of the polarized state, this approach results in the following additional terms:

$$
\begin{aligned}
\psi_{\text{elast}}^{\text{h-term}}(\varepsilon_{ij}, P_i) &= \frac{h_1}{2}(\varepsilon_{11}^2 P_1^4 + \varepsilon_{22}^2 P_2^4 + \varepsilon_{33}^2 P_3^4) + \\
&+ \frac{h_2}{2}\left((\varepsilon_{22}^2\varepsilon_{33}^2)P_1^4 + (\varepsilon_{11}^2\varepsilon_{33}^2)P_2^4 + (\varepsilon_{11}^2\varepsilon_{22}^2)P_3^4\right) + \\
&+ h_3\left((\varepsilon_{11}\varepsilon_{22} + \varepsilon_{11}\varepsilon_{33})P_1^4 + (\varepsilon_{11}\varepsilon_{22} + \varepsilon_{22}\varepsilon_{33})P_2^4 + (\varepsilon_{11}\varepsilon_{33} + \varepsilon_{22}\varepsilon_{33})P_3^4\right) + \\
&+ h_4\left(\varepsilon_{22}\varepsilon_{33}P_1^4 + \varepsilon_{11}\varepsilon_{33}P_2^4 + \varepsilon_{11}\varepsilon_{22}P_3^4\right) + \\
&+ \frac{h_5}{2}((\varepsilon_{12}^2 + \varepsilon_{21}^2 + \varepsilon_{13}^2 + \varepsilon_{31}^2)P_1^4 + (\varepsilon_{12}^2 + \varepsilon_{21}^2 + \varepsilon_{23}^2 + \varepsilon_{32}^2)P_2^4 + \\
&+ (\varepsilon_{13}^2 + \varepsilon_{31}^2 + \varepsilon_{23}^2 + \varepsilon_{32}^2)P_3^4) + \\
&+ \frac{h_6}{2}((\varepsilon_{23}\varepsilon_{32})P_1^4 + (\varepsilon_{13}\varepsilon_{31})P_2^4 + (\varepsilon_{12}\varepsilon_{21})P_3^4.)
\end{aligned}
\tag{3.7}
$$

This extension has not appeared in previous literature. As illustrated in figure 3.2 b, the six additional coefficients h_i are employed to ensure that the polarization-dependent elastic stiffness $C(P)$ will not become zero and still has the required properties $C(P=0) = C^{\text{cub}}$ and $C(P=P_0) = C^{\text{tetr}}$ for describing both the elastic properties of the paraelectric cubic and the polarized tetragonal state.

Finally, the Landau energy term of the free energy is extended by introducing two polarization terms of eighth order for the purpose of improving the adjustment of the domain wall properties:

$$
\begin{aligned}
\psi_{\text{Landau}}^{\text{extended}}(P_i) &= \frac{a_1}{2}(P_1^2 + P_2^2 + P_3^2) + \frac{a_2}{4}(P_1^4 + P_2^4 + P_3^4) + \\
&+ \frac{a_3}{4}(P_1^2 P_2^2 + P_1^2 P_3^2 + P_2^2 P_3^2) + \frac{a_4}{6}(P_1^6 + P_2^6 + P_3^6) + \\
&+ \frac{a_5}{4}(P_1^4 P_2^4 + P_1^4 P_3^4 + P_2^4 P_3^4) + \frac{a_7}{6}(P_1^2 P_2^2 P_3^2) + \\
&+ \frac{a_6}{6}(P_1^4(P_2^2 + P_3^2) + P_2^4(P_1^2 + P_3^2) + P_3^4(P_1^2 + P_2^2)) + \\
&+ \frac{a_8}{2}(P_1^8 + P_2^8 + P_3^8).
\end{aligned}
\tag{3.8}
$$

Here, the a_8-term renders an additional degree of freedom for fitting the 180° domain wall properties, while the a_5-term only has an impact on the free energy's saddle point in $\langle 110 \rangle$ direction and therefore influences the 90° domain wall properties. The a_5-term was first introduced by

Zhang and Bhattacharya [85, 86] in order to allow for a independent adjustment of the dielectric properties and the $90°$ switching barrier in $BaTiO_3$. The two remaining parts of the free energy – the gradient energy ψ_{grad} (eqn. 1.66) and the electric field energy ψ_{elec} (eqn. 1.73) – are not modified. Therefore, the expanded total free energy is given as

$$\begin{aligned}
\Psi^{extended}(P_i, P_{i,j}, \varepsilon_{ij}, D_i) &= \psi_{grad}(P_{i,j}) + \psi_{Landau}^{extended}(P_i) + \psi_{coup}^{extended}(P_i, \varepsilon_{ij}) + \\
&+ \psi_{elast}^{extended}(\varepsilon_{ij}, P_i) + \psi_{elast}^{h-term}(\varepsilon_{ij}, P_i) + \psi_{elec}(P_i, D_i). \quad (3.9)
\end{aligned}$$

For reasons of clarity, the full form of this expanded free energy are provided in Appendix A.2. Proceeding in the same manner as in chapter 2, all coefficients of the extended form of the free energy will be identified in the following.

3.2. Sensitivity analysis for the expanded free energy

Due to the additional energy terms introduced in the last section, the number of coefficients has increased from 15 in the basic form of the free energy (eqn. 1.64) to 32 in its expanded form. Furthermore, the nonlinearity of the free energy function has grown significantly. In order to prepare the challenging adjustment process of these coefficients to results from atomistic calculations, their impact on the properties of the phase-field model has been investigated in a sensitivity analysis. Closely following the methodology demonstrated in section 2.2, the small signal parameters (piezoelectric, dielectric and elastic coefficients), the spontaneous parameters (P_0, $e_\parallel$ and $e_\perp$) as well as the domain wall properties were obtained from the expanded form of the free energy. Then, each coefficient of the free energy was separately increased by 10%, and the effect on the properties of the phase-field model was determined. Table 3.2 presents the results of this sensitivity analysis. The columns contain the physical properties of the phase-field model, whereas the rows represent the coefficient of the expanded free energy $\Psi^{extended}$. If the variation by 10% of a coefficient causes a change in one of the physical properties, the positive or negative magnitude of this change is indicated in per cent. Comparing Table 2.2 and Table 3.2 reveals a significant increase of the free energy's nonlinearity. While in the basic form of the free energy a 10% change of one coefficient caused at most a 12.6% reaction in one physical property (e.g. effect of coefficient α_{12} on d_{15}), the same variation of the coefficients of the expanded form of the free energy induces changes of up to 175% in the physical properties of the phase-field model (e.g. effect of coeffient a_8 on d_{33}). From the sensitivity study, also the benefit of the additional energy terms becomes apparent. With the f-terms and the h-terms, a completely tetragonal adjustment of the elastic properties can be achieved, since all six tetragonal components of the elasticity tensor can be varied independently. Furthermore, the g-term provides three additional degrees of freedom influencing all three independent components of the piezoelectricity tensor. As anticipated, the a_5 coefficient allows for an adjustment

Table 3.2.: Sensitivity analysis for all coefficients of the expanded form of the free energy Ψ^{extended}. Each coefficient (rows) is increased separately by 10%, and the impact of this change on the physical properties (columns) of the free energy is indicated in per cent. Due to the strong nonlinearity of the free energy, the effort of investigating the coefficients' influence on the domain wall properties has risen significantly, so that only those coefficients relevant for the adjustment of the domain wall properties have been investigated. The analysis is based on PTO input parameters (Table A.1).

	P_0	$e_\perp$	$e_\parallel$	κ_{11}	κ_{33}	C_{11}	C_{33}	C_{12}	C_{13}	C_{44}	C_{66}	d_{33}	d_{31}	d_{15}	ξ_{180}	γ_{180}	ξ_{90}	γ_{90}
a_1	1,3	5,9	3,6	4,7	1,4							-21,7	-16,2	-1,5	-3,0	7,1		
a_2	-0,5	-2,4	-1,5		-1,5							8,9	6,4	2,3	-0,3	0,2		
a_3				-3,5										-3,6			0,7	0,3
a_4	-2,3	-10,7	-7,1		-9,9							36,6	25,3	10,3	-0,3	-2,9		
a_5																	-1,5	-14,0
a_6				-12,5										-12,7				
a_8	-7,9	-52,6	-30,6		-32,9							175	118	61,1	2,2	-1,7		
b_1	1,9	19,7	15,3	4,5	-2,7							-31,3	-25,1	-4,4				
b_2	-1,2	-18,7	-7,6	1,4	-1,8							18,3	9,3	6,8				
b_3														11,2				
c_1	-7,0	-65,0	-49,6	-13,0	8,7	11,5	34,5					35,2	16,9	17,9				
c_2	2,3	47,9	24,8	8,2	-3,8			11,6	15,9			-31,8	-21,7	-2,2				
c_3										9,3	22,5			-18,6				
f_1	13,5	155	123	8,3	42,1			-49,1				-140	-117	-17,6				
f_2	0,2	4,6	1,8	2,5	1,4	-3,0						-1,1	2,6	1,4				
f_3	-2,1	-29,8	-15,0	-3,6	-5,7				-11,8			10,7	-6,9	5,7				
f_4	0,1	1,8	0,7	-0,2	0,5			-3,2				-0,4	1,0	-0,6				
f_5											-25,0			34,1				
f_6										0,7								
g_1	0,3	2,1	1,5	0,4	0,6							-3,2	-2,4	-0,7				
g_2	1,4	19,0	7,7	1,1	7,1							-15,1	-4,0	-4,9				
g_3														-0,9				
h_1	-6,1	-47,7	-37,3	-10,8	-12,0		24,5					0,8	-3,5	17,6				
h_2	-0,1	-2,2	-0,9	-0,1	-1,1	1,5						0,1	-2,1	0,5				
h_3	1,6	23,1	11,7	2,5	12,2				5,9			-6,0	6,5	-4,5				
h_4	-0,1	-0,9	-0,4	-0,1	-0,5			1,6					-0,9	0,2				
h_5											12,5			-11,3				
h_6										2,0								
G_{11}																	12,7	12,7
G_{12}																	-14,6	-14,6
G_{44}																	5,0	4,9

of the 90° domain wall properties while having no influence on any other material property, and the a_8 coefficient provides a further degree of freedom for fitting the 180° domain wall properties. It also becomes apparent that a direct adjustment of the spontaneous strains using the electromechancial coupling coefficients is no longer possible: While for the basic form of the free energy the spontaneous strains $e_\parallel$ and $e_\perp$ were linearly dependent on the electromechanical coupling coefficients Q_{11} and Q_{12}, this is no longer the case for the coefficients b_1 and b_2 of the expanded form of the free energy.

Concluding the sensitivity study, the basic structure of the adjustment process for the free energy coefficients as shown in section 2.3 can be retained, but has to be amended at several stages. In a first step, the c_i, f_i and h_i coefficients will be adjusted simultaneously to the cubic and tetragonal elastic properties. After that, the b_i and g_i coefficients are employed to adjust the spontaneous strains and the piezoelectric coefficients. Finally, the Landau energy coefficients a_i and the gradient energy coefficients G_{ij} are fitted to the dielectric and domain wall properties. In the following, this expanded adjustment process will be discussed in full detail.

3.3. Expanded adjustment process

Step 1: Cubic and tetragonal elastic properties In the same manner as in the adjustment process for the basic form of the free energy, the elasic energy part consisting of the c-, f- and h-terms is adjusted first. Considering the expanded form of the free energy Ψ^{extended}, the c-term is the only part that does not depend on the polarization. This part is of cubic symmetry, and since the free energy function has to be valid for both the cubic phase (with $P = 0$) and the spontaneous polarization state (with $P = P_0$), the coefficients c_1, c_2 and c_3 can directly be identified as the components of the high-symmetry phase elasticity tensor components C_{11}^{cub}, C_{12}^{cub} and C_{44}^{cub}, because all other (polarization-dependent) terms of the free energy vanish in the cubic phase. Therefore, the c_i coefficients can directly be adjusted using the three independent components of the cubic elasticity tensor from DFT calculations:

$$c_1 = \hat{C}_{11}^{\text{cub}}, \qquad c_2 = \hat{C}_{12}^{\text{cub}}, \qquad c_3 = \hat{C}_{44}^{\text{cub}}. \tag{3.10}$$

Next, the f-term and the h-term are adjusted in order to take tetragonal elastic behavior into account. From the sensitivity study (Table 3.2) it can be seen that the six f_i coefficients are suitable for adjusting the free energy to the six independent components of the tetragonal elasticity tensor. According to equation (2.3), the elastic stiffness C_{ij} can be computed analytically from the free energy. This yields the following linear set of equations, ensuring that the elastic stiffness C_{ij}^{tetr} of the spontaneously polarized state $P = P_0$ agrees with the DFT prediction $\hat{C}_{ij}^{\text{tetr}}$:

$$C_{11}^{\text{tetr}} = C_{22}^{\text{tetr}} = \frac{\partial^2}{\partial \varepsilon_{11}^2} \Psi^{\text{extended}}(P_3 = P_0) \overset{!}{=} \hat{C}_{11}^{\text{tetr}} \tag{3.11}$$

$$C_{33}^{\text{tetr}} = \frac{\partial^2}{\partial \varepsilon_{33}^2} \Psi^{\text{extended}}(P_3 = P_0) \quad \overset{!}{=} \quad \hat{C}_{33}^{\text{tetr}} \tag{3.12}$$

$$C_{12}^{\text{tetr}} = \frac{\partial^2}{\partial \varepsilon_{11} \partial \varepsilon_{22}} \Psi^{\text{extended}}(P_3 = P_0) \quad \overset{!}{=} \quad \hat{C}_{12}^{\text{tetr}} \tag{3.13}$$

$$C_{13}^{\text{tetr}} = C_{23}^{\text{tetr}} = \frac{\partial^2}{\partial \varepsilon_{11} \partial \varepsilon_{33}} \Psi^{\text{extended}}(P_3 = P_0) \quad \overset{!}{=} \quad \hat{C}_{13}^{\text{tetr}} \tag{3.14}$$

$$C_{44}^{\text{tetr}} = C_{55}^{\text{tetr}} = \frac{\partial^2}{\partial \varepsilon_{13}^2} \Psi^{\text{extended}}(P_3 = P_0) \quad \overset{!}{=} \quad \hat{C}_{44}^{\text{tetr}} \tag{3.15}$$

$$C_{66}^{\text{tetr}} = \frac{\partial^2}{\partial \varepsilon_{12}^2} \Psi^{\text{extended}}(P_3 = P_0) \quad \overset{!}{=} \quad \hat{C}_{66}^{\text{tetr}} \tag{3.16}$$

Finally, the remaining coefficients h_i have to be determined. These coefficients do not have an explicit physical meaning. Nevertheless, they can be justified because they ensure that the elastic stiffness, which depends on the polarization in the expanded form of the free energy, cannot become negative. The h_i coefficients have to be employed in the following cases:

$$
\begin{aligned}
h_1: &\quad \text{necessary if} \quad \hat{C}_{11}^{\text{cub}} > \hat{C}_{11}^{\text{tetr}} \\
h_2: &\quad \text{necessary if} \quad \hat{C}_{11}^{\text{cub}} > \hat{C}_{33}^{\text{tetr}} \\
h_3: &\quad \text{necessary if} \quad \hat{C}_{12}^{\text{cub}} > \hat{C}_{12}^{\text{tetr}} \\
h_4: &\quad \text{necessary if} \quad \hat{C}_{12}^{\text{cub}} > \hat{C}_{13}^{\text{tetr}} \\
h_5: &\quad \text{necessary if} \quad \hat{C}_{44}^{\text{cub}} > \hat{C}_{44}^{\text{tetr}} \\
h_6: &\quad \text{necessary if} \quad \hat{C}_{44}^{\text{cub}} > \hat{C}_{66}^{\text{tetr}}
\end{aligned}
$$

In the approach suggested here, the coefficients h_i are chosen in such a way that the polarization-dependent components of the elastic stiffness $C_{ij}^{\text{tetr}}(P)$ exhibit minima at the spontaneous polarization state $P = P_0$ (see also Figure 3.2 b). If all h_i coefficients are required, this yields a set of six linear equations

$$\frac{\partial C_{11}^{\text{tetr}}}{\partial P_3} = \frac{\partial^3}{\partial \varepsilon_{11}^2 \partial P_3} \Psi^{\text{extended}}(P_3 = P_0) \quad \overset{!}{=} \quad 0 \qquad (\text{if } h_1 \text{ required}) \tag{3.17}$$

$$\frac{\partial C_{33}^{\text{tetr}}}{\partial P_3} = \frac{\partial^3}{\partial \varepsilon_{33}^2 \partial P_3} \Psi^{\text{extended}}(P_3 = P_0) \quad \overset{!}{=} \quad 0 \qquad (\text{if } h_2 \text{ required}) \tag{3.18}$$

$$\frac{\partial C_{12}^{\text{tetr}}}{\partial P_3} = \frac{\partial^3}{\partial \varepsilon_{11} \partial \varepsilon_{22} \partial P_3} \Psi^{\text{extended}}(P_3 = P_0) \quad \overset{!}{=} \quad 0 \qquad (\text{if } h_3 \text{ required}) \tag{3.19}$$

$$\frac{\partial C_{13}^{\text{tetr}}}{\partial P_3} = \frac{\partial^3}{\partial \varepsilon_{11} \partial \varepsilon_{33} \partial P_3} \Psi^{\text{extended}}(P_3 = P_0) \quad \overset{!}{=} \quad 0 \qquad (\text{if } h_4 \text{ required}) \tag{3.20}$$

$$\frac{\partial C_{44}^{\text{tetr}}}{\partial P_3} = \frac{\partial^3}{\partial \varepsilon_{13}^2 \partial P_3} \Psi^{\text{extended}}(P_3 = P_0) \quad \overset{!}{=} \quad 0 \qquad (\text{if } h_5 \text{ required}) \tag{3.21}$$

$$\frac{\partial C_{66}^{\text{tetr}}}{\partial P_3} = \frac{\partial^3}{\partial \varepsilon_{12}^2 \partial P_3} \Psi^{\text{extended}}(P_3 = P_0) \;\overset{!}{=}\; 0 \qquad (\text{if } h_6 \text{ required}). \tag{3.22}$$

The six f_i coefficients as well as the six h_i coefficients can then be determined by solving the set of 12 linear equations (3.11-3.22). If one of the h_i coefficients is not required following the above-mentioned condition, it is set zero, and the respective linear equation from (3.17-3.22) is no longer regarded. In this way, the adjustment approach remains as general as possible and is also suitable for BaTiO$_3$, where the h-terms are not required at all [71]. Note that the way of adjusting the h_i coefficients was chosen arbitrarily: It is not necessary for the polarization-dependent components of the elastic stiffness $C_{ij}^{\text{tetr}}(P)$ to have minima at $P = P_0$. Any other analytical approach ensuring $C_{ij}^{\text{tetr}}(P)$ to remain greater than zero would also be possible.

Step 2: Electromechanical coupling energy terms Next, the b- and g-terms of the expanded free energy $\Psi^{\text{extended}}(P_i, P_{i,j}, \varepsilon_{ij}, D_i)$ are to be adjusted. Considering an equilibrium monodomain state polarized in $\langle 001 \rangle$ direction, the free energy can be reduced to the form $\Psi_{\text{mono}}^{\text{extended}}(P_3, \varepsilon_{11}, \varepsilon_{22}, \varepsilon_{33})$, and the equilibrium strains depending on polarization $\varepsilon_{ij}^{\text{equil}}(P_3)$ can be determined by solving the set of equations

$$\left. \begin{aligned} \frac{\partial}{\partial \varepsilon_{11}} \Psi_{\text{mono}}^{\text{extended}}(P_3, \varepsilon_{11}, \varepsilon_{22}, \varepsilon_{33}) = \sigma_{11} \overset{!}{=} 0 \\ \frac{\partial}{\partial \varepsilon_{22}} \Psi_{\text{mono}}^{\text{extended}}(P_3, \varepsilon_{11}, \varepsilon_{22}, \varepsilon_{33}) = \sigma_{22} \overset{!}{=} 0 \\ \frac{\partial}{\partial \varepsilon_{33}} \Psi_{\text{mono}}^{\text{extended}}(P_3, \varepsilon_{11}, \varepsilon_{22}, \varepsilon_{33}) = \sigma_{33} \overset{!}{=} 0 \end{aligned} \right\} \quad \begin{aligned} \varepsilon_{11}^{\text{equil}}(P_3) \\ \varepsilon_{22}^{\text{equil}}(P_3) \\ \varepsilon_{33}^{\text{equil}}(P_3). \end{aligned} \tag{3.23}$$

Then, the coefficients b_1 and b_2 can be computed from the equilibrium strains, which have to correspond to the spontaneous strains $\hat{e}_\perp$ and $\hat{e}_\parallel$ from DFT calculations for $P = P_0$:

$$\left. \begin{aligned} \varepsilon_{11}^{\text{equil}}(P_3 = P_0) \overset{!}{=} \hat{e}_\perp \\ \varepsilon_{33}^{\text{equil}}(P_3 = P_0) \overset{!}{=} \hat{e}_\parallel \end{aligned} \right\} \quad \begin{aligned} b_1(g_1, g_2) \\ b_2(g_1, g_2) \end{aligned} \tag{3.24}$$

The coefficients $b_1(g_1, g_2)$ and $b_2(g_1, g_2)$ depend on both g_1 and g_2. They ensure that the spontaneous strains $e_\perp$ and $e_\parallel$ encoded in the free energy hold for any arbitrary combination of g_1 and g_2, therefore decoupling the b-term and the g-term. Now the coefficients g_1 and g_2 can be adjusted using the piezoelectric coefficients d_{33} and d_{31}. From the sensitivity analysis (Table 2.2) it becomes apparent that the Landau coefficients a_i influence the piezoelectric coefficients d_{ij} significantly, while the coefficients g_1 and g_2 have an impact on P_0, κ_{11} and κ_{33}, which are in turn target parameters of the Landau coefficients. Therefore, an independent adjustment of P_0, κ_{11}, κ_{33}, d_{33} and d_{31} is not possible, making an iterative approach necessary. Before formulating the conditions for the Landau coefficients, g_1 and g_2 (as well as b_3 and g_3) can be set to any arbitrary values at this point.

Step 3: Landau energy term   The Landau coefficients a_i are determined closely following the adjustment method presented in section 2.3, and only minor extensions are necessary to take the additional a_5- and a_8-terms into account. Using the equilibrium energy function as defined in equation (2.10) as well as information on the spontaneous polarization $\hat{P}_0$ and the dielectric permittivities $\hat{\kappa}_{11}$ and $\hat{\kappa}_{33}$ from DFT calculations and SMP simulations yields the set of three equations

$$
\left.
\begin{aligned}
\frac{\partial}{\partial P_3}\Psi^{\text{equil}}(0,0,\hat{P}_0) &= 0 \\
\frac{\partial^2}{\partial P_3^2}\Psi^{\text{equil}}(0,0,\hat{P}_0) &= \frac{1}{\hat{\kappa}_{33}} \\
\frac{\partial^2}{\partial P_1^2}\Psi^{\text{equil}}(0,0,\hat{P}_0) &= \frac{1}{\hat{\kappa}_{11}}
\end{aligned}
\right\}
\begin{aligned}
&a_1(a_2,a_8) \\
&a_4(a_2,a_8) \\
&a_6(a_2,a_3,a_8),
\end{aligned}
\tag{3.25}
$$

which can be solved with respect to the Landau coefficients a_1, a_4 and a_6. As expected from the sensitivity analysis (Table 2.2), they are independent of a_5. The four remaining Landau coefficients a_2, a_3, a_5 and a_8 are now completely decoupled and are available for adjusting the 180° and 90° domain wall properties. However, the g-term has to be adjusted first to the piezoelectric coefficients $\hat{d}_{33}$, $\hat{d}_{31}$ and $\hat{d}_{15}$. Since all Landau coefficients are now determined or decoupled, arbitrary values for g_1 and g_2 can be chosen, and after repeating Step 3, the piezoelectric properties d_{33} and d_{31} of the free energy (obtained by eqn. 2.4) can be checked against the DFT prediction. This iterative approach has to be repeated until the free energys piezoelectric properties coincide with the DFT results. In principle, the g_1 and g_2 coefficients could be varied randomly in this approach until a matching set is found. However, caused by the high nonlinearity of the expanded form of the free energy, the computational effort for proceeding this way would be immense. Since it turned out that the piezoelectric properties d_{33} and d_{31} depend almost linearly on g_1 and g_2, an alternative approach has proven very useful: Both coefficients g_1 and g_2 are increased by a certain step width three times each, resulting in a (3x3) array of g_1/g_2 combinations. For each of these nine sets, the piezoelectric properties of the free energy are determined. Figure 3.3 shows the dependence of d_{33} and d_{31} on the coefficients g_1 and g_2. Calculating the mean slope and offset of the straight lines in Figure 3.3 by means of linear regression yields two linear equations for the piezoelectric coefficients $d_{33}(g_1,g_2)$ and $d_{31}(g_1,g_2)$. Together with the DFT prediction $\hat{d}_{33}$ and $\hat{d}_{31}$, these equations can be solved with respect to g_1 and g_2:

$$
\left.
\begin{aligned}
d_{33}(g_1,g_2) &\overset{!}{=} \hat{d}_{33} \\
d_{31}(g_1,g_2) &\overset{!}{=} \hat{d}_{31}
\end{aligned}
\right\}
\quad \Rightarrow g_1,\ g_2
\tag{3.26}
$$

At the same time, the remaining coefficients g_3 and b_3 can be determined: Since both these coefficients solely have an influence on d_{15}, the adjustment to the DFT prediction $\hat{d}_{15}$ is straight-
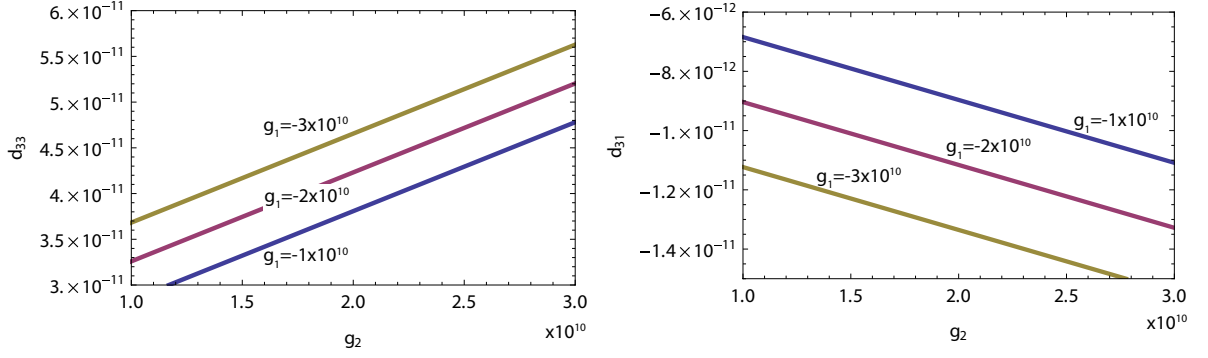
Figure 3.3.: Dependence of the piezoelectric properties d_{33} (left) and d_{31} (right) on the coefficients g_1 and g_2 for PTO input parameters. Both diagrams show the respective piezoelectric coefficient plotted versus the free energy coefficient g_2 for three different values of g_1.

forward. Theoretically, one of the coefficients can be chosen zero while the other one is tuned until $d_{15}(g_3, b_3)$ matches $\hat{d}_{15}$. Due to the significantly higher impact of b_3 compared to g_3 (see Table 2.2), in this work the coefficient b_3 was used for a rough approximation of d_{15}, while g_3 allowed for a fine tuning.

Step 4: Domain wall properties For the expanded form of the free energy (eqn. 3.9) containing polarization terms up to the 8th order, an analytical solution is available neither for the 180° nor for the 90° domain wall. Therefore, the domain wall properties have to be adjusted numerically, using the same procedure as discussed in sections 2.3 and 2.4.2. From the sensitivity analysis in Table 2.2 it becomes apparent that the coefficients a_2, a_8 and G_{44} can be used to adjust the properties of the 180° domain wall, whereas the coefficients a_3, a_5, G_{11} and G_{12} are available for adjusting the 90° domain wall properties. Although the system is under-determined, all additional energy coefficients are necessary in order to increase the range of accessible γ/ξ ratio as will be shown in section 3.4.2. Hence, the coefficients a_2, a_8 and G_{44} are varied iteratively until a set is found for which the 180° domain wall thickness ξ_{180} and energy γ_{180} of the phase-field model coincide with the respective predictions from atomistic calculations. Next, the coefficients a_3, a_5, G_{11} and G_{12} are adjusted in the same manner to the 90° domain wall thickness $\hat{\xi}_{90}$ and energy $\hat{\gamma}_{90}$ obtained from DFT calculations or SMP simulations. Finally, the Landau coefficient a_7 is chosen in such a way that the saddle points of the free energy in $\langle 110 \rangle$ and $\langle 111 \rangle$ crystal direction are on the same energetical level. Concluding the adjustment process of the expanded form of the free energy, Figure 3.4 illustrates its structure in a flow chart.
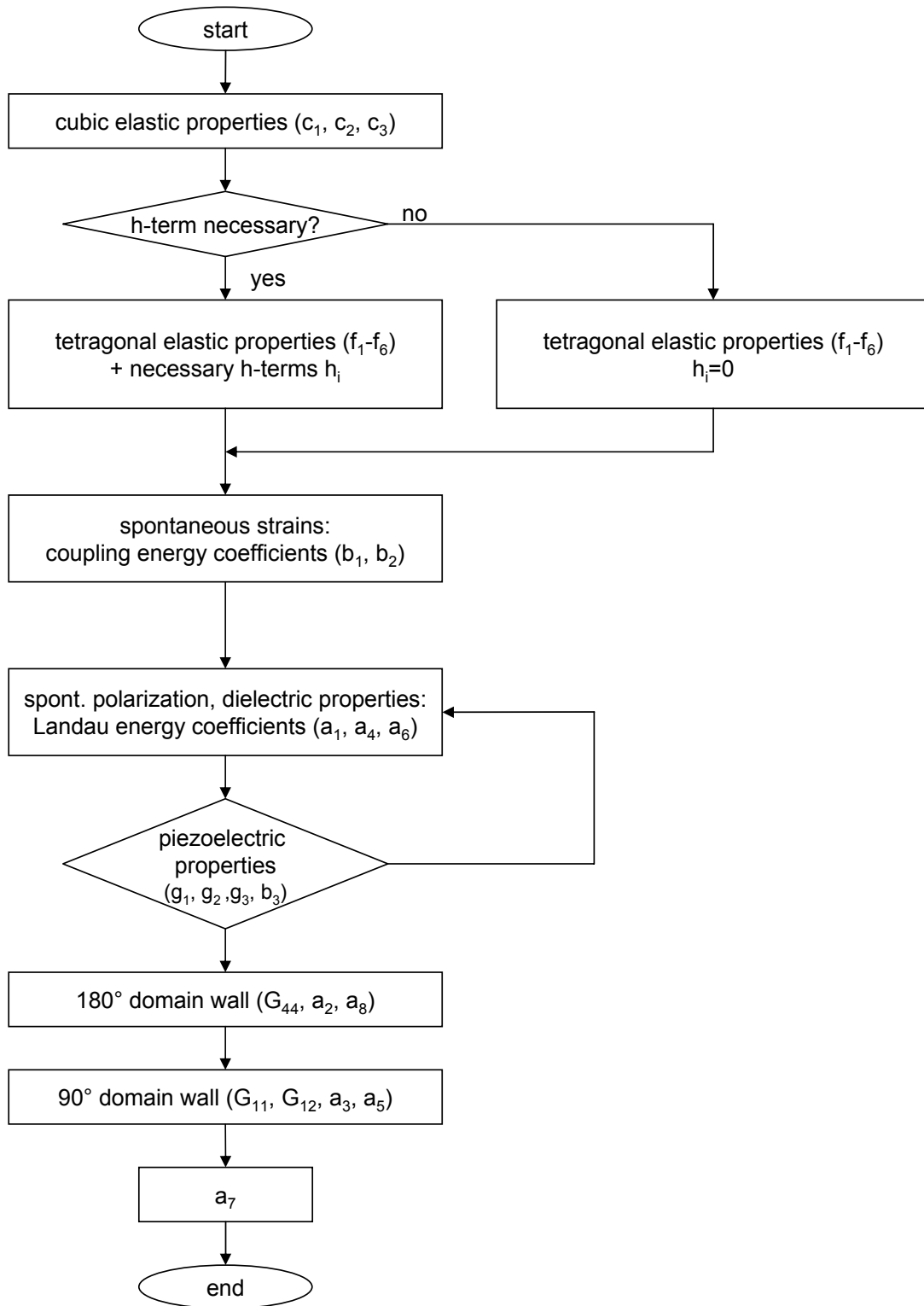
Figure 3.4.: Flow chart illustrating the structure of the adjustment process for the coefficients of the expanded form of the free energy.

3.4. Results and discussion

3.4.1. Application of the adjustment process for PTO and PZT

In order to determine the coefficients of the free energy in its expanded form, the improved adjustment process developed in the last section has been applied to input parameters of two materials: PTO and PZT. As before in section 2.4.1, DFT calculations and SMP simulations provided the necessary input parameters, shown in the left columns of Table 3.3. DFT calculations yielded all the intrinsic parameters: spontaneous polarization and strain, dielectric permittivities, piezoelectric coefficients, components of the cubic elastic stiffness tensor C_{ij}^{cub} and the now regarded components of the tetragonal stiffness tensor C_{ij}^{tetr}. In the case of PTO, all domain wall properties used in the adjustment process were obtained from DFT calculations[1], whereas for PZT the 180° domain wall properties stem from DFT calculations and the 90° domain wall properties from SMP simulations.

After applying the adjustment process to both sets of input parameters, the properties of the now adjusted free energy functions were computed as shown in the sensitivity study in section 2.2 in order to verify the adjustment process. The right columns of Table 3.3 show these properties for PTO and PZT in comparision with the input parameters from first-principles DFT calculations and SMP simulations. Finally, the 32 adjusted coefficients of the expanded form of the free energy for both PZT and PTO can be found in the appendix in Table A.1.

3.4.2. Discussion

When introducing the additional terms of the free energy discussed in section 3.1, the motivation was to find an improved form of the free energy that can also take tetragonal elastic behavior and the independent adjustment of the piezoelectric coefficients into account. The success of this approach becomes apparent from Table 3.3, comparing the atomistic target data and the properties of the adjusted phase-field models for PTO and PZT. For all intrinsic parameters, a full agreement between the atomistic input data and the adjusted free energy has been achieved. Compared to the adjustment process of the basic form of the free energy shown in Table 2.3, this represents a significant improvement. The benefit of the additional energy terms becomes clearly visible: A complete adjustment of the tetragonal elastic properties was accomplished as well as an independent adjustment of the spontaneous strains and all piezoelectric coefficients. Furthermore, the adjustment approach turned out powerful enough to ensure that also the spontaneous polarization, the dielectric permittivities and the elastic properties of the cubic high-temperature phase can be adjusted to match the DFT predictions exactly.

Aroused by the introduction of the 8th order polarization terms to the Landau energy, the range of adjustable γ/ξ (domain wall energy to domain wall thickness) ratio could be increased con-

---

[1]Since PTO-DFT can now be adjusted almost completely, the case of PTO-SMP is no longer considered.

Table 3.3.: Atomistic target data compared to the adjusted phase-field models for PTO and PZT. All input parameters for the phase-field models were obtained by Marton and Elsässer [76] using DFT calculations, with the exception of the 90° domain wall properties of PZT (marked with a † symbol), stemming from SMP simulations.

	unit	PTO		PZT	
		first-principles data (input)	phase-field model (adjusted)	first-principles data (input)	phase-field model (adjusted)
P_0	[C/m^2]	0.88	0.88	0.58	0.58
$\hat{a}_{\text{cub}}$	[Å]	3.8845	-	4.0119	-
$\hat{a}_{\text{tetr}}$	[Å]	3.8558	-	4.0047	-
$\hat{c}_{\text{tetr}}$	[Å]	4.0480	-	4.0602	-
$e_{\parallel}$		0.04209	0.04209	0.012039	0.012039
$e_{\perp}$		-0.007388	-0.007388	-0.0017946	-0.0017946
κ_{33}		$17\kappa_0$	$17\kappa_0$	$18\kappa_0$	$18\kappa_0$
κ_{11}		$54\kappa_0$	$54\kappa_0$	$76\kappa_0$	$76\kappa_0$
C_{11}^{cub}	[Pa]	342×10^9	342×10^9	361×10^9	361×10^9
C_{12}^{cub}	[Pa]	131×10^9	131×10^9	115×10^9	115×10^9
C_{44}^{cub}	[Pa]	108×10^9	108×10^9	91×10^9	91×10^9
C_{11}^{tetr}	[Pa]	285×10^9	285×10^9	327×10^9	327×10^9
C_{33}^{tetr}	[Pa]	91×10^9	91×10^9	178×10^9	178×10^9
C_{12}^{tetr}	[Pa]	119×10^9	119×10^9	110×10^9	110×10^9
C_{13}^{tetr}	[Pa]	88×10^9	88×10^9	107×10^9	107×10^9
C_{44}^{tetr}	[Pa]	65×10^9	65×10^9	73×10^9	73×10^9
C_{66}^{tetr}	[Pa]	108×10^9	108×10^9	92×10^9	92×10^9
d_{33}	[C/m]	2.46×10^{-11}	2.46×10^{-11}	1.57×10^{-11}	1.57×10^{-11}
d_{31}	[C/m]	-8.04×10^{-12}	-8.04×10^{-12}	-4.32×10^{-12}	-4.32×10^{-12}
d_{15}	[C/m]	1.72×10^{-11}	1.72×10^{-11}	1.53×10^{-12}	1.53×10^{-12}
γ_{180}	[mJ/m^2]	112	208	96	96
γ_{90}	[mJ/m^2]	24	24	$(36)^{\dagger}$	36
ξ_{180}	[m]	4.5×10^{-10}	4.5×10^{-10}	6.7×10^{-10}	6.7×10^{-10}
ξ_{90}	[m]	5.4×10^{-10}	5.4×10^{-10}	$(4.9 \times 10^{-10})^{\dagger}$	4.9×10^{-10}

siderably for both the 180° and the 90° domain wall, as can be seen from Figure 3.5: When adjusting the 90° domain wall properties, the Landau coefficient a_5 allows for phase-field models with a relatively high domain wall thickness and a small domain wall energy at the same time. This was required in particular to match the DFT predictions of the 90° domain wall properties for PTO, as illustrated in Figure 2.9 b. Note that the coefficient a_5 only influences the 90° domain wall properties and has no influence on any other system parameters at all. Therefore, the γ_{90}/ξ_{90} ratio in the complete lower part of Figure 3.5 b can be accessed, and the 90° domain wall properties for PTO (and also PZT) could be adjusted exactly to the DFT and SMP predictions.

In the case of the 180° domain wall, the additional Landau coefficient a_8 also allowed for the adjustment of the free energy to a broader range of γ_{180}/ξ_{180} ratio. The 180° domain wall properties of PZT could be fitted to results of DFT calculations without any problems. However, in the case of PTO even with the additional a_8 term the domain wall input parameters lie out-
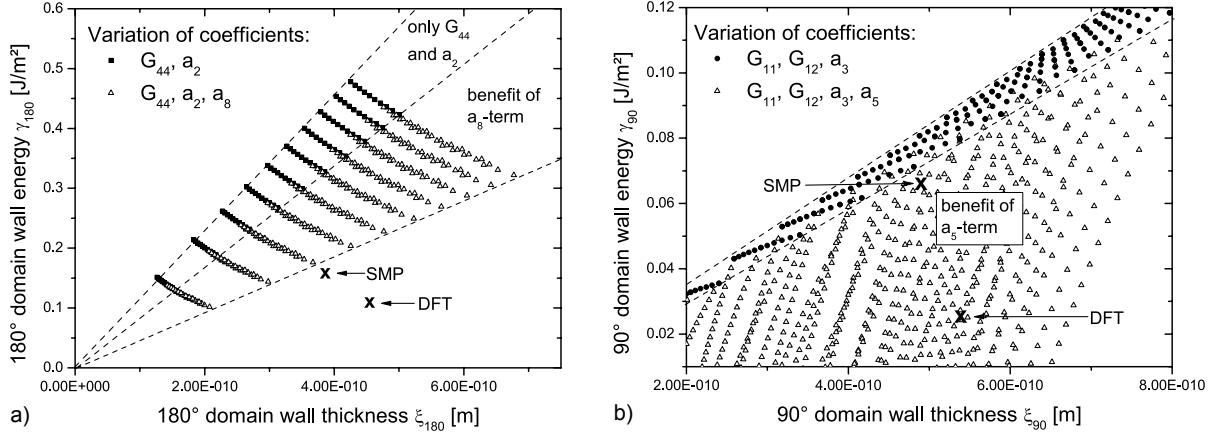
Figure 3.5.: Adjustment of the domain wall properties, exemplarily shown for PTO. In both cases, the mentioned coefficients of the free energy were varied and the respective domain wall thickness and energy calculated. The atomistic DFT and SMP predictions for the domain wall thickness and energy are marked in both diagrams (a) 180° domain wall properties: The benefit of the additional a_8-term in the Landau energy is evident. Nevertheless, for PTO the free energy could not be fitted exactly to the DFT or SMP predictions for $\hat{\gamma}_{180}$. (b) 90° domain wall properties: Caused by the additional a_5-term in the Landau energy, the complete range of γ_{90}/ξ_{90} in the lower part of the diagram can be accessed, so that the free energy could be fitted exactly to the atomistic DFT or SMP predictions.

side the accessible region of the γ_{180}/ξ_{180} ratio and can not be fitted exactly into the phase-field model. When comparing the domain wall adjustment of the basic form of the free energy (Figure 2.9) to that of the expanded form of the free energy (Figure 3.5) it can be seen that the additional terms evoke a shift of the accessible γ/ξ ratio. This shift is caused by the altered elastic behavior of the expanded form of the free energy, which in turn influences the domain wall properties. Introducing even higher order polarization terms, e.g. a 10th order polarization term in the Landau energy, would not solve this problem: The condition $a_1 > 0$ also has to be fulfilled, guaranteeing that the free energy has minima only at the spontaneous polarization states. Since a_1 already depends linearly on a_2 and a_8 (and would also depend on any additionally introduced higher order polarization term), a limit of adjusting the free energy has been reached here.

The success of the newly introduced h-term is illustrated in Figure 3.6. For the case of PTO, all six independent tetragonal components of the elastic stiffness $C_{ij}(P)$ are plotted versus the polarization. All polarization-dependent components of the elasticity tensor show minima for $P = P_0$, corresponding to the state of spontaneous polarization, and go towards positive infinity for big polarizations. The h-term prevents the elastic stiffness from becoming zero (given that $C^{\text{cub}} > C^{\text{tetr}}$, and C(P) is a strictly monotonically decreasing function of the polarization), which would cause a divergence of the free energy. Figure 3.6 also reveals that the expanded form of the free energy describes the elastic properties of both the high and the low symmetry ferroelectric phase: For instance, $C_{11}(P)$ and $C_{33}(P)$ coincide for $P = 0$, which corresponds

to the cubic high-symmetry phase, and show different values for $P = P_0$, as demanded in the tetragonal low-symmetry phase.
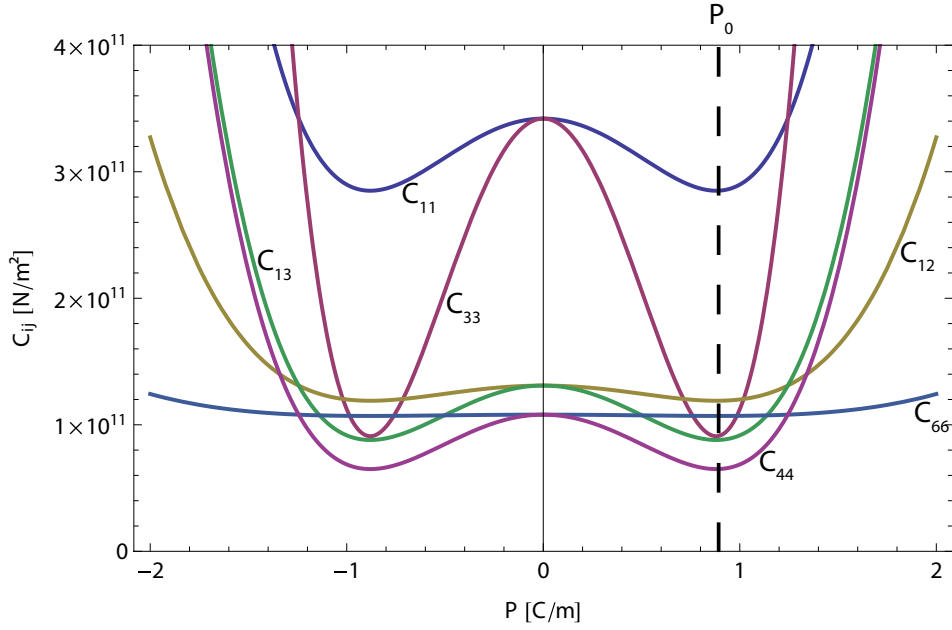
Figure 3.6.: In the expanded form of the free energy, the additional f- and h-terms induce a polarization-dependence of the components of the elastic stiffness tensor. For the case of the adjusted free energy of PTO, this polarization-dependence of all six independent components is shown here: As required, the elastic properties of the cubic and tetragonal phase are adjusted seperately, and all components of the elastic stiffness tensor cannot become zero because of the h-term.

The considerably higher non-linearity caused by the additional energy terms becomes obvious when plotting the polarization-dependent stress-free strains $\varepsilon_{11}(P)$ and $\varepsilon_{33}(P)$, computed as

$$\frac{\partial \Psi(P_i, \varepsilon_{ij},)}{\partial \varepsilon_{ij}} = \sigma_{ij}(P_i, \varepsilon_{ij}) \overset{!}{=} 0 \tag{3.27}$$

$$\Rightarrow \varepsilon_{ij}(P_i), \tag{3.28}$$

for both the basic form and the expanded form of the free energy. For the example of PZT, this is illutrated in Figure 3.7. The stress-free strains obtained from the basic form of the free energy exhibit a quadratic behavior (dashed lines), whereas the respective strains obtained from the expanded form of the free energy (solid lines) show a significantly non-linear behavior. This highly non-linear behavior can be explained when solving the set of equations (3.27) for the expanded form of the free energy. Assuming a one-dimensional configuration with a spontaneous polarization along the x_3-axis, the strains ε_{11} and ε_{33} take the schematic forms

$$\varepsilon_{11}(P_3) \propto P_3^2 \left(\frac{P_3^2 + P_3^4 + \cdots + P_3^{22}}{P_3^2 + P_3^4 + \cdots + P_3^{22}} \right) \quad \text{and} \quad \varepsilon_{33}(P_3) \propto P_3^2 \left(\frac{P_3^2 + P_3^4 + \cdots + P_3^{14}}{P_3^2 + P_3^4 + \cdots + P_3^{14}} \right), \tag{3.29}$$
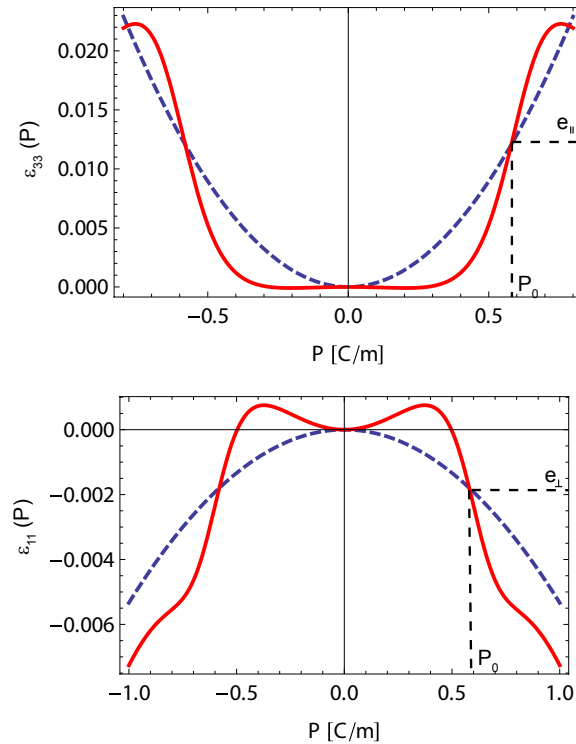
Figure 3.7.: Comparison of the polarization-dependent stress-free strains $\varepsilon_{11}(P)$ and $\varepsilon_{33}(P)$ calculated from the basic form (dashed lines) and the expanded form (solid lines) of the free energy. For the basic form, the strains show a quadratic behavior, whereas the strains obtained from the expanded form of the free energy exhibit a high non-linearity.

where all constant coefficients have been omitted for reasons of clarity and from which the highly non-linear behavior becomes cleary visible. These higher order polarization terms (up to the 22nd order!) make the adjustment process numerically very challenging. Note that for obtaining the equilibrium free energy needed to adjust the Landau coefficients as shown in (3.25), the stress-free strains are substituted in the expanded form of the free energy, causing polarization terms of even higher order. From the diagrams in Figure 3.7, also the spontaneous strains $e_{\parallel}$ and $e_{\perp}$ can be read for $P = P_0$. Here, the polarization-dependent strains of the basic and the expanded form of the free energy intersect as required.

Finally, plots of the adjusted free energy for PZT are shown in Figure 3.8. The notation is the same as in Figure 2.8 for the adjusted basic form of the free energy. In Figure 3.8 a, the expanded form of the free energy is plotted versus the polarization in different crystallographic directions. Compared to the respective plot of the basic form of the free energy in Figure 2.8, a much higher tetragonal behavior can be found. This also becomes apparent from the contour plots in Figure 3.8 b and c, showing the expanded form of the free energy in the [100] and the [110] planes, respectively. It can be explained by the fact that in the expanded form of the free energy the elastic behavior is fully tetragonal due to the f-term, while in the basic form of the free energy only cubic elastic behavior could be taken into account. Note that while developing

the adjustment method it has been found that the g-term, introduced to allow for an adjustment of the piezoelectric coefficients, only becomes effective when also the f-term is regarded in the free energy. In the abscense of the f-term, a non-vanishing g-term always leads to an instability of the free energy, since the free energy then tends towards negative infinity for big polarizations in any crystallographic direction. On the other hand, the f-term can exist without the g-term.
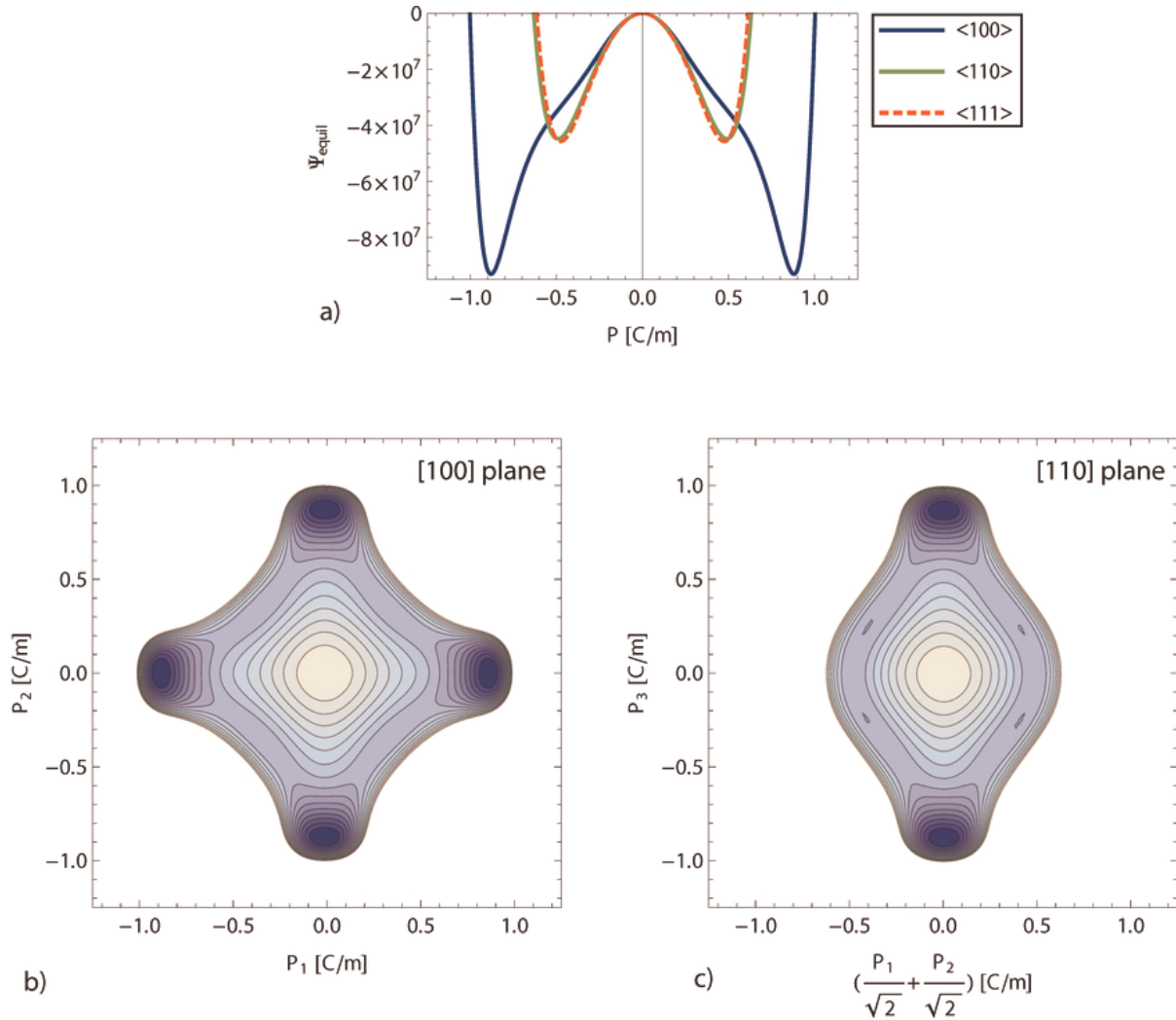
Figure 3.8.: Plots of adjusted free energy in the expanded form for PZT. (a) Free energy versus polarization for different crystallographic directions. The absolute minima in $\langle 100 \rangle$ direction define the tetragonal phase. (b) Contour plot of the free energy in the $[100]$ plane showing the four equivalent tetragonal minima in $\langle 100 \rangle$ direction. (c) Contour plot of the free energy in the $[110]$ plane.

Summarizing the expanded form of the free energy and the improved adjustment process discussed in this chapter, it can be found that the extensions of the free energy made it possible to fully take tetragonal elastic behavior into account and to adjust all piezoelectric coefficients independently from the spontaneous strains. It has been shown that the f- and g-terms, which were adopted from literature [71] for BaTiO$_3$, are not sufficient for describing the elastic properties

of PTO and PZT predicted from first-principles DFT calculations. Therefore, the free energy has been extended by a new energy term, denoted h-term, that has not appeared in literature before. Together with adding 8th order polarization terms to the Landau energy, the free energy for PZT could be adjusted to exactly match the atomistic target parameters used as input for the adjustment process. In the adjusted free energy of PTO, only the $180°$ domain wall energy could not be fitted exactly and was higher than the DFT prediction, while for all other adjusted intrinsic and extrinsic ferroelectric properties a full accordance with the DFT input parameters was achieved. Hence, the first interface in the multi-scale simulation chain for ferroelectrics has been successfully established.

However, the additional energy terms discussed in this chapter also significantly raise the numerical complexity of the phase-field model. Since the increased non-linearity of the phase-field model multiplies the numerical effort for solving the Ginzburg-Landau equation, the basic form of the adjusted free energy as discussed in chapter 2 will be used for the now following development of the second interface in the simulation chain between phase-field modeling and micromechanical modeling.

4. Interface between phase-field and micromechanical methods

In the previous chapters, the first interface of the knowledge based multi-scale simulation chain has successfully been developed, linking atomistic methods and phase-field modeling. In order to completely bridge the remaining gap between phase-field methods and micromechanical modeling, a second interface will be developed in the following, as illustrated in Figure 4.1:

nano-scale   **meso-scale**   **micro-scale**

atomistic methods   phase-field methods   micromechanical methods

knowledge based multi-scale simulation chain
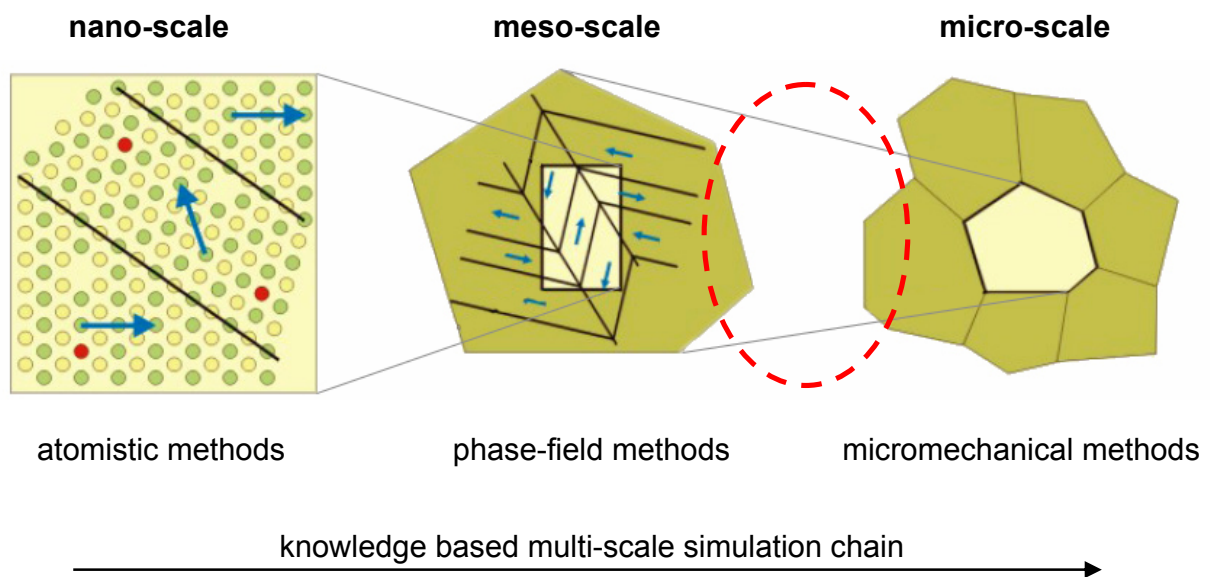
Figure 4.1.: In order to link phase-field and micromechanical methods within the knowledge based multi-scale simulation chain for ferroelectrics, a second interface has to be developed.

The concept of the second interface is to use phase-field simulations in order to analyse typical ferroelectric domain structures under electromechancial loading. These calculations are supposed to yield domain-effective material parameters, which can subsequently be used as input for micromechanical models. As described in chapter 2, the employed phase-field model has been adjusted to atomistic input parameters before, allowing for a completely knowledge based transfer of ferroelectric properties from the atomistic to the micromechanical level.

This chapter deals with the numeric implementation of the phase-field theory. Using the finite-element platform COMSOL Multiphysics, the governing equations of the phase-field method will be implemented in the weak formulation for one-, two-, and three-dimensional configurations. In order to enable the computation of bulk material behavior, periodic boundary conditions will also be implemented in COMSOL Multiphysics, as well as formulations to investigate

point defects and grain boundaries. The numeric implementation will be verified by calculating a domain configuration that also has an analytical solution, and comparing both. Finally, a mesh study for the finite-element mesh will be performed, showing the mesh densitiy necessary for investigating ferroelectric domain structures.

4.1. Finite-element implementation: Basic principles

4.1.1. Weak formulation of the phase-field theory

In order to solve the governing equations (1.1), (1.2), (1.50)-(1.55), (1.57), (1.60), (1.61), and (1.63) of the phase-field model numerically, the finite-element formulation introduced by Su and Landis [71] is used to implement the phase-field theory into the finite-element platform COMSOL Multiphysics. As for the conventional finite-element approach in electromechanics, the three components of the mechanical displacement u_i and the electric potential ϕ are choosen as nodal degrees of freedom [2]. Additionally, the three components of the polarization P_i, denoting the order parameter of the phase-field model, have to be taken into account, resulting in a total of seven degrees of freedom per node. From them, the strain components ε_{ij}, the polarization gradient components $P_{i,j}$ and the electric field components E_i can be derived, respectively. In this case, the constitutive equations have to take P_i, $P_{i,j}$, ε_{ij} and E_i as independent variables. However, since the Helmholtz free energy Ψ as introduced in equation (1.64) depends on P_i, $P_{i,j}$, ε_{ij} and D_i, a Legendre transformation has to be applied in order to replace D_i by E_i, yielding the electric enthalpy $\mathfrak{h}$:

$$
\begin{aligned}
\mathfrak{h}(P_i, P_{i,j}, \varepsilon_{ij}, E_i) &= \Psi(P_i, P_{i,j}, \varepsilon_{ij}, D_i) - E_i D_i = \\
&= \psi_{\text{Landau}}(P_i) + \psi_{\text{grad}}(P_{i,j}) + \psi_{\text{coup}}(P_i, \varepsilon_{ij}) + \psi_{\text{elast}}(\varepsilon_{ij}) - \frac{1}{2}\kappa_0 E_i E_i - E_i P_i.
\end{aligned}
\tag{4.1}
$$

From the electric enthalpy $\mathfrak{h}$, the stresses σ_{ij}, the dielectric displacements D_i and the micro-forces ξ_{ij} and η_i are computed by partial derivation with respect to the independent variables:

$$
\sigma_{ij} = \frac{\partial \mathfrak{h}}{\partial \varepsilon_{ij}}, \quad D_i = -\frac{\partial \mathfrak{h}}{\partial E_i}, \quad \xi_{ij} = \frac{\partial \mathfrak{h}}{\partial P_{i,j}}, \quad \text{and} \quad \eta_i = \frac{\partial \mathfrak{h}}{\partial P_i}.
\tag{4.2}
$$

Following the work of Su and Landis [71], the variational statement

$$
\begin{aligned}
\int_V \beta_{ij}\dot{P}_j \delta P_i \mathrm{d}V + \int_V \rho \ddot{u}_i \delta u_i \mathrm{d}V + \int_V \sigma_{ji}\delta\varepsilon_{ij} - D_i\delta E_i + \eta_i\delta P_i + \xi_{ji}\delta P_{i,j}\mathrm{d}V = \\
= \int_V b_i\delta u_i - q\delta\phi + \gamma_i\delta P_i\mathrm{d}V + \int_S t_i\delta u_i - \omega\delta\phi + \xi_{ji}n_j\delta P_i\mathrm{d}S
\end{aligned}
\tag{4.3}
$$

describes the governing phase-field equations in the weak formulation. This principle of virtual work builds the foundation of the finite-element implementation, where the nodal degrees of freedom u_i, P_i and ϕ are computed within the elements, and the state variables σ_{ij}, D_i, ξ_{ij} and η_i are derived using equations (4.1) and (4.2).

4.1.2. Implementation in COMSOL Multiphysics

The finite-element platform COMSOL Multiphysics provides the possibility of directly implementing finite-element problems in the so-called weak form. This mathematically weak formulation is more flexible than the strong partial differential equation (PDE) formulation of a specific problem. It is especially suited for solving strongly nonlinear models and takes the form of a variational principle under certain conditions. Therefore, equations derived from energy principles can be entered in a very compact and convenient form in COMSOL Multiphysics.

In a volume Ω confined by a boundary $\partial\Omega$, the general form of the weak formulation in COMSOL Multiphysics can be written as

$$
\begin{cases}
0 = \int_\Omega \left(\nabla v_l \Gamma_l + v_l \mathfrak{F}_l \right) \mathrm{d}V + \int_{\partial\Omega} v_l \mathfrak{G}_l \mathrm{d}A \\
0 = R_m \quad \text{on} \quad \partial\Omega,
\end{cases}
\tag{4.4}
$$

where v_l are arbitrary functions on Ω called test functions, and Γ_l, $\mathfrak{F}_l$, $\mathfrak{G}_l$ and R_m are functions of the dependent variables $\mathfrak{u}_l$, which in turn depend on the independent variables of the system. Here, functions $\mathfrak{u}_l$ are to be found that hold for all test functions v_l and satisfy the boundary condition $R_m = 0$ on $\partial\Omega$. If the energy of the considered system is given as an integral of some expression involving $\mathfrak{u}_l$, then the stationary condition of the solution, i.e. the state of lowest energy is precisely the weak formulation shown above. When comparing equation (4.4) with equation (4.3) it becomes obvious that the governing equations of the phase-field theory formulated in the form of a variational statement can directly be entered into the general formulation of the weak form in COMSOL Multiphysics. Provided that the system is stationary, i.e. $\dot{P}_i = 0$ and neglecting the inertia of the material, i.e. assuming mechanically quasi-static conditions $\ddot{u}_i = 0$, it can be seen that $\Gamma_l = 0$. Furthermore, the quantities σ_{ij}, D_i, η_i, ξ_{ij}, b_i, q and γ_i from equation (4.3) are directly identified as $\mathfrak{F}_l$ in equation (4.4), and the quantities t_i, ω and $\xi_{ij}n_i$ are identified as $\mathfrak{G}_l$.

The implementation in COMSOL Multiphysics is carried out in the following way: As discussed above, the nodal degrees of freedom `ux`, `uy`, `uz`, `Px`, `Py`, `Pz`, and `phi` are the components of the mechanical displacement u_i, the components of the polarization P_i and the electric potential ϕ, respectively. Partial derivatives in the COMSOL Multiphysics environment are described as follows: `uxx` denotes the derivative of `ux` with respect to the coordinate x, whereas `uxy` is the spatial derivative of `ux` with respect to the coordinate y. Then, as illustrated in Figure 4.2, the

volume terms of equation (4.4) can be entered into the weak edit field of Ω in the *Subdomain Settings* dialog box of COMSOL Multiphysics as

```
sigmaxx*test(uxx)+sigmayy*test(uyy)+...-Dx*test(-phix)-Dy*test(-phiy)-
...+etax*test(Px)+etay*test(Py)+...+xixx*test(Pxx)+xiyy*test(Pyy)+...,
```

where `sigmaxx`$= \sigma_{11}$, `sigmayy`$= \sigma_{22}$, `etax`$= \eta_1$, `etay`$= \eta_2$, `Dx`$= D_1$, `Dy`$= D_2$, `xixx`$= \xi_{11}$, `xiyy`$= \xi_{22}$ etc., and `test(..)` denotes the test functions depending on the nodal degrees of freedom. Additionally, all expressions $\mathfrak{F}_l$ have to be entered into the *Scalar Expressions* dialog box.
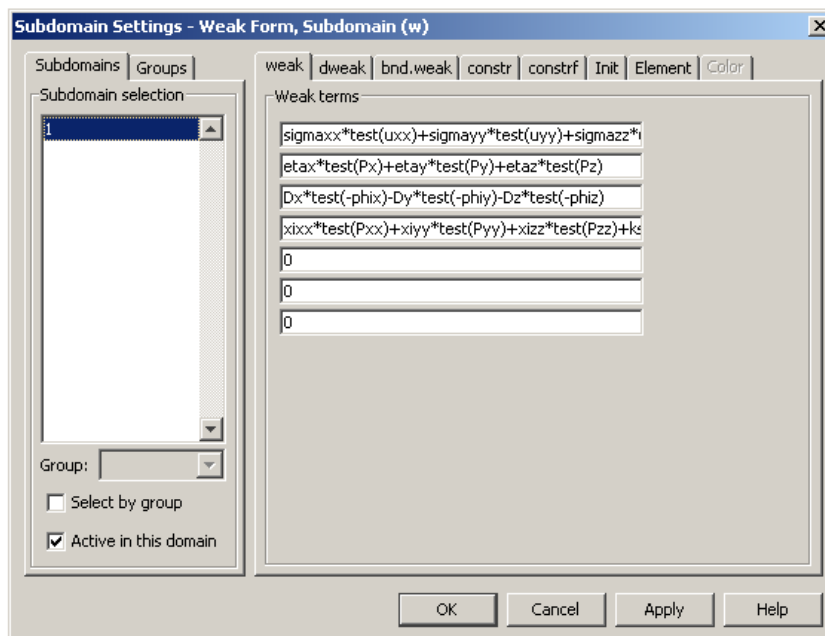
Figure 4.2.: Implementation of the weak formulation of the phase-field theory in COMSOL Multiphysics: entering the volume terms of equation (4.4) in the *Subdomain Settings* dialog box.

4.2. Boundary conditions

4.2.1. Weak and strong boundary constraints

The next step in the finite-element implementation of the phase-field theory is the definition of the boundary conditions. In a three-dimensional model, there are surface, edge and point boundaries present. However, for reasons of clarity a two-dimensional configuration will be considered in the following, containing only edge and point boundaries.

Two different kinds of boundary conditions can be distinguished: strong constraints, where the independent variables of the system, i.e. the nodal degrees of freedom are directly defined on the boundary, and weak constraints, where only $\mathfrak{G}_l$, i.e. functions of the dependent variables in equation (4.4) are defined on the boundary, while the independent variables remain free. In

Figure 4.3, these two types of boundary conditions and their implementation in COMSOL Multiphysics are shown exemplarily. Boundary conditions in COMSOL Multiphysics are entered
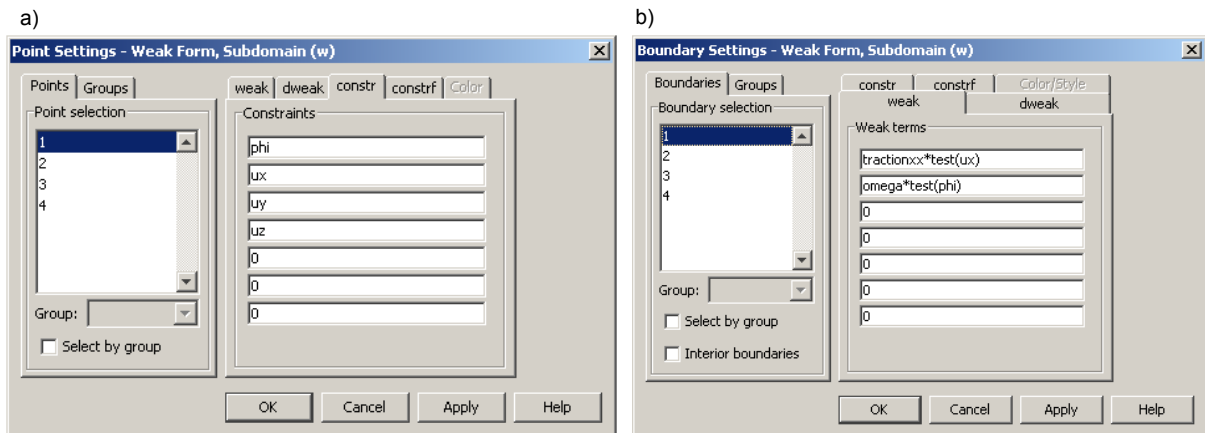
Figure 4.3.: Implementation of boundary conditions in COMSOL Multiphysics. (a) Strong constraints on a point boundary: The components of the mechanical displacements ux, uy, uz as well as the electric potential phi are set to zero using the *Point Settings* dialog box. (b) Weak boundary constraints applied to an edge boundary, entered in the *Boundary Settings* dialog box: surface traction tractionxx in x-direction and surface charge density omega.

in the form $0 = R_m$, where R_m can be a function of the dependent variables in the case of a weak constraint or the nodal degrees of freedom for a strong constraint. An example for strong boundary constraints on a point boundary in the model, e.g. a corner of the geometry, is shown in Figure 4.3 a: Here, the components of the mechanical displacements as well as the electric potential are set to zero on the selected point "1" in the *Point Settings* dialog box:

$$0=phi$$
$$0=ux$$
$$0=uy$$
$$0=uz$$

Such a boundary condition can for example be used for defining a reference point in the model. On the contrary, Figure 4.3 b shows an example of a weak boundary condition on an edge boundary of the model. Following eqn. (4.4), such boundary conditions can take external loading of the model into account, which are then to be entered in the *Boundary Settings* dialog box as weak terms, e.g.:

- traction t_x applied to surface "1" in x-direction: 0=tractionxx*test(ux)

- electric charges density ω on surface "1" : 0=omega*test(phi).

4.2.2. Periodic boundary conditions

In order to investigate the volume behavior (or bulk behavior) of a system, the application of so-called periodic boundary conditions is a common approach. By periodically replicating the simulation box in all considered space dimensions, a system of virtually infinite size without any surface is generated. This is especially useful when the investigated system is of small size and therefore the surface-to-volume ratio is big, so that the system without periodic boundary conditions would almost exclusively show a surface behavior. In general, periodic boundary conditions are applied for computing large systems, far away from any edges and edge effects. Hence, they allow for investigating the bulk part of a system with no surface present, and no knowledge of the surface is necessary. In the following, periodic boundary conditions for the mechanic displacements, the polarization and the electric potential as well as their implementation in COMSOL Multiphysics will be discussed in detail.

4.2.3. Electric periodic boundary conditions

Of course, periodic boundary conditions have to be applied for all considered nodal degrees of freedom. In Figure 4.4, the implementation of periodic boundary conditions is illustrated schematically for the electric potential ϕ as well as for the components of the polarization P_i. This two-dimensional example can be extended to higher or lower dimensions without loss of generality. The source boundary "1" is to be continued periodically by replicating it on the destination boundary "3" (and also the source boundary "2" on the destination boundary "4", respectively). Therefore, the value of the degrees of freedom P_x, P_y, P_z and ϕ on each source boundary node of the finite element mesh has to be copied to the respective node of the destination boundary.

In COMSOL Multiphysics this can be realized by using the *Periodic Boundary Conditions* dialog box: For each nodal degree of freedom, a constraint name is defined on the source boundary. In the next step, this constraint is linked to the respective degree of freedom on the destination boundary. Finally, the start and end vertices both on the source and destination boundary are appointed to ensure the direction of rotation in which the periodic continuation is applied and the boundaries are linked. This option would also allow for introducing a point symmetry into the model. By adding the offsets V_i to the electric potential between the source and the destination boundary, an electric voltage V_i and therefore an electric field can be applied to the periodically continued model.

4.2.4. Mechanical periodic boundary conditions

As the simulation box is allowed to deform, periodic boundary conditions for the components of the mechanical displacement u_i ensure a form closure between adjacent simulation boxes
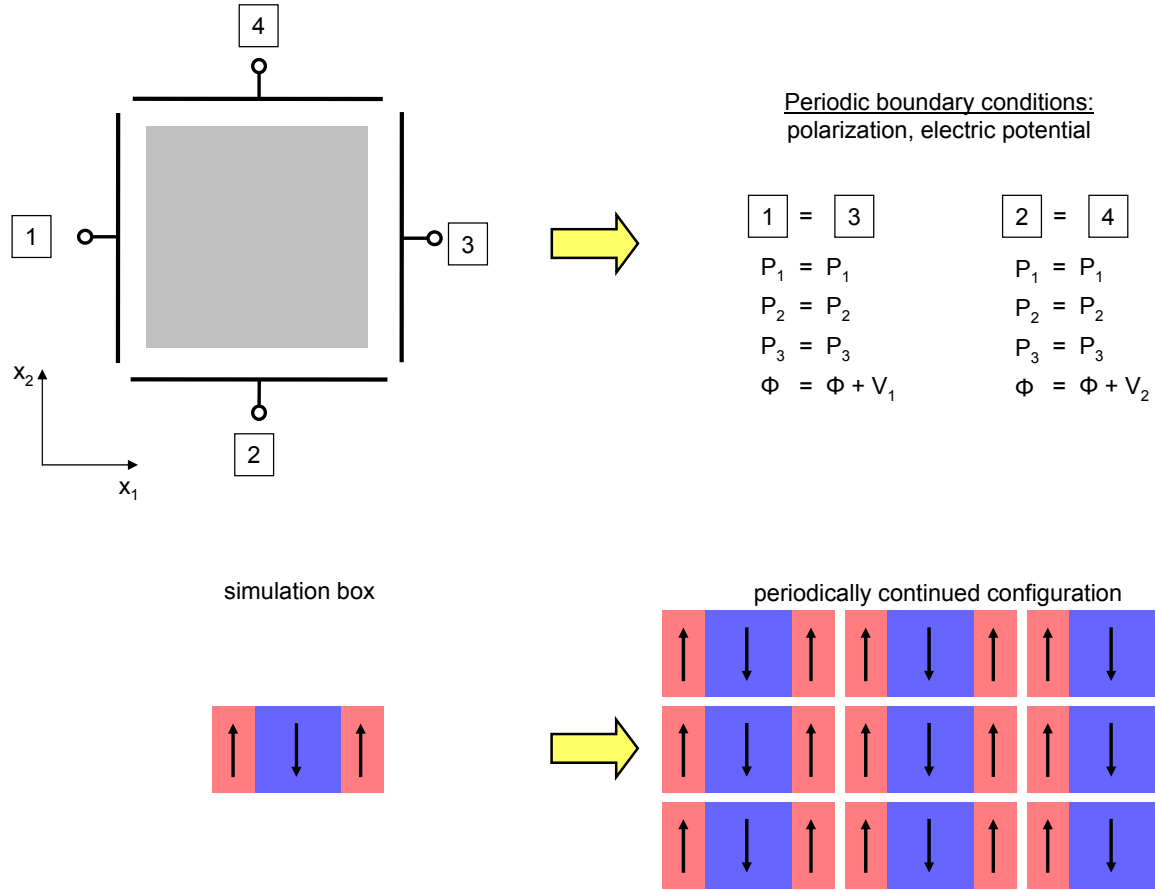
Figure 4.4.: Schematic illustration of the periodic boundary conditions for the components of the polarization P_i and the electric potential ϕ.

of the periodically continued configuration. Since the mechanical displacements are obtained from summing up the mechanical strains over the size of the simulation box, the components of the mechanical displacements cannot be replicated on the boundary to be continued, as shown above for the electric potential and the components of the polarization. In Figure 4.5, the basic principles of the implementation of periodic boundary conditions for the mechanical displacements u_i are illustrated schematically. In a first step, a reference node on the source boundary located at an arbitrary position $x_i^{\text{ref,scr}}$ as well as a reference node located at $x_i^{\text{ref,dst}}$ on the destination boundary are defined. The components of the mechanical displacement on these nodes are $u_i^{\text{ref,src}}(x_i^{\text{ref,src}})$ for the node on the source boundary and $u_i^{\text{ref,dst}}(x_i^{\text{ref,dst}})$ for the node on the destination boundary. The distance between the two nodes is $\Delta\Theta_i = x_i^{\text{ref,dst}} - x_i^{\text{ref,src}}$. Then, the strain

$$\tilde{S}_{ij} = \frac{u_i^{\text{ref,dst}}(x_i^{\text{ref,dst}}) - u_i^{\text{ref,src}}(x_i^{\text{ref,src}})}{\Delta\Theta_j} \tag{4.5}$$
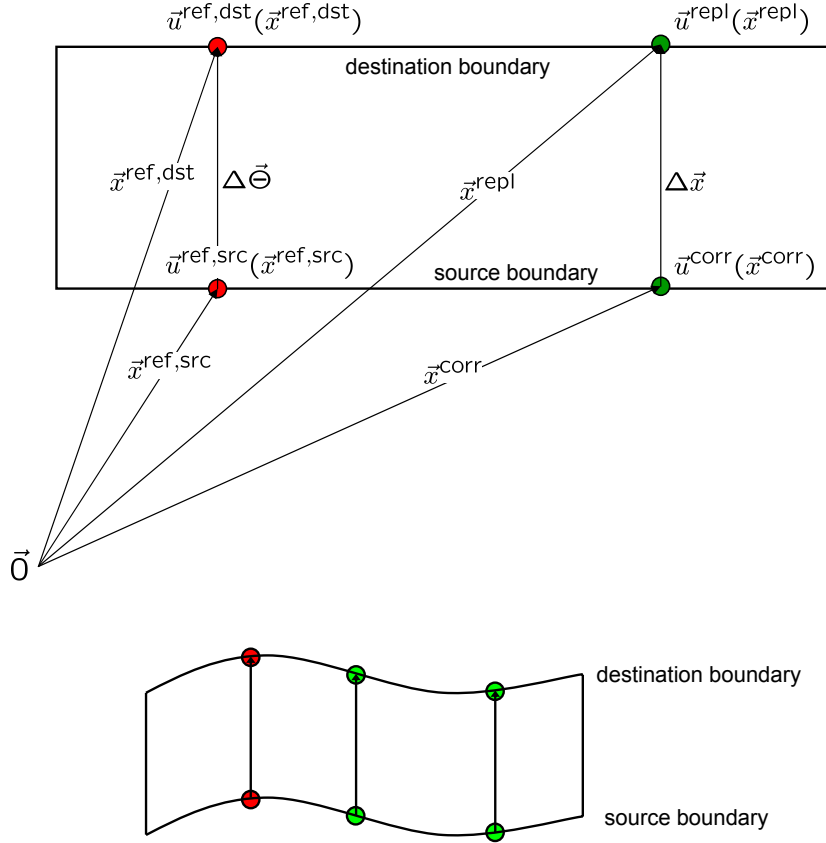
Figure 4.5.: Implementation of periodic boundary conditions for the components of the mechanical displacements u_i. Once the source and destination boundary are connected, the boundaries are allowed to deform while still ensuring form closure between adjacent simulation boxes, as illustrated schematically in the lower part of the figure.

between the reference node on the source boundary and the reference node on the destination boundary can be calculated. In order to mechancially connect all remaining nodes on the destination boundary to their corresponding nodes on the source boundary, the following relation is applied:

$$u_i^{\text{repl}}(x_i^{\text{repl}}) = u_i^{\text{corr}}(x_i^{\text{corr}}) + \tilde{S}_{ij}\Delta x_j. \tag{4.6}$$

Here, $u_i^{\text{repl}}(x_i^{\text{repl}})$ are the replicated components of the mechanical displacement on the destination boundary, $u_i^{\text{corr}}(x_i^{\text{corr}})$ are the corresponding components of the mechancial displacement on the source boundary, and $\Delta x_i = x_i^{\text{repl}} - x_i^{\text{corr}}$ is the distance between the pair of nodes that is to be linked. Hence, for each of the linked node pairs, the mechanical displacement of the replicated node on the destination boundary is obtained by taking the mechanical displacement of the node on the source boundary and adding a global displacement $\tilde{S}_{ij}\Delta x_j$. Therefore, the boundary problem has been decreased to one remaining degree of freedom, which is the global

strain $\tilde{S}_{ij}$ between the source and destination boundaries.

The only problem of this approach is that the reference node pair allegorizes distinguished points in the periodically continued system. While this does not matter when a completely homogeneous polarization state is considered, problems arise once the domain state is inhomogeneous and contains domain walls. If the position of a domain wall randomly coincides with the locations $x_i^{\mathrm{ref,scr}}$ or $x_i^{\mathrm{ref,dst}}$ of the reference nodes on the source or destination boundary, the local mechanical strains within the domain wall are projected in the form of a global strain $\tilde{S}_{ij}$ on all other boundary nodes, resulting in a divergence of the calculation. An appropriate way of avoiding this problem is to define the global strain $\tilde{S}_{ij}$ in a more general way. Instead of choosing a pair of reference nodes on the source and destination boundaries that is subsequently used to calculate the global strain, the mean mechanical displacements $\langle u_i^{\mathrm{src}} \rangle$ and $\langle u_i^{\mathrm{dst}} \rangle$ on the source and destination boundary are computed by averaging the components of the mechanical displacement on all boundary nodes. After that, a mean strain

$$\langle \tilde{S}_{ij} \rangle = \frac{\langle u_i^{\mathrm{dst}} \rangle - \langle u_i^{\mathrm{src}} \rangle}{\langle \Delta \Theta_j \rangle} \tag{4.7}$$

is defined with $\langle \Theta_i \rangle$ being the mean distance between source and destination boundary. Subsequently this global strain is applied in a similar manner as shown in eqn. (4.6) in order to link the nodes on the source and destination boundaries periodically:

$$u_i^{\mathrm{repl}}(x_i^{\mathrm{repl}}) = u_i^{\mathrm{corr}}(x_i^{\mathrm{corr}}) + \langle \tilde{S}_{ij} \rangle \Delta x_j. \tag{4.8}$$

In COMSOL Multiphysics this can be realized by integrating the components of the mechanical displacements using *Boundary Integration Coupling Variables*: For all boundaries that are to be continued periodically, the components of the mechanical displacements u_i are integrated and divided by the length of the respective boundaries, yielding mean mechanical displacements $\langle u_i \rangle$ of all boundaries. These mean mechanical displacements are then taken to compute the mean strains in the *Global Expressions* environment as shown in eqn. (4.7). Finally, source and destination boundaries are connected using the *Periodic Boundary Conditions* dialog box following eqn. (4.8). Summarizing the implementation of periodic boundary conditions, Figure 4.6 shows a deformation plot of a periodically continued domain configuration. A form closure between adjacent simulation boxes as well as a periodically continued domain pattern have been achieved.

4.3. Different orientations: rotation of energy function

Within the FE-implementation of the phase-field theory, the crystallographic orientation of the considered model is determined by the free energy used, strictly speaking by the direction of the
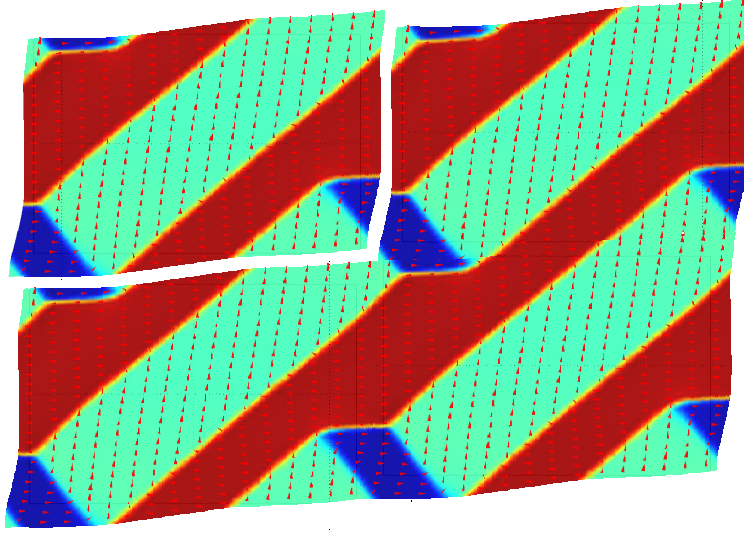
Figure 4.6.: Periodically continued domain configuration: the deformation illustrates the mechancial displacements u_i whereas both the color coding and the arrows depict the polarization P_i.

free energy's minima that define the spontaneously polarized state. For the energy function as shown in eqn. (4.1), the spontaneous polarization is oriented along the $\langle 100 \rangle$ axes, and therefore the crystallographic orientation coincides with the coordinate system of the simulation box in COMSOL Multiphysics.

In order to investigate e.g. grain boundaries or pure $90°$ domain wall systems using periodic boundary conditions, it has to be possible to vary the crystallographic orientation of the model with respect to the orientation of the COMSOL Multiphysics simulation box, or that the simulation box contains several subdomains of different crystallographic orientation. For this reason, the employed free energy containing all material information in the phase-field model has to be rotated spatially. This is shown in the approach below.

Two coordinate systems are considered in the following, as illustrated in Figure 4.7: In the crystallographic coordinate system $(x_1^{\mathrm{crys}}, x_2^{\mathrm{crys}}, x_3^{\mathrm{crys}})$, the electric enthalpy used for the FE-implementation is denoted $\mathfrak{h}^{\mathrm{crys}}(P_i^{\mathrm{crys}}, P_{i,j}^{\mathrm{crys}}, \varepsilon_{ij}^{\mathrm{crys}}, E_i^{\mathrm{crys}})$. The independent variables are the components of the polarization P_i^{crys}, the gradient of the polarization $P_{i,j}^{\mathrm{crys}}$, the mechanical strains $\varepsilon_{ij}^{\mathrm{crys}}$ and the electric field E_i^{crys}, whereas the dependent variables are the components of the mechanical stresses $\sigma_{ij}^{\mathrm{crys}}$, the dielectric displacement D_i^{crys} as well as the microforces η_i^{crys} and ξ_{ij}^{crys}. In the coordinate system of the simulation box in COMSOL Multiphysics $(x_1^{\mathrm{coms}}, x_2^{\mathrm{coms}}, x_3^{\mathrm{coms}})$ – referred to as COMSOL coordinate system – all quantities are denoted in like manner.

In a first step, the rotation matrix is to be chosen. Throughout this work, only rotations around
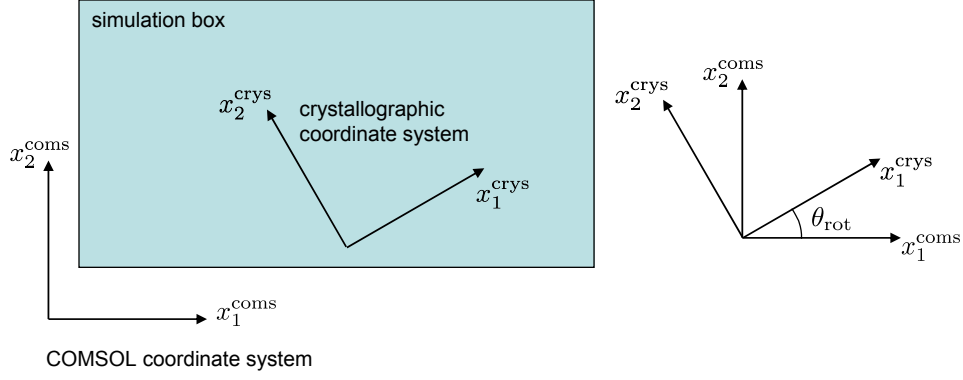
Figure 4.7.: Illustration of the two considered coordinate systems: the crystallographic coordinate system $(x_1^{\text{crys}}, x_2^{\text{crys}}, x_3^{\text{crys}})$ and the COMSOL coordinate system $(x_1^{\text{coms}}, x_2^{\text{coms}}, x_3^{\text{coms}})$.

the x_3 axis will be performed. Therefore, the rotation matrix

$$M_{ij}^{\text{coms}\rightarrow\text{crys}}(\theta_{\text{rot}}) = \begin{pmatrix} \cos(\theta_{\text{rot}}) & -\sin(\theta_{\text{rot}}) & 0 \\ \sin(\theta_{\text{rot}}) & \cos(\theta_{\text{rot}}) & 0 \\ 0 & 0 & 1 \end{pmatrix} \tag{4.9}$$

is sufficient, rotating points and vectors from the COMSOL coordinate system to the crystallographic coordinate system counterclockwise in the x_1-x_2 plane through an angle θ_{rot}.

In the crystallographic coordinate system, the dependent variables can be obtained by partial derivation of the electric enthalpy with respect to the independent variables, and in general the dependent variables are functions of all independent variables:

$$\eta_i^{\text{crys}}(P_i^{\text{crys}}, P_{i,j}^{\text{crys}}, \varepsilon_{ij}^{\text{crys}}, E_i^{\text{crys}}) = \frac{\partial \mathfrak{h}^{\text{crys}}(P_i^{\text{crys}}, P_{i,j}^{\text{crys}}, \varepsilon_{ij}^{\text{crys}}, E_i^{\text{crys}})}{\partial P_i^{\text{crys}}} \tag{4.10}$$

$$\xi_{ij}^{\text{crys}}(P_i^{\text{crys}}, P_{i,j}^{\text{crys}}, \varepsilon_{ij}^{\text{crys}}, E_i^{\text{crys}}) = \frac{\partial \mathfrak{h}^{\text{crys}}(P_i^{\text{crys}}, P_{i,j}^{\text{crys}}, \varepsilon_{ij}^{\text{crys}}, E_i^{\text{crys}})}{\partial P_{i,j}^{\text{crys}}} \tag{4.11}$$

$$\sigma_{ij}^{\text{crys}}(P_i^{\text{crys}}, P_{i,j}^{\text{crys}}, \varepsilon_{ij}^{\text{crys}}, E_i^{\text{crys}}) = \frac{\partial \mathfrak{h}^{\text{crys}}(P_i^{\text{crys}}, P_{i,j}^{\text{crys}}, \varepsilon_{ij}^{\text{crys}}, E_i^{\text{crys}})}{\partial \varepsilon_{ij}^{\text{crys}}} \tag{4.12}$$

$$D_i^{\text{crys}}(P_i^{\text{crys}}, P_{i,j}^{\text{crys}}, \varepsilon_{ij}^{\text{crys}}, E_i^{\text{crys}}) = -\frac{\partial \mathfrak{h}^{\text{crys}}(P_i^{\text{crys}}, P_{i,j}^{\text{crys}}, \varepsilon_{ij}^{\text{crys}}, E_i^{\text{crys}})}{\partial E_i^{\text{crys}}}. \tag{4.13}$$

Then, the independent variables in the crystallographic coordinate system can be expressed in terms of the independent variables in the COMSOL coordinate system by performing the rotation operations

$$P_j^{\text{crys}}(P_i^{\text{coms}}) = M_{ij}^{\text{coms}\rightarrow\text{crys}}(\theta_{\text{rot}}) \cdot P_i^{\text{coms}} \tag{4.14}$$

$$P_{k,l}^{\text{crys}}(P_{i,j}^{\text{coms}}) = M_{ki}^{\text{coms}\to\text{crys}}(\theta_{\text{rot}}) \cdot M_{lj}^{\text{coms}\to\text{crys}}(\theta_{\text{rot}}) \cdot P_{i,j}^{\text{coms}} \tag{4.15}$$

$$\varepsilon_{kl}^{\text{crys}}(\varepsilon_{ij}^{\text{coms}}) = M_{ki}^{\text{coms}\to\text{crys}}(\theta_{\text{rot}}) \cdot M_{lj}^{\text{coms}\to\text{crys}}(\theta_{\text{rot}}) \cdot \varepsilon_{ij}^{\text{coms}} \tag{4.16}$$

$$E_{j}^{\text{crys}}(E_{i}^{\text{coms}}) = M_{ij}^{\text{coms}\to\text{crys}}(\theta_{\text{rot}}) \cdot E_{i}^{\text{coms}}. \tag{4.17}$$

Substituting the independent variables in equations (4.10-4.13) with the expressions from (4.14-4.17) yields a set of dependent variables in the crystallographic coordinate system that depend on the independent variables expressed in the COMSOL coordinate system:

$$\eta_{i}^{\text{crys}}(P_{i}^{\text{coms}}, P_{i,j}^{\text{coms}}, \varepsilon_{ij}^{\text{coms}}, E_{i}^{\text{coms}}) \tag{4.18}$$

$$\xi_{ij}^{\text{crys}}(P_{i}^{\text{coms}}, P_{i,j}^{\text{coms}}, \varepsilon_{ij}^{\text{coms}}, E_{i}^{\text{coms}}) \tag{4.19}$$

$$\sigma_{ij}^{\text{crys}}(P_{i}^{\text{coms}}, P_{i,j}^{\text{coms}}, \varepsilon_{ij}^{\text{coms}}, E_{i}^{\text{coms}}) \tag{4.20}$$

$$D_{i}^{\text{crys}}(P_{i}^{\text{coms}}, P_{i,j}^{\text{coms}}, \varepsilon_{ij}^{\text{coms}}, E_{i}^{\text{coms}}). \tag{4.21}$$

Finally, the dependent variables in the COMSOL coordinate system can be computed by performing a rotation operation on the dependent variables in the crystallographic coordinate system depending on the independent variables in the COMSOL coordinate system:

$$\eta_{j}^{\text{coms}} = M_{ij}^{\text{coms}\to\text{crys}}(\theta_{\text{rot}}) \cdot \eta_{i}^{\text{crys}}(P_{i}^{\text{coms}}, P_{i,j}^{\text{coms}}, \varepsilon_{ij}^{\text{coms}}, E_{i}^{\text{coms}}) \tag{4.22}$$

$$\xi_{kl}^{\text{coms}} = M_{ki}^{\text{coms}\to\text{crys}}(\theta_{\text{rot}}) \cdot M_{lj}^{\text{coms}\to\text{crys}}(\theta_{\text{rot}}) \cdot \xi_{ij}^{\text{crys}}(P_{i}^{\text{coms}}, P_{i,j}^{\text{coms}}, \varepsilon_{ij}^{\text{coms}}, E_{i}^{\text{coms}}) \tag{4.23}$$

$$\sigma_{kl}^{\text{coms}} = M_{ki}^{\text{coms}\to\text{crys}}(\theta_{\text{rot}}) \cdot M_{lj}^{\text{coms}\to\text{crys}}(\theta_{\text{rot}}) \cdot \sigma_{ij}^{\text{crys}}(P_{i}^{\text{coms}}, P_{i,j}^{\text{coms}}, \varepsilon_{ij}^{\text{coms}}, E_{i}^{\text{coms}}) \tag{4.24}$$

$$D_{j}^{\text{coms}} = M_{ij}^{\text{coms}\to\text{crys}}(\theta_{\text{rot}}) \cdot D_{i}^{\text{crys}}(P_{i}^{\text{coms}}, P_{i,j}^{\text{coms}}, \varepsilon_{ij}^{\text{coms}}, E_{i}^{\text{coms}}). \tag{4.25}$$

This set of the dependent variables η_{i}^{coms}, ξ_{ij}^{coms}, $\sigma_{ij}^{\text{coms}}$ and D_{i}^{coms} in the COMSOL coordinate system depends on the independent variables P_{i}^{coms}, $P_{i,j}^{\text{coms}}$, $\varepsilon_{ij}^{\text{coms}}$ and E_{i}^{coms} that are also expressed in the COMSOL coordinate system. Equations (4.22-4.25) constitute the core of the weak formulation (cf. eqn. 4.3) and can therefore directly be implemented in COMSOL Multiphysics as shown in chapter 4.1.2. In summary, the approach shown above allows for arbitrary rotations of the crystallographic coordinate system with respect to the COMSOL coordinate system in the x_1-x_2-plane. Note that the rotation operations of the free energy were performed in MATHEMATICA, and a tool was developed for directly transfering the results into COMSOL Multiphysics.

4.4. FE-implementation for one-, two- and three-dimensional configurations

The finite-element implementation of the phase-field theory in COMSOL Multiphysics as shown in section 4.1.2 has been performed for one-, two- and three-dimensional configurations. After verifying the FE-implementation by comparing an analytical one-dimensional solution to

a numerically computed solution, the two-dimensional FE-implementation used in chapter 5 in order to investigate typical domain structures will be discussed in detail. Finally, the three-dimensional FE-implementation will be shown exemplarily.

4.4.1. One-dimensional FE-implementation

As discussed in section 2.3, Cao and Cross [9] found an analytical solution for the one-dimensional $180°$ domain wall in a perfect, infinite and stress-free monocrystal. This analytical solution, based on a free energy function of 6th order in terms of the polarization, can be used in order to verify the FE-implementation by comparing it to a numerically obtained solution of a $180°$ domain wall under the same conditions as assumed for the analytical solution. For a one-dimensional $180°$ domain wall located in the x_2-x_3-plane, the polarization component $P_3(x_1)$ changes in x_1-direction from $P_3(x_1 \to -\infty) = P_0$ to $P_3(x_1 \to \infty) = -P_0$, while $P_1 = P_2 = 0$. Considering the symmetry of the infinitely expanded problem, the strains in x_2- and x_3-direction are set to $\varepsilon_{22} = e_\perp$ and $\varepsilon_{33} = e_\parallel$, and only the strain $\varepsilon_{11}(x_1)$ varies in x_1-direction. Furthermore, it is assumed that there are no shear strains. Following Cao and Cross [9], the analytical solution of the polarization $P_3(x_1)$ across the domain wall is given as

$$P_3(x_1) = \frac{P_0 \sinh(\frac{x_1}{\eta})}{\sqrt{A + \sinh^2(\frac{x_1}{\eta})}} \tag{4.26}$$

and the strain $\varepsilon_{11}(x_1)$ across the domain wall as

$$\varepsilon_{11}(x_1) = e_\parallel - \frac{q_{12}}{C_{11}} \frac{P_0^2}{1 + A^{-1} \sinh^2(\frac{x_1}{\eta})}, \tag{4.27}$$

where A and η are constants as defined in equations (2.19-2.20). Then, the gradient of the polarization component $P_3(x_1)$ in x_1-direction is calculated as

$$P_{3,1}(x_1) = \frac{\partial P_3(x_1)}{\partial x_1} \tag{4.28}$$

by taking the partial derivative of equation (4.26) with respect to x_1. Finally, an expression of the free energy $\Psi(x_1)$ across the $180°$ domain wall is found by substituting equations (4.26-4.28) in (1.64), yielding

$$\Psi(P_3(x), P_{3,1}(x), \varepsilon_{11}(x)). \tag{4.29}$$

In order to numerically compute the $180°$ domain wall, the polarization component P_3, the mechanical displacement component u_1 as well as the electric potential ϕ are taken as nodal degrees of freedom in the one-dimensional FE-implementation. The considered model has a

length of 4nm, and as a strong boundary constraint the electric potential ϕ is set to zero at both ends of the configuration so that no electric field is applied. At one end of the configuration the mechanical displacement is fixed ($u_1 = 0$) while at the other end u_1 remains free so that the configuration is stress-free in x_1-direction. In Figure 4.8 a comparison between the analytical solution and the numerical solution of the 180° domain wall is shown. A high degree of agreement between both solutions can be seen, verifying the FE-implementation.
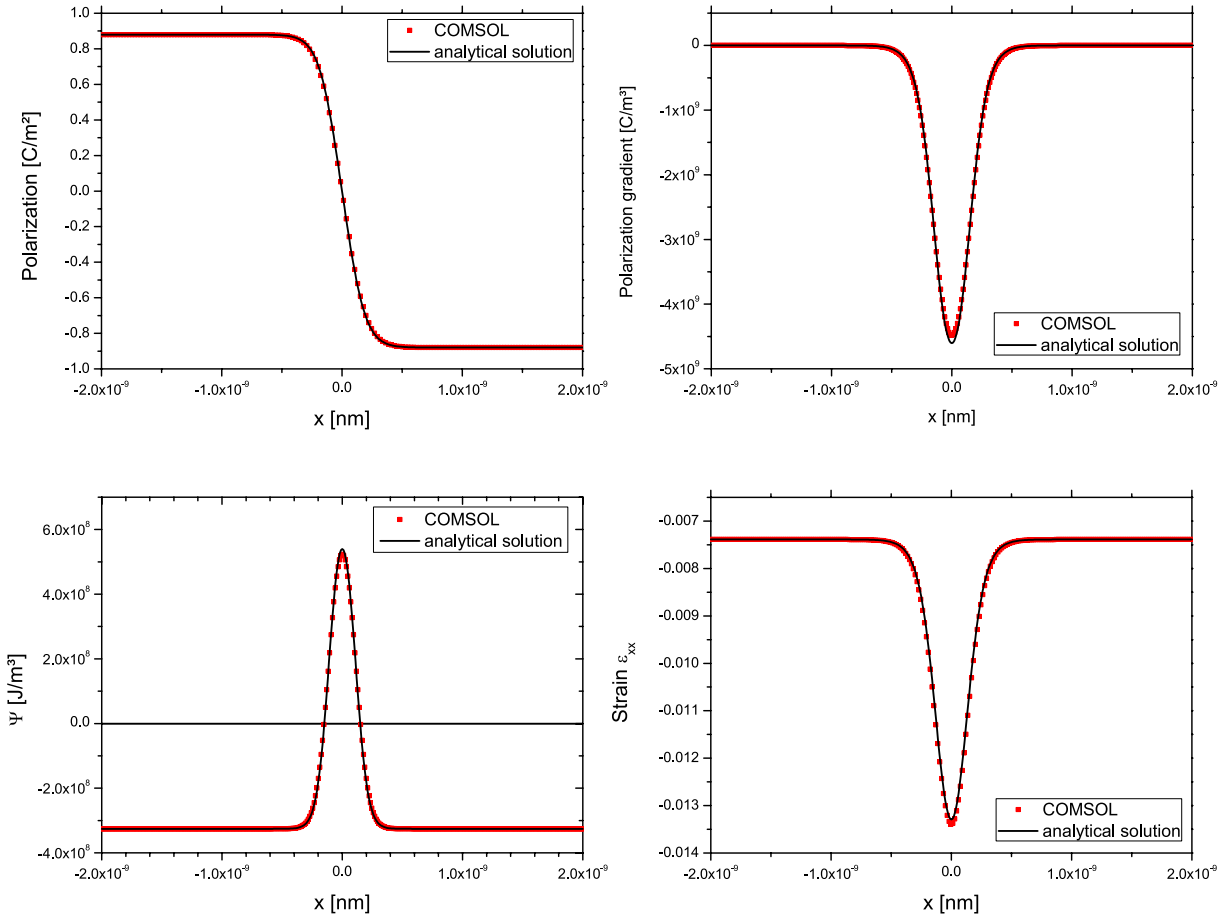
Figure 4.8.: Comparison between the analytical solution of a one-dimensional 180° domain wall and the respective numerical solution obtained from the FE-implemention in COMSOL Multiphysics. The high degree of agreement between both solutions verifies the FE-implementation.

4.4.2. Two-dimensional FE-implementation

In order to investigate ferroelectric domain structures under electromechanical loading, a two-dimensional FE-model will be employed in the course of this work. As the seven nodal degrees of freedom, the three components of the polarization P_1, P_2, P_3, the three components of the mechanical displacement u_1, u_2, u_3, as well as the electric potential ϕ are chosen. Components in x_3-direction are also considered, although the model is spatially confined to the two-dimensional

x_1-x_2-plane. Therefore, all derivatives with respect to x_3 have to be set to zero: $P_{1,3} = 0$, $P_{2,3} = 0$, $P_{3,3} = 0$, $u_{1,3} = 0$, $u_{2,3} = 0$. For all nodal degrees of freedom, periodic boundary conditions are applied in the x_1-x_2-plane.

In a system confined by periodic boundary conditions and containing only one crystallographic orientation, the state of lowest total energy is a monodomain, as long as no external electric fields or mechanical strains are applied. Hence, such a system will always strive towards a state that is completely polarized in one direction and does not contain any domain walls. In order to investigate ferroelectric domain patterns, a way of stabilizing the domain configuration has to be found. One approach is controlling the global strain in at least one dimension of the system. If the global strain is chosen appropriately, a stable domain configuration can be obtained that can then be further investigated, e.g. by electromechanical loading. This global strain can be entered into the mechanical periodic boundary conditions as discussed in section 4.2.4.

Below, the concept of controlling the global strain in order to stabilize a domain configuration is illustrated by the example of a 90° domain stack. Such a configuration consists of two types of ferroelectric domains, which are separated by equidistant 90° domain walls. Figure 4.9 a schematically shows a 90° domain stack containing two domains of orientation $(P_1, 0)$ and $(0, -P_2)$. Within the domain $(P_1, 0)$, the (spontaneous) equilibrium strain has the components
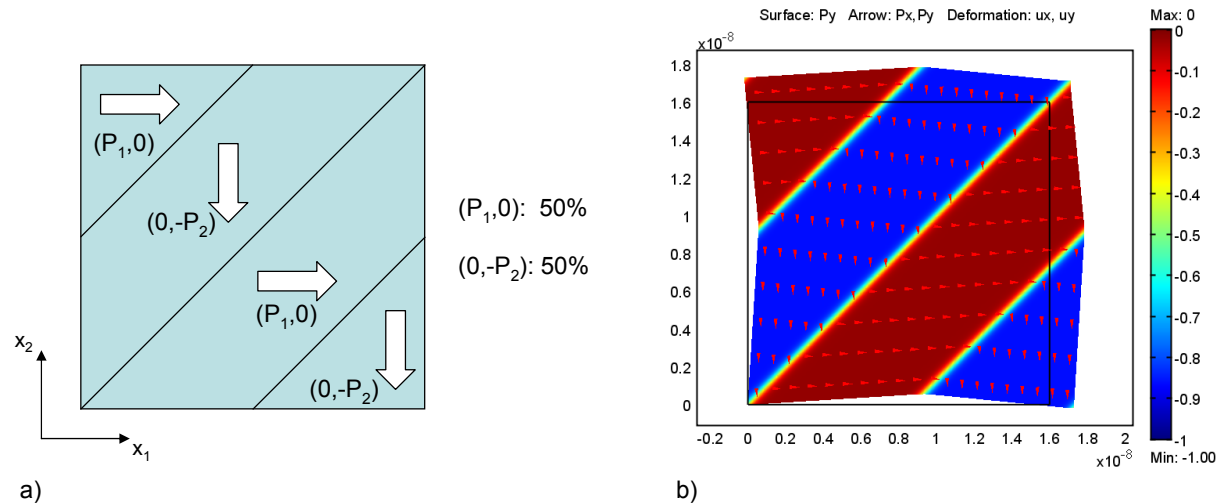
Figure 4.9.: (a) Schematical illustration of a 90° domain stack consisting of the two domain types $(P_1, 0)$ and $(0, -P_2)$ (b) FE-solution of the 90° domain stack: The surface color and the arrows indicate the direction of the polarization, while the deformation illustrates the mechanical displacements in the x_1-x_2-plane. Note that the deformation is magnified by a factor of 4 in order to enhance visibility.

$\varepsilon_{11} = e_\parallel$ and $\varepsilon_{22} = e_\perp$, whereas the strain in the domain $(0, -P_2)$ is inverted: $\varepsilon_{11} = e_\perp$ and $\varepsilon_{22} = e_\parallel$. Therefore, the global strains $\tilde{S}_{11}$ and $\tilde{S}_{22}$ of the configuration are chosen as a combination of the strains in both types of domains, weighted by the fraction of the respective domains. Since both considered domains are equally represented in a 90° domain stack, the global strains are

calculated as

$$\tilde{S}_{11} = 0.5 \cdot e_{\parallel} + 0.5 \cdot e_{\perp} = \tilde{S}_{22} \tag{4.30}$$

and can subsequently be implemented into the mechanical periodic boundary conditions using equation (4.6). Figure 4.9 b shows the numerical solution of a $90°$ domain stack that is stabilized by applying global strains. From the deformation plot it can be seen that the boundaries of the configuration are allowed to deform while the configuration can still be continued periodically. Within the domains both the polarization and the strains almost reach their spontaneous values, indicating that the global strains $\tilde{S}_{11}$ and $\tilde{S}_{22}$ were chosen adequately. An explanation for the deviation of about 1-2% from the equilibrium spontaneous values are the domain walls present in the configuration and their internal strains, which were not considered in the calculation (4.30) of the global strains. The concept of controlling the global strain can be motivated physically by the fact that bulk domain structures in a real ferroelectric ceramic are always strained and affected by their surroundings, e.g. by neighboring grains. Hence, controlling the strain in the configuration can be considered as an appropriate way of stabilizing ferroelectric bulk domain configurations when periodic boundary conditions are applied.

Within the two-dimensional FE-implementation, two conditions for the mechanical displacement in x_3-direction are possible: the state of plain strain and the state of plain stress. In the case of a plain strain state, a uniform strain $\varepsilon_{33} = u_{3,3}$ is applied to all nodes of the configuration. In contrast to the periodically continued x_1-x_2-plane where the strains can vary spatially and only the global (averaged) strains are controlled, all nodes experience the same strain in x_3-direction. The strain chosen in x_3-direction shows a significant impact on the ferroelectric domain pattern, especially on the polarization P_3 in x_3-direction: If for instance the strain $\varepsilon_{33} = u_{3,3} = e_{\perp}$, the prevailing polarization components in the configuration are P_1 and P_2, while fractions of P_3 only arise in the proximity of head-to-head or tail-to-tail polarization configurations in the x_1-x_2-plane. This behavior is illustrated in Figure 4.11: The three polarization components of a domain configuration with a plain strain state in x_3-direction are shown separately, and contributions of P_3 can only be found at positions where $180°$ domain walls and $90°$ domain walls collide and interact. At these positions the depolarization fields caused by head-to-head or tail-to-tail configurations force the polarization out of the x_1-x_2-plane, yielding P_3 contributions.

In the case of a plain stress state in x_3-direction, a uniform stress σ_{33} is applied to all nodes, whereas the strain $\varepsilon_{33} = u_{3,3}$ is now free. By controlling the stress, for instance a stress-free state in x_3-direction can be realized. In order to implement the state of plain stress, a Legendre transformation has to be performed for replacing ε_{33} with σ_{33} in the electric enthalpy:

$$\frac{\partial \mathfrak{h}(P_i, P_{i,j}, \varepsilon_{ij}, E_i)}{\partial \varepsilon_{33}} = \sigma_{33} \quad \Rightarrow \quad \varepsilon_{33}(\sigma_{33}) \quad \Rightarrow \quad \tilde{\mathfrak{h}}(P_i, P_{i,j}, \varepsilon_{11}, \varepsilon_{22}, \sigma_{33}, ..., E_i) \tag{4.31}$$
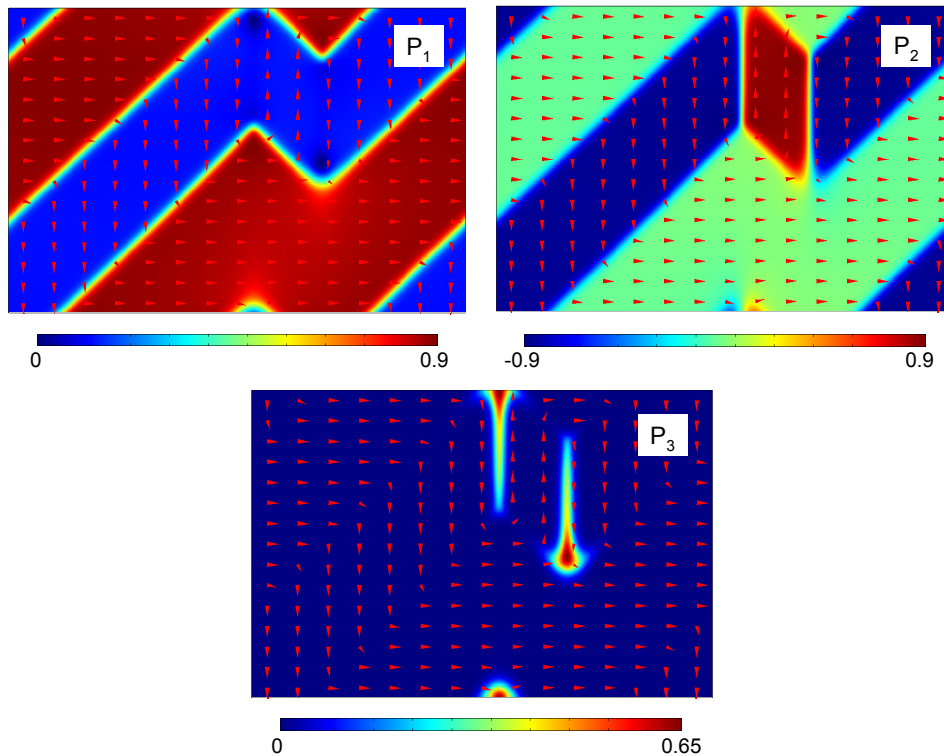
Figure 4.10.: Two-dimensional FE-model containing a ferroelectric domain configuration. The three components of the polarization are plotted separately, with the color coding indicating the respective polarization in C/m^2. In x_3-direction a state of plain strain is assumed.

Because the strain in x_3-direction is allowed to vary spatially, the plain stress state has less impact on the polarization component P_3. However, since the focus of this work is on the investigation of ferroelectric bulk domain structures stabilized by a global strain control in the periodically continued x_1-x_2-plane, the plain stress state will not be used in order to avoid a mixture of stress and strain control in the configuration.

In summary, a two-dimensional FE-implementation is available that is periodically continued in the x_1-x_2-plane and contains degrees of freedom for the polarization and the mechanical displacement in x_3-direction. Domain configurations can be stabilized by controlling the global strain in the x_1-x_2-plane, and a plain strain state is applied in x_3-direction. Therefore, a three-dimensional electromechanical loading of the configuration is possible.

4.4.3. Three-dimensional FE-implementation

In the progress of this work, also a three-dimensional FE-implementation of the phase-field theory in COMSOL Multiphysics has been performed. In doing so, the same nodal degrees of freedom as for the two-dimensional FE-implementation discussed in the previous section were used. An example of a three-dimensional ferroelectric domain structure is illustrated in Figure 4.11: The size of the configuration is $24 \times 16 \times 1$nm, and periodic boundary conditions are

applied for all nodal degrees of freedom in all spatial directions. In order to stabilize the domain pattern, the global strain is controlled in the configuration. The major difference between the two-dimensional and the three-dimensional implementation arises in x_3-direction, which is no longer confined by the state of plain strain: The domain configuration is now allowed to deform out of the x_1-x_2-plane.
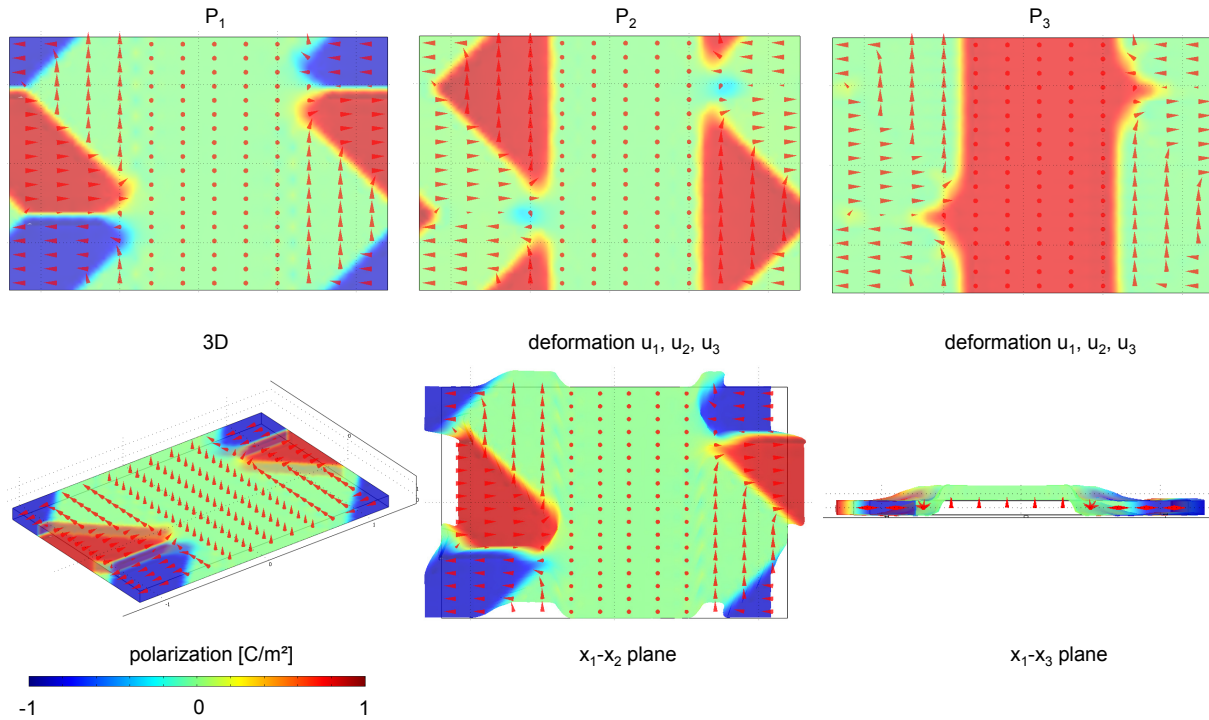
Figure 4.11.: Three-dimensional FE-implementation: The dimensions of the example are $24 \times 16 \times 1$nm, and the periodically continued domain configuration is stabilized by a global strain control.

While the three-dimensional FE-implementation would be the most natural model for investigating ferroelectric bulk behavior, it could not be used in this work due to the massive computational effort necessary to solve it. For instance, computing the configuration shown in Fig. 4.11 took a computation time of 70 hours on a 2.67GHz quad core CPU using 42GB of main memory. Although the height of the configuration is only 1nm, it already consists of 7,680 elements, resulting in a total of about 121,000 degrees of freedom. This corresponds to a mesh density of only 2 nodes/nm, but, as will be shown in section 4.6, a mesh density of at least 7 nodes/nm would be necessary in order to investigate the ferroelectric small-signal behavior. Therefore, the computation and investigation of real three-dimensional models with comparable dimensions in all three spatial directions is not possible with the currently available computational power, and the two-dimensional FE-implementation discussed in the previous section will be used throughout this work.

4.5. Implementation of defects

Real ferroelectric ceramics are never free from defects, which are an important aspect since they can significantly influence the ferroelectric behavior by interacting with the domain structure. Effects of charged defects [71] and dislocations [49] on individual domain walls have been studied before using phase-field modeling. The focus of this work is investigating the effects of charged defects on the small-signal and large-signal behavior of ferroelectric domain configurations. Therefore, charged defects are included in the form of positive or negative charges at specific points of the configuration. In the weak formulation of the phase-field theory, point charges are taken into account as the part

$$\int_V -q\delta\phi \mathrm{d}V \qquad (4.32)$$

of the variational statement (4.3), where q is the charge of the point defect. In COMSOL Multiphysics, charged defects can be implemented by defining the location of the defect as a geometric point and entering `q*test(phi)` into the weak edit field of the *Point settings* dialog box. Note that in a two-dimensional model (x_1-x_2-plane) a point defect becomes a line defect, and q is a charge per length continuously spread in x_3-direction. For periodically continued configurations it is of utmost importance to maintain charge neutrality: Positive charges have to be compensated by negative charges so that eqn. (4.32) becomes zero, otherwise the configuration charges up infinitely.

4.6. FE-mesh studies

A main aspect of the finite-element method is the mesh discretization: The geometry of the considered problem is discretized into a number of sub-domains, the so-called elements. The size of these finite elements, and therefore the mesh density substantially influences the accuracy of the finite-element approximate computation. On the one hand the mesh density is to be chosen as coarse as possible in order to reduce the necessary computational resources and time, but on the other hand as fine as necessary to avoid artefacts caused by a too coarse mesh.

When calculating small signal parameters of domain configurations, external loads are applied and their effect on the domain structure is determined. In chapter 5 it will be found that a considerable effect on the small-signal parameters is caused by the displacement of the domain structure, i.e. by the movement of domain walls. Hence, it is very important that domain walls do not interact with the FE-mesh and that their movement is not influenced by the FE-mesh in any way. Two kinds of artefacts can occur if domain walls are pinned by a too coarse FE-mesh: Firstly, the domain pattern might not represent the configuration of lowest total energy, i.e. domain walls can be pinned and thereby prevented from taking their equilibrium position.

Secondly, even if the FE-mesh is fine enough for the domain walls to reach their equilibrium position, they might still get pinned by the FE-mesh if the configuration is loaded externally by small fields. In this case, the determined small signal parameters would not contain the contribution of domain wall movements and therefore show a systematical error.

In order to find an optimum mesh density that takes all the above-mentioned requirements into account, a mesh study has been performed. A well-known domain configuration has been meshed with different mesh densities, and to each of these configurations an external load has been applied. Then, the resulting change of the system parameters was determined and compared.

One of the most elementary configurations that can be found is the ideal, periodically continued 90° domain stack. It consists of a succession of domains tilted to each other by an angle of 90° and separated by 90° domain walls. Considering a periodically continued configuration stabilized by a global strain control, the domain walls are arranged equidistantly for the state of lowest total energy, i.e. in equilbrium without any applied external fields. Figure 4.12 illustrates the testing configuration with a length of 24nm, and therefore a domain width (distance between domain walls) of 12nm. Since the 90° domain stack can practically be treated as a one-dimensional configuration, the size of the model in x_2-direction is only 0.5nm.
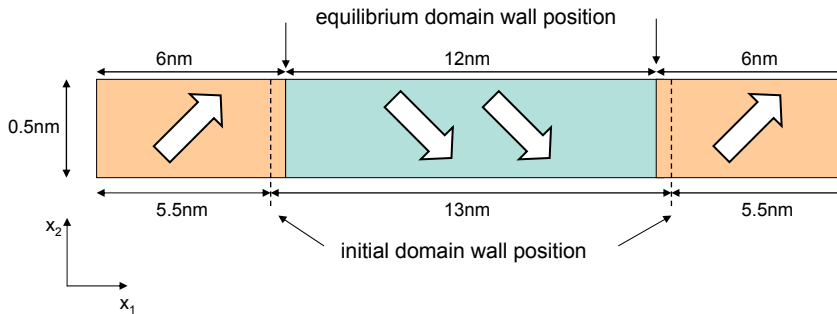
Figure 4.12.: Testing configuration for the FE-mesh study showing the initial and equilibrium domain wall positions of the investigated perfect 90° domain stack.

For the testing configuration, a rectangular FE-mesh was chosen. In the x_2-direction, the mesh contains two elements, whereas the model is meshed with densities from 2 nodes/nm up to 7 nodes/nm in x_1-direction. As an initial condition for the FE-computation, the domain walls are shifted 0.5nm from their equilibrium condition, so that the initial domain widths in the simulation box are 11nm and 13nm, respectively (cf. Fig. 4.12). For each of these configurations, first the equilibrium state without any applied external loadings is computed. Subsequently, an electric field in x_2-direction is applied to this solution.

Figure 4.13 shows the results of the FE-mesh study: For all considered mesh densities, the variation of the dielectric displacement $\Delta D_2 = D_2 - D_2^0$ is plotted versus the applied electric field E_2 in x_2-direction, where D_2^0 denotes the equilibrium value of the dielectric displacement.
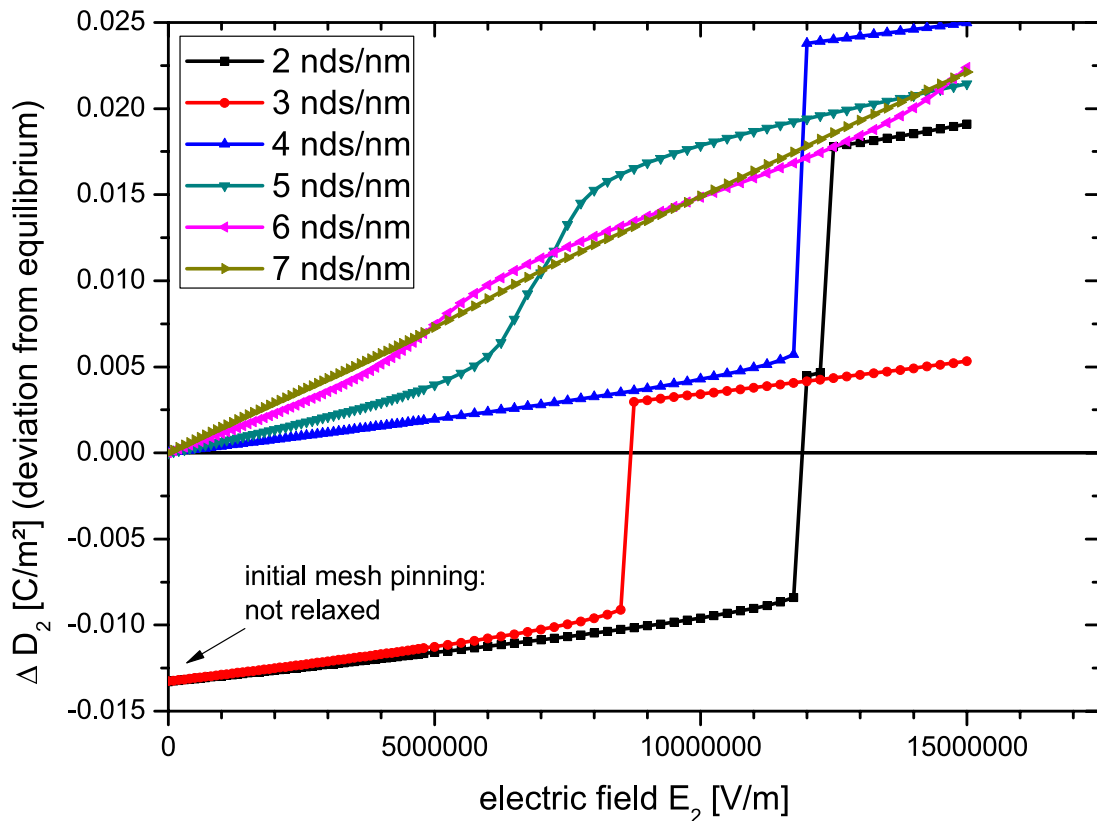
Figure 4.13.: Results of the FE-mesh study: deviation of the dielectric displacement D_2 from its equilibrium value plotted versus the applied electric field E_2 for different mesh densitites. A linear dependence is not achieved until a mesh density of 7 nodes/nm.

Therefore, the slope of the curves depicts a component of the dielectric permittivity tensor and is one of the domain effective small signals to be determined in chapter 5. For a mesh densitiy of three and less nodes/nm, the system is not able to relax from the initial condition (domain widths 11nm/13nm) into its equilibrium state (two domains of width 12nm). This can be explained by a massive pinning of the domain walls by the FE-mesh. For high enough applied electric fields, the domain wall tears off the FE-mesh and jumps to the next node in the FE-mesh where it is pinned again, as can be seen from the slope of the curve that is approximately the same before and after the jump. This behavior is a completely artificial artefact solely caused by the too coarse FE-mesh. For a mesh density of four nodes/nm, the configuration is able to relax into the equilibrium state when no external field is applied. Nevertheless, the FE-mesh still prevents the domain wall from moving freely, as can be seen from the occurring jump as well as from the slope of the curve, which is similar to that of configurations having a coarser FE-mesh and much smaller than that of configurations having a higher mesh density. It is not until a mesh density of 7 nodes/nm that an approximately linear dependence of $\Delta D_2(E_2)$ can be observed. This corresponds to a mesh density of 2-3 nodes on the slope of the domain wall as illustrated in Figure 4.14 b. In summary, a mesh density of 7 nodes/nm in the vicinity of domain walls

is necessary in order to avoid artefacts from a too coarse FE-mesh like the pinning of domain walls and will therefore be used throughout this work.
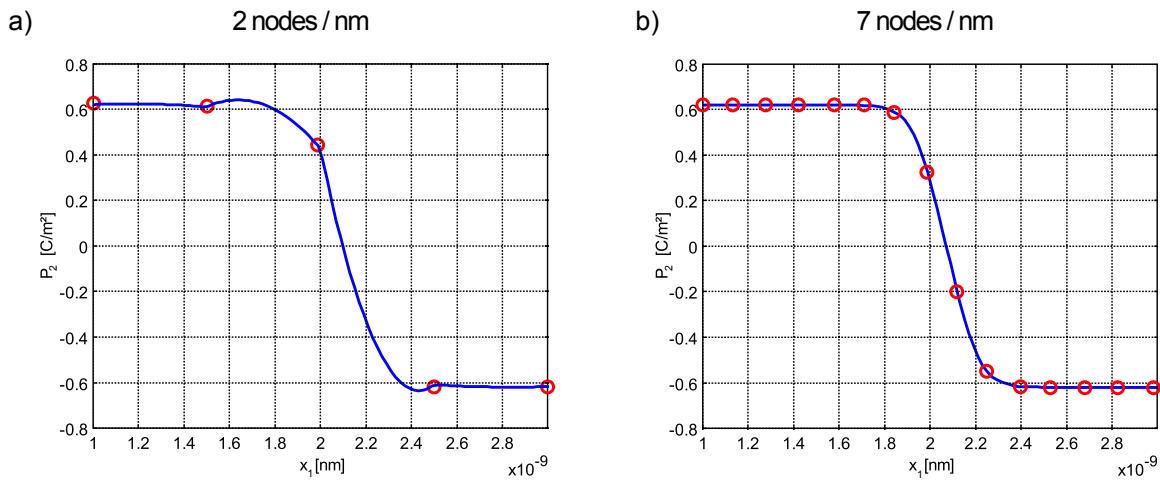
Figure 4.14.: Profile of the polarization component P_2 in a 90° domain wall for two mesh densities. The red circles indicate the nodes of the FE-mesh. While the polarization profile of the coarsely meshed (2 nodes/nm) domain wall shows bucklings and kinks, it is smooth in the fine meshed configuration (7 nodes/nm). In order to avoid artefacts like mesh pinning of domain walls, a FE-mesh containing 2-3 nodes on the slope of the domain wall as illustrated in (b) has to be used.

5. Interface between phase-field and micromechanical methods - Investigation of domain structures

After adjusting the free energy function of the phase-field model to atomistic input parameters (chapter 2) and fully implementing the phase-field theory into the FE-Platform COMSOL Multiphysics (chapter 4), a basis is established for bridging the gap between phase-field methods and micromechanical modeling in the aspired multi-scale simulation chain for ferroelectric materials (Fig. 4.1). The aim of this chapter is to investigate various ferroelectric bulk domain structures under electromechancial loading, providing domain effective input parameters for micromechanical modeling.

First of all, typical domain structures occurring in ferroelectric ceramics are identified and discussed as well as methods for analyzing and investigating them. For micromechanical modeling methods, the so-called small-signal and large-signal parameters of domain structures are of interest. In order to determine small-signal parameters, small electric and mechanical loads are applied to domain configurations, and the linear response of the system is examined. For such small loads all processes in the material are reversible, so that upon unloading the initial domain configuration is restored. When applying higher loads, irreversible switching processes take place, yielding the large-signal parameters, i.e. critical electrical and mechanical loads that are necessary for initiating an irreversible reorientation of ferroelectric domains. Here, the initial state is not restored again after unloading, so that a hysteresis behavior can be observed. Various domain structures of increasing complexity will be investigated, also taking domain-wall interactions as well as effects of charged defects and grain boundaries into account. Trends will be shown regarding the development of the small-signal parameters and critical switching fields with respect to the complexity of the domain structure. Finally, the results of this chapter will be discussed and validated in the context of the multi-scale simulation chain.

5.1. Typical domain structures in ferroelectric ceramics

In ferroelectric ceramics like PZT or PTO, a variety of ferroelectric domain patterns is found on the meso-scale. Figure 5.1 shows a microscope image of a tetragonal PZT ($Pb(Zr_{0.5}Ti_{0.5})O_3$) ceramic[1] obtained by piezoresponse force microscopy (PFM) [21]. Several structures typically occurring on the meso-scale are schematically sketched into the image: regions of perfect structure, $90°$ domain walls, $180°$ domain walls, as well as imperfections and grain boundaries.

---

[1]PZT samples by PI Ceramic GmbH and CeramTec AG, produced in the scope of the BMBF project COMFEM
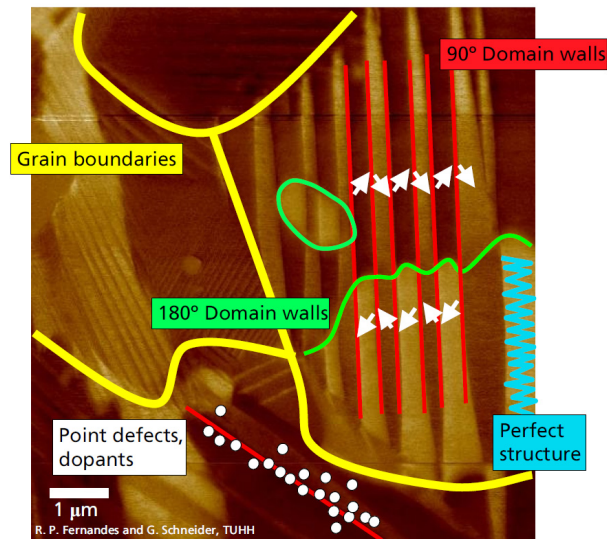
Figure 5.1.: Microscopic PFM-image showing typical bulk domain structures in PZT (PFM-image: R.P. Fernandes and G. Schneider, TU Hamburg-Harburg. Illustration: Pavel Marton, IWM Freiburg)

In between domain walls, regions of perfect structure can be found, only consisting of the perfect polarized crystal lattice and forming single domains. Therefore, such regions are also referred to as monodomains. Since they contain no domain walls, these regions show a purely intrinsic behavior, where only the crystal lattice contributes to the piezoelectric effect.

The most prominent and frequently recurring domain structure found in tetragonal ferroelectric ceramics is the 90° domain stack. This fishbone-like structure consists of a sequence of domains tilted by an angle of 90° towards each other, in which the polarization direction is arranged head-to-tail. The 90° domain walls run parallelly and show a high regularity. This is caused by the fact that curved 90° domain walls would charge up electrically due to resulting depolarization fields. Since the crystallographic lattices of the two adjacent domains separated by a 90° domain wall are mechanically incompatible, shear strains arise within the domain stack, so that equidistant domain walls become energetically favorable. On the contrary, the crystal lattices of two domains separated by a 180° domain wall are mechanically compatible, allowing them to be curved and appearing mainly irregularly in the domain structure.

Also a number of defect mechanisms exist in real ferroelectric ceramics that can interfere with the domain structures described above. Imperfections like charged and neutral defects as well as dopants cannot be resolved using piezoresponce force microscopy and are therefore only schematically illustrated in Figure 5.1. Nevertheless they are always present in real ferroelectric ceramics and can significantly influence the piezoelectric and ferroelectric behavior. At grain boundaries, the crystal lattice orientation mismatch of the adjacent grains evokes internal mechanical stresses and depolarization fields, which can in turn induce electric charges at the grain boundary, showing an influence on the domain structure.

As mentioned above, the aim of this work is investigating the described domain formations and their interaction with the listed defect mechanisms. However, if one tried to exactly replicate the experimentally observed ferroelectric domain pattern of a whole grain using a FE-model and taking all the described effects into account at the same time, certain difficulties would arise. No knowledge is available about the boundary conditions *inside* the ferroelectric ceramic, i.e. what mechanical stress and electric field distributions are caused for instance by neighboring grains. This knowledge is essential for a numeric FE-model, since the domain configuration in such a model has to be stabilized using boundary conditions. But even if this information were available, it would still have to be possible to interpret the obtained solution physically, which cannot be ensured when all effects are considered simultaneously due to the information overflow caused by their complex mutual interaction.

Therefore, the following approach has been chosen in this work: The experimentally found typical domain structures described above will be investigated separately, and defect mechanisms will be added to the numeric model step by step. Starting with a defect-free monodomain state, the complexity of the domain structure will be increased by considering the perfect 90° domain stack as well as bulk multidomain configurations in single crystals, i.e. inside one grain of the ceramic. Furthermore, the interaction of charged defects and grain boundaries with different domain configurations will be examined in detail.

5.2. Determination of small-signal parameters from domain structures

5.2.1. Basics of a small-signal analysis

An important input quantity for micromechanical modeling methods are the so-called small-signal parameters, characterizing the linear behavior of a ferroelectric material under small electrical or mechanical loading. When determined from a phase-field model, the small-signal parameters not only contain the intrinsic material behavior caused by the crystal lattice, but also extrinsic non-lattice contributions caused by the ferroelectric domain pattern on the meso-scale, like for instance reversible domain wall motion. Therefore, using phase-field modeling in order to investigate ferroelectric domain structures yields *domain effective* small-signal parameters, averaged over the entire domain configuration.

In order to determine domain effective small-signal parameters, the FE-model developed in section 4.4.2 is utilized to apply small electrical and mechanical loads to ferroelectric domain structures. These loads have to be small enough for the system to remain in the linear regime, and all processes in the material must be completely reversible upon unloading of the FE-model. Electrical loads are applied by controlling the electric field E_i in the simulation box as described in section 4.2.3, whereas mechanical loads are applied by varying the global strains that stabilize the periodically continued domain configuration (cf. section 4.2.4). Note that the

loading process is quasistatic: Starting from an initial equilibrium configuration in the abscence of any applied electric or mechanical fields, a first loading step will be applied. The equilibrium solution of the first loading step will then be taken as the initial configuration of the next loading step, and so forth. All loading steps therefore represent equilibrium states.

5.2.2. Evaluation of the small-signal analysis

As mentioned above, the small-signal parameters are quantities averaged over the entire domain configuration. The average value $\langle X_i \rangle$ of any (dependent of independent) variable X_i can be obtained from the FE-solution as

$$\langle X_i \rangle = \frac{1}{A_0} \int X_i(x_1, x_2) \mathrm{d}x_1 \mathrm{d}x_2, \tag{5.1}$$

where A_0 is the geometrical area of the investigated two-dimensional configuration in the x_1-x_2-plane. Since the electric field E_i and the mechanical strains ε_{ij} are the independent variables and controlled for loading the domain configuraion electrically and mechanically, the (averaged) dependent variables $\langle D_i \rangle$ and $\langle \sigma_{ij} \rangle$ are the system parameters of interest for the evaluation of the small-signal analysis. For this combination of dependent and independent variables, the constitutive piezoelectric equations take the form

$$\langle \sigma_{ij} \rangle = c^E_{ijkl}\langle \varepsilon_{kl} \rangle - e_{ikl}\langle E_i \rangle \tag{5.2}$$

$$\langle D_i \rangle = e_{ikl}\langle \varepsilon_{kl} \rangle + \kappa^\varepsilon_{ik}\langle E_k \rangle, \tag{5.3}$$

where c^E_{ijkl} are the components of the elastic stiffness tensor for a constant electric field, e_{ikl} are the components of the piezoelectricity tensor, and κ^ε_{ik} are the components of the dielectric permittivity tensor for a constant mechanical strain. These are the requested domain effective small-signal parameters. Loading the domain configuration electrically while keeping the global strain constant yields

$$\kappa^\varepsilon_{ij} = \frac{\partial \langle D_i \rangle}{\partial \langle E_j \rangle} \tag{5.4}$$

$$e_{ikl} = -\frac{\partial \langle \sigma_{kl} \rangle}{\partial \langle E_i \rangle}, \tag{5.5}$$

whereas applying a mechanical load at a constant electric field yields

$$c^E_{ijkl} = \frac{\partial \langle \sigma_{ij} \rangle}{\partial \langle \varepsilon_{kl} \rangle} \tag{5.6}$$

$$e_{ikl} = \frac{\partial \langle D_i \rangle}{\partial \langle \varepsilon_{kl} \rangle}. \tag{5.7}$$

In order to numerically determine the small-signal parameters c_{ijkl}^E, e_{ikl} and κ_{ik}^ε from the FE-solution, the respective dependent variables are plotted versus the independent variable for each loading case. Then, according to equations (5.4-5.7), the small-signal parameters are obtained by linear regression from the slopes of those curves. To illustrate the resulting domain effective elasticity and piezoelectricity tensors in the form of matrix arrays, the compressed matrix notation (also denoted as Voigt notation) is used, following the IEEE Standard 176-1987 [1]. Therefore, the identities

$$c_{ijkl}^E \equiv c_{pq}^E, \qquad e_{ikl} \equiv e_{ip}, \tag{5.8}$$

are defined, and the indices i, j, k, l are replaced by p, q as shown in Table 5.1.

Table 5.1.: Index replacement for the compressed matrix notation according to the IEEE standard on piezoelectricity [1]

ij or kl	p or q
11	1
22	2
33	3
23 or 32	4
13 or 31	5
12 or 21	6

5.3. Determination of domain portions

The small-signal parameters discussed in the previous section represent the averaged behavior of the domain structure. For micromechanical modeling methods, information about the exact domain fractions of the domain configuration is also of importance. In a monocrystalline model of a tetragonally polarized ferroelectric material, the vector of the spontaneous polarization can point in any of the six equivalent $\langle 100 \rangle$ crystalline directions, resulting in the following domain types:

$$P_1^+ = \begin{pmatrix} +P_0 \\ 0 \\ 0 \end{pmatrix} \quad P_2^+ = \begin{pmatrix} 0 \\ +P_0 \\ 0 \end{pmatrix} \quad P_3^+ = \begin{pmatrix} 0 \\ 0 \\ +P_0 \end{pmatrix}$$

$$P_1^- = \begin{pmatrix} -P_0 \\ 0 \\ 0 \end{pmatrix} \quad P_2^- = \begin{pmatrix} 0 \\ -P_0 \\ 0 \end{pmatrix} \quad P_3^- = \begin{pmatrix} 0 \\ 0 \\ -P_0 \end{pmatrix}. \tag{5.9}$$

When loading ferroelectric domain configurations in the phase-field model in order to determine small-signal (or large-signal) parameters, the fraction of each of the domain types found in the domain configuration is of interest as an input parameter for the micromechanical model. Therefore, the FE-solution of the phase-field model has to be analyzed with respect to the domain portions: The solution is discretized by a grid, and every grid point is assigned to one of the domain types. However, when considering ferroelectric domain structures consisting of multiple domains, no sharp segmentation of the domain types as shown in (5.9) is possible, since the equilibrium polarization in large parts of the domain configuration will deviate from its exact spontaneous value P_0 due to domain walls as well as internal electric and mechanical fields affecting the polarization. Instead, a certain interval for the polarization vector is assigned to each domain type:

$$
\begin{aligned}
P_1^+ &= \begin{pmatrix} +P_{0,\text{dec}} \pm 0.5\Delta P_{0,\text{dec}} \\ \pm 0.5\Delta P_{0,\text{dec}} \\ \pm 0.5\Delta P_{0,\text{dec}} \end{pmatrix} \quad
P_1^- = \begin{pmatrix} -P_{0,\text{dec}} \pm 0.5\Delta P_{0,\text{dec}} \\ \pm 0.5\Delta P_{0,\text{dec}} \\ \pm 0.5\Delta P_{0,\text{dec}} \end{pmatrix} \\[2mm]
P_2^+ &= \begin{pmatrix} \pm 0.5\Delta P_{0,\text{dec}} \\ +P_{0,\text{dec}} \pm 0.5\Delta P_{0,\text{dec}} \\ \pm 0.5\Delta P_{0,\text{dec}} \end{pmatrix} \quad
P_2^- = \begin{pmatrix} \pm 0.5\Delta P_{0,\text{dec}} \\ -P_{0,\text{dec}} \pm 0.5\Delta P_{0,\text{dec}} \\ \pm 0.5\Delta P_{0,\text{dec}} \end{pmatrix} \\[2mm]
P_3^+ &= \begin{pmatrix} \pm 0.5\Delta P_{0,\text{dec}} \\ \pm 0.5\Delta P_{0,\text{dec}} \\ +P_{0,\text{dec}} \pm 0.5\Delta P_{0,\text{dec}} \end{pmatrix} \quad
P_3^- = \begin{pmatrix} \pm 0.5\Delta P_{0,\text{dec}} \\ \pm 0.5\Delta P_{0,\text{dec}} \\ -P_{0,\text{dec}} \pm 0.5\Delta P_{0,\text{dec}} \end{pmatrix} .
\end{aligned} \tag{5.10}
$$

$P_{0,\text{dec}}$ and $\Delta P_{0,\text{dec}}$ are two parameters defining the intervals, as schematically illustrated in Figure 5.2 for a two-dimensional example. After assigning all grid points to their respective domain type, the domain fractions v can be defined, indicating the percentage of each domain type in the domain configuration. The domain fractions v have to satisfy the condition

$$
v(P_1^+) + v(P_1^-) + v(P_2^+) + v(P_2^-) + v(P_3^+) + v(P_3^-) + v(DW) = 1, \tag{5.11}
$$

where $v(DW)$ is the percentage that is unassigned according to (5.10) and represents the fraction of domain walls. Finally, a relation for the parameters $P_{0,\text{dec}}$ and $\Delta P_{0,\text{dec}}$ has to be found. By defining the size of the decision interval for the polarization in (5.10), they control the fraction of unassigned domains. For a specific set of the parameters $P_{0,\text{dec}}$ and $\Delta P_{0,\text{dec}}$, a total approximate polarization of the configuration based on the obtained domain fractions can be calculated by multiplying all domain fractions with their respective (monodomain) polarization vectors
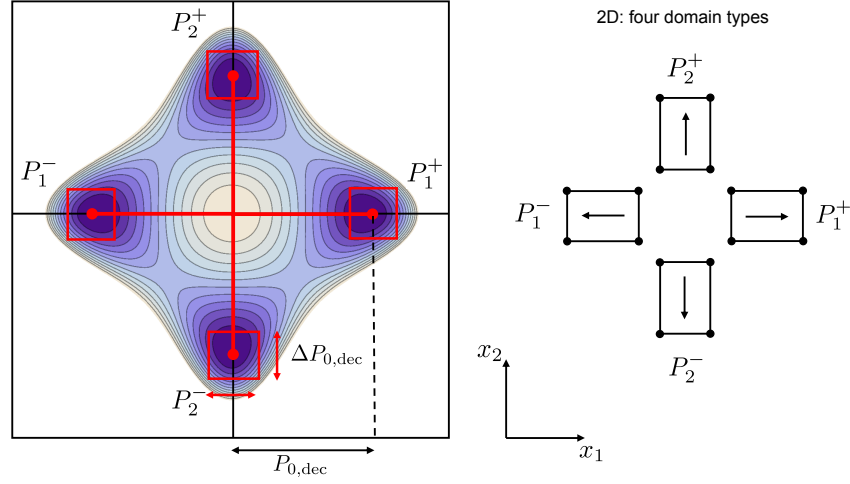
Figure 5.2.: In order to assign the domain types in domain structures as shown in (5.10), intervals are defined by the parameters $P_{0,\text{dec}}$ and $\Delta P_{0,\text{dec}}$: If the polarization vector of a grid point lies within one of these interval, it is assigned to the respective domain type. Here, the intervals associated with the four domain types of the two-dimensional example are schematically illustrated, together with a contour plot of the free energy. Within the domains, the polarization will be near the minima of the free energy and inside the intervals. Only at domain walls the polarization will be outside the intervals.

from (5.9):

$$v(P_1^+) \begin{pmatrix} +P_0 \\ 0 \\ 0 \end{pmatrix} + v(P_1^-) \begin{pmatrix} -P_0 \\ 0 \\ 0 \end{pmatrix} + \cdots + v(DW) \begin{pmatrix} 0 \\ 0 \\ 0 \end{pmatrix} = \begin{pmatrix} P_1^{\text{calc}} \\ P_2^{\text{calc}} \\ P_3^{\text{calc}} \end{pmatrix} \tag{5.12}$$

This polarization P_i^{calc} represents an approximation for the total polarization of the considered domain structure, where every grid point inside a domain is weighted by its respective spontaneous polarization, and unassigned grid points, i.e. areas of domain walls are weighted with zero polarization. By making use of eqn. (5.1), the actual average polarization $\langle P_i \rangle$ of the domain configuration can be determined and compared with the approximation P_i^{calc}. Now, the parameters $P_{0,\text{dec}}$ and $\Delta P_{0,\text{dec}}$ can be chosen so that the total deviation

$$\Delta_{\text{total}} = \sqrt{(P_1^{\text{calc}} - \langle P_1 \rangle)^2 + (P_2^{\text{calc}} - \langle P_2 \rangle)^2 + (P_3^{\text{calc}} - \langle P_3 \rangle)^2} \tag{5.13}$$

reaches its minimum, indicating that the segmentation of the domain configuration in the respective domain types has been performed in an appropriate way. Figure 5.3 shows the total deviation Δ_{total} between P_i^{calc} and $\langle P_i \rangle$ in dependence of the parameters $P_{0,\text{dec}}$ and $\Delta P_{0,\text{dec}}$ for an exemplary domain configuration. Here, a total deviation of $\Delta_{\text{total}} = 1.1\%$ was achieved for a certain set of the parameters $P_{0,\text{dec}}$ and $\Delta P_{0,\text{dec}}$. In Figure 5.4, an example of an analyzed domain configuration is illustrated: The two-dimensional model has a size of 35×20nm and
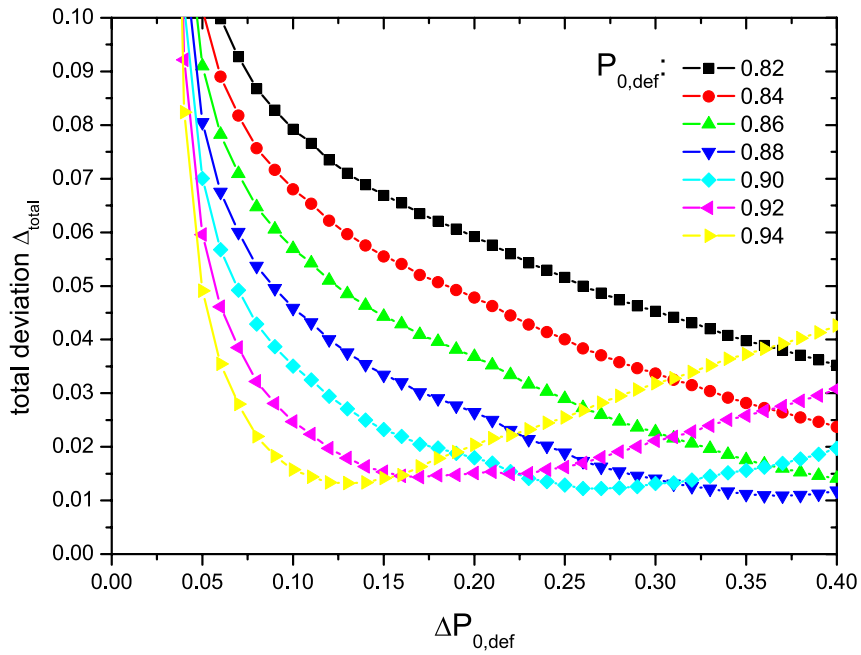
Figure 5.3.: Total deviation Δ_{total} between P_i^{calc} and $\langle P_i \rangle$ according to equation (5.13) for an exemplary domain configuration. For $P_{0,\text{dec}} = 0.88$ and $\Delta P_{0,\text{dec}} = 0.34$ a minimum of Δ_{total} is reached.
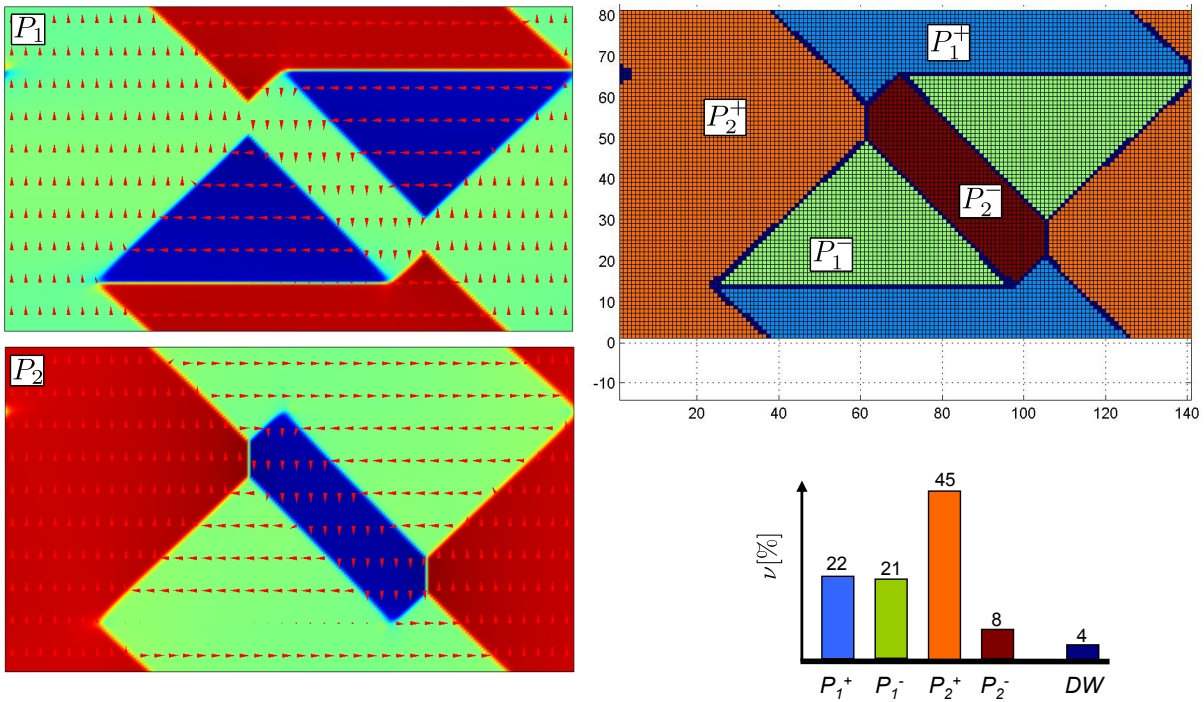
Figure 5.4.: Evaluation of the domain fractions of an exemplary domain structure. On the left side, contour plots of the polarization components P_1 and P_2 are shown. The dimensions of the domain configuration are 35×20nm, and it has been discretized by a grid of 140×80 grid points as illustrated on the right side. Also the domain fractions in per cent are depicted in a bar diagram.

is discretized by a grid of 140×80 points. Also the calculated domain fractions are shown: Condition (5.11) is fulfilled, and a domain wall fraction of 4% is a typical value for domain configurations of this size.

The evaluation of the domain fractions has been realized technically by making use of the interface between MATLAB and COMSOL Multiphysics: The FE-solution obtained with COMSOL Multiphysics is transferred to MATLAB, where it is then discretized and the domain fractions are assigned.

5.4. Investigation of typical bulk domain structures

In the following, the small-signal and large-signal behavior of typical ferroelectric bulk domain structures as discussed in section 5.1 will be investigated in detail. The utilized phase-field model is based on the free energy function (1.64), and the coefficients of this free energy have been adjusted to input parameters from atomistic calculations as shown in chapter 2. Domain configurations for both PTO and PZT will be considered subsequently, and the respective sets of free energy coefficients can be found in Table 2.4. For the case of PTO the PTO-SMP coefficients will be employed, since for them a more precise adjustment to the input parameters from atomistic calculations had been achieved when compared to the PTO-DFT coefficients. All numerical calculations will be performed using the two-dimensional FE-Model discussed in section 4.4.2.

5.4.1. Monodomain

The first ferroelectric domain configuration to be considered is the monodomain. This perfect structure contains no domain walls or imperfections and is entirely polarized in one of the six equivalent tetragonal crystallographic directions. Since the monodomain is completely homogeneous in all directions, the size of the simulation box has no influence on the investigation at all. Therefore, the size of the simulation box has been chosen as 10×10nm, and the configuration is completely polarized in x_3-direction. In the absence of any electrical or mechanical fields, a monodomain describes the energetically lowest possible state, since only the Landau energy term ψ_{Landau} contributes to the free energy. Hence, a monodomain configuration does not have to be stabilized by a global strain control. Nevertheless, in order to enable a comparison with the small-signal parameters obtained from more complex domain structures, the global strain in the model is controlled as follows:

$$\tilde{S}_{11} = \tilde{S}_{22} = e_\perp, \qquad \tilde{S}_{33} = e_\parallel. \tag{5.14}$$

From this configuration, small-signal parameters have been obtained for PTO and PZT. An example of the small-signal analysis is illustrated in Figure 5.5: By applying an electric field in

x_2-direction, i.e. perpendicular to the direction of the spontaneous polarization, the dielectric permittivity tensor component $\kappa_{22}^{\varepsilon}$ for constant strain can be obtained according to eqn. (5.4) by determining the slope of the resulting change of the dielectric displacement D_2. Likewise, the component e_{311} of the piezoelectricity tensor can be obtained by loading the monodomain mechanically and determining the slope of the dielectric displacement D_3 as described by equation (5.7).
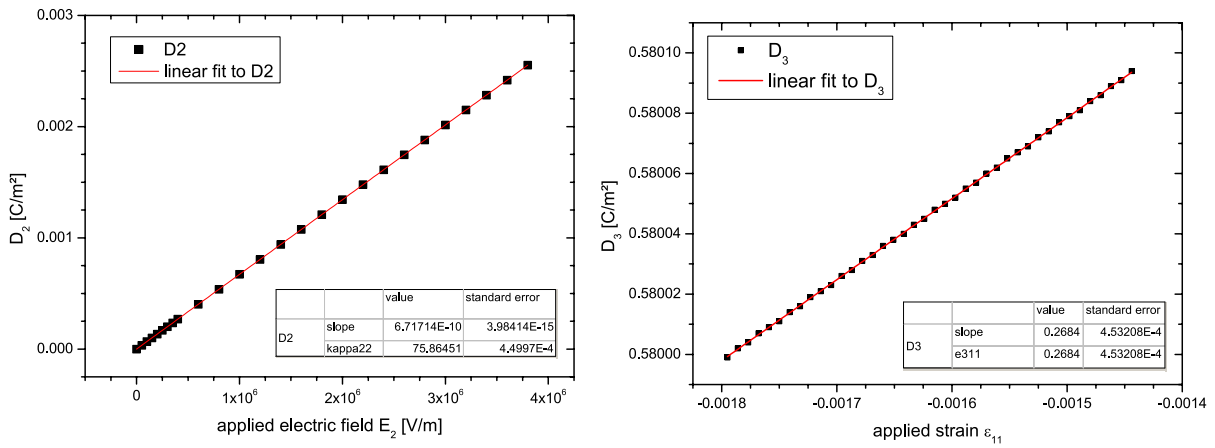

Figure 5.5.: Exemplary determination of the small-signal parameters $\kappa_{22}^{\varepsilon}$ and e_{311} from a PZT monodomain state homogeneously polarized in x_3-direction.

Proceeding as described in section 5.2.2, the monodomain has been loaded electrically and mechanically in all directions, yielding the following set of small-signal parameters for PTO that are expressed in the compressed matrix notation:

$$\kappa_{ij}^{\varepsilon}(\text{PTO}) = \begin{pmatrix} 53.1 & 0 & 0 \\ 0 & 53.1 & 0 \\ 0 & 0 & 12.2 \end{pmatrix} \kappa_0 \tag{5.15}$$

$$e_{ij}(\text{PTO}) = \begin{pmatrix} 0 & 0 & 0 & 0 & 1.74 & 0 \\ 0 & 0 & 0 & 1.74 & 0 & 0 \\ 0.497 & 0.497 & 3.06 & 0 & 0 & 0 \end{pmatrix} \text{C/m}^2 \tag{5.16}$$

$$c_{ij}^E(\text{PTO}) = \begin{pmatrix} 339.8 & 128.2 & 113.3 & 0 & 0 & 0 \\ 128.8 & 339.8 & 117.0 & 0 & 0 & 0 \\ 113.3 & 117.0 & 232.8 & 0 & 0 & 0 \\ 0 & 0 & 0 & 101.4 & 0 & 0 \\ 0 & 0 & 0 & 0 & 101.4 & 0 \\ 0 & 0 & 0 & 0 & 0 & 108.0 \end{pmatrix} \text{GPa} \qquad (5.17)$$

Here, $\kappa_0 = 8.854 \times 10^{-12} F/m$ denotes the vacuum permittivity constant. The obtained small-signal parameters can be used for verifying the FE-implementation by comparing them to small-signal parameters determined from the employed electric enthalpy $\mathfrak{h}$, which has been fitted to atomistic monodomain input parameters before. Below, this is illustrated exemplarily for the dielectric permittivity tensor component κ_{33}^ε: Proceeding in a similar manner as described in eqn. (2.9), κ_{33} can be determined from the electric enthalpy $\mathfrak{h}$ as

$$\frac{\partial^2}{\partial P_3^2}\mathfrak{h}(P_3 = P_0, \varepsilon_{11} = \varepsilon_{22} = e_\perp, \varepsilon_{33} = e_\parallel, E_i = 0) = \frac{1}{\kappa_{33}^\varepsilon}$$

$$\Rightarrow \quad \kappa_{33}^\varepsilon = 12.23\kappa_0,$$

corresponding to the input $\hat{\kappa}_{33}^\varepsilon$ from DFT calculations. All strains in the free energy have been assigned to the respective spontaneous strains in order to allow for a direct comparison with κ_{33}^ε that was calculated using the FE-model with a global strain control. A good agreement can be seen, approving the sucessfull FE-implementation.

For PZT, the following monodomain small-signal parameters have been determined:

$$\kappa_{ij}^\varepsilon(\text{PZT}) = \begin{pmatrix} 75.9 & 0 & 0 \\ 0 & 75.9 & 0 \\ 0 & 0 & 17.5 \end{pmatrix} \kappa_0 \qquad (5.18)$$

$$e_{ij}(\text{PZT}) = \begin{pmatrix} 0 & 0 & 0 & 0 & 1.35 & 0 \\ 0 & 0 & 0 & 1.35 & 0 & 0 \\ 0.268 & 0.268 & 1.99 & 0 & 0 & 0 \end{pmatrix} \text{C/m}^2 \qquad (5.19)$$

$$
c_{ij}^E(\text{PZT}) = \begin{pmatrix}
360.5 & 114.5 & 111.4 & 0 & 0 & 0 \\
114.5 & 360.5 & 111.2 & 0 & 0 & 0 \\
111.4 & 111.2 & 332.9 & 0 & 0 & 0 \\
0 & 0 & 0 & 88.3 & 0 & 0 \\
0 & 0 & 0 & 0 & 88.3 & 0 \\
0 & 0 & 0 & 0 & 0 & 91.0
\end{pmatrix} \text{GPa} \tag{5.20}
$$

Also the large-signal behavior of PTO and PZT monodomains has been examined. For determining large-signal parameters, i.e. characteristic electric fields causing irreversible domain switching processes, the boundary conditions of the FE-model are chosen in a way that ensures that the model is mechanically stress-free ($\sigma_{ij} = 0$), i.e. the strains ε_{ij} are not controlled. Starting with a monodomain configuration completely polarized in x_3-direction, an electric field
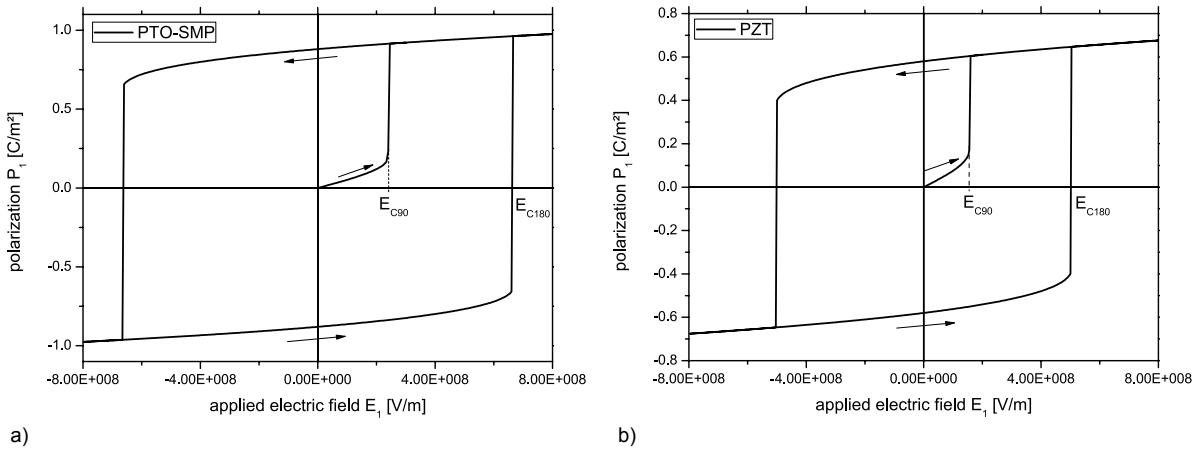
Figure 5.6.: Large-signal behavior of PTO and PZT monodomains: In both cases ferroelectric domains that are initially entirely polarized in x_3-direction are loaded electrically in x_1-direction, yielding the coercive field strengths E_{C90} and E_{C180}.

E_1 is applied in x_1-direction as illustrated in Figure 5.6. For a certain electric field E_1 the polarization switches by $90°$ from domain type P_3^+ to P_1^+. This coercive field strength is denoted E_{C90}. Upon reaching this coercive field strength, the polarization of the entire system switches simultaneously to the domain type orientated in the direction of the applied electric field, describing a characterisic behavior of monodomains. This homogeneous switching is caused for instance by a lack of imperfections in the model that could act as nucleation centers for new domains. When the electric field is reversed and reduced to zero, the configuration remains in the P_1^+ state, indicating an irreversible switching process. By applying an electric field in negative x_1-direction, i.e. contrarily to the direction of the spontaneous polarization, the second characteristic coercive field strength E_{C180} can be obtained, for which the polarization of the

whole system switches simultaneously from P_1^+ to P_1^-. Note that the electric field required for 180° switching processes exceeds the coercive field for 90° switching processes. In Table 5.2, the determined coercive switching fields E_{C180} and E_{C90} for PTO and PZT monodomains are listed, and in Figure 5.6 the respective hysteresis curves are shown.

Table 5.2.: Coercive field strengths of PTO and PZT monodomains that were determined as illustrated in Figure 5.6.

	PTO	PZT
E_{C90} [V/m]	2.43×10^8	1.58×10^8
E_{C180} [V/m]	6.63×10^8	5.02×10^8

5.4.2. Monodomain containing charged defects

A monodomain that contains an electrically charged defect is the next domain configuration to be considered, with the aim of examining the influence of charged defects on the small-signal and large-signal behavior of monodomains. The testing configuration utilized is similar to the one described in the previous chapter: As illustrated in Figure 5.7, it consists of a 10×10nm monodomain containing a defect of charge q in its center. This electrically charged defect is incorporated into the FE-model as described in section 4.5. At one corner of the configuration the electric potential is grounded ($\phi = 0$), so that a mirror charge $-q$ of opposite polarity is induced in this place. Since the configuration is periodically continued in the x_1-x_2-plane, the mirror charge appears at all four corners of the simulation box, ensuring charge neutrality in the model.
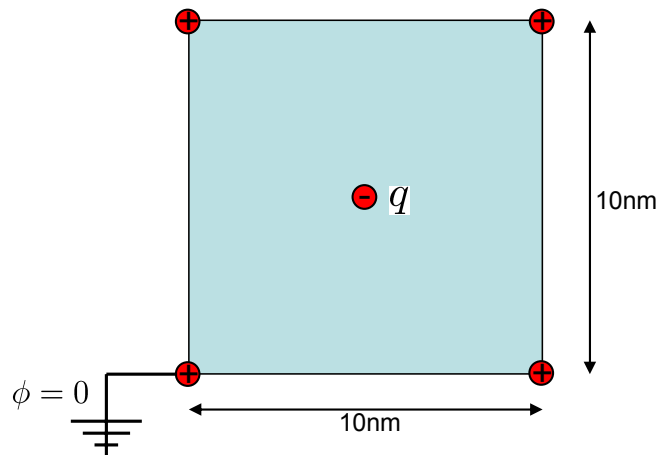
Figure 5.7.: Schematical illustration of the monodomain setup containing a defect of charge q located in its center. The periodically continued model is grounded at the corners, where mirror charges $-q$ arise due to electrostatic induction.

First, the influence of electrically charged defects on the large-signal behavior of a monodomain is regarded. Proceeding in like manner as for the pure monodomain state, a configuration initially entirely polarized in x_3-direction (P_3^+) is loaded by applying an electric field E_1 in positive x_1-direction until the coercive field strength E_{C90} is reached and the polarization switches to P_1^+. Then, the electric field is reversed and the configuration is loaded in negative x_1-direction, yielding the coercive field strength E_{C180} at which point the polarization switches by $180°$ to a P_1^- polarization state. This approach is illustrated in Figure 5.8 for different electric defect charges q. Note that an electric point charge in a two-dimensional model is actually a line charge, with the electric charge continuously spread in x_3-direction. The (line) charge densities q considered in the following range from 0.8×10^{-10}C/m to 8×10^{-10}C/m. Assuming a unit cell size of about 4Å as found for PZT (cf. Table 2.3), this corresponds to a line charge density of 0.2-2 elementary charges per unit cell.

The incorporated electrically charged defect causes a variety of effects on the behavior of the monodomain under electric loading that can be seen from Figure 5.8. For an increasing charge density q of the defect, both coercive field strengths E_{C90} and E_{C180} are reduced significantly. When loading the initial domain configuration in x_1-direction, a small jump in the dielectric displacement D_1 occurs for charge densities bigger than 2×10^{-10}C/m before E_{C90} is reached. As the charge density q increases, the threshold for this jump in D_1 shifts to smaller applied electric fields E_1. Finally, for charge densities exceeding 6.5×10^{-10}C/m, even the unloaded equilibrium configuration ($E_1 = 0$) obtains an initial dielectric displacement D_1 of about 0.03C/m (which is small compared to the spontaneous polarization P_3=0.58C/m in x_3-direction). A similar small jump of the dielectric displacement D_1 can be observed before reaching the coercive field strength E_{C180} for charge densities of 6.5×10^{-10}C/m and higher. The dependence of the coercive fields E_{C90} and E_{C180} on the electric charge density of the incorporated defect is illustrated in Figure 5.9. The coercive field E_{C180} is affected considerably more by the defect than E_{C90}, and with an increasing charge density the coercive fields E_{C180} and E_{C90} for $180°$ and $90°$ switching processes converge more and more.

All effects described above can be explained by the nucleation of ferroelectric domains at the site of the charged defect, as illustrated exemplarily in Figure 5.10 for a charge density of 6.5×10^{-10}C/m. In the initial unloaded configuration, only the close vicinity of the defect in the center of the configuration is affected by its electric charge (and also the vicinity of the mirror charges of opposite polarity at the corners of the configuration). Upon applying a small electric field E_1, a new domain is nucleated between the charged defect and the mirror charge at the corner of the configuration. This domain is tilted by an angle of $90°$ with respect to the poling direction of the monodomain and oriented in the direction of the applied electric field. It initiates the $90°$ switching process of the polarization when the electric field E_1 is increased further and therefore lowers the coercive field strength E_{C90} compared to the case of
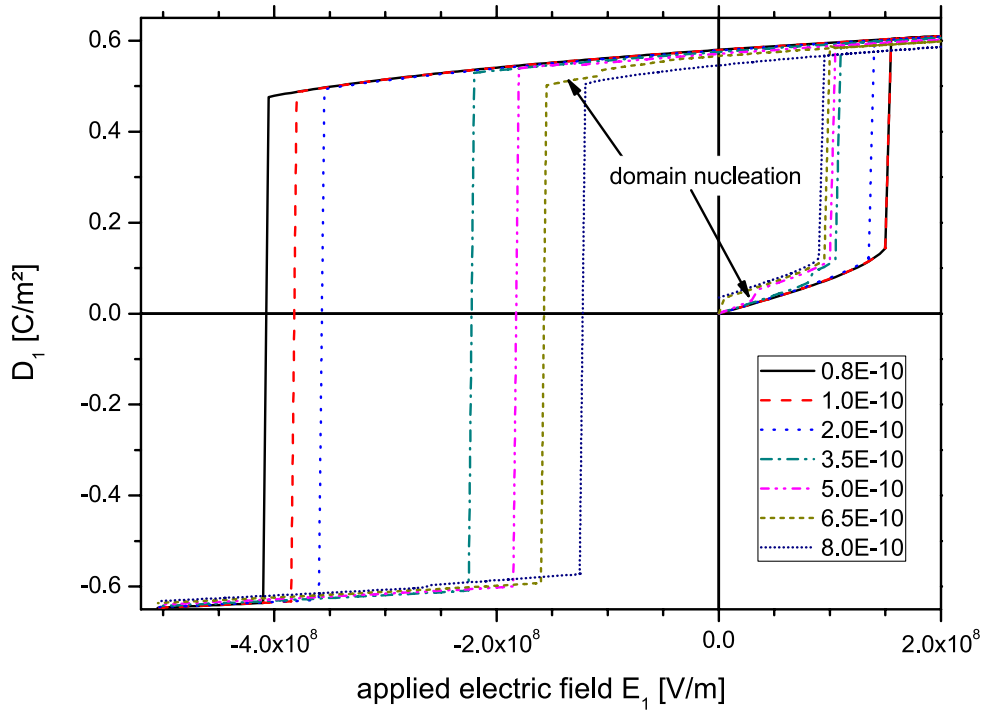
Figure 5.8.: Large-signal behavior investigation of the PZT monodomain state depicted in Figure 5.7. The diagram shows the component of the dielectric displacement D_1 versus the applied electric field E_1. Increasing (line) charge densities of the incorporated electrically charged defect show a significant effect on the coercive field strengths E_{C90} and E_{C180}, and kinks in the dielectric displacement indicate the nucleation of domains as will be discussed in Figure 5.10.
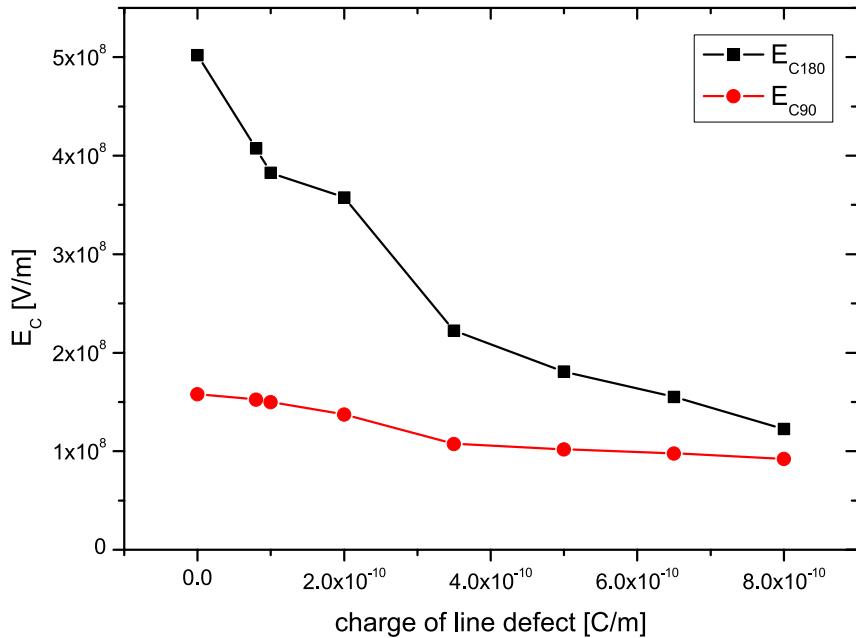

Figure 5.9.: Influence of the defect's charge density on the coercive fields E_{C180} and E_{C90} of a monodomain: With increasing charge density, E_{C180} and E_{C90} converge.

a defect-free monodomain. When the configuration is subsequently loaded in the negative x_1-direction, i.e. oppositely to the polarization direction P_1^+ of the monodomain, two new domains P_2^+ and P_2^- arise in the configuration. Both new domains are oriented perpendicular to the monodomain. As the electric field in negative x_1-direction is raised further, a second effect of the electrically charged defect becomes obvious: The 180° switching process is separated into two 90° switching processes caused by the nucleated domains P_2^+ and P_2^-. This would not be possible in a defect-free monodomain state and explains the converging fields E_{C180} and E_{C90} when an electrically charged defect is present.

The influence of electrically charged defects on the small-signal behavior of monodomains is illustrated in Figure 5.11: An electric field E_1 that is small compared to the coercive field strength is applied to a monodomain configuration polarized in x_3-direction, and the change of the dielectric displacement is plotted for a variety of defect charge densities. Therefore, the slope of these curves corresponds to the dielectric permittivity tensor component κ_{11}^σ for constant stress. For defect charge densities of 2×10^{-10}C/m and lower there is almost no influence on the small-signal parameter. However, as the charge densitiy is raised, a domain nucleates at the charged defect (cf. Figure 5.10), leading to a notable increase of κ_{11}^σ just before the new domain nucleates. For high enough defect charge densities, i.e. when nucleated domains are present in the configuration, κ_{11}^σ is increased consistently by about 15% compared to the defect-free monodomain configuration. The reason for this are the domain walls now present in the system that can shift reversibly, so that the small-signal parameters not only imply the intrinsic material behavior, but also extrinsic contributions as will be discussed in the next sections.

In summary, electrically charged imperfections show a strong impact on the large-signal behavior of monodomains. Even small defect charge densities can influence the coercive field strength E_{C180} as illustrated in Figure 5.9. An explanation has been shown for this behavior: Ferroelectric domains nucleate at the site of electrically charged defects, so that the spatial homogeneity of the monodomain state is broken. Nucleated domains are able to initiate 90° switching processes as well as to separate 180° switching processes into two successive 90° switching processes.

5.4.3. Perfect 90° domain stack

After the monodomain state, which consists of only one domain type, the next more complex ferroelectric domain configuration is the ideal 90° domain stack as depicted in Figure 5.12: It consist of a periodically continued regular array of two domain types separated by 90° domain walls. For investigating the ideal 90° domain stack it is most convenient to rotate the crystallographic coordinate system by an angle of 45° with respect to the simulation box coordinate system as shown in section 4.3. Hence, the 90° domain walls always run parallel to the x_2-x_3-plane of the simulation box coordinate system, causing a homogeneous behavior in x_2- and
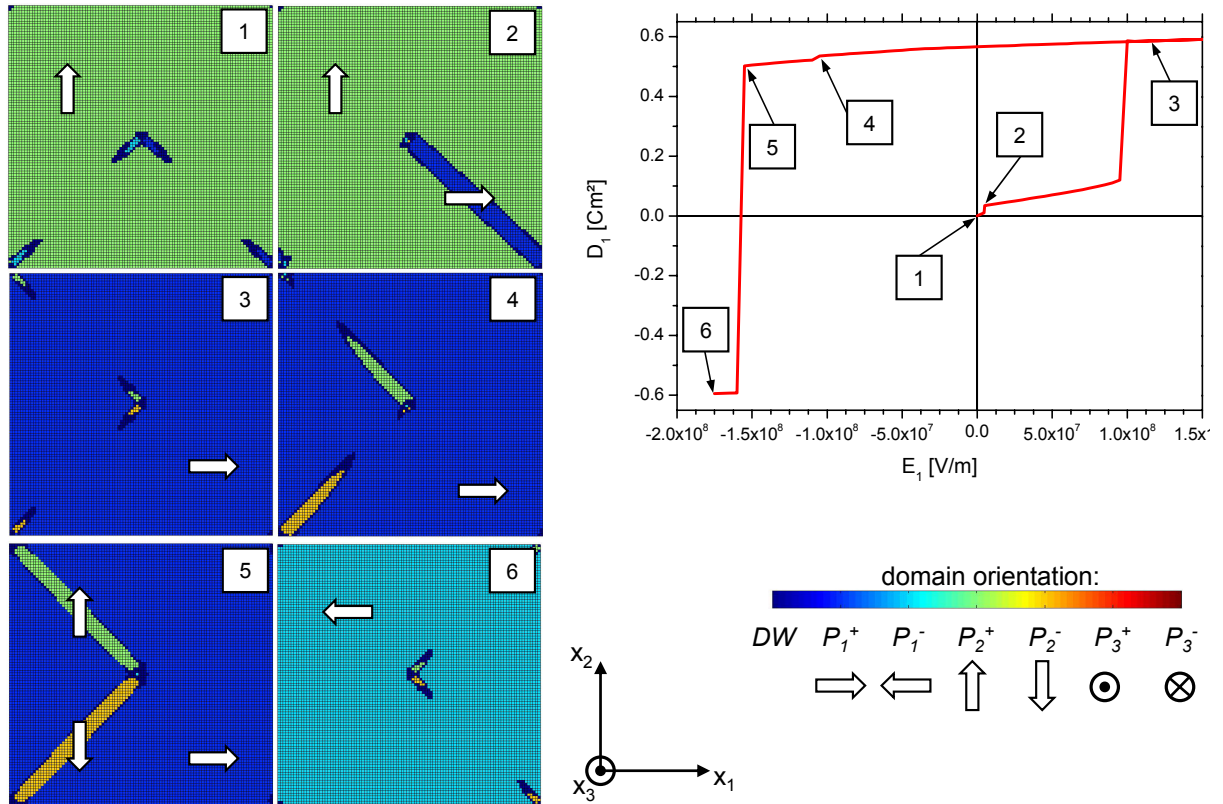
Figure 5.10.: Domain nucleation initiated by a charged defect in a monodomain state: For a charge density of q=6.5×10^{-10}C/m, the hysteresis curve is shown, along with plots of the domain structure at certain loading steps. Domains nucleate from the charged defect in the center of the configuration as well as from the mirror charges at the corners, showing a strong influence on the large-signal behavior.
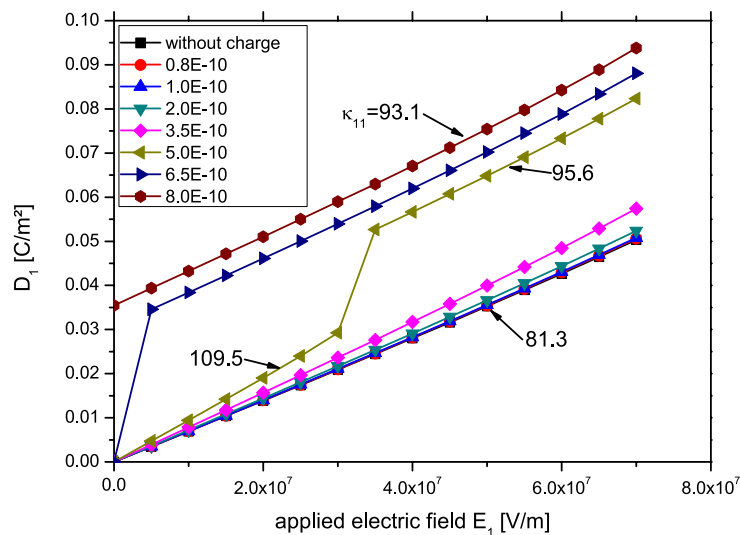

Figure 5.11.: Influence of charged defects on the small-signal behavior of a PZT monodomain state: Thus, the linear regime of Figure 5.8 is considered. The numbers in the diagram indicate the slopes and therefore the component κ_{11}^σ of the dielectric permittivity tensor.

117
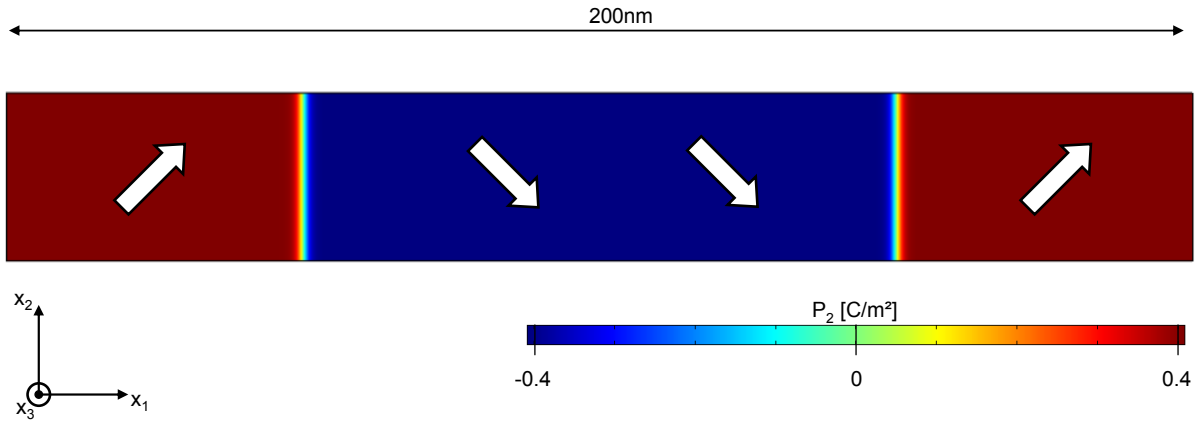
Figure 5.12.: Equilibrium solution of the investigated ideal 90° domain stack. The crystallographic coordinate system has been rotated in the x_1-x_2-plane by 45° with respect to the simulation box coordinate system, and the color coding depicts the polarization component P_2.

x_3-direction. Typical domain widths (i.e. the distance between domain walls in x_1-direction) of approximately 100nm were determined from PFM experiments[2], so that the dimensions of the simulation box were chosen as 200×0.5nm. In order to mechanically stabilize the periodically continued domain configuration, a global strain

$$\tilde{S}_{11} = \tilde{S}_{22} = \frac{e_\parallel + e_\perp}{2} \tag{5.21}$$

is applied in the x_1-x_2-plane, and a plain strain state $\varepsilon_{33} = e_\perp$ is deployed in x_3-direction. Basic properties of the 90° domain stack are depicted in Figure 5.13: While the polarization component P_2 changes across the domain wall at x_1=50nm from $+\frac{\sqrt{P_0}}{2}$ to $-\frac{\sqrt{P_0}}{2}$, the polarization component P_1 remains unaltered except for a small spike at the center of the domain wall. As expected the electric potential rises steeply within the domain walls and exhibits the same value on both sides of the configuration since no electric field E_1 is applied in the example. While the strain ε_{11} remains the same in both domain types involved, the equilibrium shear strain ε_{21} is positive in the $(+\frac{\sqrt{P_0}}{2},+\frac{\sqrt{P_0}}{2},0)$ domain and negative, but yet of same value in the $(+\frac{\sqrt{P_0}}{2},-\frac{\sqrt{P_0}}{2},0)$ domain. However, when averaged over the entire configuration, the shear strain ε_{21} adds up to zero as requested by the global strain control. Due to the non-zero equilibrium shear strains in both domains, the ideal 90° domain stack would not be stable if periodically continued: If the fraction of one of the two involved domains becomes (e.g. by a fluctuation) slightly bigger compared to the other, a global shear strain arises in the configuration. Due to this global shear strain, the domain type of bigger fraction would become energetically favorable compared to the other, and it would grow on the expense of the smaller domain until reaching a monodomain state. Therefore, the ideal periodically continued 90° domain stack can only be investigated

---

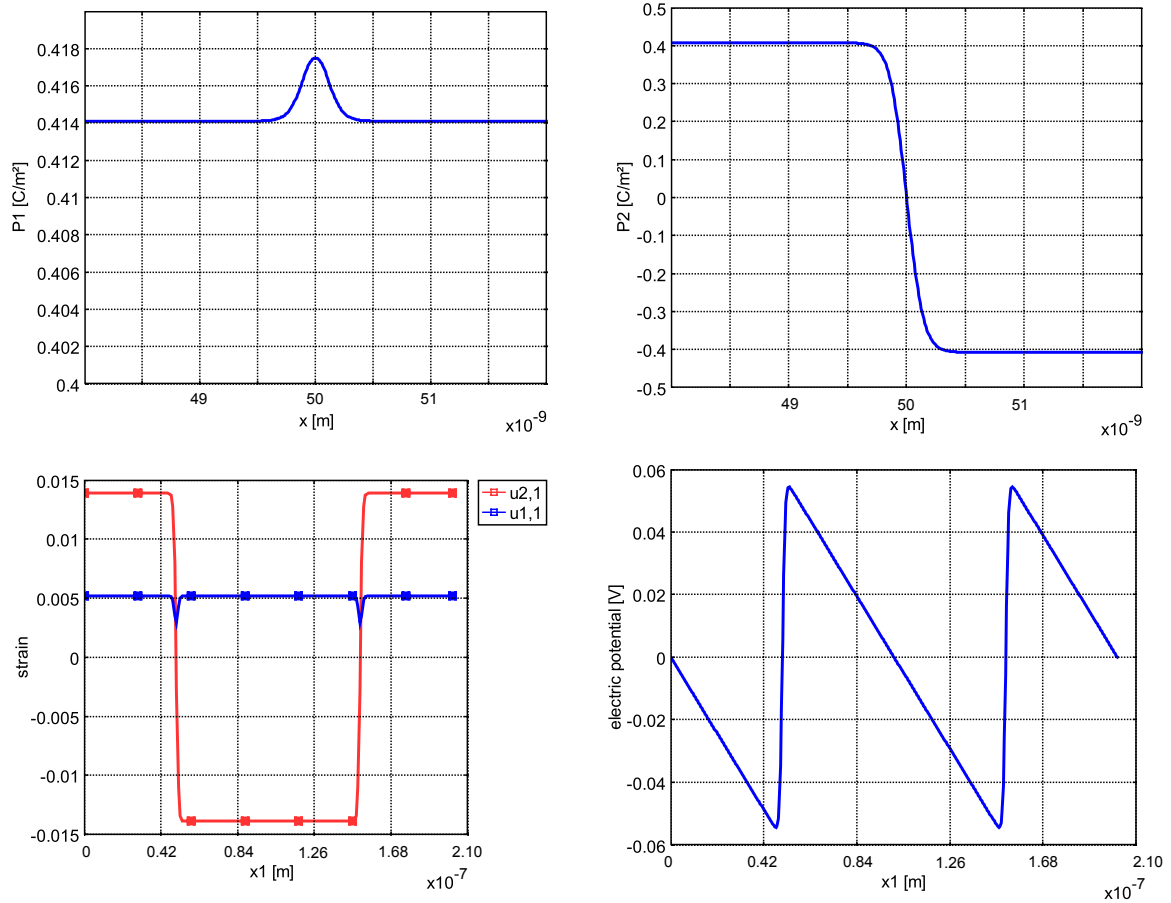[2]COMFEM report by R.P. Fernandes and G.A. Schneider, TU Hamburg-Harburg

Figure 5.13.: Basic properties of the investigated 90° domain stack: Along with the polarization components P_1 and P_2 within the domain walls, the strains $u_{1,1} = \varepsilon_{11}$ and $u_{2,1} = \varepsilon_{21}$ as well as the electric potential in x_1-direction of the 90° domain stack are illustrated. Note that ε_{21} changes its sign for the present domain types. The strong rising of the electric potential indicates internal electric fields within the 90° domain walls.

when it is mechanically stabilized.

The domain stack has been loaded electromechanically along the axes of the simulation box, yielding the following set of small-signal parameters for PTO:

$$\kappa_{ij}^{\varepsilon}(\text{PTO}) = \begin{pmatrix} 33.0 & 0 & 0 \\ 0 & 182 & 0 \\ 0 & 0 & 67.3 \end{pmatrix} \kappa_0 \tag{5.22}$$

$$e_{ij}(\text{PTO}) = \begin{pmatrix} 2.62 & 0.21 & 0.40 & 0 & 0 & 0 \\ 0 & 0 & 0 & 0 & 0 & 13.5 \\ 0 & 0 & 0 & 0 & 1.58 & 0 \end{pmatrix} \text{C/m}^2 \tag{5.23}$$

$$c_{ij}^E(\text{PTO}) = \begin{pmatrix} 304.2 & 100.8 & 121.5 & 0 & 0 & 0 \\ 100.8 & 303.3 & 121.4 & 0 & 0 & 0 \\ 121.5 & 121.4 & 339.3 & 0 & 0 & 0 \\ 0 & 0 & 0 & 104.8 & 0 & 0 \\ 0 & 0 & 0 & 0 & 103.8 & 0 \\ 0 & 0 & 0 & 0 & 0 & \rightarrow 0 \end{pmatrix} \text{GPa} \tag{5.24}$$

Analogously, the small-signal parameters for PZT were obtained:

$$\kappa_{ij}^\varepsilon(\text{PZT}) = \begin{pmatrix} 45.1 & 0 & 0 \\ 0 & 801 & 0 \\ 0 & 0 & 84.8 \end{pmatrix} \kappa_0 \tag{5.25}$$

$$e_{ij}(\text{PZT}) = \begin{pmatrix} 1.73 & 0.12 & 0.19 & 0 & 0 & 0 \\ 0 & 0 & 0 & 0 & 0 & 29.3 \\ 0 & 0 & 0 & 0 & 1.08 & 0 \end{pmatrix} \text{C/m}^2 \tag{5.26}$$

$$c_{ij}^E(\text{PZT}) = \begin{pmatrix} 317.3 & 140.7 & 112.7 & 0 & 0 & 0 \\ 140.7 & 317.2 & 112.8 & 0 & 0 & 0 \\ 112.7 & 112.8 & 360.5 & 0 & 0 & 0 \\ 0 & 0 & 0 & 89.7 & 0 & 0 \\ 0 & 0 & 0 & 0 & 89.4 & 0 \\ 0 & 0 & 0 & 0 & 0 & \rightarrow 0 \end{pmatrix} \text{GPa} \tag{5.27}$$

For both PTO and PZT, the obtained small-signal parameters show a similar behavior. From the structure of the piezoelectricity tensors e_{ij}, the net polarization of the 90° domain stack in x_1-direction can be seen. The components κ_{22}^ε of the dielectric permittivity tensor and e_{26} of the piezoelectricity tensor are anomalously high, while the component c_{66} of the elasticity tensor becomes zero. Therefore, the ideal 90° domain stack responds very sensitively to electric fields applied in x_2-direction and to shear strains ε_{12} applied in the x_1-x_2-plane.

This behavior can not be explained when only the intrinsic material behavior of both involved domain types is considered. Instead, the motion of the domain walls in the configuration has to be taken into account: As the 90° domain stack is loaded by an electric field E_2, a domain wall shift in x_1-direction becomes energetically favorable for the system so that domain type

$(+\frac{\sqrt{P_0}}{2},+\frac{\sqrt{P_0}}{2},0)$ grows and domain type $(+\frac{\sqrt{P_0}}{2},-\frac{\sqrt{P_0}}{2},0)$ shrinks in order to lower the electrostatic energy of the system by converting it into elastic energy. In like manner, the elastic energy of the $90°$ domain stack can be reduced and converted into electrostatic energy by moving the domain wall once a shear strain ε_{12} in the x_1-x_2-plane is applied to the configuration. This domain wall motion under shearing in the x_1-x_2-plane becomes evident from Figure 5.14: Once a shear strain ε_{12} is applied, the domain walls shift, and no shear stress σ_{12} arises in the configuration. Therefore, the ideal $90°$ domain stack shows a completely soft response under shearing in the x_1-x_2-plane, explaining c_{66}^{E} to become zero.
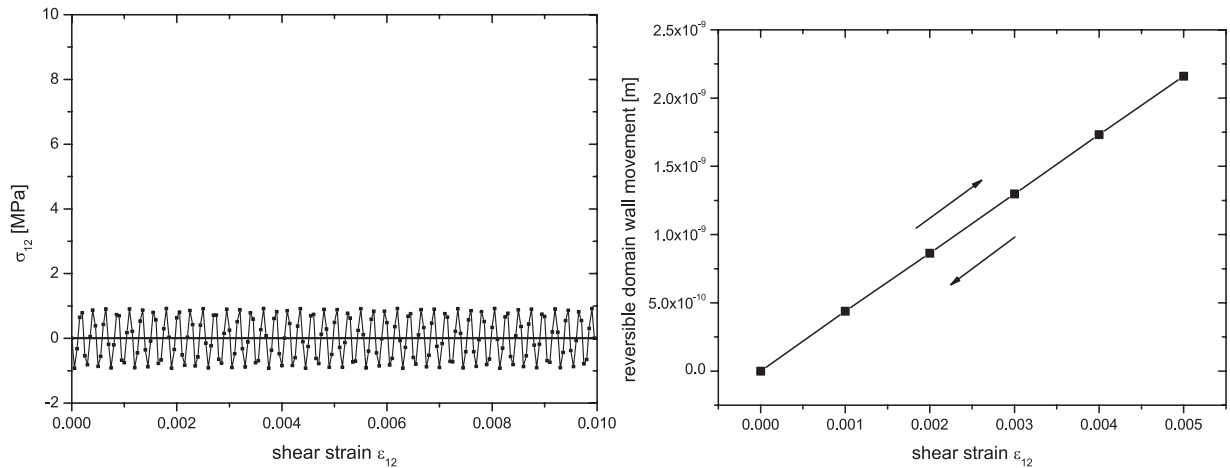
Figure 5.14.: The diagrams show the total shear stress σ_{12} in a $90°$ domain stack as depicted in Figure 5.13 as well as the domain wall position under an applied shear strain ε_{12}, respectively. As the external shear strain is increased, the domain wall shifts (reversibly), so that no shear stress σ_{12} arises and the configuration shows an ideally soft behavior.

An important issue is the complete reversibility of the described domain wall motion: Upon unloading, the configuration returns to its initial state. Therefore, the reversible domain wall motion in the linear small-signal behavior regime is not to be confused with irreversible ferroelectric switching. Although the domain walls are only shifted by small distances typically below 1nm, the reversible domain wall motion has a significant effect on the small-signal parameters. This shall be illustrated by a small example: A 0.5nm shift of both domain walls towards each other in a configuration as depicted in Figure 5.12 evoked by an applied electric field $E_2=1.6\times10^5$V/m results in a change $\Delta D_2=1.16\times10^{-3}$C/m^2 averaged over the complete system. On the contrary, when considering a monodomain state without domain walls, an electric field of $E_2=2.8\times10^6$V/m would be necessary to evoke a similar change of D_2 in the configuration. An investigation of the large-signal behavior of the $90°$ domain stack shows the high idealization of this domain structure: For instance, upon loading the configuration by applying an electric field E_2, the domain walls shift towards each other until one domain type is extincted and a monodomain state is reached. When the load on the system is increased further, it exhibits a pure monodomain behavior. Since there are no imperfections in the material where domains

could nucleate, the system remains in the monodomain state when the applied load is reversed. Therefore, no representative coercive field strength can be determined for the 90° domain stack, since the electric field required to switch the configuration to a monodomain state just represents the electric field necessary to overcome the externally applied mechanical strain and is therefore predefined by the boundary conditions.

Although the regarded 90° domain stack represents a highly idealized system and therefore shows artificial behavior like for instance the completely soft response under shearing in the x_1-x_2-plane, it is very well suited for understanding the effect of reversible domain wall motion. This effect will turn out to be the governing process on domain effective small-signal parameters.

5.4.4. 90° domain stack containing charged defects

In the previous section, the idealized 90° domain stack without any imperfections has been considered. In the next step, electrically charged defects as they occur in real ferroelectric ceramics will be taken into account additionally. Their interactions with 90° domain walls will be investigated as well as the influence of electrically charged defects on the small-signal and large-signal behavior of the 90° domain stack.

For this, basically the same configuration as for investigating the ideal 90° domain stack is employed, except for two charged defects of different polarity located at the center of the equilibrium domain walls that are added to the configuration. Due to the incorporated charged defects, the periodically continued configuration is no longer homogeneous in x_2- and x_3-direction as it was for the ideal 90° domain stack, since the dimension of the simulation box in x_2-direction now defines the distance between neighboring charged defects in x_2-direction. The dimensions of the simulation box are chosen 25×60nm, representing the biggest possible configuration[3] that still allows for a mesh-density of seven nodes per nanometer in the surrounding of the domain walls as requested by the meshing study performed in section 4.6. In Figure 5.15 the structure and the equilibrium solution of the considered 90° domain stack are plotted, showing the impact of the oppositely charged defects on the shape of the domain wall.

Proceeding in the same manner as for the ideal 90° domain stack, a configuration containing defects charged by $q=\pm5\times10^{-10}$C/m has been loaded electrically and mechanically along the axes of the simulation box, yielding the following set of small-signal parameters for PTO:

$$\kappa_{ij}^{\varepsilon}(\text{PTO}) = \begin{pmatrix} 33.7 & 0 & 0 \\ 0 & 64.2 & 0 \\ 0 & 0 & 61.3 \end{pmatrix} \kappa_0 \tag{5.28}$$
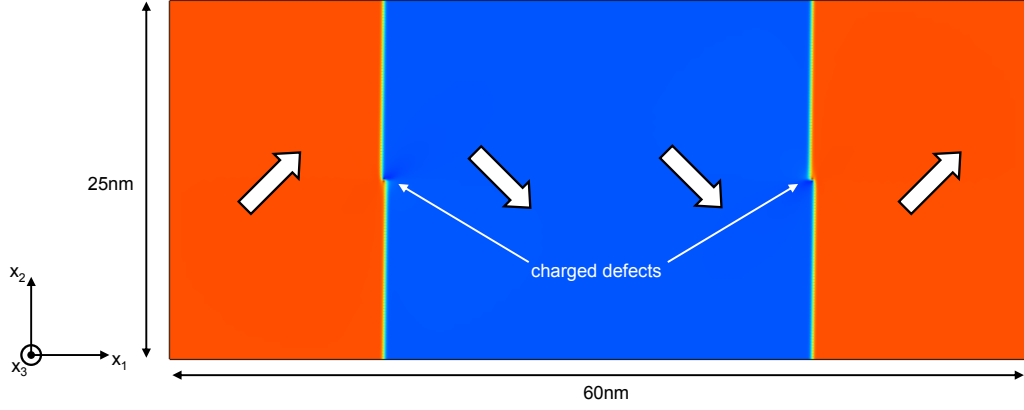
---

[3]regarding the available computational resources

122

Figure 5.15.: Equilibrium solution of the investigated 90° domain stack containing two defects electrically charged by $q=\pm5\times10^{-10}$C/m. The color coding illustrates the polarization component P_2. It can be seen that the electrically charged defects affect the shape of the 90° domain walls.

$$e_{ij}(\text{PTO}) = \begin{pmatrix} 2.66 & 0.23 & 0.41 & 0 & 0 & 0 \\ 0 & 0 & 0 & 0 & 0 & 4.53 \\ 0 & 0 & 0 & 0 & 1.38 & 0 \end{pmatrix} \text{C/m}^2 \tag{5.29}$$

$$c_{ij}^E(\text{PTO}) = \begin{pmatrix} 303.9 & 100.8 & 121.5 & 0 & 0 & 0 \\ 100.8 & 303.6 & 121.4 & 0 & 0 & 0 \\ 121.5 & 121.4 & 339.3 & 0 & 0 & 0 \\ 0 & 0 & 0 & 104.7 & 0 & 0 \\ 0 & 0 & 0 & 0 & 104.3 & 0 \\ 0 & 0 & 0 & 0 & 0 & 67.2 \end{pmatrix} \text{GPa} \tag{5.30}$$

Due to the same loading and boundary conditions, these small-signal parameters can directly be compared to those obtained from the ideal 90° domain stack. The main difference arises for the elasticity tensor component c_{66}^E: It is non-zero for the 90° domain stack containing charged defects, implying that this configuration no longer exhibits a completely soft response to applied shear strains ε_{12} in the x_1-x_2-plane. This indicates an interaction of the electrically charged defect with the 90° domain wall: The charged defects obviously pin the domain walls and thereby hinder them from moving freely as found for the ideal 90° domain stack. The effect of domain wall pinning by electrically charged defects also explains the significantly lowered dielectric permittivity tensor component κ_{22}^ε (35% of its original value) as well as the piezoelectricity tensor component e_{26} (34%) compared to the respective values obtained from the ideal 90° domain stack. However, the respective small-signal parameters for an applied electric field

in x_2-direction as well as for applied shear strains ε_{12} in the x_1-x_2-plane are elevated with respect to the monodomain values, indicating that the domain walls are in fact pinned by the electrically charged defects, but allowed to bend in between and therefore contributing to the small-signal parameters. The effect of domain wall bending becomes evident from Figure 5.16: The domain configuration as shown in Figure 5.15 containing charged defects of $q=\pm 5 \times 10^{-10}$C/m is loaded electrically in x_2-direction. The diagram illustrates the polarization profile P_2 along a path in x_2-direction at the equilibrium domain wall position, i.e. for x_1=15nm. The sharp spike of P_2 at the center indicates the position of the charged defect in the domain wall. For the unloaded case, i.e. E_2=0, the polarization P_2 becomes zero at the edges, implying that the center of the domain wall is located exactly at x_1=15nm. As the electric field E_2 is increased, the domain wall moves in x_1-direction at the edges of the configuration while it is still pinned to the charged defect at the center, and a bending of the domain wall can be observed. For E_2=2.5$\times 10^7$V/m, the polarization P_2 reaches its spontaneous value $\frac{P_0}{\sqrt{2}}$ in wide parts of the considered path: Hence, the domain wall that is still pinned to the charged defect has passed the position x_1=15nm by bending. Like the domain wall motion observed for the ideal 90° domain stack, the domain wall bending under small electrical or mechanical loading is a completely reversible phenomenon.

The large-signal behavior of a 90° domain stack that contains electrically charged defects is illustrated in Figure 5.17: The configuration is loaded electrically in x_2-direction for two differently charged defects pinning the 90° domain walls. For a critical electric field E_2, the domain wall can tear off the charged defect. This critical field depends on the charge density of the defect. Once the domain wall has separated from the defect, it behaves like a free domain wall in an ideal 90° domain stack. Note that the small deviations from the ideal 90° domain stack originate from perturbed regions in the close vicinity of the charged defects.

5.4.5. Monocrystalline multidomain configurations

So far, the behavior of monodomains as well as elementary domain structures has been discussed. In order to further increase the complexity towards realistic ferroelectric bulk domain structures, the next step is considering multidomain structures consisting of a combination of the domain patterns investigated in the previous sections. At first, configurations are treated that contain no imperfections and are monocrystalline, i.e. do not contain grain boundaries.

Figure 5.18 illustrates such a PZT multidomain configuration. The domain structure in the two-dimensional FE-model (cf. section 4.4.2) is stabilized in the x_1-x_2-plane by controlling the global strains

$$\tilde{S}_{11} = \tilde{S}_{22} = \frac{e_{\parallel} + e_{\perp}}{2}, \tag{5.31}$$

while in x_3-direction a state of plain strain $\varepsilon_{33} = e_{\perp}$ is deployed. A random polarization dis-
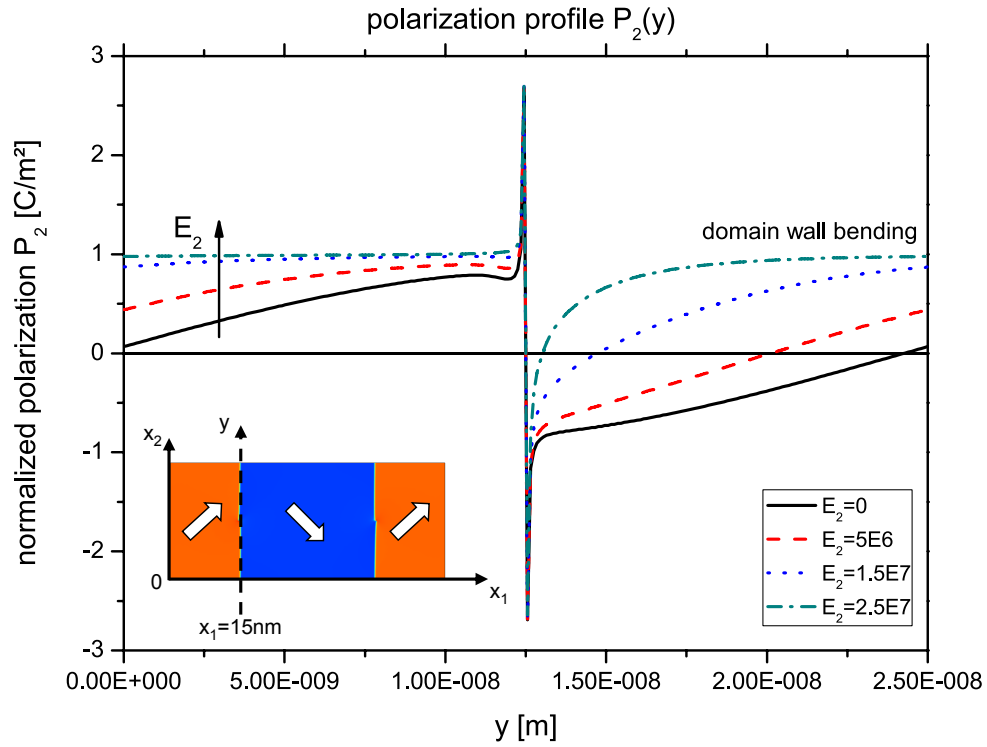
Figure 5.16.: A 90° domain stack containing electrically charged defects ($q=\pm5\times10^{-10}$C/m) is loaded by an applied electric field E_2. For different loading steps, the profile of the normalized polarization $P_2(y)$ along the path y as depicted in the schematical inset is plotted. While the domain wall is pinned by the charged defect (polarization spike at y=12.5nm), the polarization profile indicates a growing domain wall bending as the electric field E_2 is increased.
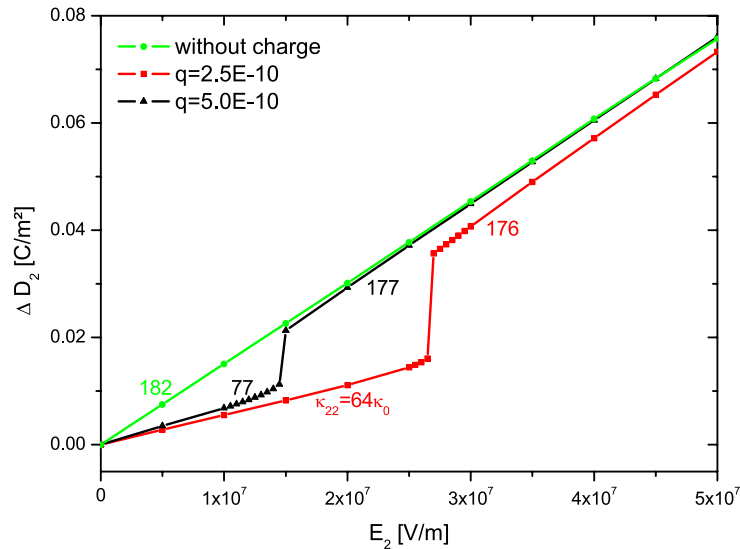

Figure 5.17.: Large-signal behavior of the 90° domain stack containing charged defects: For a critical electric field, the pinned domain walls can tear off the charged defect and afterwards show the behavior of free domain walls. The numbers in the plot indicate the respective dielectric permittivity components $\kappa_{22}\varepsilon$ when the domain is pinned and after it is torn off the charged defect.

tribution has been chosen as an initial condition for the 25×40nm sized configuration. The resulting domain pattern exhibits a net polarization of

$$\vec{P}^{\text{net}} = \begin{pmatrix} 0.33 \\ -0.17 \\ 0.01 \end{pmatrix} \text{C/m}^2 \tag{5.32}$$

and consists of five of the six possible tetragonal domain types. Due to the plain strain condition in x_3-direction the polarization is mainly oriented in the x_1-x_2-plane, and it is only at locations where different domain walls intersect that the polarization fractions P_3^+ and P_3^- arise. Electrical and mechanical loading along the axes of the simulation box yields the following set of small-signal parameters:
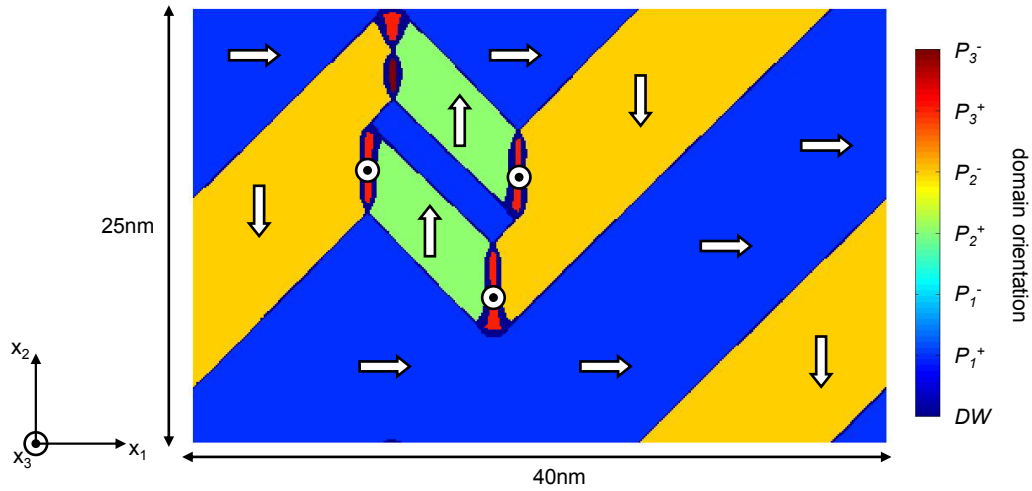
Figure 5.18.: Monocrystalline PZT multidomain structure: The 25×40nm sized configuration contains five different domain types.

$$\kappa_{ij}^{\varepsilon}(\text{PZT}) = \begin{pmatrix} 536 & 345 & -15.7 \\ 345 & 401 & -9.2 \\ -16.4 & -9.7 & 123 \end{pmatrix} \kappa_0 \tag{5.33}$$

$$e_{ij}(\text{PZT}) = \begin{pmatrix} 26.2 & -24.2 & -0.67 & 0 & 0 & -0.34 \\ 16.4 & -16.5 & -0.58 & 0 & 0 & 1.27 \\ -0.89 & 0.44 & 0.40 & -0.45 & 0.93 & 0 \end{pmatrix} \text{C/m}^2 \tag{5.34}$$

$$c_{ij}^E(\text{PZT}) = \begin{pmatrix} 200.9 & 250.9 & 117.3 & 0 & 0 & 0 \\ 250.6 & 211.6 & 110.2 & 0 & 0 & 0 \\ 117.3 & 110.2 & 358.5 & 0 & 0 & 0 \\ 0 & 0 & 0 & 89.6 & 0 & 0 \\ 0 & 0 & 0 & 0 & 89.3 & 0 \\ 0 & 0 & 0 & 0 & 0 & 88.2 \end{pmatrix} \text{GPa} \tag{5.35}$$

An exact interpretation of all components of the small-signal parameter tensors obtained from multidomain configurations is complicated due to the fact that they represent superpositions of various effects: In addition to the intrinsic behavior of all involved domains they contain extrinsic contributions from reversible domain wall motion and bending as well as interactions between different domain walls. Nevertheless, some conclusions can be drawn based on the small-signal parameters: For instance, the off-diagonal components of the dielectric permittivity tensor must originate from extrinsic effects like reversible domain wall motion since they cannot be explained by a linear combination of the intrinsic properties of the tetragonal domain types. Negative off-diagonal components of the dielectric permittivity tensor indicate growing domains in the direction of the applied electric field at the expense of perpendicularly oriented ones. In order to analyze and interpret single components of the small-signal parameter tensors, the information about the present domain fractions and their development under the specific loading condition is essential, as will be shown exemplarily for the component e_{22} of the piezoelectricity tensor: The relatively high value (compared e.g. to the monodomain) indicates extrinsic contributions like the reversible domain wall motion. An analysis of the domain types present in the configuration is shown in Figure 5.19a. For e_{22}, the development of the domain types P_2^+ and P_2^- under an applied strain ε_{22} is of interest (Fig. 5.19b): While P_2^- increases by 0.09% under the applied strain, P_2^+ grows by only 0.4% at the same time, decreasing the net polarization P_2 in the configuration and thereby causing a negative e_{22}. This example reveals the necessity of tracking the domain fractions in the system while obtaining small-signal parameters in order to allow for a proper interpretation of the results.

For the purpose of attaining input parameters for micromechanical modeling methods, various multidomain configurations for both PTO and PZT have been investigated concerning small-signal parameters and domain fractions under electromechanical loading. Several parameters can be varied in the phase-field model and show implications on the resulting domain structure:

- The size of the simulation box defines the periodicity of the occurring domain pattern and therefore the maximum allowed size of individual domains in the system.

- The aspect ratio between the x_1-dimension and the x_2-dimension of the simulation box is an important issue affecting the resulting domain structure since the polarization, the
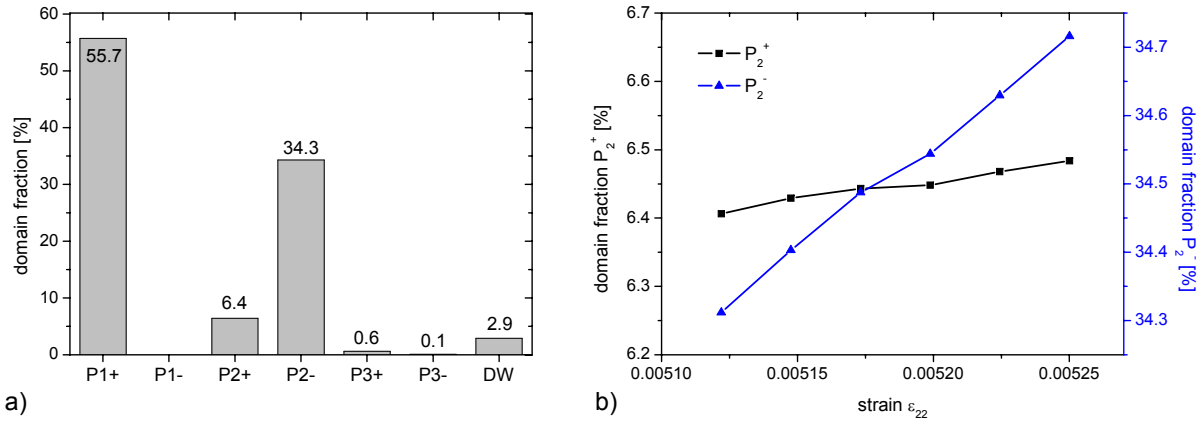
Figure 5.19.: (a) Domain fractions of the monocrystalline multidomain configuration shown in Figure 5.18 (b) Influence of an applied strain ε_{22} on the resulting development of the domain fractions P_2^+ and P_2^-.

electric potential and the mechanical strains are periodically continued at the edges of the structure. For instance, when the axes of the simulation box coincide with the crystallographic orientation, a perfect 90° domain stack is only possible for a whole-number aspect ratio, whereas other aspect ratios enforce a domain structure consisting of at least three different domain types.

- In order to mechanically stabilize the domain configuration, a global strain is applied in the x_1-x_2-plane as a boundary condition, showing an impact on the resulting domain structure, and especially on the development of polarization fractions in x_3-direction.

- For a specific set of parameters for the configuration size, the aspect ratio and the global strain boundary condition, more than one domain configuration can evolve. Therefore, different (random) initial conditions for the polarization distribution are taken into account, yielding different domain patterns. This is caused by the underlying free energy landscape which can exhibit more than one stable minimum due to the respective boundary conditions.

In Appendix A.3, a compilation of all investigated monocrystal multidomain configurations for PTO and PZT is shown. For all configurations the obtained domain effective small-signal parameters as well as the domain fractions were transferred to the COMFEM project partners und served as input parameters for micromechanical modeling methods. A detailed evaluation of the considered monocrystalline multidomain configurations can be found in [50].

5.4.6. Monocrystalline domain configuration containing charged defects

The influence of defects on the monodomain and the 90° domain stack has already been discussed in sections 5.4.2 and 5.4.4. In the following, electrically charged (line) defects in

monocrystalline multidomain configurations are taken into account in order to investigate their impact on the resulting domain structure and their influence on the small-signal behavior. In Figure 5.20 the considered PTO multidomain configuration is illustrated. The same boundary
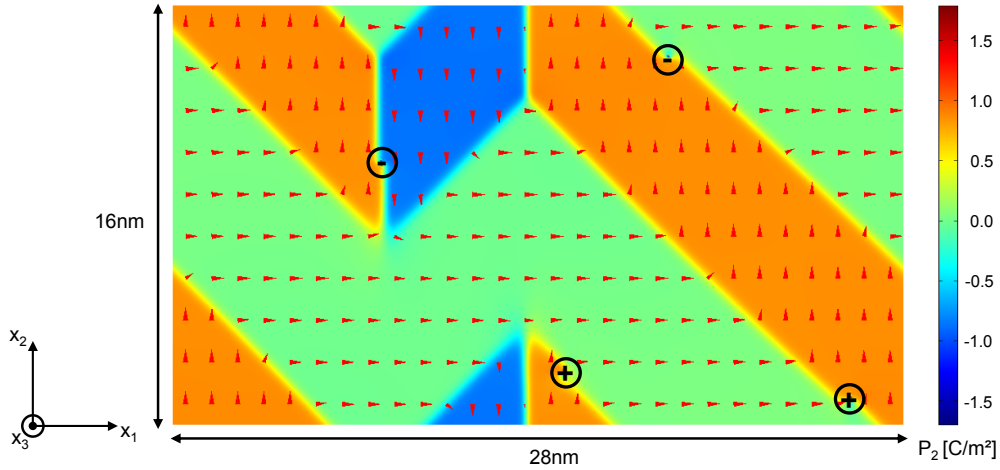

Figure 5.20.: Monocrystalline PTO multidomain configuration containing four electrically charged defects, which are randomly distributed. All charged defects are located within 90° and 180° domain walls, which is remarkable since a random polarization distribution had been chosen as initial condition for the FE-calculation.

conditions as in the previous section are applied to the 16x28nm sized simulation box, which now contains four randomly distributed electrically charged defects: Two defects are positively charged by $q=5\times10^{-10}$C/m and two are negatively charged by $q=-5\times10^{-10}$C/m, thereby ensuring the neutrality of charges in the configuration.

A random distribution of the polarization served as the initial condition for the FE-calculation, yielding the ferroelectric domain structure depicted. It consists of three domain types and exhibits a net polarization of

$$\vec{P}^{\text{net}} = \begin{pmatrix} 0.47 \\ 0.24 \\ 0 \end{pmatrix} \text{C/m}^2. \tag{5.36}$$

A remarkable effect of charged defects on multidomain configurations becomes evident from the resulting domain structure: All defects are located within the domain walls. In other words, it becomes energetically favorable for both 90° and 180° domain walls to agglomerate at immobile electrically charged defects in a ferroelectric multidomain configuration. The FE-calculation has been repeated for several randomly chosen polarization distributions, every time yielding domain configurations for which the charged defects coincide with the domain walls. Furthermore, kinks in the domain walls are observed at the sites of the charged defects as already found before in the 90° domain stack containing charged defects (cf. Figure 5.15).

The shape of these kinks in the domain walls depends on the polarity of the charged defect, indicating an electrical interaction between the defect and the domain wall.

In order to describe this interaction quantitatively, the permittivity tensor $\kappa_{ij}^{\varepsilon,\mathrm{q}=5\mathrm{E}-10}$ for the configuration shown in Figure 5.20 has been evaluated. Additionally, the same configuration has been computed in the absence of charged defects: Taking the equilibrium solution of the multidomain configuration that contains charged defects as initial configuration, a FE-calculation has been performed omitting the electrically charged defects. From the resulting defect-free domain structure that exhibits approximately the same domain fractions as the configuration with defects, the permittivity tensor $\kappa_{ij}^{\varepsilon,\mathrm{q}=0\mathrm{E}-10}$ was obtained. Both permittivity tensors can now be compared directly by computing the relative difference $\kappa_{ij}^{\varepsilon,\mathrm{diff}}$ between them:

$$
\left.
\begin{aligned}
\kappa_{ij}^{\varepsilon,\mathrm{q}=0\mathrm{E}-10} &= \begin{pmatrix} 219 & -135 & 0 \\ -135 & 204 & 0 \\ 0 & 0 & 62 \end{pmatrix} \kappa_0 \\
\kappa_{ij}^{\varepsilon,\mathrm{q}=5\mathrm{E}-10} &= \begin{pmatrix} 178 & -132 & 0 \\ -120 & 217 & 0 \\ 0 & 0 & 62 \end{pmatrix} \kappa_0
\end{aligned}
\right\}
\kappa_{ij}^{\varepsilon,\mathrm{diff}} = \begin{pmatrix} -19\% & -1\% & 0 \\ -12\% & +7\% & 0 \\ 0 & 0 & 0 \end{pmatrix} \quad (5.37)
$$

A clear influence of the electrically charged defects on the dielectric permittivity in the x_1-x_2-plane can be seen. Since the domain configurations exhibit no polarization in x_3-direction, the permittivity component κ_{33} remains unaffected by the charged line defects. It can be assumed that the decline of some components of the permittivity tensor is caused by the same mechanisms as discussed for the 90° domain stack containing charged defects (cf. section 5.4.4): Domain walls become pinned by their interaction with electrically charged defects so that the reversible domain wall motion for small applied loads is restricted. However, a main difference becomes obvious: Although the multidomain system is clamped by the charged defects, their influence on the permittivity is much lower than that of the 90° domain stack. This is caused by the multiple domains available in the configuration and by interactions between 90° and 180° domain wall systems, providing more flexibility for the configuration to respond to external loads. Therefore, by clamping certain domain types while not affecting others, charged defects can even enhance single components of the dielectric permittivity tensor as found for κ_{22} while decreasing other components at the same time.

5.4.7. Polycrystalline multidomain configurations

Up to this point, only domain configurations in monocrystals have been taken into account. However, ferroelectric ceramics like PTO and PZT exhibit a polycrystalline structure on the

micro-scale and grain boundaries, i.e. interface regions between grains of different crystallographic orientation that represent an essential part of such polycrystalline structures. The influence of grain boundaries on the small-signal and large-signal behavior of ferroelectric multidomain configurations is the subject of the following investigation.

In order to take grain boundaries in the FE phase-field model into account, a configuration needs to be found that contains several regions of different crystallographic orientation while still providing the possibility of being continued periodically. A honeycomb-like structure as depicted in Figure 5.21a turned out to fulfill those requirements: The unit cell of this structure
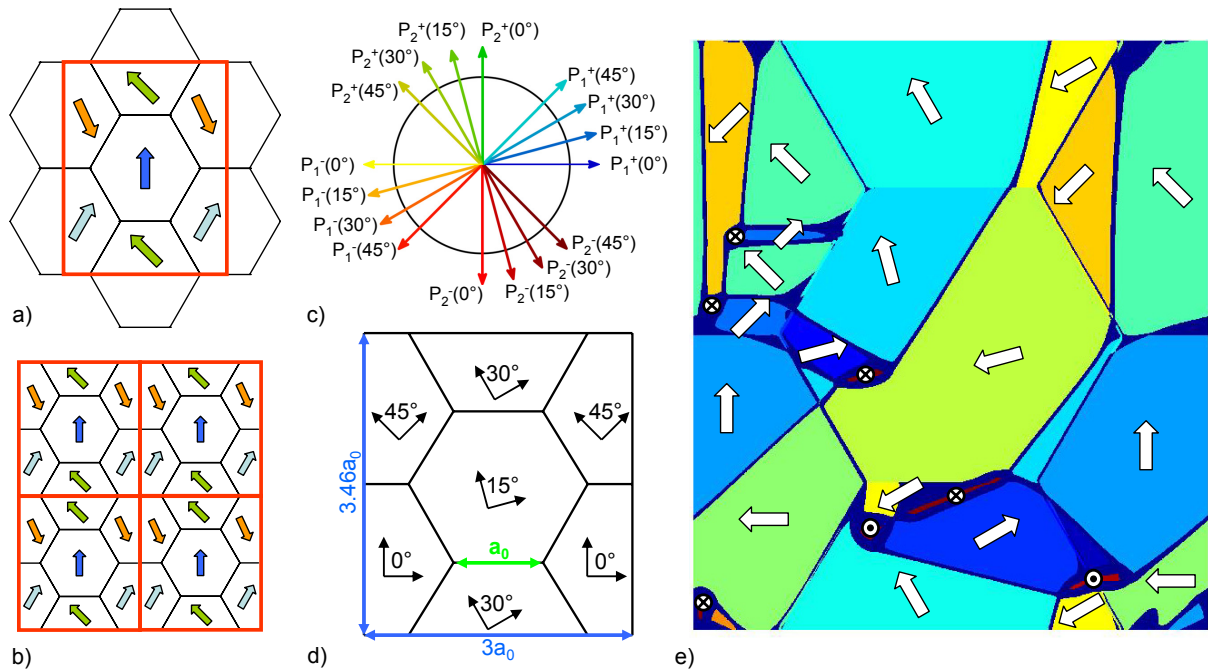
Figure 5.21.: Polycrystalline multidomain configuration: (a) Unit cell (i.e. simulation box) of the honeycomb-like configuration. (b) Periodically continued unit cells, yielding an infinitely expanded honeycomb structure consisting of four distinguished regions. (c) & (d) Different crystallographic orientations are assigned to the hexagons in the unit cell, resulting in a configuration of 18 available domain types: four domain types in the x_1-x_2-plane for each crystallographic orientation plus two domain types in x_3-direction. (e) Resulting polycrystalline PZT multidomain configuration (a_0=10nm) containing 15 different domain types.

consists of a regular hexagon at the center and parts of its six next neighbors. As the unit cell, i.e. the simulation box, is continued periodically, an infinitely expanded regular honeycomb structure arises that consists of four different regions (Fig. 5.21b): They represent the regions of different crystallographic orientation in the polycrystal model. The edges of the regular hexagons represent a basic length a_0. Thus, as depicted in Figure 5.21d, the dimensions of the unit cell (and therefore the simulation box) become $3a_0$ in x_1-direction and $2 \times \sqrt{3}a_0 = 3.46a_0$ in x_2-direction.

For the subsequent investigation of the small-signal behavior, a PZT configuration with a_0=10nm

will be considered, resulting in a 30×34.6nm sized simulation box. In the four regions of different crystallographic orientation, the crystallographic coordinate system is rotated in the x_1-x_2-plane with respect to the simulation box coordinate system by angles of $0°$, $15°$, $30°$ and $45°$, respectively, as illustrated in Figure 5.21d. Therefore the directions of polarization as classified in Figure 5.21c are possible in the x_1-x_2-plane. In combination with the two available domain orientations in x_3-directions this makes a total of 18 available domain types in the configuration. Taking a random polarization distribution as initial condition yields the polycrystalline multidomain configuration illustrated in Figure 5.21e. It consists of 15 different domain types (out of 18 available) and exhibits a net polarization of

$$\vec{P}^{\text{net}} = \begin{pmatrix} -0.278 \\ 0.242 \\ -0.003 \end{pmatrix} \text{C/m}^2. \tag{5.38}$$

It has been discussed before that periodically continued monocrystalline domain configurations require a mechanical domain stabilization, in order to keep them from striving towards a monodomain state when the periodically continued configuration is held globally stress-free. As it turns out, this is no longer necessary for polycrystalline configurations as depicted in Figure 5.21: The mismatch of the differently oriented regions and the resulting inhomogenities in the honeycomb structure supress the developement of a pure monodomain state, and even in the abscence of a global strain control a stable multidomain configuration arises in the x_1-x_2-plane. However, in order to ensure comparability with previously calculated small-signal parameters, the same global strain control as for the monocrystalline multidomain configuration is applied in the x_1-x_2-plane (cf. eqn. 5.31), and a state of plain strain $\varepsilon_{33} = e_\perp$ is employed in x_3-direction.

Proceeding in the same manner as for the monocrystalline multidomain configurations, electrical and mechanical loading along the axes of the simulation box yields the following set of small-signal parameters:

$$\kappa_{ij}^\varepsilon(\text{PZT}) = \begin{pmatrix} 212 & 172 & 1.9 \\ 116 & 501 & 10.8 \\ 4.2 & 14.8 & 142 \end{pmatrix} \kappa_0 \tag{5.39}$$

$$e_{ij}(\text{PZT}) = \begin{pmatrix} -8.47 & 6.12 & -0.11 & 0.04 & -0.01 & -3.08 \\ -14.9 & 11.6 & -0.45 & 0.09 & -0.06 & -13.8 \\ -0.27 & 0.25 & -0.03 & 0.93 & -0.94 & -0.134 \end{pmatrix} \text{C/m}^2 \tag{5.40}$$

$$c_{ij}^E(\text{PZT}) = \begin{pmatrix} 299.7 & 157.2 & 113.4 & 0 & 0 & 0 \\ 157.7 & 309.8 & 114.6 & 0 & 0 & 0 \\ 113.2 & 114.5 & 358.0 & 0 & 0 & 0 \\ 0 & 0 & 0 & 89.3 & 0 & 0 \\ 0 & 0 & 0 & 0 & 89.3 & 0 \\ 0 & 0 & 0 & 0 & 0 & 74.0 \end{pmatrix} \text{GPa} \qquad (5.41)$$

These small-signal parameters not only represent a superposition of the intrinsic and extrinsic behavior of different domain types as was the case for monocrystalline multidomain structures, but also a superposition of various crystallographically oriented regions. Although this complicates an exact interpretation of all components of the small-signal tensors, certain trends become obvious. For instance, the plain strain condition in x_3-direction becomes apparent from the components κ_{33}^ε and c_{33}^E which are similar to their counterparts from the investigation of monocrystalline multidomain configurations. The configuration shows a high sensitivity to electrical loads in x_2-direction and to applied shear strains in the x_1-x_2-plane, as can be seen from the relatively high κ_{22}^ε and e_{26} as well as a relatively low c_{66}^E. This indicates a similarity to the 90° domain stacks discussed in sections 5.4.3 and 5.4.4. Indeed, as can be found from Figure 5.21e, the domain pattern within the grains mainly consists of 90° domain walls and it partially shows the behavior of a 90° domain stack as expected. When comparing the small-signal parameters of the polycrystalline multidomain configuration to those obtained from a monocrystalline configuration, most components are found to be smaller. This denotes an interaction between the domain walls and the grain boundaries: The lattice mismatch, and therefore the polarization mismatch, evokes internal electric fields at grain boundaries, which in turn may influence domain walls as well as mechanisms like the reversible domain wall motion and bending, and consequently influence the dielectric, piezoelectric and elastic sensitivity. Note that domain walls in the discussed configurations are able to intersect grain boundaries.

In order to investigate the large-signal behavior of polycrystalline multidomain structures, a PTO configuration with a_0=5nm, i.e. a 15×17.3nm sized simulation box, has been considered, exhibiting an initial net polarization of (-0.58 / 0.27 / 0) C/m^2. First, an electrical load E_1 is applied to the configuration in positive x_1-direction as illustrated in Figure 5.22. The domain walls start shifting from their equilibrium positions, and domains exhibiting an energetically favorable orientation with respect to the applied electric field grow at the expense of others. In this regime, all processes are reversible, and unloading the configuration would yield the initial state again. For a critical electric field (corresponding to approx. $0.2E_{C180}$), macroscopic domain switching in the configuration is initiated, leading to a completely different domain structure that now shows a net polarization in positive x_1-direction. Note that the spontaneously
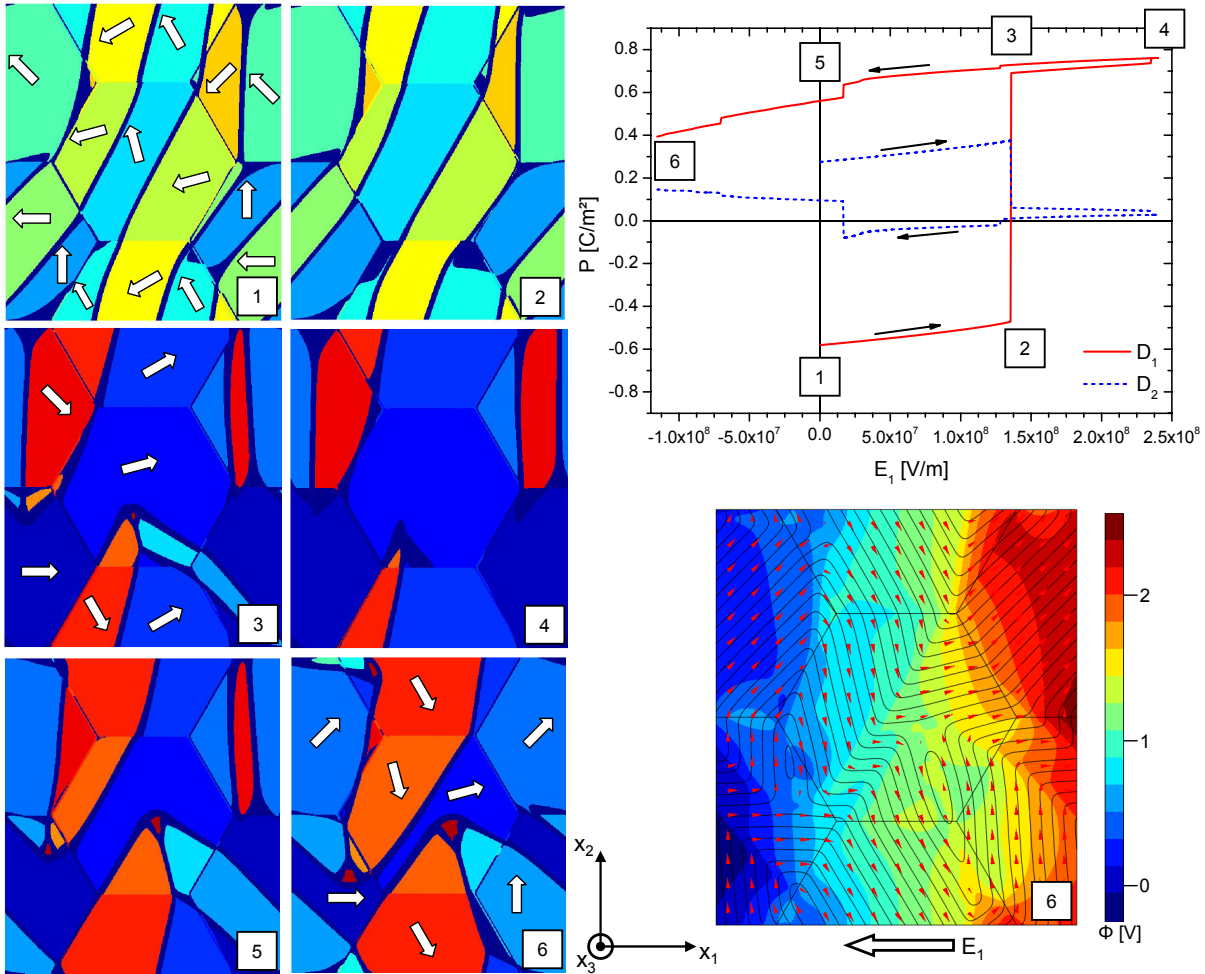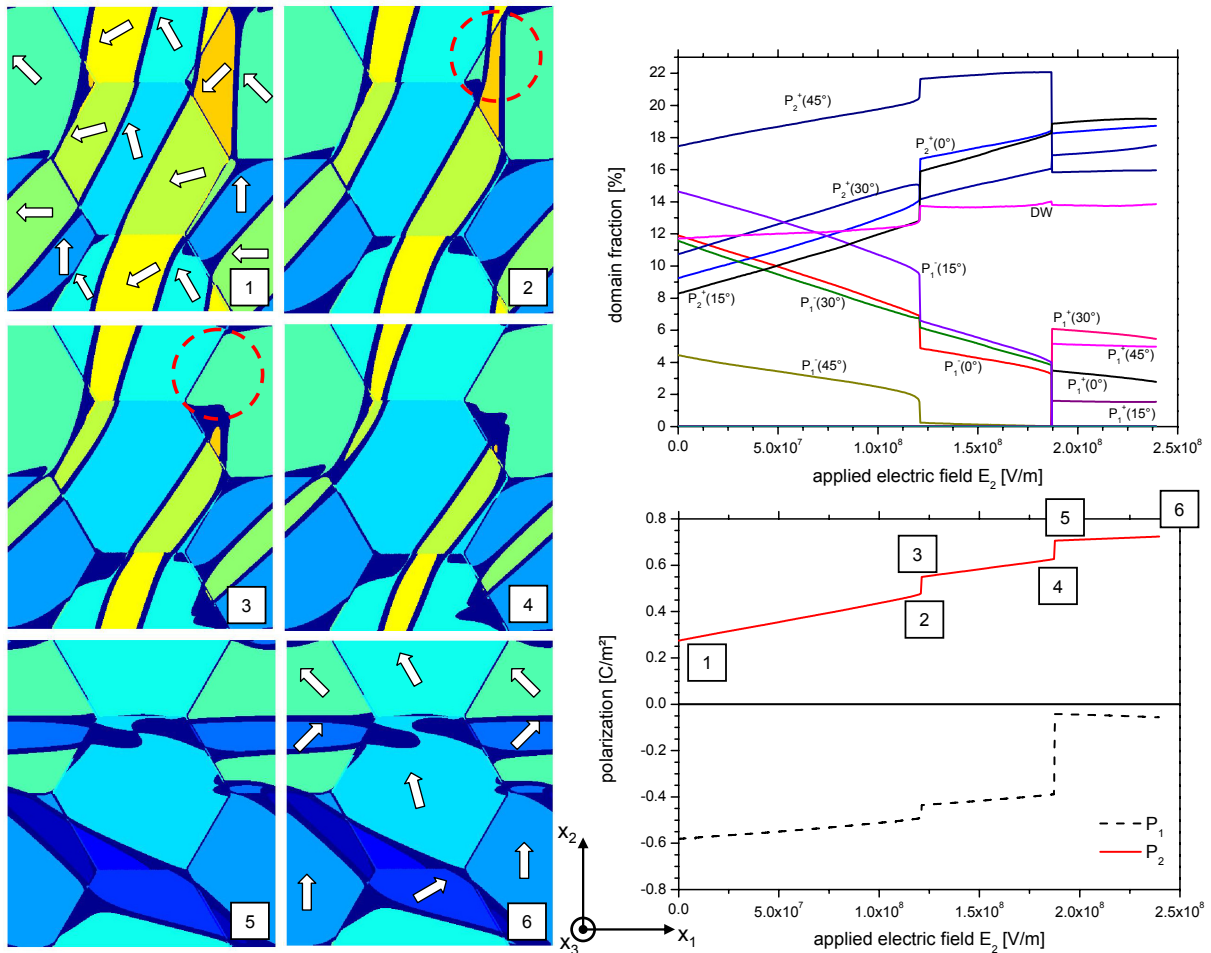
Figure 5.22.: Investigating the large-signal behavior of polycrystalline PTO multidomain configurations: Starting with an initial configuration (1), an electric field E_1 is applied in x_1-direction, initiating irreversible switching (2→3). Upon unloading a hysteresis behavior is found, so that the initial configuration cannot be restored. For one loading case (6) the electric potential within the configuration is plotted, showing internal fields caused by domain walls and grain boundaries.

initiated switching is caused by the quasistatic loading of the configuration. As the electric field is raised further, only minor switching processes take place, poling the configuration increasingly in the direction of the applied field. Upon unloading the electric field, the configuration relaxes, and new domain types nucleate at grain boundaries. This back-switching is indicated by small steps in the unloading polarization curves. The domain configuration of the field-free state significantly differs from the initial domain state, indicating irreversible switching processes and a hysteresis behavior. For an exemplary loading step in negative x_1-direction, the electric potential within the polycrystalline domain structure is illustrated in Figure 5.22: The internal inhomogeneity of the system caused by grain boundaries and domain walls becomes cleary visible.

Furthermore, as shown in Figure 5.23, the polycrystalline multidomain structure was electrically loaded in x_2-direction, starting with the same initial condition as before. Here, the development of the domain fractions under electric loading is depicted additionally. In contrast to the loading in x_1-direction, the first occurring irreversible switching process (2→3) does not cause a reorientation of the whole domain configuration, but only the extinction of one certain domain type. Nevertheless this represents an irreversible process, so that unloading the configuration would not restore the initial state. As the electric field E_2 is further increased, a second irreversible

Figure 5.23.: Investigating the large-signal behavior of polycrystalline PTO multidomain configurations: The same configuration as analyzed in Figure 5.22 is now loaded electrically in x_2-direction. Along with the development of the polarization components, the domain fractions under electric loading are shown. Irreversible switching occurs in steps (2→3) and (4→5).

switching process is initiated (4→5), now poling the domain configuration in the direction of the applied electric field. When analyzing the large-signal behavior of various polycrystalline multidomain configurations, a strong anisotropy has been found regarding the direction of the applied field and the net polarization of the domain pattern: When the electric field was applied in the direction of the net polarization, irreversible switching was initiated for higher electric

fields compared to the case of a net polarization orientation opposite or perpendicular to the applied field. Coercive switching fields, i.e. electric fields that initiate irreversible reorientations of the ferroelectric domain pattern were found in the range from approximately 0.005 to $0.2E_{C180}$ for both PTO and PZT.

As for the monocrystalline multidomain configurations, several polycrystalline configurations have been computed and subsequently analyzed regarding the small-signal and large-signal behavior. The domain effective small-signal parameters as well as the development of the domain fractions under electromechanical loading provided input parameters for micromechanical modeling methods. A detailed analysis of the investigated polycrystalline multidomain configurations can be found in [50].

5.5. Discussion

In order to bridge the gap between phase-field modeling and micromechanical modeling methods in the multi-scale simulation chain, a phase-field model based on atomistic input parameters has been implemented into the FE-platform COMSOL Multiphysics. Miscellaneous ferroelectric domain structures on the meso-scale have been considered and investigated under electrical and mechanical loadings with the objective of gaining input parameters for micromechanical modeling methods. Therefore, numeric tools have been developed in order to evaluate small-signal and large-signal properties from the computed domain structures. Governing mechanisms taking place within the ferroelectric domain structure have been identified that strongly influence the electromechanical small-signal and large-signal behavior of ferroelectric ceramics on the meso-scale. In the following, the investigated domain configurations will be assessed and the results of the small-signal and large-signal analysis will be discussed in the context of a multi-scale simulation chain. Furthermore, possible enhancements of the phase-field model concerning point defects, temperature-dependence and the maximum possible configuration size will be presented in an outlook.

Assessment of investigated typical domain structures

As motivated in section 5.1, various domain configurations of increasing complexity have been investigated separately with respect to their behavior under electromechanical loading. Now, these typical domain structures shall be assessed with respect to their significance regarding real polycrystalline ferroelectric ceramics:

- The *monodomain state* represents regions of perfect structure in the material without any domain walls or imperfections. It shows the purely intrinsic behavior under electromechanical loading and therefore enables a verification of the FE-implementation, since the phase-field model itself has been adjusted to intrinsic input parameters from atomistic

calculations in the first place. More important, the coercive fields obtained from the monodomain state represent an upper limit, since no domain walls or imperfections are present that could initiate switching or the nucleation of new domains.

- The *90° domain stack* represents a two-domain configuration found in wide regions on the meso-scale of ferroelectric ceramics. Although the idealized model considered in section 5.4.3 exhibits artificial characteristics like a completely soft response when loaded by a shear strain ε_{12}, it represents the perfect model for investigating reversible domain wall motion as well as for providing upper limits of this extrinsic effect on the small-signal parameters. Properties of the 90° domain stack can directly be used as input parameters for micromechanical models describing configurations that mainly consist of this domain pattern: For instance, the small-signal parameters of the 90° domain stack obtained for PTO and PZT served as input parameters for a micromechanical model describing $\langle 111 \rangle$-oriented ferroelectric thin-films [75].

- *Monocrystalline multidomain configurations* exhibit an increased complexity of the domain structure when compared to the ideal 90° domain stack. Due to their monocrystalline character, the resulting domain patterns, mostly consisting of at least three different domain types, are highly symmetric. Though these domain patterns are artificial, the monocrystalline multidomain configurations are well-suited for investigating interactions between different domain walls as well as different domain systems.

- *Polycrystalline multidomain configurations* represent the most complex and inhomogeneous domain structures considered in this work. They allow for studying the effect of the crystallographic mismatch at grain boundaries on the domain configuration, especially the interaction between domain walls and grain boundaries. Polycrystalline multidomain configurations take all mentioned effects on the meso-scale into account, thus representing the most realistic domain structure considered. Note that the differently oriented regions are not to be understood as grains of a real ceramic, since their dimensions (the biggest diameter considered was 17nm) are much smaller than experimentally found grain diameters that are in the order of micrometers. Nevertheless, as will be shown below, polycrystalline multidomain configurations exhibit the most realistic large-signal behavior, therefore providing both small-signal and large-signal parameters for micromechanical modeling methods [50].

Small-signal analysis

In the course of the small-signal analysis of the domain configurations mentioned above, the effects of reversible domain wall motion and bending were identified as the governing mechanisms occurring in the ferroelectric domain structure under small applied external loadings.

Both effects, also denoted domain wall oscillation and domain wall bowing in literature, have been observed experimentally [16, 33, 83, 84] and represent extrinsic contributions to the piezo-electric, elastic and dielectric small-signal parameters. Being able to take the effects of reversible domain wall motion and bending into account represents one of the most striking benefits when using phase-field modeling in a multi-scale simulation chain for ferroelectric ceramics, since these effects, taking place on the meso-scale, exhibit a significant impact on the electromechanical behavior of ferroelectric materials.

Figure 5.24 illustrates a summary of both effects: For a $90°$ domain stack as discussed in Figure 5.12, three conditions for the domain walls under electrical loading are considered: For completely fixed domain walls, the ferroelectric material shows only the purely intrinsic behavior. If the domain walls are allowed to move ideally freely instead, the extrinsic contribution of the reversible domain wall motion becomes clearly visible, resulting in a dielectric response of the material that can exceed the intrinsic contribution up to a factor of 15-20. In the last con-
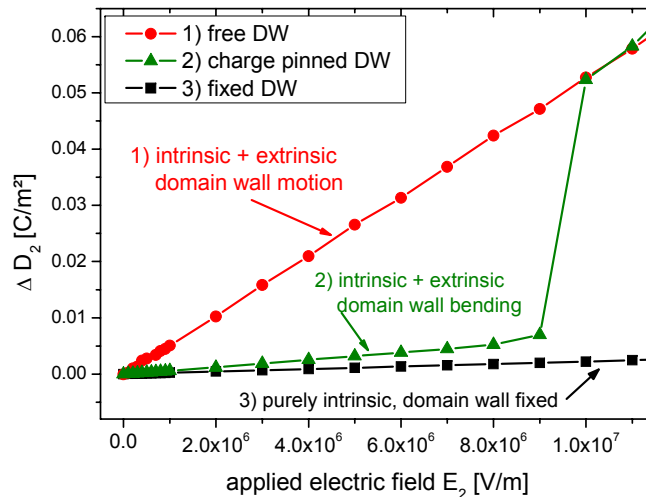
Figure 5.24.: A $90°$ domain stack is electrically loaded for three different conditions applied to the domain walls. The extrinsic contributions of reversible domain wall motion and bending become clearly visible from the different dielectric response behavior.

sidered case, the domain wall is pinned by electrically charged defects: Until a certain electric field is reached, the domain wall bends, exhibiting an extrinsic contribution that outranges the intrinsic contribution by a factor of up to 1-3. For higher applied electric fields, the domain wall tears off the charged defect and shows the behavior of the completely free domain wall. In real ferroelectric materials, extrinsic contributions of reversible domain wall motion and bending to the piezoelectric and dielectric small-signal properties have been observed that are at least in the order of the intrinsic effect caused by the lattice [17]. This indicates that domain wall bending is the dominant effect in real ferroelectric ceramics, corresponding to the fact that they nearly always contain electrical and mechanical effects that interfere with domain walls: By

mechanisms of clamping and pinning, the domain walls are inhibited from moving freely.

The effect of reversible domain wall motion can also be demonstrated by electrically loading a 90° domain stack as shown in Figure 5.12 under different angles in the x_1-x_2-plane. Figure 5.25 illustrates the change of the dielectric displacements ΔD_1 and ΔD_2 for electric fields applied
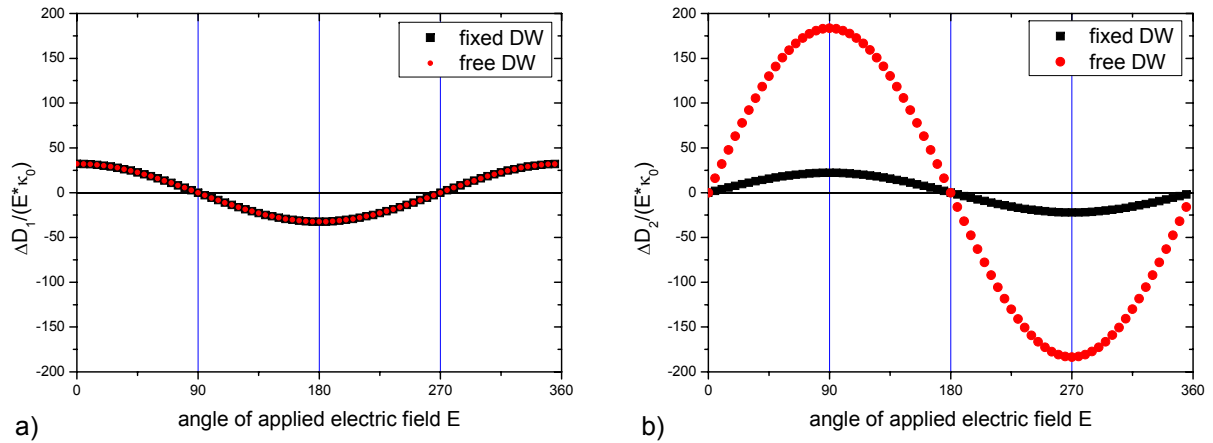

Figure 5.25.: In order to demonstrate the effect of reversible domain wall motion, a 90° domain stack is electrically loaded at different angles in the x_1-x_2-plane for the cases of completely fixed and completely free domain walls. An angle of zero degrees corresponds to the x_1-direction.

at different angles. Due to the symmetry of the considered 90° domain stack, only a domain wall motion in x_1-direction is permitted. The two cases of artificially fixed and completely free domain walls are considered. While ΔD_1 shows the same behavior in both cases, the extrinsic contribution of the reversible domain wall motion becomes apparent from the change of the dielectric displacement ΔD_2 (Fig. 5.25b): As expected for a shift of the domain walls in x_1-direction, ΔD_2 of the free domain walls exhibits a strongly amplified sensitivity when compared to the case of the fixed domain walls. Furthermore, the maxima of ΔD_2 appear at angles of 90° and 270°, corresponding to the directions that are most sensitive for initiating a reversible domain wall motion in x_1-direction.

Large-signal analysis

In the course of investigating typical ferroelectric domain structures, also their large-signal behavior has been taken into account. In this process, the coercive field strengths E_{C180} for 180° switching of a monodomain state have been determined from phase-field models that were adjusted to atomistic input parameters for PTO and PZT. In both cases, these coercive field strengths E_{C180} are in the order of 10^8V/m (cf. Table 5.2), which is about two orders of magnitude higher than experimentally measured coercive fields of polycrystalline ferroelectric ceramics [45]. Furthermore, when comparing the coercive fields (i.e. applied electric fields necessary for initiating irreversible switching processes) of the other investigated domain structures to

experimentally found coercive fields, the values obtained from the phase-field models are systematically too high. This deviation has several reasons: On the one hand, the coercive field strengths E_{C180} and E_{C90} are directly encoded in the free energy function of the phase field model. Figure 5.26 illustrates a hysteresis curve as well as contour plots of the electric enthalpy density ħ of 90° and 180° switching of a stress-free monodomain state. In this case, only the
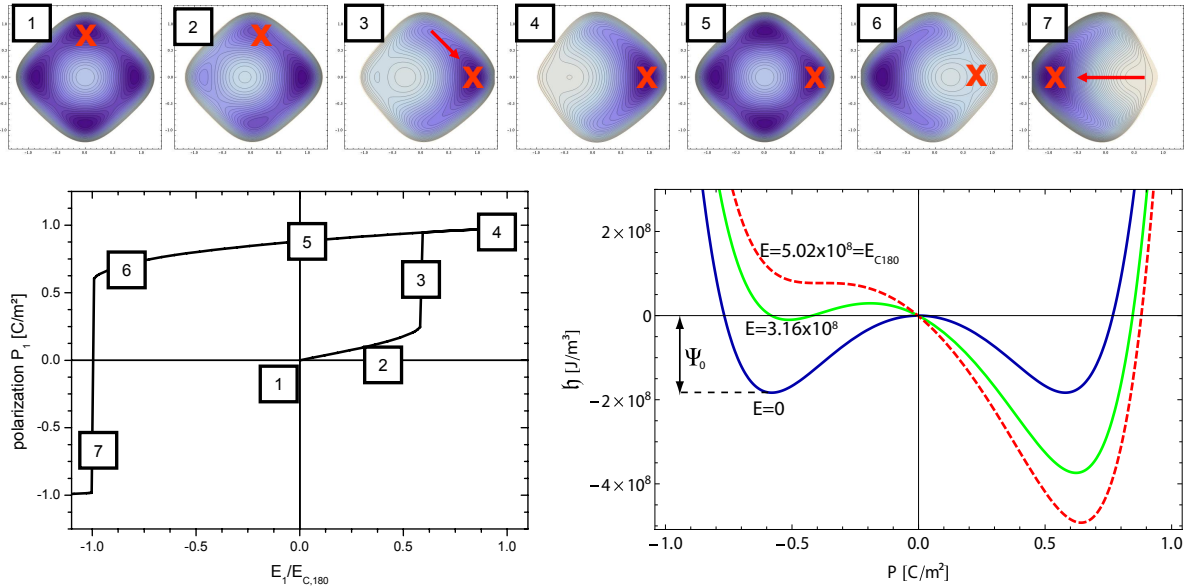

Figure 5.26.: Hysteresis curve for a PZT monodomain state. For certain loading steps, contour plots of the electric enthalpy function are depicted, and the state of the system in the energy landscape is indicated, respectively. The diagram on the lower right side illustrates the equilibrium state (E=0) of the electric enthalpy in $\langle 100 \rangle$ -direction as well as the impact of applied electric fields on the electric enthalpy. Switching does not occur until the elevated minimum becomes instable (E=E_{C180}).

Landau energy term and the electric field energy have to be taken into account, whereas the elastic energy term and the electromechanical coupling term compensate each other. The energy landscape of the electric enthalpy is tilted in the respective direction of the applied electric field, and switching occurs not until the local minimum, in which the system is located, becomes extinced. For 90° switching the system only has to overcome the energy barrier directly separating two minima. On the contrary, for 180° switching in a completely uniform and undisturbed monodomain state, the system takes the direct path for reaching the (global) minimum on the opposite side instead of switching two times by 90°. This behavior takes place due to the high symmetry of the perfect monodomain state and explains the fact that E_{C180} exceeds E_{C90}. However, once the symmetry is broken, for instance by a small disturbance in the form of an electrically charged defect, the 180° switching process becomes separated in two 90° switching processes, as already discussed in section 5.4.2. From the described switching behavior, it becomes apparent that the coercive fields of the monodomain state are encoded in the free energy

as the height of the energy wells to be overcome for the respective switching process. As illustrated in Figure 5.26 for a PZT energy function, Ψ_0 denotes the height of the 180° switching barrier in equilibrium, and therefore the coercive field strength E_{C180} can be roughly estimated as

$$E_{C180} \approx \frac{\Psi_0}{P_0} = \frac{1.833 \times 10^8 \text{J/m}^3}{0.58 \text{C/m}^2} = 3.16 \times 10^8 \text{V/m}, \tag{5.42}$$

being close to E_{C180}=5.02$\times 10^8$V/m determined in the respective simulation. The height of the energy barrier Ψ_0 cannot be adjusted directly in the free energy function. Instead, Ψ_0 is predefined in the adjustment process as described in chapter 2 by the spontaneous polarization P_0, the 180° domain wall energy as well as the dielectric permittivity component κ_{33}, which describes the curvature of the free energy function at the spontaneous polarization state and therefore exhibits the main impact on Ψ_0. Hence, the dielectric permittivity component κ_{33} and the coercive field strength E_{C180} cannot be adjusted independently.

On the other hand, it is reasonable that the coercive field strength of the monodomain state exceeds coercive fields that are measured experimentally for polycrystalline ferroelectric ceramics: While the simulated domain configurations always represent idealized and mostly highly symmetric systems, real ferroelectric ceramics contain numerous domain systems, imperfections as well as a complicated domain and grain structure. All these mechanisms have an impact on the coercive field strength, as illustrated in Figure 5.27: For various domain configurations of increasing complexity and inhomogeneity, the respective coercive field strengths are plotted. Both PTO and PZT domain configurations are presented in the diagram, and the coercive fields are normalized with respect to the particular E_{C180}. A clear trend becomes apparent from Figure 5.27: As the complexity of the investigated domain structures is increased by taking defects, multiple domain systems and grain boundaries into account, the configurations become more realistic, and the electric fields necessary for initiating irreversible switching processes in the configurations are decreased.

From the large-signal analysis it becomes apparent that phase-field simulations will not yield a specific coercive field strength E_C valid for a particular ferroelectric material, which then can be directly compared to experiments. However, trends can be shown regarding the influence of charged defects, domain systems and grain boundaries on the resulting coercive field strength in a specific material. The most realistic domain structure considered in this work, regarding the configuration size and mechanisms taken into account, are polycrystalline multidomain configurations as shown in Figure 5.21, containing multiple domain systems as well as grain boundaries. For such domain configurations, the phase-field model yields coercive fields in the order of experimental values, and for larger configurations containing also imperfections or less symmetric grain boundaries, a further drop of the coercive fields can be expected.
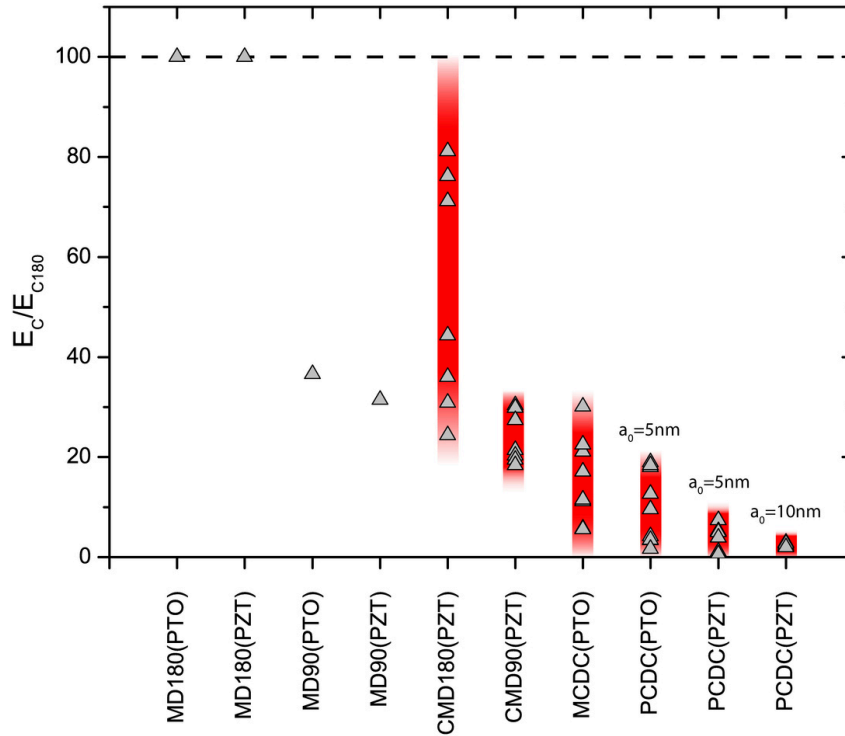
Figure 5.27.: Coercive fields E_C obtained from various domain structures of increasing complexity. For both PTO and PZT configurations, E_C has been normalized with respect of to the coercive field strength for 180° switching of a monodomain state (MD180). Furthermore, 90° switching of a monodomain state is considered (MD90), as well as 180° and 90° switching of monodomains containing differently charged defects (CMD180, CMD90). In addition, coercive fields of various monocrystalline domain configurations (MCDC) as well as polycrystalline domain configurations (PCDC) are presented. Since the coercive field strength is influenced by various parameters, such as the size of the configuration, boundary conditions, initial conditions and the direction of the applied electric field, the beams in the diagram indicate approximation intervals for possible coercive fields strengths of the respective domain configurations. A clear correlation between the complexity of the domain configuration and the resulting coercive field strength becomes visible.

Role of electrically charged defects

Defects in ferroelectric materials are of special interest since they are supposed to play an important role in ferroelectric fatigue [17]. Within a multi-scale approach, interactions between defects and the ferroelectric domain system can be taken into account and investigated by means of phase-field modeling. Electrically charged defects emerging in real ferroelectric ceramics are for instance dopants, interstitial defects or vacancy defects. The most commonly encountered vacancy defect is the oxygen vacancy which is doubly positively charged [55]. This concurs to the highest charge density considered in this work, corresponding to two elementary charges per unit cell.

By phase-field simulations, several effects of electrically charged defects on the ferroelectric domain structure have been identified in the course of this work. A strong interaction between

charged defects and domain walls was observed: Domain walls were pinned and clamped, showing a significant impact on the small-signal behavior. Furthermore, charged defects were found serving as nucleation sites for domain walls in monodomains when exposed to a high electric field, therefore alleviating switching processes and influencing the large-signal behavior. When considering multidomain configurations, phase-field simulation results showed evidence that coinciding with charged defects is energetically favorable for domain walls, which then become pinned.

Experimentally, the agglomeration of charged defects in domain walls has been identified as an important mechanism of ferroelectric fatigue [64], while the charged defects in all calculations of this work were considered stationary. A possible approach for taking the ferroelectric fatigue mechanism of defect agglomeration into account in a multi-scale simulation chain would be expanding the phase-field model to allow for defect migration. However, such efforts are beyond the scope of this work.

Temperature dependence

In the utilized phase-field model, all calculations were performed under isothermal conditions, i.e. for a constant temperature. This is due to the input parameters used for adjusting the free energy function of the phase-field model which were obtained from first-principles calculations and atomistic simulations, both performed at T=0K. In general, a temperature-dependence of the phase-field model can be taken into account by allowing the Landau energy coefficient α_1 to depend on temperature [18], as discussed in section 1.3.3. When additionally allowing all Landau free energy coefficients to depend on the mole fraction of titanate and zirconate, the complete system of PZT solid solutions can be represented by a single free energy function. Figure 5.28 illustrates a computed PZT phase diagram based on input parameters experimentally obtained by Amin et. al. [3]. If such temperature-dependent input parameters were available from atomistic calculations, they could directly be considered in the present phase-field model by using them for adjusting the free energy and adding the temperature as a degree of freedom in the FE-implementation as described by Su and Landis [71].

Influence of configuration size

The last issue to be discussed is the influence of the configuration dimensions on the small-signal and large-signal results obtained from the phase-field model. Figure 5.29 illustrates the dependence of the dielectric permittivity tensor component κ_{22} on the configuration size L in x_1-direction for a perfect 90° domain stack as investigated in section 5.4.3. Configuration dimensions from 10nm to 240nm are considered, corresponding to domain widths from 5nm to 120nm. A slight size-dependence of κ_{22} can only be found for L<80nm, whereas for larger configurations a saturation value for κ_{22} is reached. This can be explained by the fact that the
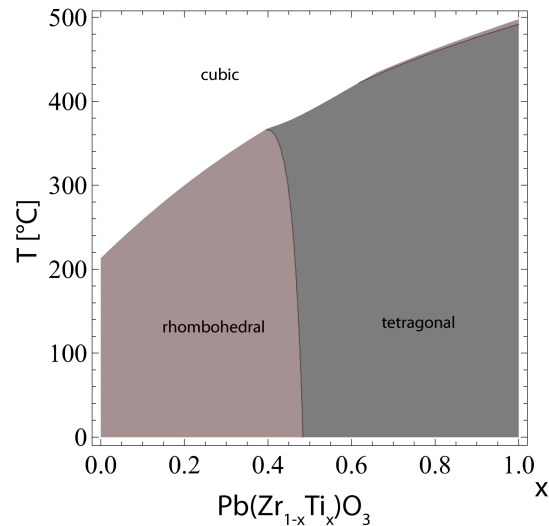
Figure 5.28.: PZT phase diagram computed from a free energy function based on experimental input parameters [3]. In order to encode the information of the phase diagram into the free energy function, all Landau coefficients depend on the zirconate/titanate mole fraction, and the coefficient α_1 additionally depends on the temperature.

volume fraction of material in domain walls in the system increases when the configuration size is reduced: The region within domain walls itself cannot contribute to intrinsic or extrinsic effects since the polarization is constrained within the domain wall. Therefore, the dielectric response is decreased once the fraction of domain walls in the configuration reaches a noticeable level. However, this size-effect is relatively small: Even for a domain width of 5nm, corresponding to a domain wall fraction of 10% in the configuration, κ_{22} only deviates by 3.5%. A comparable trend of the size-dependence on the small-signal parameters has been observed for all considered mechanically stabilized domain configurations.

On the contrary, a clear influence of the configuration size on the large-signal behavior has been found, as becomes apparent from Figure 5.27: For the considered PZT polycrystalline multidomain configuration, an increase of the basic configuration dimension a_0 from 5nm to 10nm induces a significant decrease of the coercive field strength. This is due to the more complex domain structure resulting for the scaled-up configuration. However, several difficulties arise once the configuration size is further increased. On the one hand, the numerical solution process becomes increasingly challenging because of a manifoldness of possible solutions for a specific model size: A variety of resulting domain patterns with approximately the same total energy is available, so that convergence problems can arise. On the other hand, by increasing the configuration size also the number of finite elements of the system and therefore the computational effort is raised significantly. A possible approach to solve this problem is using adaptive meshing techniques: Inhomogeneous regions in the domain configuration, e.g. domain walls, are meshed with the required mesh density in order to avoid mesh artefacts (cf. section 4.6), whereas homogeneous regions of the domain configuration are meshed coarsely, thereby sig-
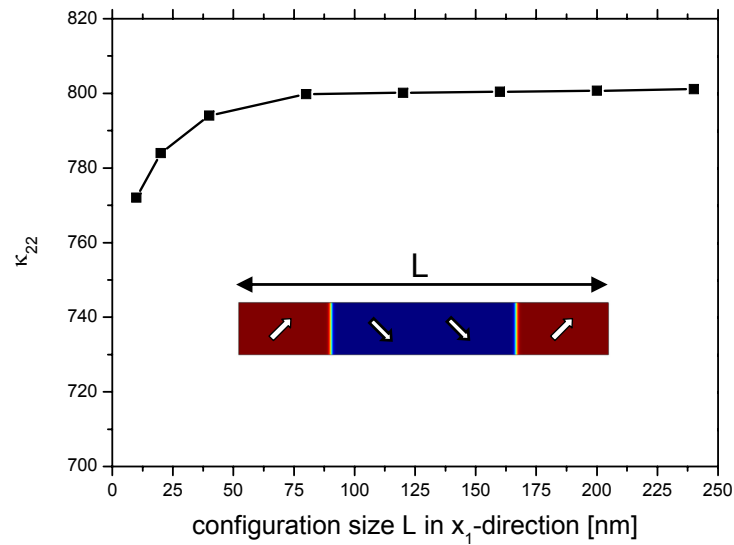
Figure 5.29.: Dependence of the dielectric permittivity tensor component κ_{22} on the configuration size L of an ideal $90°$ domain stack as discussed in section 5.4.3.

nificantly reducing the required number of finite elements. Furthermore, adaptive meshing techniques might also render the possibility of computing and investigating three-dimensional ferroelectric domain configurations of reasonable size.

6. Summary

The primary objective of this thesis was applying phase-field modeling in a knowledge based multi-scale approach for the ferroelectric polycrystalline ceramics PTO and PZT. Within this virtual material development approach, phase-field modeling bridges the gap between predictive atomistic methods on one side and micromechanical modeling methods on the other side. Therefore, two interfaces in this multi-scale simulation chain have been developed and established in this work.

In order to link the atomic level to the meso-scale, the thermodynamical free energy function of the phase-field model has been adjusted to results from first-principles calculations and atomistic shell-model simulations [76]. Such "ab-initio" input parameters exhibit a high predictive power when compared to empirical input parameters, since they are solely based on quantum-mechanical theories. In a first step, a standard free energy function of 6th order in polarization was taken from literature [9, 52], and the sensitivity of all energy coefficients was analyzed. On that basis, an adjustment method for the energy coefficients was developed: For the first time, a phase-field model describing ferroelectric materials has been adjusted to input parameters from atomistic calculations using a completely knowledge based approach, in contrast to the common Devonshire approach [18, 19, 20], which needs experimental input. Especially the direct and simultaneous adjustment of the phase-field model to both the thickness and energy of 180° and 90° domain walls represents an innovation when compared to previous approaches [3, 20, 38, 71].

Furthermore, an extension of the phase-field model's free energy has been presented in this work. The standard free energy function of 6th order in polarization is subject to certain restrictions and exhibits not enough degrees of freedom for an independent adjustment of the elastic properties in the cubic and the tetragonal phase. Also, the spontaneous strains are coupled to the piezoelectric coefficients, inhibiting a separate tuning. An expansion of a free energy function for barium titanate published by Su and Landis [71] in order to remedy this deficiencies cannot be applied to PTO and PZT as demonstrated in this work. Instead, the free energy function has been further developed by introducing a novel elastic energy term. The benefit of this higher-order term is that it allows for a separate adjustment of the cubic and tetragonal elastic properties for PTO and PZT, as well as an independent fitting of the spontaneous strains and the piezoelectric coefficients. Though developed for PTO and PZT, the new approach is general enough to also describe the simpler case of barium titanate. Subsequently, the adjustment method of the free energy coefficients has been improved to take the new energy term into account, and

energy coefficients for PTO and PZT have been presented.

The second part of this work regards the definition and development of the interface between phase-field modeling and micromechanical modeling methods in the multi-scale approach, i.e. linking the meso-scale to the micro-scale. Therefore, ferroelectric domain configurations have been investigated under electromechanical loading, yielding domain effective small-signal and large-signal parameters that served as input parameters for micromechanical modeling methods [50, 75]. In order to prepare this approach, the phase-field theory has been implemented into the finite-element platform COMSOL Multiphysics. Since the focus of this work is investigating ferroelectric bulk behavior, periodic boundary conditions for the phase-field model have been developed as well as techniques for mechanically stabilizing the periodically continued domain configurations. One-, two-, and three-dimensional finite-element implementations of the phase-field model have been presented to which arbitrary electromechanical far fields can be applied, and the FE implementation has been verified. Due to the massive computational effort necessary for a three-dimensional FE implementation, a two-dimensional FE-model has been used throughout this work, containing seven degrees of freedom per node: three components of the polarization, three components of the mechanical displacement as well as the electric potential. Furthermore, a FE-mesh study has been performed, yielding a required mesh density of 7 nodes per nanometer (or 2-3 nodes within a domain wall, respectively) in order to eliminate mesh artefacts in a small-signal analysis, such as the artificial pinning of domain walls by the FE-mesh.

In the scope of the project COMFEM, piezoresponse force microscopy studies on PZT were conducted that identified typical ferroelectric domain configurations on the meso-scale. In this work, these domain structures have been investigated separately regarding their small-signal and large-signal behavior under electromechanical loading: the monodomain state, the (ideal) 90° domain stack as well as monocrystalline multidomain configurations. Additionally, the interactions of electrically charged point defects on these domain configurations have been considered, as well as the impact of grain boundaries on the ferroelectric domain structure. For the latter, a FE-model consisting of crystallographically differently oriented regions has been employed, yielding a polycrystalline multidomain configuration.

The small-signal analysis provides a profound understanding of mechanisms and processes taking place on the meso-scale in ferroelectric domain patterns. Using methods and tools that were developed for evaluating small-signal parameters as well as domain fractions under electromechanical loading, a significant difference has been demonstrated between intrinsic (lattice) and extrinsic (non-lattice) contributions to the piezoelectric, dielectric and elastic small-signal parameters. Two extrinsic effects in the small-signal regime have been identified and investigated in detail: reversible domain wall motion as well as bending of domain walls, which are pinned by electrically charged point defects. Although pinned domain walls are hindered from moving

freely under an applied electric field, they can still bend and therefore show extrinsic contributions. Being able to take the effects of reversible domain wall motion and bending into account represents one of the most striking benefits when using phase-field modeling in a multi-scale simulation chain for ferroelectric ceramics, since these effects, taking place on the meso-scale, show a significant impact on the small-signal parameters of ferroelectric materials. Since the initial configuration is restored upon unloading the configuration, they are not to be confused with irreversible switching processes.

Phase-field simulations of domain configurations that contain electrically charged defects and therefore pinned domain walls indicate that domain wall bending is the dominant effect in real ferroelectric ceramics: The extrinsic contributions found in such simulations are comparable to experimentally observed extrinsic contributions of reversible domain wall motion and bending to the piezoelectric and dielectric small-signal properties in ferroelectric ceramics [17]. This corresponds to the fact that real ferroelectric materials almost always contain electrical and mechanical effects that interfere with domain walls: By mechanisms of clamping and pinning, the domain walls are inhibited from moving freely.

From the large-signal analysis, a correlation of the complexity of the domain configuration and the coercive field, i.e. the electric field necessary for initiating irreversible switching processes, has become obvious: As the complexity and inhomogeneity of the domain configuration is increased, for instance by taking electrically charged point defects, multiple domain systems or grain boundaries into account, the coercive field strength is reduced. Charged point defects play an especially important role, since they can act as nucleation centers for new domains under electric loading, thereby significantly reducing the coercive field strength.

Finally, possible improvements and expansions of the phase-field model have been illustrated which allow for taking ferroelectric fatigue and temperature-dependence in a multi-scale simulation chain for ferroelectrics into account. Moreover, by employing adaptive meshing techniques, the configuration size of the FE-model could be increased in the future.

A. Appendix

A.1. Structure of compliance tensors

Cubic symmetry

For the symmetry point group $m3m$, the compliance tensors take the following form:

$$\kappa_{ij} = \begin{pmatrix} \kappa_{11} & 0 & 0 \\ 0 & \kappa_{11} & 0 \\ 0 & 0 & \kappa_{11} \end{pmatrix} \tag{A.1}$$

$$d_{ij} = \begin{pmatrix} 0 & 0 & 0 & 0 & 0 \\ 0 & 0 & 0 & 0 & 0 \\ 0 & 0 & 0 & 0 & 0 \end{pmatrix} \tag{A.2}$$

$$c_{ij} = \begin{pmatrix} c_{11} & c_{12} & c_{12} & 0 & 0 & 0 \\ c_{12} & c_{11} & c_{12} & 0 & 0 & 0 \\ c_{12} & c_{12} & c_{11} & 0 & 0 & 0 \\ 0 & 0 & 0 & c_{44} & 0 & 0 \\ 0 & 0 & 0 & 0 & c_{44} & 0 \\ 0 & 0 & 0 & 0 & 0 & c_{44} \end{pmatrix} \tag{A.3}$$

Tetragonal symmetry

For the symmetry point group $4mm$ and a polar axis in x_3-direction, the compliance tensors take the following form:

$$\kappa_{ij} = \begin{pmatrix} \kappa_{11} & 0 & 0 \\ 0 & \kappa_{11} & 0 \\ 0 & 0 & \kappa_{33} \end{pmatrix} \tag{A.4}$$

$$d_{ij} = \begin{pmatrix} 0 & 0 & 0 & 0 & d_{15} \\ 0 & 0 & 0 & d_{15} & 0 \\ d_{31} & d_{31} & d_{33} & 0 & 0 \end{pmatrix} \tag{A.5}$$

$$c_{ij} = \begin{pmatrix} c_{11} & c_{12} & c_{13} & 0 & 0 & 0 \\ c_{12} & c_{11} & c_{13} & 0 & 0 & 0 \\ c_{13} & c_{13} & c_{33} & 0 & 0 & 0 \\ 0 & 0 & 0 & c_{44} & 0 & 0 \\ 0 & 0 & 0 & 0 & c_{44} & 0 \\ 0 & 0 & 0 & 0 & 0 & c_{66} \end{pmatrix} \tag{A.6}$$

A.2. Expanded form of the free energy

Considering the additional energy terms introduced and discussed in chapter 3, the expanded free energy takes the following form:

$$
\begin{aligned}
\Psi \;=\; & \frac{G_{11}}{2}(P_{1,1}^2 + P_{2,2}^2 + P_{3,3}^2) + G_{12}(P_{1,1}P_{2,2} + P_{1,1}P_{3,3} + P_{2,2}P_{3,3}) + \\
& + \frac{G_{44}}{2}\big((P_{1,2}+P_{2,1})^2 + (P_{1,3}+P_{3,1})^2 + (P_{2,3}+P_{3,2})^2\big) + \\
& + \frac{a_1}{2}(P_1^2 + P_2^2 + P_3^2) + \frac{a_2}{4}(P_1^4 + P_2^4 + P_3^4) + \\
& + \frac{a_3}{4}(P_1^2 P_2^2 + P_1^2 P_3^2 + P_2^2 P_3^2) + \frac{a_4}{6}(P_1^6 + P_2^6 + P_3^6) + \\
& + \frac{a_5}{4}(P_1^4 P_2^4 + P_1^4 P_3^4 + P_2^4 P_3^4) + \frac{a_7}{6}(P_1^2 P_2^2 P_3^2) + \\
& + \frac{a_6}{6}(P_1^4(P_2^2 + P_3^2) + P_2^4(P_1^2 + P_3^2) + P_3^4(P_1^2 + P_2^2)) + \\
& + \frac{a_8}{2}(P_1^8 + P_2^8 + P_3^8) \\
& + \frac{b_1}{2}(\varepsilon_{11}P_1^2 + \varepsilon_{22}P_2^2 + \varepsilon_{33}P_3^2) + \frac{b_2}{2}\big((\varepsilon_{22}+\varepsilon_{33})P_1^2 + (\varepsilon_{11}+\varepsilon_{33})P_2^2 + (\varepsilon_{11}+\varepsilon_{22})P_3^2\big) + \\
& + b_3\big((\varepsilon_{12}+\varepsilon_{21})P_1P_2 + (\varepsilon_{13}+\varepsilon_{31})P_1P_3 + (\varepsilon_{23}+\varepsilon_{32})P_2P_3\big) + \\
& + \frac{c_1}{2}(\varepsilon_{11}^2 + \varepsilon_{22}^2 + \varepsilon_{33}^2) + c_2(\varepsilon_{11}\varepsilon_{22} + \varepsilon_{11}\varepsilon_{33} + \varepsilon_{22}\varepsilon_{33}) + \\
& + \frac{c_3}{2}(\varepsilon_{12}^2 + \varepsilon_{21}^2 + \varepsilon_{13}^2 + \varepsilon_{31}^2 + \varepsilon_{23}^2 + \varepsilon_{32}^2) + \\
& + \Big(\frac{f_1}{2}\varepsilon_{11}^2 + \frac{f_2}{2}(\varepsilon_{22}^2 + \varepsilon_{33}^2) + f_3(\varepsilon_{11}\varepsilon_{22} + \varepsilon_{11}\varepsilon_{33}) + f_4\varepsilon_{22}\varepsilon_{33} + \\
& + \frac{f_5}{2}(\varepsilon_{12}^2 + \varepsilon_{21}^2 + \varepsilon_{13}^2 + \varepsilon_{31}^2) + \frac{f_6}{2}(\varepsilon_{23}^2 + \varepsilon_{32}^2)\Big) P_1^2 + \\
& + \Big(\frac{f_1}{2}\varepsilon_{22}^2 + \frac{f_2}{2}(\varepsilon_{11}^2 + \varepsilon_{33}^2) + f_3(\varepsilon_{11}\varepsilon_{22} + \varepsilon_{22}\varepsilon_{33}) + f_4\varepsilon_{11}\varepsilon_{33} + \\
& + \frac{f_5}{2}(\varepsilon_{12}^2 + \varepsilon_{21}^2 + \varepsilon_{23}^2 + \varepsilon_{32}^2) + \frac{f_6}{2}(\varepsilon_{13}^2 + \varepsilon_{31}^2)\Big) P_2^2 + \\
& + \Big(\frac{f_1}{2}\varepsilon_{33}^2 + \frac{f_2}{2}(\varepsilon_{11}^2 + \varepsilon_{22}^2) + f_3(\varepsilon_{11}\varepsilon_{33} + \varepsilon_{22}\varepsilon_{33}) + f_4\varepsilon_{11}\varepsilon_{22} + \\
& + \frac{f_5}{2}(\varepsilon_{13}^2 + \varepsilon_{31}^2 + \varepsilon_{23}^2 + \varepsilon_{32}^2) + \frac{f_6}{2}(\varepsilon_{12}^2 + \varepsilon_{21}^2)\Big) P_3^2 + \\
& + \Big(\frac{g_1}{4}\varepsilon_{11} + \frac{g_2}{4}(\varepsilon_{22}\varepsilon_{33})\Big) P_1^4 + \frac{g_3}{4}(\varepsilon_{12} + \varepsilon_{21})(P_1 P_2^3 + P_2 P_1^3) + \\
& + \Big(\frac{g_1}{4}\varepsilon_{22} + \frac{g_2}{4}(\varepsilon_{11}\varepsilon_{33})\Big) P_2^4 + \frac{g_3}{4}(\varepsilon_{23} + \varepsilon_{32})(P_2 P_3^3 + P_3 P_2^3) + \\
& + \Big(\frac{g_1}{4}\varepsilon_{33} + \frac{g_2}{4}(\varepsilon_{11}\varepsilon_{22})\Big) P_3^4 + \frac{g_3}{4}(\varepsilon_{13} + \varepsilon_{31})(P_1 P_3^3 + P_3 P_1^3) + \\
& + \frac{h_1}{2}(\varepsilon_{11}^2 P_1^4 + \varepsilon_{22}^2 P_2^4 + \varepsilon_{33}^2 P_3^4) +
\end{aligned}
$$

$$+ \quad \frac{h_2}{2} \left((\varepsilon_{22}^2 \varepsilon_{33}^2) P_1^4 + (\varepsilon_{11}^2 \varepsilon_{33}^2) P_2^4 + (\varepsilon_{11}^2 \varepsilon_{22}^2) P_3^4 \right) +$$

$$+ \quad h_3 \left((\varepsilon_{11} \varepsilon_{22} + \varepsilon_{11} \varepsilon_{33}) P_1^4 + (\varepsilon_{11} \varepsilon_{22} + \varepsilon_{22} \varepsilon_{33}) P_2^4 + (\varepsilon_{11} \varepsilon_{33} + \varepsilon_{22} \varepsilon_{33}) P_3^4 \right) +$$

$$+ \quad h_4 \left(\varepsilon_{22} \varepsilon_{33} P_1^4 + \varepsilon_{11} \varepsilon_{33} P_2^4 + \varepsilon_{11} \varepsilon_{22} P_3^4 \right) +$$

$$+ \quad \frac{h_5}{2} \left((\varepsilon_{12}^2 + \varepsilon_{21}^2 + \varepsilon_{13}^2 + \varepsilon_{31}^2) P_1^4 + (\varepsilon_{12}^2 + \varepsilon_{21}^2 + \varepsilon_{23}^2 + \varepsilon_{32}^2) P_2^4 + (\varepsilon_{13}^2 + \varepsilon_{31}^2 + \varepsilon_{23}^2 + \varepsilon_{32}^2) P_3^4 \right) +$$

$$+ \quad \frac{h_6}{2} \left((\varepsilon_{23} \varepsilon_{32}) P_1^4 + (\varepsilon_{13} \varepsilon_{31}) P_2^4 + (\varepsilon_{12} \varepsilon_{21}) P_3^4 \right) +$$

$$+ \quad \frac{1}{2\kappa_0} \left((D_1 - P_1)^2 + (D_2 - P_2)^2 + (D_3 - P_3)^2 \right) \tag{A.7}$$

Applying the adjustment process developed in section 3.3 yields the coefficients of the expanded form of the free energy, which are depicted in Table A.1.

Table A.1.: Adjusted coefficients of the Helmholtz free energy based on input parameters from atomistic calculations. PTO and PZT. Expanded form of the free energy.

coefficient	PTO	PZT
a_1	$-5.549 \times 10^8 \, \mathrm{JmC^{-2}}$	$-4.440 \times 10^8 \, \mathrm{JmC^{-2}}$
a_2	$4.012 \times 10^9 \, \mathrm{Jm^5C^{-4}}$	$1.4 \times 10^9 \, \mathrm{Jm^5C^{-4}}$
a_3	$-5.000 \times 10^9 \, \mathrm{Jm^5C^{-4}}$	$-8.0 \times 10^9 \, \mathrm{Jm^5C^{-4}}$
a_4	$-1.136 \times 10^{10} \, \mathrm{Jm^9C^{-6}}$	$-2.377 \times 10^{10} \, \mathrm{Jm^9C^{-6}}$
a_5	$1.250 \times 10^{11} \, \mathrm{Jm^{13}C^{-8}}$	$2.395 \times 10^{12} \, \mathrm{Jm^{13}C^{-8}}$
a_6	$2.609 \times 10^{10} \, \mathrm{Jm^9C^{-6}}$	$8.976 \times 10^{10} \, \mathrm{Jm^9C^{-6}}$
a_7	$3.200 \times 10^{10} \, \mathrm{Jm^9C^{-6}}$	$9.2 \times 10^{10} \, \mathrm{Jm^9C^{-6}}$
a_8	$2.500 \times 10^9 \, \mathrm{Jm^{13}C^{-8}}$	$1.9 \times 10^{10} \, \mathrm{Jm^{13}C^{-8}}$
b_1	$7.577 \times 10^9 \, \mathrm{JmC^{-2}}$	$1.372 \times 10^9 \, \mathrm{JmC^{-2}}$
b_2	$1.326 \times 10^{10} \, \mathrm{JmC^{-2}}$	$7.733 \times 10^{10} \, \mathrm{JmC^{-2}}$
b_3	$1.520 \times 10^9 \, \mathrm{JmC^{-2}}$	$1.52 \times 10^8 \, \mathrm{JmC^{-2}}$
c_1	$342 \times 10^9 \, \mathrm{Jm^{-3}}$	$361 \times 10^9 \, \mathrm{Jm^{-3}}$
c_2	$131 \times 10^9 \, \mathrm{Jm^{-3}}$	$115 \times 10^9 \, \mathrm{Jm^{-3}}$
c_3	$108 \times 10^9 \, \mathrm{Jm^{-3}}$	$91 \times 10^9 \, \mathrm{Jm^{-3}}$
f_1	$-6.482 \times 10^{11} \, \mathrm{JmC^{-2}}$	$-1.088 \times 10^{12} \, \mathrm{JmC^{-2}}$
f_2	$-1.472 \times 10^{11} \, \mathrm{JmC^{-2}}$	$-2.021 \times 10^{11} \, \mathrm{JmC^{-2}}$
f_3	$-1.112 \times 10^{11} \, \mathrm{JmC^{-2}}$	$1.189 \times 10^{10} \, \mathrm{JmC^{-2}}$
f_4	$-3.100 \times 10^{10} \, \mathrm{JmC^{-2}}$	$-5.945 \times 10^9 \, \mathrm{JmC^{-2}}$
f_5	$-1.112 \times 10^{11} \, \mathrm{JmC^{-2}}$	$-1.070 \times 10^{11} \, \mathrm{JmC^{-2}}$
f_6	$-2.583 \times 10^9 \, \mathrm{JmC^{-2}}$	$2.973 \times 10^9 \, \mathrm{JmC^{-2}}$
g_1	$2.695 \times 10^9 \, \mathrm{Jm^5C^{-4}}$	$-5.249 \times 10^{10} \, \mathrm{Jm^5C^{-4}}$
g_2	$2.946 \times 10^{10} \, \mathrm{Jm^5C^{-4}}$	$2.331 \times 10^{10} \, \mathrm{Jm^5C^{-4}}$
g_3	$1.021 \times 10^9 \, \mathrm{Jm^5C^{-4}}$	$1.1 \times 10^8 \, \mathrm{Jm^5C^{-4}}$
h_1	$4.185 \times 10^{11} \, \mathrm{Jm^5C^{-4}}$	$1.617 \times 10^{12} \, \mathrm{Jm^5C^{-4}}$
h_2	$9.505 \times 10^{10} \, \mathrm{Jm^5C^{-4}}$	$3.004 \times 10^{11} \, \mathrm{Jm^5C^{-4}}$
h_3	$7.170 \times 10^{10} \, \mathrm{Jm^5C^{-4}}$	0
h_4	$2.001 \times 10^{10} \, \mathrm{Jm^5C^{-4}}$	$8.837 \times 10^9 \, \mathrm{Jm^5C^{-4}}$
h_5	$7.170 \times 10^{10} \, \mathrm{Jm^5C^{-4}}$	$1.591 \times 10^{11} \, \mathrm{Jm^5C^{-4}}$
h_6	$1.668 \times 10^9 \, \mathrm{Jm^5C^{-4}}$	0
G_{11}	$11 \times 10^{-11} \, \mathrm{Jm^3C^{-2}}$	$15 \times 10^{-11} \, \mathrm{Jm^3C^{-2}}$
G_{12}	$6 \times 10^{-11} \, \mathrm{Jm^3C^{-2}}$	$3 \times 10^{-11} \, \mathrm{Jm^3C^{-2}}$
G_{44}	$3 \times 10^{-11} \, \mathrm{Jm^3C^{-2}}$	$6.4 \times 10^{-11} \, \mathrm{Jm^3C^{-2}}$

A.3. Monocrystalline multidomain configurations

In the following, a selection of typical monocrystalline multidomain configurations for PZT is shown along with the applied global strain in order to mechanically stabilize the configurations:

$$\tilde{S}_{11} = \tilde{S}_{22} = \frac{e_\perp + e_\parallel}{2} \quad \tilde{S}_{33} = e_\perp$$

$$\tilde{S}_{11} = \tilde{S}_{22} = 0 \quad \tilde{S}_{33} = e_\perp$$

$$\tilde{S}_{11} = \tilde{S}_{22} = 0 \quad \tilde{S}_{33} = 0$$

$$\tilde{S}_{11} = \tilde{S}_{22} = 0 \quad \tilde{S}_{33} = 0$$

$$\tilde{S}_{11} = \tilde{S}_{22} = 0 \quad \tilde{S}_{33} = 0$$

$$\tilde{S}_{11} = \tilde{S}_{22} = \frac{e_\perp + e_\parallel}{2} \quad \tilde{S}_{33} = e_\perp$$

domain orientation:

DW	P_1^+	P_1^-	P_2^+	P_2^-	P_3^+	P_3^-
⟹	⟸	⇧	⇩	⊙	⊗

A. Appendix
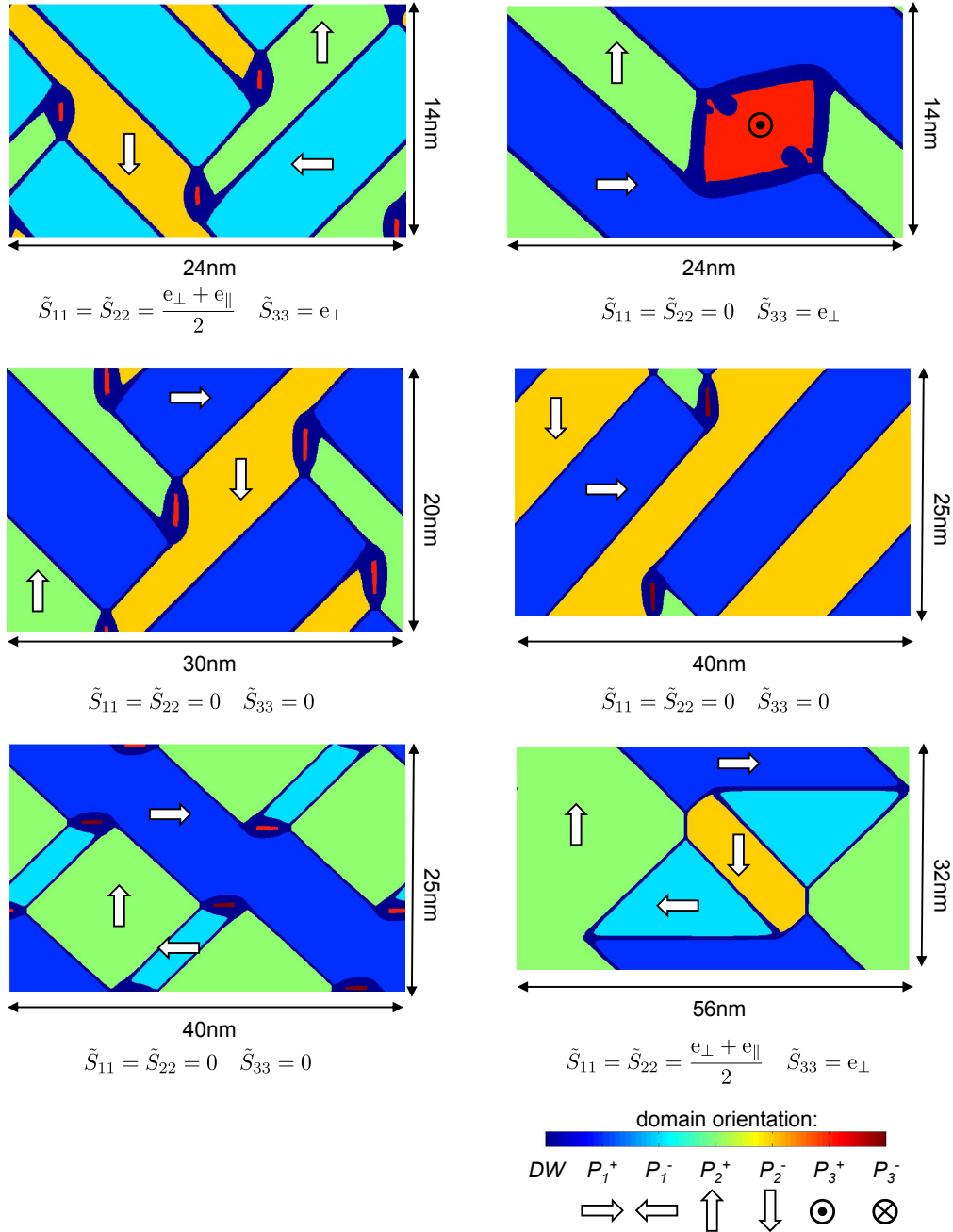
B. Bibliography

[1] IEEE Standard on Piezoelectricity. ANSI/IEEE Standards 176-1987, 1988.

[2] H. Allik and T. Hughes. Finite element method for piezoelectric vibration. *International Journal for Numerical Methods in Engineering*, 2:151–157, 1970.

[3] A. Amin, M. J. Haun, B. Badger, H. McKinstry, and L. E. Cross. A phenomenological gibbs function for the single cell region of the $PbZrO_3$:$PbTiO_3$ solid solution system. *Ferroelectrics*, 65(1):107, 1985.

[4] L. Bellaiche and D. Vanderbilt. Intrinsic piezoelectric response in perovskite alloys: PMN-PT versus PZT. *Phys. Rev. Lett.*, 83(7):1347–1350, 1999.

[5] K. Binder. Theory of first-order phase transitions. *Rep. Prog. Phys.*, 50:783–859, 1987.

[6] J. Bragard, A. Karma, Y. H. Lee, and M. Plapp. Linking phase-field and atomistic simulations to model dendritic solidification in highly undercooled melts. *Interface Science*, 10(2):121–136, 2002.

[7] U. Böttger. *Polar Oxides: Properties, Characterization, and Imaging*. Wiley-VCH Verlag GmbH & Co.KGaA Weinheim, 2005.

[8] J. W. Cahn and J. E. Hilliard. Free energy of a nonuniform system. I. interfacial free energy. *The Journal of Chemical Physics*, 28(2):258–267, 1958.

[9] W. Cao and L. E. Cross. Theory of tetragonal twin structures in ferroelectric perovskites with a first-order phase transition. *Phys. Rev. B*, 44(1):5, 1991.

[10] P. Chandra and P. B. Littlewood. *Physics of Ferroelectrics - A Modern Perspective*, volume 105 of *Topics in Applied Physics*. Springer, 2007.

[11] P. Chandra and P. B. Littlewood. *Physics of Ferroelectrics - A Modern Perspective*, chapter A Landau Primer for Ferroelectrics, pages 69–115. Topics in Applied Physics. Springer, Berlin, 2007.

[12] L.-Q. Chen. Phase-field models for microstructure evolution. *Annu. Rev. Mater. Res.*, 32(1):113, 2002.

[13] L. Q. Chen and J. Shen. Applications of semi-implicit fourier-spectral method to phase field equations. *Computer Physics Communications*, 108(2-3):147–158, 1998.

[14] R. E. Cohen. Origin of ferroelectricity in perovskite oxides. *Nature*, 358(6382):136–138, 1992.

[15] B. D. Coleman and W. Noll. The thermodynamics of elastic materials with heat conduction and viscosity. *Arch. Rational Mech. Anal.*, 13:167–178, 1963.

[16] D. Damjanovic. Stress and frequency dependence of the direct piezoelectric effect in ferroelectric ceramics. *J. Appl. Phys.*, 82(4):1788–1797, 1997.

[17] D. Damjanovic. Ferroelectric, dielectric and piezoelectric properties of ferroelectric thin films and ceramics. *Rep. Prog. Phys.*, 61:1267–1324, 1998.

[18] A. F. Devonshire. Theory of barium titanate. *Philosophical Magazine*, 40:1040–1063, 1949.

[19] A. F. Devonshire. Theory of barium titanate. *Philosophical Magazine*, 42:1065–1079, 1951.

[20] A. F. Devonshire. Theory of ferroelectrics. *Advances in Physics*, 3(10):85, 1954.

[21] L. M. Eng, H. J. Guntherodt, G. A. Schneider, U. Kopke, and J. M. Saldana. Nanoscale reconstruction of surface crystallography from three-dimensional polarization distribution in ferroelectric barium-titanate ceramics. *Applied Physics Letters*, 74 (2):233–235, 1999.

[22] P. Erhart, R.-A. Eichel, P. Träskelin, and K. Albe. Association of oxygen vacancies with impurity metal ions in lead titanate. *Phys. Rev. B*, 76(17):174116, 2007.

[23] J. Frantti, S. Ivanov, S. Eriksson, H. Rundlof, V. Lantto, J. Lappalainen, and M. Kakihana. Phase transitions of $Pb(Zr_xTi_{1-x})O_3$ ceramics. *Phys. Rev. B*, 66(6):064108, 2002.

[24] B. C. Frazer, H. R. Danner, and R. Pepinsky. Single-crystal neutron analysis of tetragonal $BaTiO_3$. *Phys. Rev.*, 100(2):745, 1955.

[25] E. Fried and M. E. Gurtin. Continuum theory of thermally induced phase transitions based on an order parameter. *Physica D: Nonlinear Phenomena*, 68(3-4):326–343, 1993.

[26] E. Fried and M. E. Gurtin. Dynamic solid-solid transitions with phase characterized by an order parameter. *Physica D: Nonlinear Phenomena*, 72:287–308, 1994.

[27] M. Fujimoto. *The physics of structural phase transitions*. Springer, 2nd edition edition, 2005.

[28] P. Ghosez, E. Cockayne, U. V. Waghmare, and K. M. Rabe. Lattice dynamics of $BaTiO_3$, $PbTiO_3$, and $PbZrO_3$: A comparative first-principles study. *Phys. Rev. B*, 60(2):836–843, 1999.

[29] V. Ginzburg and L. Landau. On the theory of superconductivity. *Zh. Eksp. Teor. Fiz.*, 20:1064, 1950.

[30] R. Gonzáles-Cinca, R. Folch, R. Benítez, L. Ramírez-Piscina, J. Casademunt, and A. Hernández-Machado. *Advances in Condensed Matter and Statistical Physics*, chapter Phase-Field Models in Interfacial Pattern Formation out of Equilibrium, pages 203–236. Nova Science Publishers New York, 2004.

[31] M. E. Gurtin. Generalized ginzburg-landau and cahn-hilliard equations based on micro-force balance. *Physica D: Nonlinear Phenomena*, 92:178–192, 1996.

[32] G. H. Haertling. Ferroelectric ceramics: History and technology. *J. Am. Ceram. Soc.*, 82(4):797–818, 1999.

[33] H.-J. Hagemann. Loss mechanisms and domain stabilization in doped $BaTiO_3$. *J. Phys. C: Solid State Phys.*, 11:3333–3344, 1978.

[34] T. R. Halemane, M. J. Haun, L. E. Cross, and R. E. Newnham. A phenomenological theory for phase transitions in perovskite ferroelectrics with oxygen octahedron tilts. *Ferroelectrics*, 62(1):149, 1985.

[35] M. J. Haun, E. Furman, T. R. Halemane, and L. E. Cross. Thermodynamic theory of the lead zirconate-titanate solid solution system, part iv: Tilting of the oxygen octahedra. *Ferroelectrics*, 99(1):55, 1989.

[36] M. J. Haun, E. Furman, S. J. Jang, and L. E. Cross. Thermodynamic theory of the lead zirconate-titanate solid solution system, part i: Phenomenology. *Ferroelectrics*, 99(1):13, 1989.

[37] M. J. Haun, E. Furman, S. J. Jang, and L. E. Cross. Thermodynamic theory of the lead zirconate-titanate solid solution system, part v: Theoretical calculations. *Ferroelectrics*, 99(1):63, 1989.

[38] M. J. Haun, E. Furman, S. J. Jang, H. A. McKinstry, and L. E. Cross. Thermodynamic theory of $PbTiO_3$. *J. Appl. Phys.*, 62(8):3331–3338, 1987.

[39] M. J. Haun, E. Furman, H. A. McKinstry, and L. E. Cross. Thermodynamic theory of the lead zirconate-titanate solid solution system, part ii: Tricritical behavior. *Ferroelectrics*, 99(1):27, 1989.

[40] M. J. Haun, Z. Q. Zhuang, E. Furman, S. J. Jang, and L. E. Cross. Thermodynamic theory of the lead zirconate-titanate solid solution system, part iii: Curie constant and sixth-order polarization interaction dielectric stiffness coefficients. *Ferroelectrics*, 99(1):45, 1989.

[41] J. Hlinka and P. Marton. Phenomenological model of a 90° domain wall in BaTiO$_3$-type ferroelectrics. *Phys. Rev. B*, 74(10):104104, 2006.

[42] H.-L. Hu and L. Q. Chen. Three-dimensional computer simulation of ferroelectric domain formation. *J. Am. Ceram. Soc.*, 81(3):492–500, 1998.

[43] T. Ikeda. *Fundamentals of Piezoelectricity*. Oxford University Press, Oxford, 1990.

[44] J. D. Jackson. *Classical Electrodynamics*. John Wiley & Sons, Inc., 1962.

[45] B. Jaffe, W. R. C. Jr., and H. Jaffe. *Piezoelectric Ceramics*. Academic Press, London, 1971.

[46] A. G. Kalinichev, J. Bass, B. Sun, and D. Payne. Elastic properties of tetragonal PbTiO$_3$ single crystals by brillouin scattering. *J. Mater. Res.*, 12(10):2623–2627, 1997.

[47] T. Kitamura, Y. Umeno, F. Shang, T. Shimada, and K. Wakahara. Development of inter-atomic potential for Pb(Zr,Ti)O$_3$ based on shell model. *J. Solid. Mech. Mat. Engineering*, 1:1423, 2007.

[48] A. Kontsos and C. M. Landis. Computational modeling of domain wall interactions with dislocations in ferroelectric crystals. *International Journal of Solids and Structures*, 46(6):1491–1498, 2009.

[49] A. Kontsos and C. M. Landis. Phase-Field modeling of domain structure energetics and evolution in ferroelectric thin films. *Journal of Applied Mechanics*, 77(4):041014–12, July 2010.

[50] L. Kunz. Mikromechanische Modellierung von Ferroelektrika im Rahmen einer Multi-skalensimulation. PhD-thesis, to be published at Karlsruhe Institut of Technology.

[51] L. D. Landau. *Collected papers of L. D. Landau*. Pergamon, Oxford, 1965.

[52] Y. L. Li, S. Y. Hu, Z. K. Liu, and L. Q. Chen. Effect of substrate constraint on the stability and evolution of ferroelectric domain structures in thin films. *Acta Mater.*, 50(2):395–411, 2002.

[53] Z. Li, M. Grimsditch, X. Xu, and S. K. Chan. The elastic, piezoelectric and dielectric constants of tetragonal PbTiO$_3$ single crystals. *Ferroelectrics*, 141(1):313, 1993.

[54] M. E. Lines and A. M. Glass. *Principles and applications of ferroelectrics and related materials*. Claredon Press, Oxford, 1979.

[55] D. C. Lupascu. *Fatigue in Ferroelectric Ceramics and Related Issues*. Springer-Verlag Berlin Heidelberg, 2004.

[56] W. P. Mason. Electrostrictive effect in barium titanate ceramics. *Phys. Rev.*, 74(9):1134, 1948.

[57] B. Meyer and D. Vanderbilt. Ab initio study of ferroelectric domain walls in pbtio$_3$. *Phys. Rev. B*, 65(10):104111, 2002.

[58] N. Moelans, B. Blanpain, and P. Wollants. An introduction to phase-field modeling of microstructure evolution. *Computer Coupling of Phase Diagrams and Thermochemistry*, 32:268–294, 2008.

[59] I. Münch and J. E. Huber. A hexadomain vortex in tetragonal ferroelectrics. *Applied Physics Letters*, 95(2):022913, 2009.

[60] S. Nambu and D. A. Sagala. Domain formation and elastic long-range interaction in ferroelectric perovskites. *Phys. Rev. B*, 50(9):5838, 1994.

[61] R. E. Newnham. *Properties of Materials: Anisotropy, Symmetry, Structure*. Oxford University Press, Oxford, 2005.

[62] B. Noheda, J. A. Gonzalo, L. E. Cross, R. Guo, S. E. Park, D. E. Cox, and G. Shirane. Tetragonal-to-monoclinic phase transition in a ferroelectric perovskite: The structure of PbZr$_{0.52}$Ti$_{0.48}$O$_3$. *Phys. Rev. B*, 61(13):8687–8695, 2000.

[63] B. Noheda, L. Wu, and Y. Zhu. Low-temperature superlattice in monoclinic PbZr$_{0.52}$Ti$_{0.48}$O$_3$. *Phys. Rev. B*, 66(6):060103, 2002.

[64] J. Nuffer, D. C. Lupascu, A. Glazounov, H. J. Kleebe, and J. Rödel. Microstructural modifications of ferroelectric lead zirconate titanate ceramics due to bipolar electric fatigue. *J. Eur. Ceram. Soc.*, 22:2133–2142, 2002.

[65] G. Sághi-Szabó, R. E. Cohen, and H. Krakauer. First-principles study of piezoelectricity in tetragonal PbTiO$_3$ and PbZr$_{1/2}$Ti$_{1/2}$O$_3$. *Phys. Rev. B*, 59(20):12771–12776, 1999.

[66] J. F. Scott. Applications of modern ferroelectrics. *Science*, 315(5814):954–959, 2007.

[67] M. Sepliarsky, A. Asthagiri, S. R. Phillpot, M. G. Stachiotti, and R. L. Migoni. Atomic-level simulation of ferroelectricity in oxide materials. *Curr. Opin. Solid State Mater. Sci.*, 9(3):107, 2005.

[68] N. Setter and R. Waser. Electroceramic materials. *Acta Mater.*, 48:151–178, 2000.

[69] T. Shimada, K. Wakahara, Y. Umeno, and T. Kitamura. Shell model potential for PbTiO$_3$ and its applicability to surfaces and domain walls. *J. Phys.: Condens. Matter*, 20(32):325225, 2008.

[70] A. S. Sonin and B. A. Strukow. *Einführung in die Ferroelektrizität*. Akademie-Verlag, Berlin, 1974.

[71] Y. Su and C. M. Landis. Continuum thermodynamics of ferroelectric domain evolution: Theory, finite element implementation, and application to domain wall pinning. *J. Mech. Phys. Solid.*, 55(2):280–305, 2007.

[72] V. Vaithyanathan, C. Wolverton, and L. Q. Chen. Multiscale modeling of precipitate microstructure evolution. *Phys. Rev. Lett.*, 88(12):125503, 2002.

[73] J. Valasek. Piezo-electric and allied phenomena in rochelle salt. *Phys. Rev.*, 17:475–481, 1921.

[74] J. D. van der Waals. Thermodynamische Theorie der Kapillarität unter Voraussetzung Stetiger Dichteänderung. *Z. Phys. Chem.*, 13:657–725, 1894.

[75] O. Vedmedenko. Micromechanical modeling of ferroelectric thin films and bulk ceramic materials. PhD-thesis, to be published at Universität Stuttgart.

[76] B. Völker, P. Marton, C. Elsässer, and M. Kamlah. Multiscale modeling for ferroelectric materials: a transition from the atomic level to phase-field modeling. to be published in "Continuum Mechanics and Thermodynamics".

[77] J. Wang and M. Kamlah. Domain control in ferroelectric nanodots through surface charges. *Applied Physics Letters*, 93(26):262904, 2008.

[78] J. Wang and M. Kamlah. Intrinsic switching of polarization vortex in ferroelectric nanotubes. *Physical Review B*, 80(1):012101, 2009.

[79] J. Wang, Y. Li, L. Q. Chen, and T.-Y. Zhang. The effect of mechanical strains on the ferroelectric and dielectric properties of a model single crystal - phase field simulation. *Acta Mater.*, 53:2495–2507, 2005.

[80] J. Wang, S.-Q. Shi, L.-Q. Chen, Y. Li, and T.-Y. Zhang. Phase-field simulations of ferroelectric/ferroelastic polarization switching. *Acta Mater.*, 52(3):749–764, 2004.

[81] J. Wang and T. Zhang. Phase field simulations of a permeable crack parallel to the original polarization direction in a ferroelectric mono-domain. *Engineering Fracture Mechanics*, 75(17):4886–4897, 2008.

[82] W. Wersing, W. Heywang, H. Beige, and H. Thomann. *Piezoelectricity: Evolution and Future of a Technology*, chapter The Role of Ferroelectricity for Piezoelectric Materials, pages 37 – 87. Springer-Verlag Berlin Heidelberg, 2008.

[83] Q. M. Zhang, W. Y. Pan, S. J. Jang, and L. E. Cross. Domain wall excitations and their contributions to the weak -signal response of doped lead zirconate-titanate ceramics. *J. Appl. Phys.*, 64(11):6445–6451, 1988.

[84] Q. M. Zhang, H. Wang, N. Kim, and L. E. Cross. Direct evaluation of domain-wall and intrinsic contributions to the dielectric and piezoelectric response and their temperature dependence on lead zirconate-titanate ceramics. *J. Appl. Phys.*, 75(1):454–459, 1993.

[85] W. Zhang and K. Bhattacharya. A computational model of ferroelectric domains. Part I: model formulation and domain switching. *Acta Mater.*, 53(1):185–198, 2005.

[86] W. Zhang and K. Bhattacharya. A computational model of ferroelectric domains. Part II: grain boundaries and defect pinning. *Acta Mater.*, 53(1):199–209, 2005.

[87] W. Zhong, R. D. King-smith, and D. Vanderbilt. Giant lo-to splitting sin perovskite ferro-electrics. *Phys. Rev. Lett.*, 72(22):3618–3621, 1994.

[88] Y. Zuo, J. Wang, and M. Kamlah. Effect of surface charges on the polarization distribution in ferroelectric nanotubes. *International Journal of Materials Research (formerly Zeitschrift fuer Metallkunde)*, 101(4):492–497, 2010.

Acknowledgment